LEAD-FREE FERROELECTRIC CERAMICS FOR ENERGY STORAGE AND ELECTROCALORIC COOLING APPLICATIONS

A Thesis Submitted to
the Graduate School of Engineering and Sciences of
İzmir Institute of Technology
in Partial Fulfillment of the Requirements for the Degree of

DOCTOR OF PHILOSOPHY

in Materials Science and Engineering

by
Merve KARAKAYA

December 2022
İZMİR

ACKNOWLEDGEMENTS

I would like to thank all the people who have contributed to my thesis study. I would like to thank my advisor Assoc. Prof. Dr. Umut Adem for giving me the opportunity to work on exciting projects and I am very grateful for his scientific guidance and encouragement in gaining deep learning skills and detailed research to accurate conclusions throughout my Ph.D. I would like to thank my committee members Prof. Dr. Ender Suvacı and Prof. Dr. Muhsin Çiftçioğlu, with whom we held many thesis progress seminars, for their great and invaluable contributions to completion of my thesis study. At the same time, I also thank my other committee members, Prof. Dr. Sedat Akkurt and Prof. Dr. Emre Yalamaç for their valuable comments and suggestions. I would like to thank my co-advisor Assoc. Prof. Dr. Yaşar Akdoğan and Assoc. Prof. Dr. Emre Erdem for their contributions and comments on EPR measurements of Mn doped samples. I would also like to thank Assoc. Prof. Dr. M. Barış Okatan for his contributions to indirect electrocaloric effect calculations and to Dr. Lovro Fulanovic for his direct electrocaloric measurements.

I would like to acknowledge the contributions of people who were members of Prof. Dr. Ender Suvacı's research group in Eskişehir Technical University; Muhammet Ali Ünal and Dr. Gökçe Yıldırım Özarslan for their synthesizing and characterizing of templated ceramics, and especially I thank very much to Ceren Aşkın Pekel for her great friendship and for XRD measurement of my energy storage ceramics.

I would like to thank Prof. Dr. Nandang Mufti, who is at State University of Malang, Indonesia, created a LabVIEW program that can automatically measure the temperature dependent dielectric constant during his visit to our laboratory. I would like to acknowledge İrem Gürbüz for her help during synthesizing of $BaTiO_3$-$Na_{0.5}Bi_{0.5}TiO_3$ ceramics.

I would like to thank Turkish Scientific and Technological Research Council (TÜBİTAK) via the project with the number 118M192 and İzmir Institute of Technology (IZTECH) for supporting me during this project.

And the thing that I felt most lucky for during my PhD process was that I had wonderful friends around me; Tuğçe Irmak, Melike Tokkan, Barış Yıldırım, Remziye Yıldız, Sümeyra Çiğdem Sözer, Tuğçe Özmen Egesoy, Cansu Akyol Karpuzcu, Eda

Argıtekin and Ezgi Oğur; I thank each of them very much for their wonderful motivations for their scientific and spiritual contributions, for the beautiful memories and friendships that I can't finish by writing here. I would also like to thank my colleagues; Ç. Meriç Güvenç, Keriman Şanlı, Arif Kurnia and Ceren Tengizdeniz with whom I worked in the laboratory, albeit for a short time for their friendships and for sharing their knowledge and experience.

Finally, I would like to thank my dear mother Hatice Günnar, dear father Şinasi Günnar, dear brother Mustafa Günnar and dear sister Semra Karaaslan for their unconditional support and always motivating me. I would like to thank so much to my dear husband Dr. Caner Karakaya for all his support and love. And I would like to thank my life my dear daughter Beyza Mina Karakaya for her joy of existence and indescribable motivation.

ABSTRACT

LEAD-FREE FERROELECTRIC CERAMICS FOR ENERGY STORAGE AND ELECTROCALORIC COOLING APPLICATIONS

This thesis study consists of five main chapters that include an introduction about the principles and applications of ferroelectrics and four chapters on different lead-free ferroelectric ceramic systems developed for the energy storage and electrocaloric cooling applications.

In the first chapter, the principles of ferroelectricity and dielectric, piezoelectric and pyroelectric properties of ferroelectrics are introduced followed by the applications considered in this thesis: Electrocaloric cooling and capacitive energy storage.

In the second chapter, the effects of bismuth lithium titanate incorporation into sodium bismuth titanate-barium titanate systems on the energy storage properties have been discussed. In addition, it has been calculated that these compositions have improved energy storage properties close to the high values obtained in the literature.

In the third chapter, the effect of two different manganese precursors on the probability of defect dipole formation, ferroelectric aging and resulting manganese valences of ceramics were investigated by manganese doping on barium strontium titanate base ceramics. In addition, their electrocaloric properties were investigated by indirect method.

In the fourth chapter, electrocaloric properties of barium titanate - sodium bismuth titanate systems has been investigated. The increase in tetragonality by sodium bismuth titanate incorporation has been verified by Rietveld refinement and those compositions were shown to be suitable for electrocaloric applications.

In the fifth chapter, a sodium bismuth titanate - potasium bismuth titanate composition which is in morphotropic phase boundary, was synthesized by templated grain growth method, and the effect of orientation on the electrocaloric effect was investigated by direct and indirect measurements.

ÖZET

ENERJİ DEPOLAMA VE ELEKTROKALORİK SOĞUTMA UYGULAMALARI İÇİN KURŞUNSUZ FERROELEKTRİK SERAMİKLER

Bu tez çalışması, ferroelektrik ilkelerin ve uygulamaların anlatıldığı bir giriş bölümü ile enerji depolama ve elektrokalorik soğutma uygulamaları için üretilen birbirinden farklı kurşunsuz ferroelektrik seramik sistemlerin ferroelektrik özelliklerini içeren beş bölümden oluşmaktadır.

Birinci bölümde, ferroelektrik ilkeleri ve ferroelektriklerin dielektrik, piezoelektrik ve piroelektrik özellikleri tanıtılmakta, ardından bu tezde ele alınan elektrokalorik soğutma ve kapasitif enerji depolama uygulamalarından bahsedilmektedir.

İkinci bölümde, bizmut lityum titanat bileşiminin sodyum bizmut titanat - baryum titanat sistemlerine katılmasının enerji depolama özellikleri üzerindeki etkileri araştırılmış ve ayrıca bu yeni kompozisyonun literatürde elde edilen yüksek değerlere yakın ve gelişmiş enerji depolama özelliklerine sahip olduğu hesaplanmıştır.

Üçüncü bölümde, baryum stronsiyum titanat bazlı seramiklerde iki farklı mangan öncülü kullanılarak mangan katkılanmasının kusur dipol oluşumu, ferroelektrik yaşlanma ve bunun sonucunda ortaya çıkan farklı mangan değerlikleri üzerindeki etkisi incelenmiştir. Ayrıca elektrokalorik özellikleri dolaylı yöntemle incelenmiştir.

Dördüncü bölümde baryum titanat - sodyum bizmut titanat sistemlerinin elektrokalorik özellikleri incelenmiştir. Sodyum bizmut titanat ilavesiyle tetragonalitedeki artış, Rietveld arıtımlarıyla doğrulanmış ve ayrıca bu bileşimlerin elektrokalorik uygulamalar için uygun olduğu gösterilmiştir.

Beşinci bölümde, şablonlu tane büyütme yöntemi ile morfotropik faz sınırında bulunan bir sodyum bizmut titanat - potasyum bizmut titanat bileşimi sentezlenmiş ve yönlendirmenin elektrokalorik etki üzerindeki etkisi doğrudan ve dolaylı ölçümlerle incelenmiştir.

TABLE OF CONTENTS

LIST OF FIGURES

Figure **Page**

Figure **Page**

Figure **Page**

Figure **Page**

LIST OF TABLES

ABBREVIATIONS

AFE	Antiferroelectric
AN	Silver Niobate, $AgNbO_3$
BLT	Bismuth Lithium Titanate, $Bi(Li_{1/3}Ti_{2/3})O_3$
BST	Barium Strontium Titanate, $Ba_{0.95}Sr_{0.05}TiO_3$
BT	Barium Titanate, $BaTiO_3$
CoP	Coefficient of Performance
DSC	Differential Scanning Calorimetry
E_b	Dielectric Breakdown Field
EC	Electrocaloric
E_c	Coercive Field
ECE	Electrocaloric Effect
E_i	Internal Defect Field
EPR	Electron Paramagnetic Resonance
ER	Ergodic Relaxor
GoF	Goodness of Fit
KBT	Potassium Bismuth Titanate, $K_{0.5}Bi_{0.5}TiO_3$
KNBT	Potassium Sodium Bismuth Titanate, $(K,Na,Bi)TiO_3$
KNN	Potassium Sodium Niobate, $K_{0.5}Na_{0.5}NbO_3$
LCR	Inductance, Capacitance and Resistance
MLCC	Multi-Layer Ceramic Capacitor
MPB	Morphotropic Phase Boundary
NBT	Sodium Bismuth Titanate, $Na_{0.5}Bi_{0.5}TiO_3$
NR	Nonergodic Relaxor
P-E	Polarization-Electric Field
P_m	Maximum Polarization
PNR	Polar-Nanoregions
P_r	Remnant Polarization
PVA	Polyvinyl Alcohol
PZT	Lead Zirconate Titanate, $Pb(Zr_{1-x}Ti_x)O_3$
RFE	Relaxor Ferroelectrics
R_{wp}	Weighted Profile R Factor

S-E	Strain-Electric Field
SEM	Scanning Electron Microscope
ST	Strontium Titanate, $SrTiO_3$
T_C	Curie Temperature
T_d	Depolarization Temperature
TGG	Templated Grain Growth
T_S	Shoulder Temperature
W_{loss}	Energy Loss
W_{rec}	Recoverable Energy Storage Density
XRD	X-Ray Diffraction
ΔT	Electrocaloric Adiabatic Temperature Change
η	Energy Storage Efficiency
$V_O^{\cdot\cdot}$	Oxygen Vacancy in Kröger Vink notation

CHAPTER 1

INTRODUCTION

1.1. Classification of Ceramics

Mainly, ceramics are classified according to their application fields and into two main categories; traditional ceramics and advanced ceramics (Figure 1.1). In our daily life, the traditional ceramics are used in numerous applications such as white wares, pottery, cement, insulators, and tiles and so on. The traditional ceramics are so named because they usually contain naturally produced clay and quartz materials.

The advanced ceramics can be subdivided into two categories; advanced structural ceramics and electroceramics (or functional ceramics) [1]. The importance of the structural ceramics is their mechanical properties and performance because they are used in withstanding areas. For examples, Alumina (Al_2O_3), Zirconia (ZrO_2), silicon carbide (SiC), silicon nitride (SiN) and Spinel ($MgAl_2O_4$) which are mostly known as structural ceramics and they are used for chemical inertness, as abrasives, cutting tools etc. [2].

Electroceramics play a crucial role in many technological areas such as energy harvesting, medical, transportation and information technologies. The materials studied in this thesis belong to the class of electroceramics. As the thesis focuses on properties of ferroelectric materials such as capacitive energy storage, electrocaloric effect and piezoelectric effect, an introduction on ferroelectricity and ferroelectric materials is necessary.

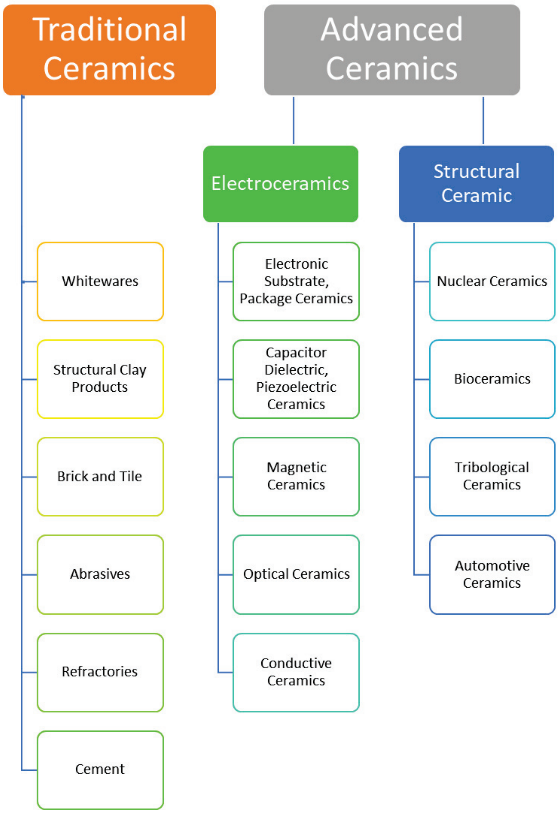

Figure 1.1. Application based classification of ceramics [1].

1.2. Ferroelectric Ceramics

Ferroelectricity was firstly discovered in 1921 by J. Valasek while his investigations on unusual dielectric and piezoelectric properties of Rochelle salt (potassium sodium tartrate tetrahydrate ($NaKC_4H_4O_6{\cdot}4H_2O$)) which was the first ferroelectric material [3]. After 14 years later the second ferroelectric material, potassium di-hydrogen phosphate (KH_2PO_4) crystal was emerged [4]. The third ferroelectric material, barium titanate ($BaTiO_3$) which is still being studied, was reported by A. von Hippel in the 1945 [5]. Barium titanate was a very significant discovery due to its ferroelectric structure without hydrogen bonds and having multiple ferroelectric phases. The most widely studied ferroelectric ceramic lead zirconate titanate (PZT), which has superior piezoelectric properties than barium titanate, was first discovered in 1952 [6]. However, since it contains lead, it is a toxic material and due to concerns of harm to the environment and human health, it is planned to ban the production of lead containing materials in several countries [7].

For that reason, lead free ferroelectric materials have received great interest due to their non-toxicity. However, there has been a need for the further development of lead-free ferroelectric materials due to their relatively lower piezoelectric properties compared to Pb-containing ones and the corrosiveness of some compositions containing alkali cations such as sodium bismuth titanate (NBT), potassium sodium niobate (KNN) and potassium bismuth titanate (KBT) [8]. On the other hand, synthesis of the some lead free ceramics might be challenging as some of them have limited sintering temperature range due to volatile characteristic of the constituting cations and therefore, it is difficult to maintain exact stoichiometry [9].

Before getting into the detail about origin and mechanism of ferrolectricity, classification of ferroelectrics should be introduced. There exist two different types of ferroelectrics according to their mechanisms of ferroelectricity; (1) displacive ferroelectrics (i.e. the off-centering of the B site cation with respect to the oxygen cage of ionic ceramics such as $BaTiO_3$ and $PbTiO_3$) and (2) order –disorder ferroelectrics (i.e. the crystals with hydrogen bonds such as KH_2PO_4 in which hydrogen atoms jump around some ordered subset of potential well).

Displacive ferroelectrics can be sub classified into four, based on their type of the crystal structure [10]; (1) Perovskite structure which has a general formula of ABO_3 (e.g. $PbTiO_3$) (2) Tungsten bronze structure which has a general formula of $(A1)_I2)_4(C)_4(B1)_2(B2)_8O_{30}$, (e.g. $SrNb_2O_6$) (3) Bismuth layered structure which has a general formula of $(Bi_2O_2)^{2+}(A_{m-1}B_mO_{3m+1})^2$ (e.g. $Bi_4Ti_3O_{12}$) and (4) Pyrochlore structure which has a general formula of $A_2B_2O_7$ (e.g. as: $La_2Zr_2O_7$).

Among these structures, the significant interest has been given to perovskite structured ferroelectric materials due to their exclusive and promoted properties by multiphase coexistence formations [11]. These perovskite type ferroelectric materials have many practical applications such as transducers, actuators, capacitors, energy harvesting, photovoltaic, electrocaloric devices, and infrared sensors [12].

1.2.1. Perovskite Structure and Ferroelectricity

Ferroelectric ceramics such as barium titanate ($BaTiO_3$), potassium niobate ($KNbO_3$), lead titanate ($PbTiO_3$), lead zirconate ($PbZrO_3$) and lead zirconium titanate ($PbZrTiO_3$) belongs to ABO_3 perovskite ferroelectrics. In this structure, A and B describe metal ions which have different ionic radii, the total charge of which is 6+. In order to exhibit ferroelectric behavior, the smaller ion must be of larger charge. For example, the radius of Ba^{2+} (1.35 Å) is bigger than the radius of Ti^{4+} ion (0.68 Å) in $BaTiO_3$. The ABO_3 type perovskite structure is demonstrated in Figure 1.2. The stability or distortion of perovskite structures is determined by Goldschmidt tolerance factor (t) which is an empirical and dimensionless number;

$$t = \frac{r_A + r_0}{\sqrt{2}(r_B + r_0)}$$

where r_A, r_B, and r_O are the ionic radii of the ions at the A and B-sites and oxygen, respectively in ABO_3 perovskite structure. For cubic perovskite structure favorable t value is in between 0.8 and 1.0 while, for tetragonal perovskite structure favorable t value is larger than 1 [13]. Tolerance factor smaller than 0.8, usually results in non-perovskite structures.

In Figure 1.2(a) unit cell of a centrosymmetric cubic perovskite structure that results in paraelectric property is shown and in Figure 1.2(b) non-centrosymmetric tetragonal perovskite structure that gives the ferroelectic property to the material is shown. Particularly, non-centrosymmetric displacement of the B-site ion causes the spontaneous polarization (dipole) along this direction and that is essential for the occurrence of ferroelectricity. Generally, ferroelectricity is defined as the property of materials which exhibits spontaneous electric polarization even in the absence of electric field and which exhibits hysteresis behavior by applying an alternating electric field. These properties are lost at the Curie temperature (T_C) at which the ferroelectric to the paraelectric phase transition occurs.

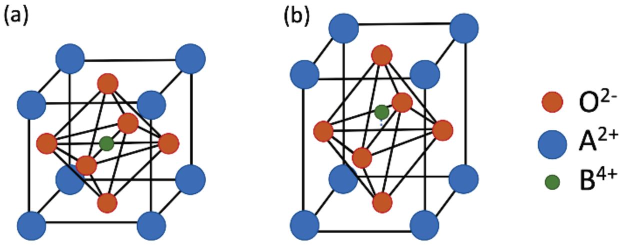

Figure 1.2. ABO_3 type perovskite structure; (a) cubic phase (paraelectric phase $T > T_C$) and (b) tetragonal phase (ferroelectric phase $T < T_C$).

Ferroelectric domains are formed by the uniform orientation of the spontaneous polarizations of the perovskite crystal together in the same direction. The separation regions of two different ferroelectric domains are called as domain walls. Ferroelectric domains are formed by the depolarizing fields minimizing their electrostatic energy [14]. A schematic representation of the 2-dimensional domain structure and 90º domain wall of a tetragonal perovskite $BaTiO_3$ sample is shown in the Figure 1.3. Ti centro-symmetric positions create spontaneous polarization dipoles and forms A and B domains. Here 2ω and ν represent the thickness and motion of the 90º domain wall separating the A and B domains.

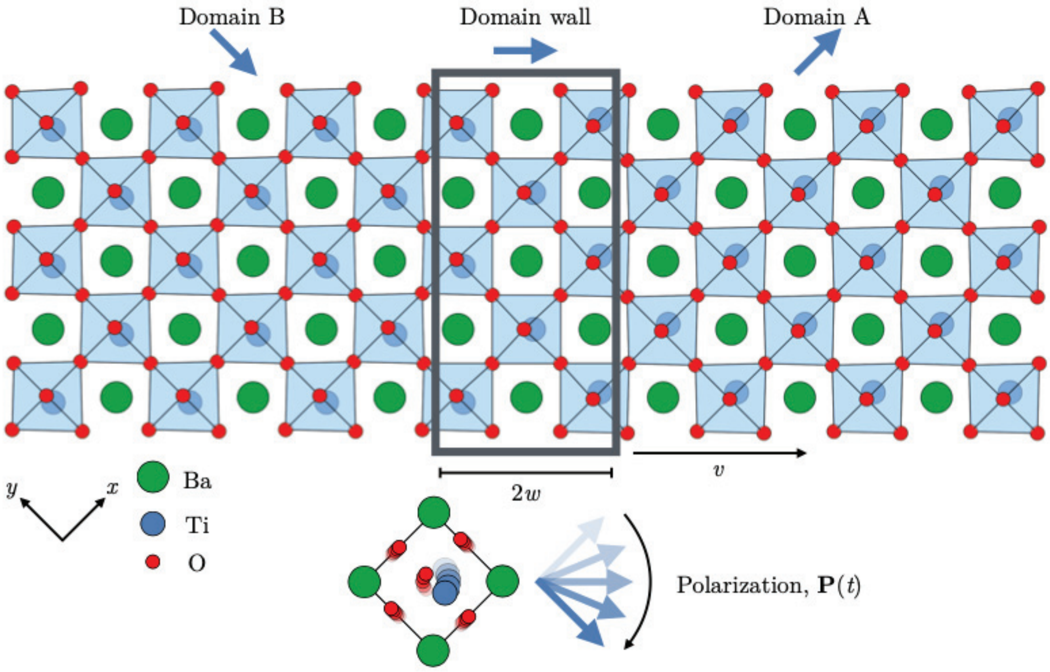

Figure 1.3. Schematic representation of the 2-dimensional domain structure and 90º domain wall of a tetragonal $BaTiO_3$ [15].

The reversing of the spontaneous polarization direction along the direction of applied electric field results in the hysteresis behavior which is caused by the presence of ferroelectric domains and consequence of the domain-wall switching. A typical polarization hysteresis loop of a ferroelectric material under alternating electric field is shown in Figure 1.4. The polarization increases linearly at initial electric field application. As the electric field increases, spontaneous polarization dipoles are gradually oriented and switch to an energetically favorable electric field direction by domain wall switching and motion. Further increase of the electric field, the amount of polarization no longer increases and begins to reach its saturation, which is called saturation polarization (P_S). The fact that to reach the maximum applied field (E_{max}) which causes the saturation polarization is important in terms of showing the real hysteresis behavior of the ferroelectric material. Consequently, the ferroelectric material has dielectric breakdown strength (E_b), and when the applied electric field is $E_{max}>E_b$, the ferroelectric material undergoes dielectric breakdown. When the electric field returns to zero, the polarization does not return back to the initial value because typical ferroelectrics display remnant polarization P_r even when the removal of electrical field. Spontaneous polarization dipoles or domains can only be switched if the applied electric field is larger than the coercive field, E_C. Therefore, E_C can be described as the electric field strength to switch the opposite polarization dipoles. Because only the coercive field which is opposite direction of polarization can bring the polarization to zero by switching domain walls into initial domain configuration. Therefore, P_r also represents the amount of switchable polarization.

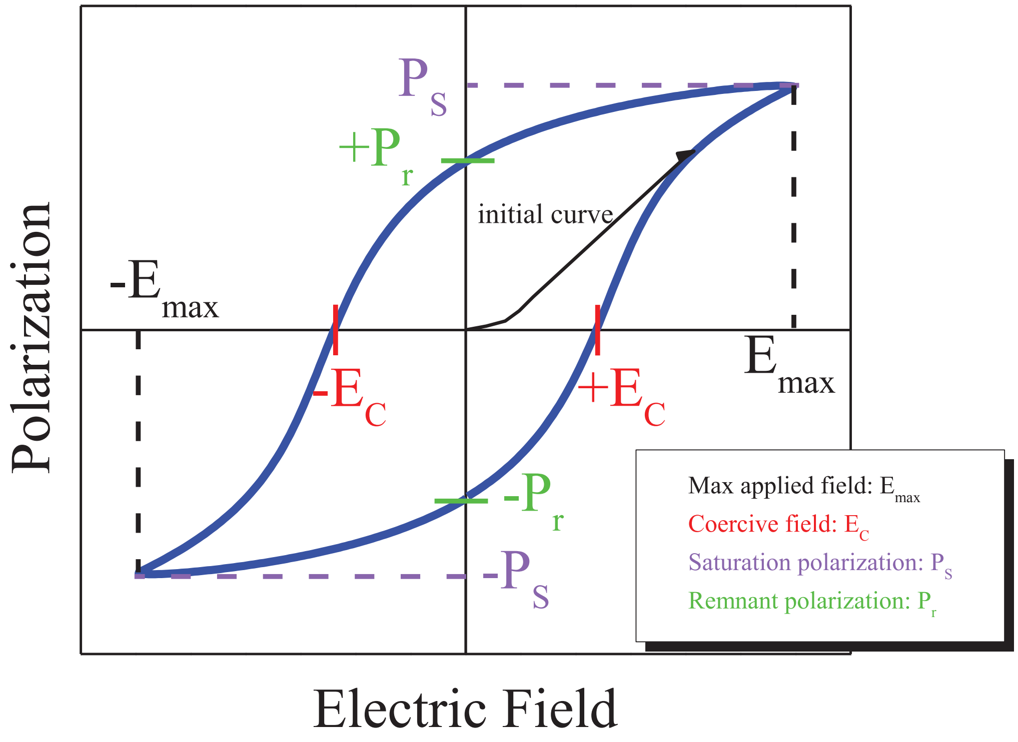

Figure 1.4. Polarization hysteresis loop of a typical ferroelectric material under alternating electric field.

1.2.2. Domain Structure in Ferroelectrics

Ferroelectric materials consist of domain regions in which the electric dipoles are oriented in the same direction. Spontaneous electric dipoles are oriented randomly in each domain that gives zero net polarization in the absence of electrical field as it seen Figure 1.5. The boundary of two neighboring domains is called a domain wall (the dashed lines in

Figure 1.5) as it is also mentioned above. Solid lines correspond grain boundaries of a polycrystalline ferroelectric. When an electric field is applied to this kind of a typical 180º domain structured ferroelectric material, the dipoles are switched along the direction of the applied electric field, and when the electric field is removed, it cannot return to its initial state remaining net polarization (P_r) inside.

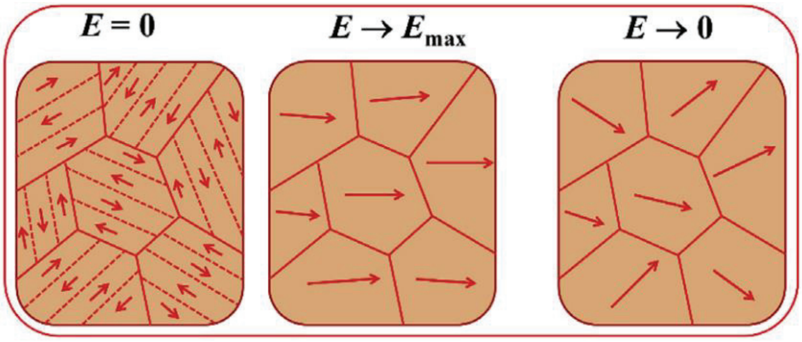

Figure 1.5. Schematic diagrams of domain wall switching in a normal ferroelectric [16].

The types of possible domain walls depend on the crystal structure type of a ferroelectric. For example an orthorhombic crystal can produce 60°, 90°, 120°, and 180° domain walls and a rhombohedral crystal can have 70.5°, 109.5° and 180° domain walls, and, a tetragonal perovskite ceramic can exhibit only two possible types of domain wall structures; 90° and 180° domain walls [17] (Figure 1.6) and consequently two types of polarization switching mechanisms are possible. The domain switching of a 180° wall requires higher activation energy than that of a 90° degree wall. On the other hand, 180° domain walls have higher internal stress and lower domain wall motion while 90° domain wall motion result enhanced electromechanical strain and piezoelectric coefficients [18].

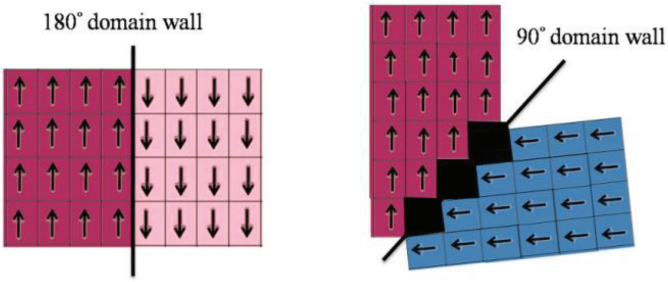

Figure 1.6. Two types of domain walls in the tetragonal crystal system: 180° and 90° domain walls [19].

Domains are generally arranged to ensure the minimum total internal energy of the sample i.e. minimizing mechanical, electrical and interfacial energy. The energy minimization states of ferroelectric domains give rise to some different patterns such as rank-1 and rank-2 laminates and vortex structures [20] (see Figure 1.7).

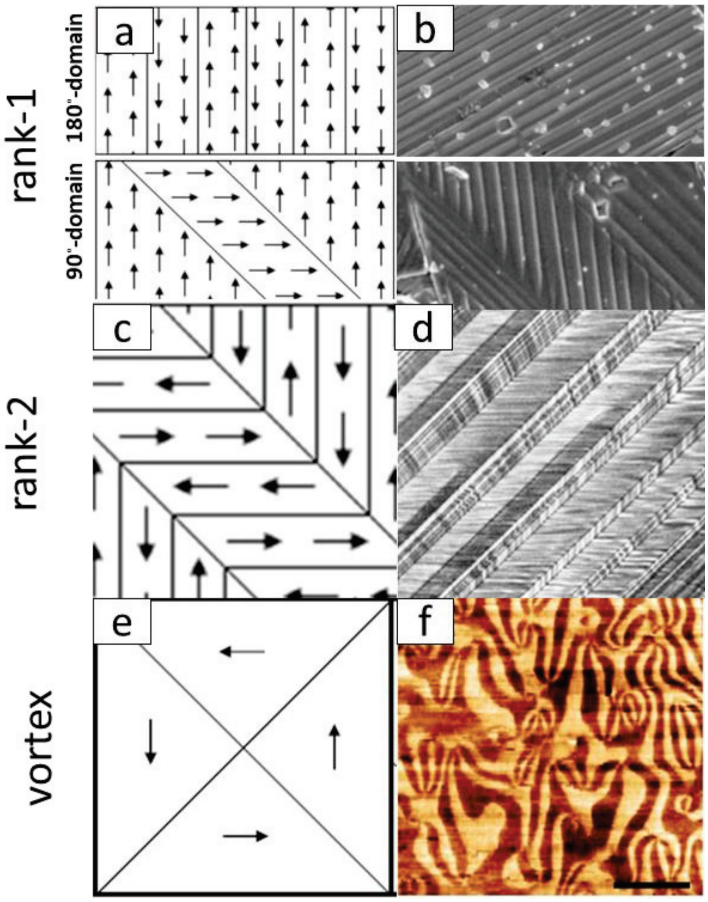

Figure 1.7. Schematic demonstrations (left) [21] and real images (right) of some kind of ferroelectric domains: (a) rank-1 laminated 90º and 180º domain patterns of (b) KNN ceramics [22], (c) rank-2 laminated (d) domain pattern in $BaTiO_3$ [23], (e) vortex domain pattern of (f) PFM image of h-$Lu_{0.6}Sc_{0.4}FeO_3$ [24].

Apart from crystal symmetry, one of the most important parameters that significantly affects the domain structure is grain size. Because, as the number of grain boundary increases, that is, as the grains get smaller, the internal stress energy will increase [25], therefore, the domain structure will be shaped according to this effect. In Figure 1.8 the relationship between grain size and domain structure is illustrated. Since the internal stress energy will decrease as the grain size increases (Figure 1.8(a)), the domain structures to provide the minimum energy configuration incline to the formation of 90° and more complex domains (for example, rank-2 type domains). In addition, it has been shown that the increase in grain size causes an increase in the domain width (Figure 1.8(b)) [26]. In another study, it was mentioned that the ceramic in the ergodic relaxor phase has small grain size and polar-nanoregions (PNRs) (Figure 1.8(c)) [27]. In (Figure 1.8(d)), the grain size dependent domain structure of $BaTiO_3$ nano-ceramics is demonstrated. While in larger grains 90° and 180° domains are both present with larger domain widths, in finer grains domain width decreases and 90° domains disappear.

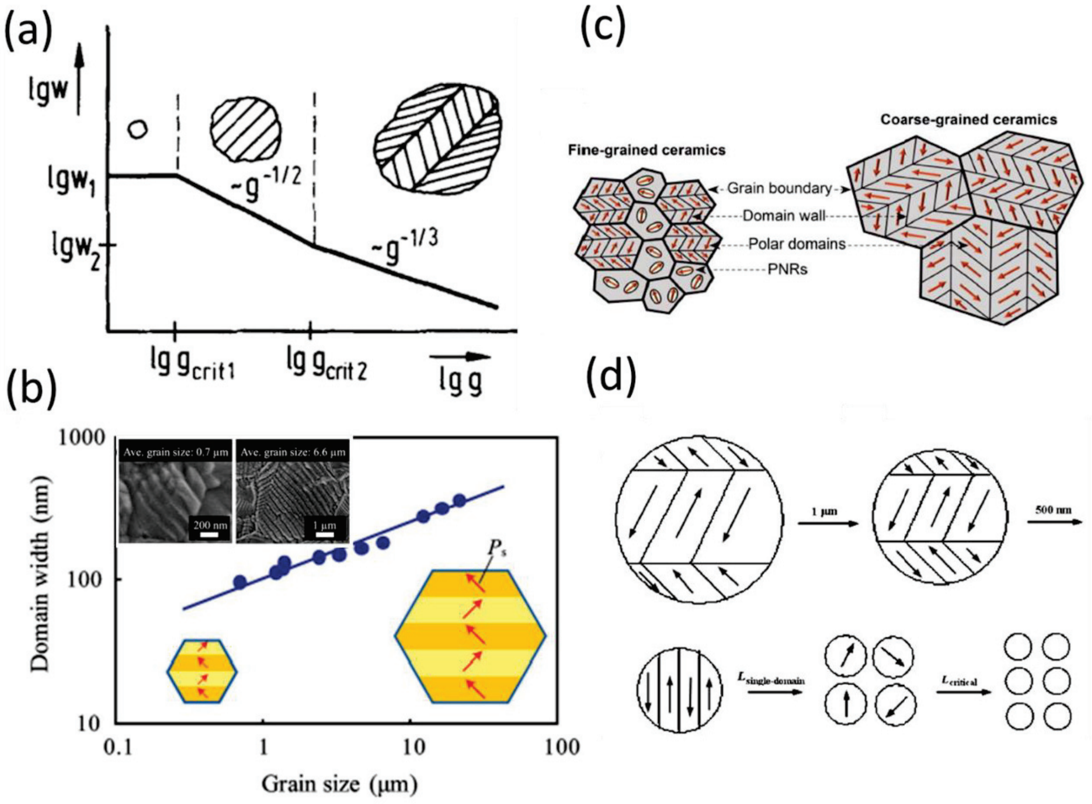

Figure 1.8. Relations between grain size and domain structure. (a) Stress energy (w) as a function of grain size (g) and domain structure in $BaTiO_3$ ceramics [25], (b) the grain size dependence of 90° domain width in $BaTiO_3$ ceramics [26], (c) long-range polar domains in coarse grained and polar-nanoregions (PNR) in fine grained NBT-xST ceramics [27], (d) the grain size dependent domain structure of $BaTiO_3$ nano-ceramics; 90° and 180° domains are both present with larger widths in larger grains [28].

Normal ferroelectric (FE) materials have large and long range ordered ferroelectric domain structures. If there are nano-sized polar regions in the ferroelectric material where the interaction of the domains with each other is weaker, this material is called a relaxor ferroelectric (RFE) material. The materials having polar nano-domain regions (PNRs) that can transform irreversibly into normal ferroelectric domains with the application of electric field are called nonergodic relaxor (NR) materials. If the PNRs transform into normal ferroelectric domains with the application of an electric field and reversibly turn back into the initial state when the electric field is removed, these materials having that kind of PNRs is called ergodic relaxor (ER) materials. Also, a NR material can transform into the ER phase as the temperature increases. The temperature at which this NR to ER phase transition takes place is defined as the depolarization temperature (T_d). Both temperature and electric field dependent phase diagram of NR, ER and FE phases of a relaxor material is shown schematically in Figure 1.9 where the black line represents the transition from the relaxor phase to the FE phase. This line disappears after a critical point (CP). Polarization-electric field (P-E) and strain-electric field (S-E) loops corresponding to NR and ER phases are shown schematically in this figure. Indeed, the P-E and S-E loops of a NR and of a normal FE material cannot be distinguished, however the difference between a normal FE and a NR material can be understood by examining the frequency dependence of the dielectric constant, because, relaxor ferroelectric materials have different polarization mechanisms depending on frequency, such as resonance polarization, beside thermally activated polarization mechanisms [29]. On the other hand, the characteristic of an ER material is the absence of negative strain and pinched P-E loops.

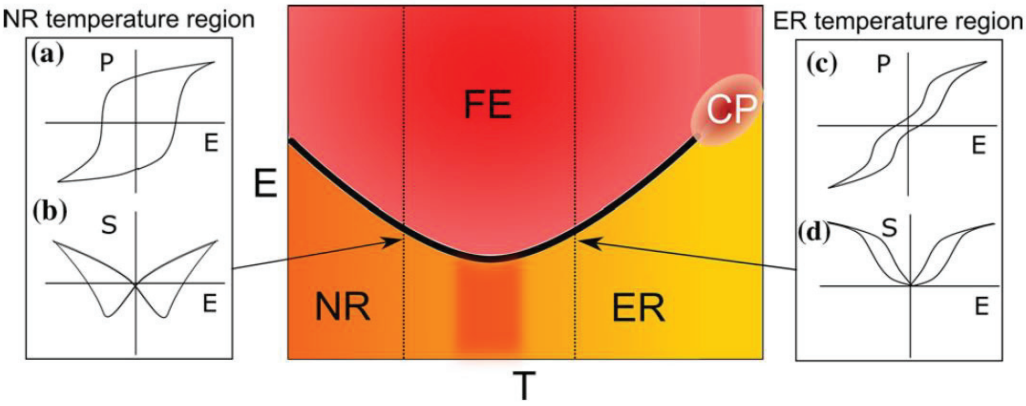

Figure 1.9. The temperature and electric field dependent phase diagram of NR, ER and FE phases of a relaxor material [30]

1.2.3. Classification of 32 Crystal Classes of Dielectrics

The Figure 1.10 demonstrates the classification of dielectrics according to crystallographic point group symmerty [31]. In total 32 types of crystallographic point groups exist (see Table A.1). Out of these 32 groups, 21 of them are in noncentrosymmetric and others are in centrosymmetric structures [32]. The only noncentrosymmetric groups can exhibit piezoelectric properties. However, one of these 21 noncentrosymmetric point groups (which is 432) cannot show piezoelectric property. The remaining noncentrosymmetric point groups that exhibit piezoelectricity are 1, 2, 3, 4, -4, 6, -6, m, 32, 23, 3m, 222, 422, 622, -42m, -43m, -62m, mm2, 4mm and 6mm. Among 10 of them, which are 1, 2, 3, 4, 6, m, 3m, mm2, 4mm, and 6mm, also exhibit pyroelectric properties [33]. There are 230 types of space groups belong to these 32 point groups [34]. $BaTiO_3$-based materials with P4mm and P4bm space group is grouped in tetragonal 4mm point group and NBT-based ceramics containing R3c space group included in the rhombohedral -3m point group were studied in this thesis (Figure 1.11).

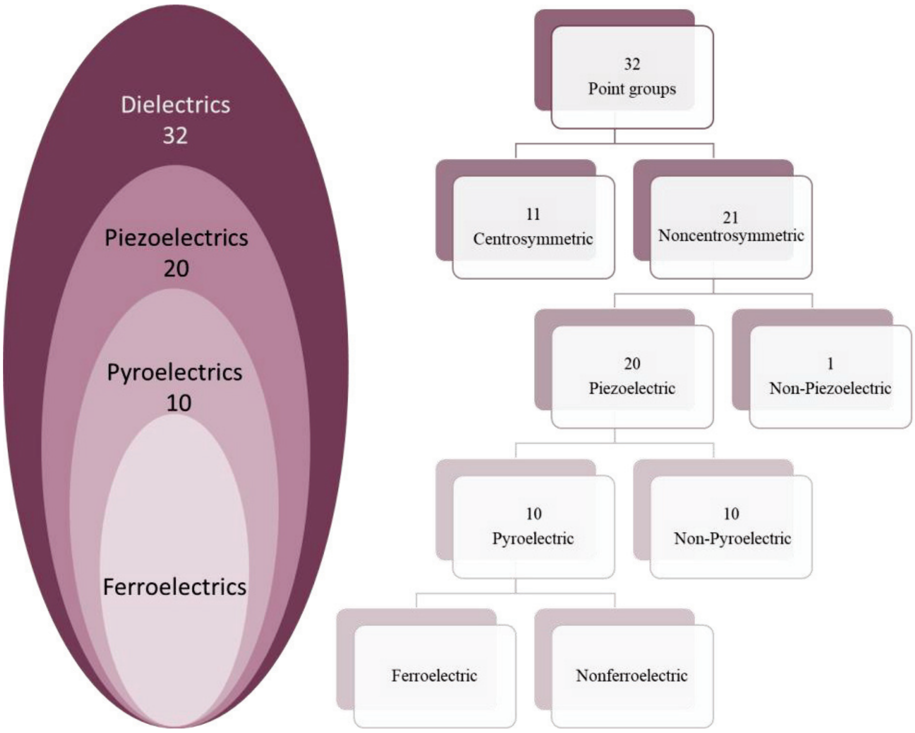

Figure 1.10. Ferroelectricity within the hierarchy of 32 crystal classes of dielectrics.

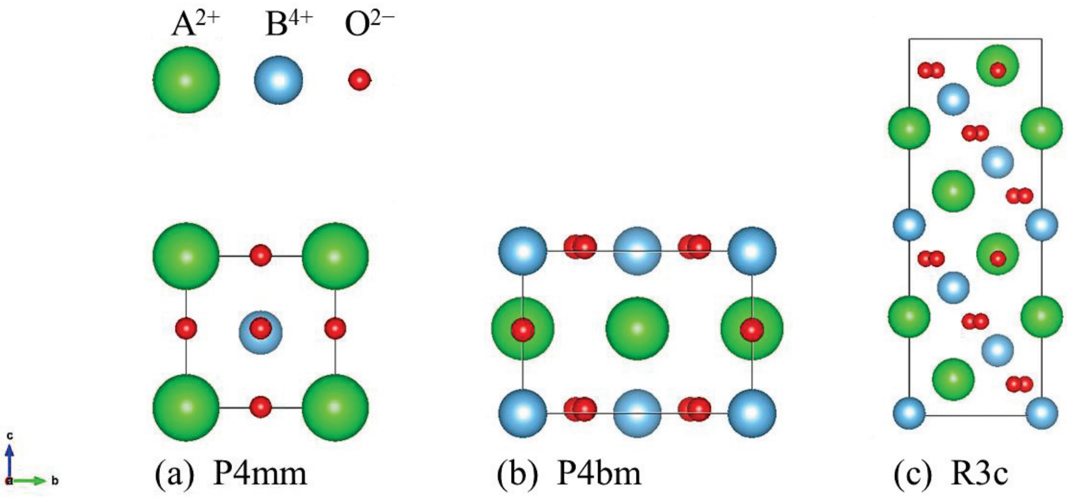

Figure 1.11. Illustrations of (a) tetragonal P4mm, (b) tetragonal P4bm and (c) rhombohedral R3c space group symmetries of ABO_3 type perovskite structures.

1.2.4. Dielectric Properties of Ferroelectrics

Dielectric constant (or relative permittivity, ε_r) describes the polarizability of a dielectric material when the application of electric field. This polarization can originate from interfacial space charges, dipolar, ionic, and electronic effects [35]. These mechanisms, which contribute to the polarization or dielectric constant, can be active or inactive depending on the material and frequency of the measurement. $BaTiO_3$ ceramic has a large dielectric constant thanks to its ferroelectric nature [5, 36].

When an electric field is applied to a dielectric material placed between conductive plates, the amount of stored charges per unit area by the orientation of the dipoles is called the electric displacement D and is expressed by the following equation;

$$\mathbf{D} = \varepsilon_0\mathbf{E} + \mathbf{P} = \varepsilon_r\varepsilon_0\mathbf{E} \tag{1.1}$$

where ε_r is relative permittivity (or dielectric constant) of the material ε_0 is the permittivity of the vacuum, P is the net polarization in material and E is the applied electric field. As P is large is ferroelectrics, P is more commonly used instead of D.

Dielectric constant of a material is determined by measuring capacitance of the material. In Figure 1.12 a dielectric material in thickness d which is sandwiched between two metal parallel plates of area A is illustrated. When these plates are attached to a circuit and applied a voltage V, the stored charge Q on plates can be measured by integrating the current with time. Therefore, the capacitance can be determined using the formula;

$$C = Q/V.$$

Using an LCR meter, capacitance (C) can be directly measured. There is also a relation between capacitance and dielectric constant (or dielectric permittivity) as follows;

$$C = \varepsilon(A/d)$$

where A is the area of the conductive plates, d is the thickness of the dielectric material and ε is the permittivity (or dielectric constant) that includes both permittivity contribution comes from air ε_o and the material, ε_r. The relation is given as; $\varepsilon = \varepsilon_o\varepsilon_r$. Therefore, the dielectric constant of material (ε_r) can be expressed as follows;

$$\varepsilon_r = \frac{C}{\varepsilon_O}\frac{d}{A}$$

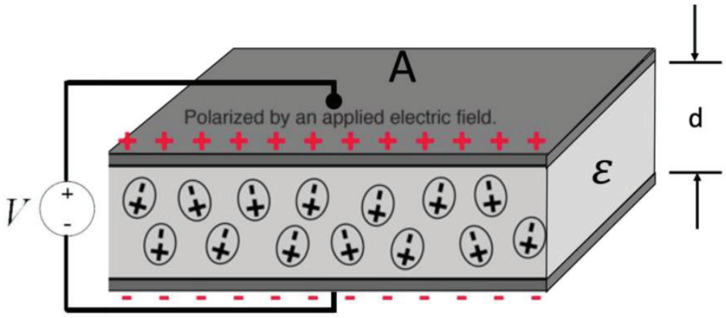

Figure 1.12. Schematic representation of parallel plate capacitor [37].

1.2.5. Structural Phase Transitions in Ferroelectrics

All ferroelectric materials lose their ferroelectric properties above the Curie temperature (T_C) which is also a structural phase transition point. At a temperature above T_C the material no more exhibits ferroelectric properties, it is in cubic structure and is paraelectric. At the transition temperatures, some properties such as dielectric constant, elastic, optical and thermal properties of the dielectric material show anomalous behavior.

The temperature dependence of the dielectric constant of a ferroelectric material gives the information about crystal symmetry, phase transition temperatures and ferroelectric domains. As shown in Figure 1.13, barium titanate undergoes three phase transitions when cooled down from high temperature: from cubic (or paraelectric phase) to tetragonal (ferroelectric phase) at T$_C$ ~ 120 °C, tetragonal to orthorhombic phase at 5 °C, and orthorhombic to rhombohedral phase at −90 °C. Note that orthorhombic and rhombohedral phases are also ferroelectric phases.

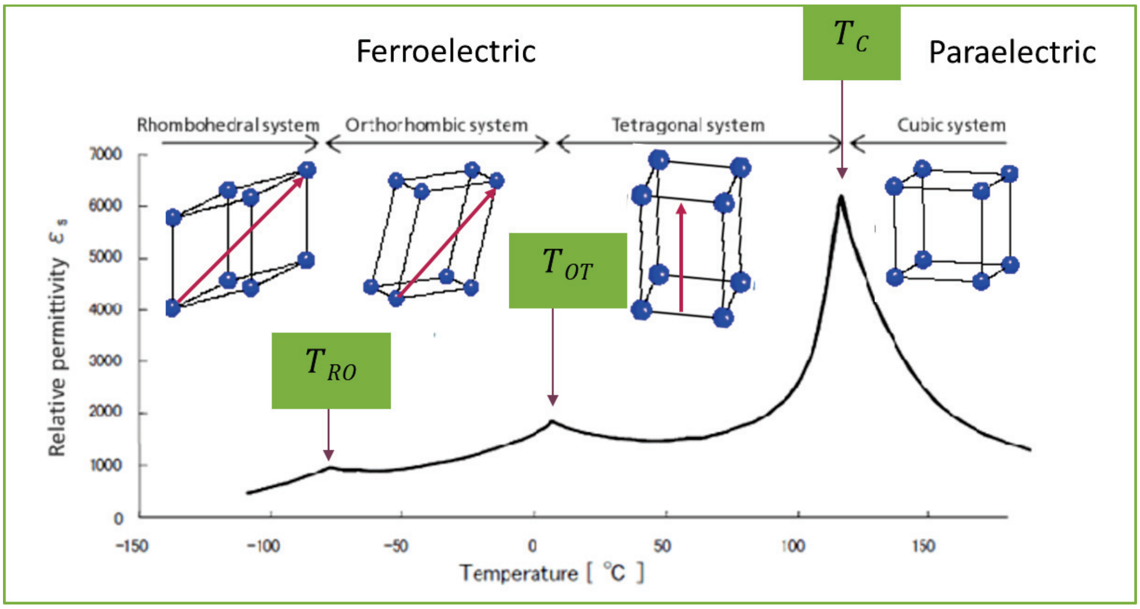

Figure 1.13. Temperature dependent dielectric constant (or relative permittivity, ε_r) of barium titanate and its structural phase transitions [38].

The phase transitions of the dielectric constant above the Curie point (T > Tc) is governed by the Curie-Weiss law:

$$\varepsilon_r - \varepsilon_0 = \frac{C}{T - T_C}$$

where C is the Curie constant and T$_C$ is the Curie temperature. This relation states that the dielectric constant decreases above T$_C$ following this Curie-Weiss law.

The spontaneous polarization might decrease to zero either continuously (second order phase transition) or discontinuously (first order phase transition) at T$_C$ in Figure 1.14. In order to explain these two types of transition characteristics, Landau theory [39] gives an approach by thermodynamical, statistical (degrees of freedom of the system) and symmetry based arguments. As the consequence of the Landau theory, the spontaneous polarization dependent free energy functions for first and second order types of transitions in ferroelectrics are shown in Figure 1.15.

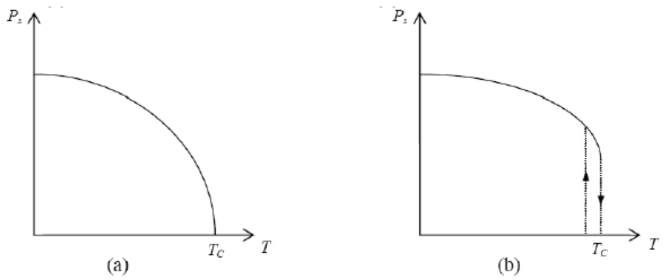

Figure 1.14. Characteristic behavior of (a) second order and (b) first order phase transition of spontaneous polarization as the function of temperature in ferroelectrics [40].

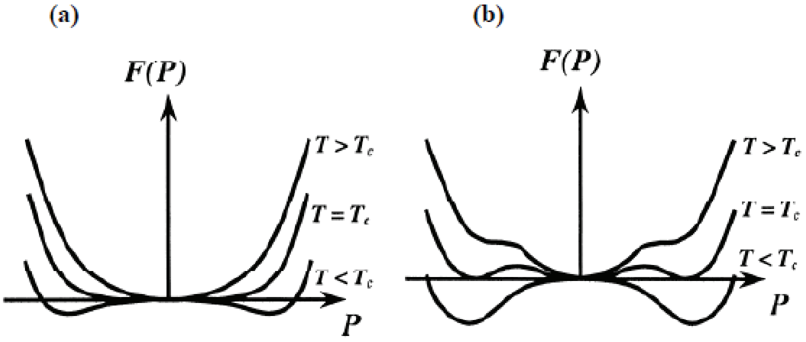

Figure 1.15. The spontaneous polarization dependent free energy functions for (a) second and (b) first order types of transitions [40].

Another important phase transition line is the morphotropic phase boundary (MPB) at which more than one ferroelectric phase exists. In Figure 1.16 the compositional phase diagram of lead zirconate titanate (PZT) is given. PZT ($Pb(Zr_{1-x}Ti_x)O_3$) ceramic is a solid solution in which Zr and Ti occupy the B site of the perovskite structure in varying proportions. The morphotropic phase boundary that corresponds exactly x = 48 mol% of $PbTiO_3$ composition is the boundary between the rhombohedral and tetragonal phases and it is most widely used composition because the coexistence of these two structural phases provides PZT its high piezoelectric coefficient [41].

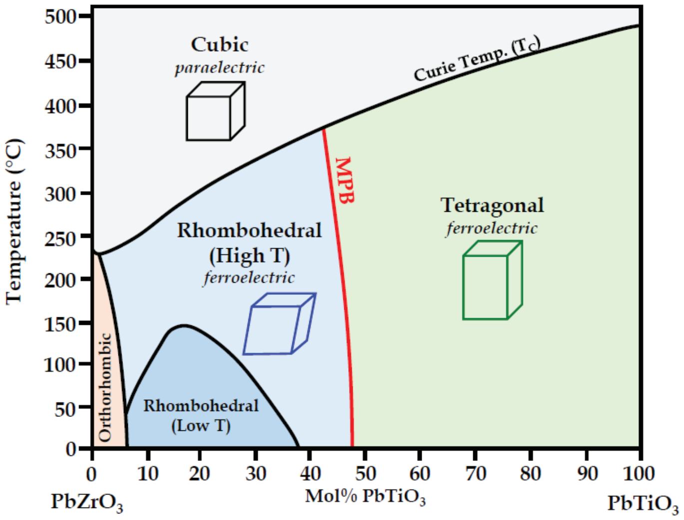

Figure 1.16. Structural phase diagram of PZT as a function of $PbTiO_3$ content. The red line represents MPB at which the rhombohedral and tetragonal phases coexist [42].

1.2.6. Piezoelectric Properties of Ferroelectrics

Piezoelectricity is ability of certain materials to develop an electric dipole moment when stress is applied, whose magnitude is directly proportional to the applied stress. This is known as the direct piezoelectric effect. It was discovered by the brothers Pierre and Jacques Curie in 1880 [43] The 'Piezo' is derived from the Greek word 'piezein' which infers to squeeze or press. Perovskite oxides exhibit piezoelectricity, among them the mostly known piezoelectric material $Pb(Zr_{0.52}Ti_{0.48})O_3$ (PZT) exhibits greater piezoelectricity due to its improved properties [44] around the morphotropic phase boundary that consists of tetragonal and rhombohedral phases as mentioned before. According to the direct piezoelectric effect, the polarization (P_i) (or electric field) is emerged within the piezoelectric material when the stress (σ_{jk}) is applied;

$$P_i = d_{ijk}\,\sigma_{jk},$$

where ijk denotes tensor elements and d_{ijk} refers the piezoelectric coefficient.

The opposite effect is also possible; according to converse piezoelectric effect, when the electric field (E_i) applied to a piezoelectric material, a strain (ε_{jk}) (or a thickness change) is emerged within the material;

$$\varepsilon_{jk} = d^{*}_{ijk}\,E_i$$

where ijk denotes tensor elements and d^{*}_{ijk} refers the converse piezoelectric coefficient.

1.2.7. Pyroelectric Properties and Electrocaloric Effect

Pyroelectricity is the ability to create an electric field when certain materials are heated or cooled. In other words, temperature change in a pyroelectric material causes the migration of positive and negative charges to opposite ends of the surfaces of its crystal structure and electric charges (Q) and hence potential differences (V) are created. The pyroelectric effect can be described as;

$$p_i = \frac{\partial P_i}{\partial T}$$

This equation describes that the change in the polarization (P_i) with temperature (T) equals to the pyroelectric coefficient (p_i). The electrocaloric effect can be thought of as a physical inverse of the pyroelectric effect, since when an electric field is applied to a pyroelectric material, a temperature change can be obtained in that material, thus the electrocaloric effect is emerged.

Electrocaloric effect (ECE) is a physical phenomenon that occurs in dielectrics [45]. When an electric field applied to dipolar material, dipoles become more regular (entropy-reducing effect), adiabatically, the lattice vibrations become more irregular (entropy- increasing effect) in order to compensate entropy, thus temperature increases. Then the isoelectric process (constant electric field) occurs automatically. While the dipoles continue to be regular, lattice vibrations are reduced to return to the previous temperature, thereby reducing total entropy. When the electric field is removed, adiabatic depolarization process starts. As dipoles become irregular again, (entropy-increasing effect) and lattice vibrations decrease (entropy reducing effect) consequently entropy is maintained thus system cools down (Figure 1.17). The system then returns to its initial state, and the electrocaloric cycle takes place where entropy and temperature change occur (Figure 1.8) [46].

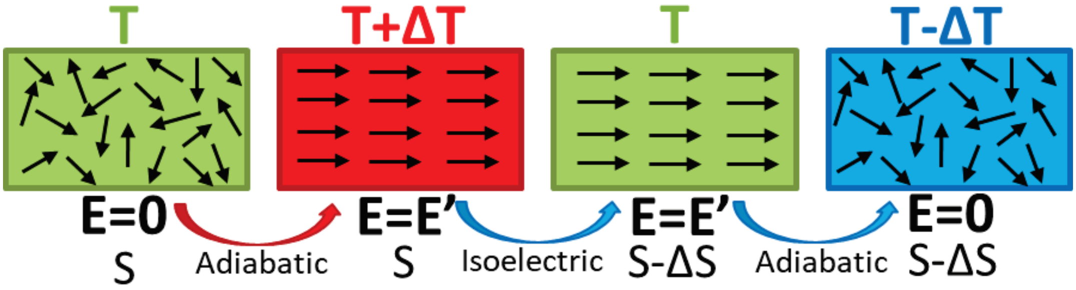

Figure 1.17. Schematic demonstration of the electrocaloric effect.

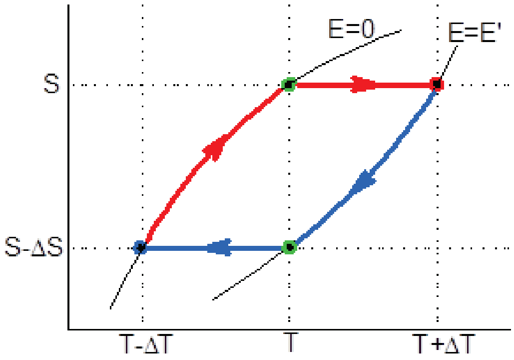

Figure 1.18. Schematic demonstration of the entropy change during the electrocaloric cycle.

The energy of this thermodynamic system is defined by Gibbs free energy (G) equation that include the entropy (S) temperature (T) polarization (P) and electric field (E) variables as follows:

$$dG = -SdT - PdE$$

According to this expression, Maxwell equations are defined as follows;

$$\left(\frac{\partial S}{\partial E}\right)_T = \left(\frac{\partial P}{\partial T}\right)_E$$

The electrocaloric effect is calculated in the case where the entropy change remains constant (adiabatic process). Therefore, the following equation expressing the entropy change is equal to zero;

$$dS = \left(\frac{\partial S}{\partial E}\right)_T dE + \left(\frac{\partial S}{\partial T}\right)_E dT = 0$$

The specific heat (C_E) expressed as;

$$C_E = \frac{T}{\rho}\left(\frac{\partial S}{\partial T}\right)_E$$

By using these equations and Maxwell equation, the electrocaloric effect or differential temperature change is expressed as follow:

$$dT = -\frac{T}{\rho C_E}\left(\frac{\partial P}{\partial T}\right)_E dE$$

where $\left(\frac{\partial P}{\partial T}\right)_E$ expression corresponds to pyroelectric coefficient. Measuring the temperature and electric field dependent polarization loops P(E,T), the adiabatic temperature change (ΔT) of the material can be calculated by integrating the above equation;

$$\Delta T = \frac{1}{\rho C_E} \int_{E_1}^{E_2} T \left(\frac{\partial P}{\partial T}\right)_E dE$$

where the specific heat C_E and the density ρ of the material are considered as temperature and electric field independent.

1.3. Cooling Applications and Electrocaloric Cooling

Cooling systems used to prevent a process or environment from overheating or to remove heat have an important place in many industries. It is crucial to develop properties of the cooling systems such as efficiency, energy saving, harmful gas emission, cost and contact sizes in order to stabilize the operating temperature precision of electronic components. In general, the energy consumed by the cooling systems covers 10% of the total electricity consumption in the world [47]. The significant environmental damage of air conditioning and refrigeration is the emission of hydrofluorocarbon (HFC) gases, and its impact on global warming can be thousands of times greater than that of CO_2 per unit mass [48]. For these reasons the development of alternative refrigeration technologies which are energy efficient with zero global warming potential is therefore regarded as a critical issue.

In refrigeration and air conditioning technologies, vapor compressors and heat pumps, which cause the harmful gas emission, are used as the essential cooling components. Alternatively, environmental-friendly and non-vapor compression based solid state cooling technologies have been developed in recent years such as thermoelectric effect (TE) [49], magnetocaloric effect (MCE) [50], electrocaloric effect (ECE) [51], elasto (baro) caloric effect [52], adsorption cooling effect [53] and enhanced radiative cooling effect [54]. Among these technologies, electrocaloric cooling materials are one of the most widely studied caloric materials due to their high efficiency potential. It was mentioned above (in section 1.2.7) that ECE is a material property that shows the adiabatic temperature change (ΔT) with an applied electric field. The ECE phenomenon is driven by electric field which eliminates need for large compressors, pumps, or magnets [46]. Because ECE has the advantages of high cooling efficiency

(>60%) [55] and environmental friendliness, an ECE cooling device has the potential to surpass conventional thermomechanical devices [56]. In recent years, tremendous progress has been made in improving the electrocaloric effect of materials that exhibit a first- or second-order ferroelectric phase transition. The electrocaloric properties of different types of ferroelectrics are listed in Table 1.1 and they are compared by using electrocaloric adiabatic temperature change (ΔT) as a function of the applied electric field in Figure 1.19.

Although polycrystalline bulk ceramics can withstand relatively lower electric field and exhibit lower ΔT value than thin films, they are important in research and development in terms of obtaining rapid information about the properties of the composition. It is seen that the increased ΔT properties are emerged for film ceramics which are produced by more advanced methods. Additionally, multi-layer ceramic capacitors (MLCCs), the commercially widely produced capacitor forms, which are devices in which 0.5-40 μm thick individual capacitors [57] are contained as multilayer stacks, have more advanced ΔT properties. On the other hand, it is seen that PVDF-based polymer and polymer-ceramic composites have the highest ΔT value. However, due to the low thermal conductivity of polymers, the use of thin films of no more than a few tens of micrometers is required for adequate heat transfer to occur. Ceramic electrocaloric materials are more advantageous than ferroelectric polymers since thicker and high-mass electrocaloric devices can be produced with ceramic materials with higher thermal conductivity and they can be processed at higher temperatures [58].. The T parameter in Table 1.1, which is the temperature value at which ΔT maximum is realized (related to the Curie temperature or depolarization temperature of the material), is around room temperature for most electrocaloric materials, while for some materials it can reach 220 °C. In other words, the working temperature, T is important in material selection according to the demands of the cooling application. On the other hand, the ECE strength expression, ΔT/ΔE is another important parameter in EC material selection since it expresses the amount of ΔT obtained per applied electric field.

Table 1.1. The list of electrocaloric properties of different types of ferroelectrics.

Sample type	Sample	ΔT (K)	E (kV/cm)	ΔT/ ΔE (K.m/MV)	T_C (°C)	Ref.
Bulk ceramic	$Pb(Sc_{0.5}Ta_{0.5})O_3$	3.7	40	0.925	25	59
Bulk ceramic	$Ba(Zr_xTi_{1-x})O_3$	2.4	30	0.800	113	60
Bulk ceramic	$Ba_{0.6}Sr_{0.4}TiO_3$	2.46	50	0.820	30	61
Bulk ceramic	$Ba(Sn_{0.11}Ti_{0.89})O_3$	0.63	20	0.315	44	62
Bulk ceramic	$Ba_{0.89}Hf_{0.11}TiO_3$	0.35	10	0.350	70	63
Bulk ceramic	$0.68Ba(Zr_{0.2}Ti_{0.8})O_3$–$0.32(Ba_{0.7}Ca_{0.3})TiO_3$	0.33	20	0.170	63	64
Bulk ceramic	$0.85K_{0.5}Na_{0.5}NbO_3$–$0.15SrTiO_3$	1.9	159	0.120	67	65
Bulk ceramic	$0.7Pb(Mg_{1/3}Nb_{2/3})O_3$–$0.3PbTiO_3$	1.55	50	0.310	170	66
Bulk ceramic	$PbZrO_3$	-1.5	100	0.150	97	67
Bulk ceramic	$Pb_{0.97}La_{0.02}(Zr_{0.80}Sn_{0.14}Ti_{0.06})O_3$	-14.1	110	1.280	50	68
Bulk ceramic	$BaTiO_3$	0.5	6	0.833	128	69
Bulk ceramic	Glass modified-$Ba_{0.65}Sr_{0.35}TiO_3$	1.7	30	0.566	25	70
Thin film	$PbZr_{0.95}Ti_{0.05}O_3$	12	480	0.250	226	71
Thin film	$(Pb_{0.86}La_{0.08})(Zr_{0.65}Ti_{0.35})O_3$	40	1200	0.333	45	72
Thin film	$PbZr_{0.8}Ti_{0.2}O_3$	0.1	67	0.015	25	73
Thick film	$BaZr_{0.2}Ti_{0.8}O_3$	4.9	97	0.510	40	74
Thick film	$0.9Pb(Mg_{1/3}Nb_{2/3})O_3$–$0.1PbTiO_3$	0.23	105	0.022	25	75
MLCCs	$(Cd_{0.83}Pb_{0.17})_2Nb_2O_7$	0.8	100	0.080	-179	76
MLCCs	$Pb(Sc_{0.5}Ta_{0.5})O_3$	3.5	125	0.280	18	77
MLCCs	Doped $BaTiO_3$	3.5	300	0.017	47	78
MLCCs	$BaTiO_3$	1.8	176	0.100	80	79
MLCCs	$BaTiO_3$	7.1	800	0.088	80	80
MLCCs	$Pb(Sc_{0.5}Ta_{0.5})O_3$	13	158	0.844	30	81
Polymer	P(VDF-TrFE) 68/32 mol. %	20	1600	0.125	33	72
Polymer	P(VDF-TrFE-CFE) 59.2/33.6/7.2 mol. %.	16	1500	0.110	30	82
Polymer	P(VDF-TrFE-CFE)	4	1000	0.040	27	83
Polymer	P(VDF-TrFE-CFE) 62.6/29.4/8 mol. %.	5.2	900	0.058	25	84
Polymer	P(VDF-TrFE-CFE)	7.5	500	0.015	36	51b
Composite	Terpolymer/BNNSs/BST67	50.5	2500	0.202	30	85
Composite	P(VDF-TrFE)/BST75 52/48 mol.% 10 vol.%	2.5	600	0.042	79	86
Composite	Terpolymer/PMN-PT 59.4/33.4/7.2 mol. %	31	1800	0.170	30	87
Composite	Polymer/graphene	5.2	400	0.130	25	88

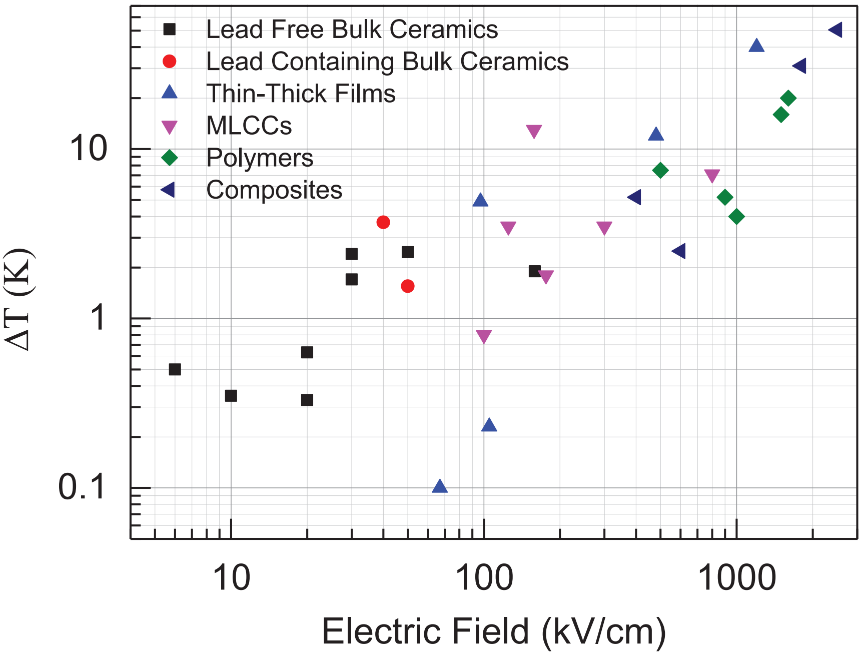

Figure 1.19. Comparison of electrocaloric adiabatic temperature change vs electric field of different types of ferroelectrics (see the references of Table 1.1).

Another important issue in cooling applications is the cooling module design and architecture. Besides ΔT, the coefficient of performance (COP) (the ratio of heat pumping power over input power) is considered in device architecture of the cooling systems. An example of an EC module design schematic is shown in Figure 1.20(a), where $Pb(Sc_{0.5}Ta_{0.5})O_3$ is used as EC material in MLCC form, which is known to have high ΔT as a bulk material.Temperature span of ΔT = 5.2 °C is obtained by designing this device structure [89]. Figure 1.20(b) shows the Brayton cycle occurring in each MLCC and schematizes how the total adiabatic temperature changes ΔT from all MLCCs increases. Figure 1.20(c), shows the photograph of an MLCC used in the module. Another example of EC prototype design is shown in Figure 1.21. In this study, a parallel plate active EC regenerator design based on lead scandium tantalate multilayer capacitors was first modeled (Figure 1.21(a)) and then the prototype was produced and the maximum temperature range of ΔT = 13.0 K was measured [81]. This study is important as it shows that EC materials are among the promising candidates for cooling applications.

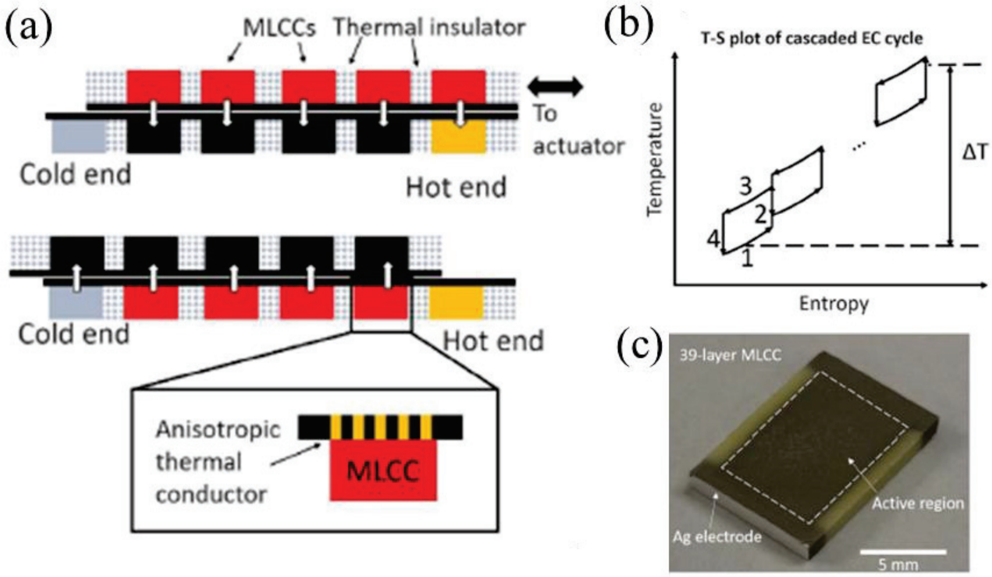

Figure 1.20. An example of EC cooling module design; (a) upper and lower units of heat transfer EC modules, (b) a schematic of the Brayton loop observed for each MLCC, and (c) an MLCC photograph. [89].

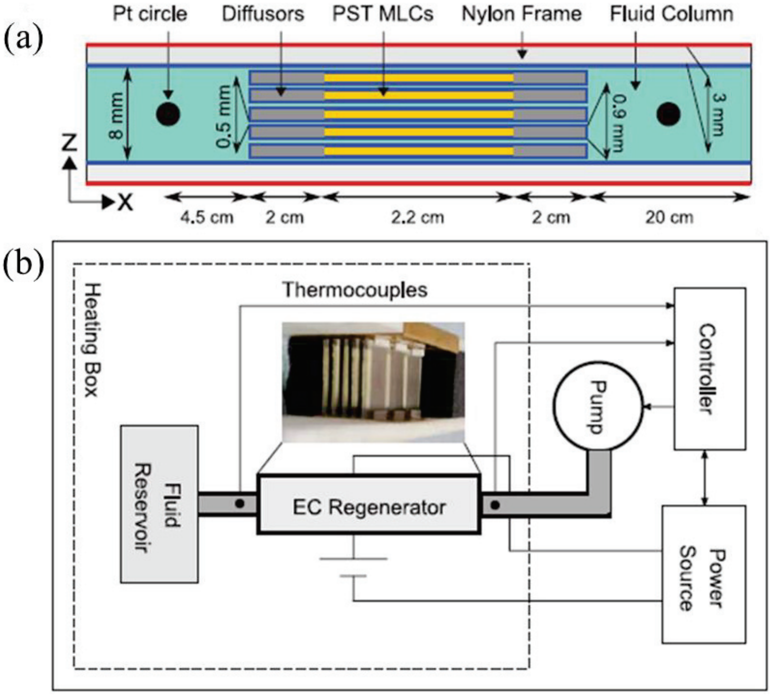

Figure 1.21. (a) A parallel plate EC regenerator model and (b) schematic of its prototype of measurement setup [81].

1.4. Experimental Methods

In this section, general information about the synthesis and characterization methods of ferroelectric ceramics produced in this study is given. More detailed information for each ceramic produced in this study is available in the experimental sections of the following chapters.

1.4.1. Synthesis Methods

Advanced ceramics are generally produced by powder processing route in four typical steps and different methods can be used in each steps [90]. These processing steps and some examples of methods are illustrated in Figure 1.8. In this study, three different types of ceramic compositions mentioned in the 2nd, 3rd and 4th chapters were produced by the conventional solid state reaction method by pressing powders into pellet form and sintering in atmospheric conditions. In 5th chapter, the textured ceramics were synthesized by templated grain growth (TGG) method [91] in which conventional solid state reaction method is used to obtain powders and tape casting is used for texturing by including single crystal templates and then samples were sintered in atmospheric conditions.

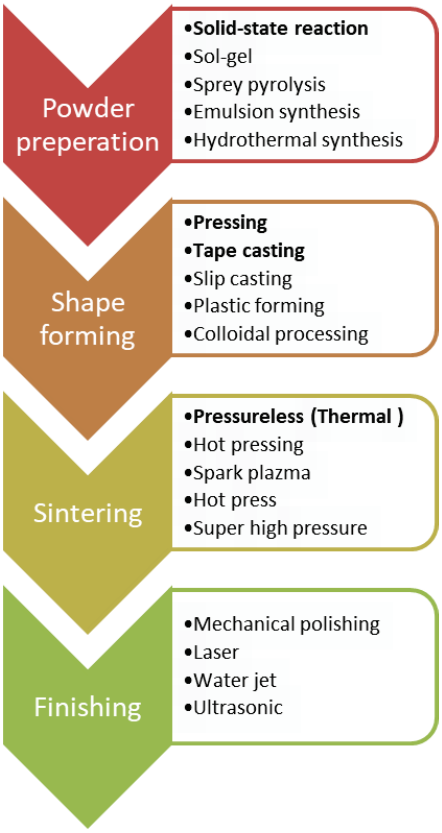

Figure 1.22. Some producing methods applied in four typical processing steps for advanced ceramics [90a].

1.4.1.1. Conventional Solid State Reaction

The conventional solid state reaction method was used to prepare the ceramics with various compositions in this thesis (Figure 1.23). The starting raw powders which are in oxide or carbonate form were pre-dried at 200 ºC for overnight. The powders were mixed in a Nalgene bottle using zirconia balls in ethanol media by planetary ball milling. After drying, the powder was ground in an agate mortar. The calcination process was carried out in pellet form. After the calcination, the pellets were again ground into powder in an agate mortar and then the powders were mixed thoroughly with 4 wt% polyvinyl alcohol (PVA) binder and water solution and then ball milled again. Then powders were dried, sieved and pressed into pellets (~10 mm in diameter, ~1 mm thick) under a pressure ~100 MPa. Then the PVA binder was burned out at 600 ºC for 4 h for all compositions. After the burnout process the pellets were sintered.

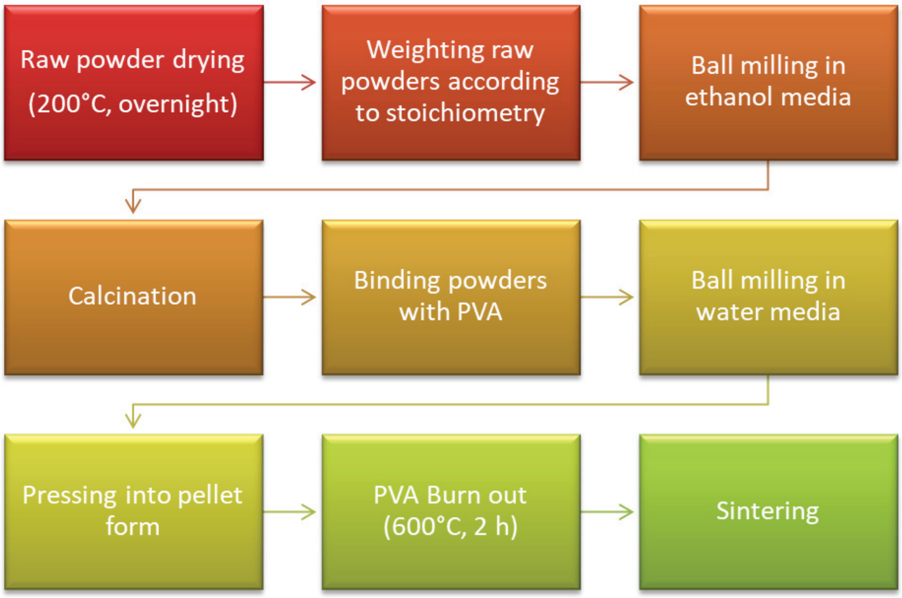

Figure 1.23. Schematic illustration of the conventional solid state synthesis routes.

1.4.1.2. Texturing and Templated Grain Growth (TGG) Process

In order to produce textured ceramics, firstly powders were calcined. After calcination, powders were homogeneously ground and mixed in an attritor mill at the desired stoichiometric ratios. The templated grain growth process steps were followed after this stage: Single crystal templates that have crystallographic surface in polar orientation were used. The tape casting production of the samples with various rates of templates was carried out. Details of the slurry recipe are available in the M. Ali Ünal's thesis study [92]. Using this recipe, ceramics were tape casted as shown schematically in Figure 1.24. Afterwards, they were cut into 1 cm^2 pieces and stacked on top of each other so that the approximate height was 1 mm after pressing and pressed with a laminating press. Pressing was done at 30 °C with a pressure of 100 MPa. Heat treatment was applied to the 1 cm^2 pieces in the furnace for binder burnout. The binder burnout process was carried out at 400 °C for 1 hour, and 600 °C for 6 hours. After binder burnout, the obtained raw samples were pressed with CIP at 300 MPa pressure for 10 seconds. Afterwards, all samples were sintered at 1150 °C for 24 hours.

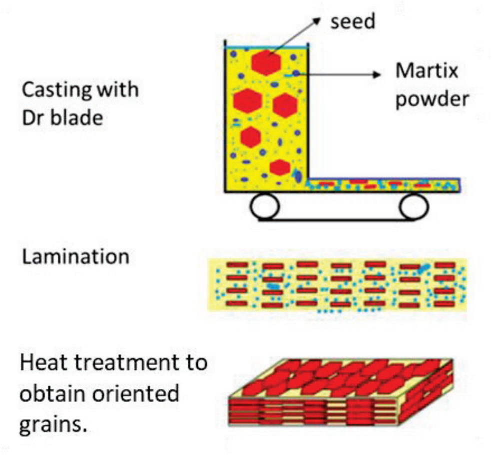

Figure 1.24. Schematic demonstration of templated grain growth [93].

1.4.2. Differential Scanning Calorimetry (DSC) Measurements

Differential Scanning Calorimetry (DSC) is a multipurpose characterization tool that is used to determine temperature dependent changes in some properties of a sample. With the changing temperature, temperature difference between sample and reference material, is determined by the instrument [94]. The sample enclosed within a pan and empty reference pan are placed on a sample holder enclosed in a furnace. The heat is transferred to the pans. The temperature difference between sample pan and empty pan is measured by thermocouples and consequently conversion into a temperature dependent heat flow data is done.

DSC measurements were carried out in order to determine structural phase transition behavior between room temperature and 250 °C in the nitrogen atmosphere and using 5 °C/min heating rate. TA Instruments Q10 device at the Geothermal Energy Research and Application Center (GEOCEN) at Izmir Institute of Technology (IZTECH) was used for this purpose.

1.4.3. X-Ray diffraction (XRD) and Rietveld Refinement

X-ray diffraction (XRD) technique was used to analyze crystal structure, unit cell parameters, preferred orientation, phase purity and phase fractions of materials. In this thesis, XRD measurements were carried out with a high-resolution Philips X'Pert Pro X-ray diffractometer at the Center for Material Research (CMR) at Izmir Institute of Technology (IZTECH). This diffractometer utilizes a copper target that can produce X-rays having wavelength of 1.5405 Å $K_{\alpha1}$ and 1.5443 Å $K_{\alpha2}$. The K_{β} radiations are eliminated with Ni filter. The fixed divergence slit size is 0.76 mm. The diffraction data were collected with a scanning speed of 0.02º/min in between 2θ = 20º - 80º to obtain suitable data for structure refinements. The General Structure Analysis System II (GSAS II) software package [95] was used for Rietveld refinement of the crystal structures. The crystal structure parameters (unit cell parameters) and phase fractions of the samples have been determined by refining some distinct parameters.

During the Rietveld refinement, the weighted profile R factor (R_{wp}) created with the least squares approach is used to test how close the calculated pattern created by the structural model is to the measured pattern. R_{wp} is tried to be minimized during the iteration of the parameters. An indicator of the accuracy of the refined parameters, the R_{wp} factor quantifies the difference between the calculated intensity ($y_{calc,i}$) and the observed intensity ($y_{obs,i}$);

$$R_{wp} = \sqrt{\frac{\sum_i^N w_i(y_{obs,i} - y_{calc,i})^2}{\sum_i^N w_i(y_{obs,i})^2}}$$

where N is the number of data points. In addition, the goodness of fit (GoF), which is related to R_{wp} and parameter P, is another factor indicating fitting quality of refinement;

$$GoF = \sqrt{\frac{\sum_i^N w_i(y_{obs,i} - y_{calc,i})^2}{N - P}}$$

Since the algorithm of the Rietveld refinement method was first developed by Hugo Rietveld, is the method is named after him. In this analysis method, the following basic parameters can be refined [96];

- Structural parameters of the specimen; unit cell parameters (a,b,c), atomic coordinates (x,y,z), site fractions and phase fractions.
- Peak Profile parameters (Lorentzianand Gaussianshape parameters ; U, V, W and X, Y, Z and their ratio)
- 2θ dependent intensity corrections due to absorptions; (sample parameters: histogram scale factor, sample displacement, surface roughness and sample transparency)

- Peak shape parameters (instrumental calibration parameters, thermal parameters (U_{ij}), preferred orientation and micro strain… etc)
- Background (background fitting functions and their coefficients)

In an XRD pattern; peak position, intensity and shape depend on the properties of crystal structure, sample and instrumental parameters, as summarized in Table 1.2.

Table 1.2. XRD pattern components and their dependence on crystal structure, specimen properties and instrument parameters [97].

Pattern component	**Crystal structure**	**Specimen property**	**Instrumental parameter**
Peak Position	Unit cell parameters; • Dimensions; a, b, c • Angles: α, β, γ	Absorption Strain-stress	Wavelength of X-ray Sample alignment Beam axial divergence
Peak Intensity	Atomic parameters; • Atomic positions: x, y, z, • Atomic fractions	Preferred orientation Absorption Porosity	Geometry/configuration Lorentz polarization factor (LP)
Peak Shape	Crystallinity: FWHM Disorder Defects	Grain size Strain-stress	Spectral purity of X-ray Geometry Beam conditioning

1.4.4. Microstructure Imaging and Analysis

In this study, the scanning electron microscope (SEM) is used to detect microstructure properties of the samples such as grain size, porosity, secondary phases and their distribution in the sample. The SEM instrument in the IZTECH CMR, FEI QUANTA 250 FEG, equipped with Secondary Electron (SE), Back Scattering Electron (BSE) and Energy Dispersive X-rays (EDX) detectors, was used.

In order to obtain clear SEM images of grain and boundaries, the surfaces of the ceramic pellets were firstly polished by 1000 and 2000 mesh SiC sandpaper and then thermally etched for one hour at 100 ºC below the sintering temperature of each ceramic which creates grooves at the grain boundaries [98].

1.4.5. Dielectric Measurements

An instrument called LCR meter is used to determine the dielectric constant of materials. The letters L, C and R stand for inductance, capacitance and resistance, respectively. An LCR meter measures a physical parameter called impedance (Z), which represents the total resistance of the circuit under alternating voltage, to determine L, C or R values of circuit elements. If the alternative voltage applied to the circuit is expressed as $V = V_m e^{i\omega t}$ in a waveform varying with the ω frequency, the L or C element in the circuit causes a phase difference (φ) in the current and the current is expressed as $I = I_m e^{i(\omega t-\varphi)}$ (Figure 1.25(a)). According to Ohm's law, the impedance [99] is expressed as;

$$Z = \frac{V}{I} = \frac{V_m e^{i\omega t}}{I_m e^{i(\omega t-\varphi)}} = \frac{V_m}{I_m} e^{i\varphi} = |Z| e^{i\varphi}$$

As it can be understood from this relation, impedance is a complex expression. If we consider a series connected RC circuit, the total impedance is expressed as $Z = R - i\frac{1}{\omega C}$ (Figure 1.25). Then the phase difference is obtained as $tan\varphi = 1/(\omega RC)$. This expression is important because it is used to find the ratio of energy stored and energy lost in a capacitor [100]. This value, called the dissipation factor (D) or dielectric loss is directly related to the phase difference between current and voltage waves;

$$D = \frac{energy\ lost}{energy\ stored} = \frac{real\ part\ of\ Z}{-imaginary\ part\ of\ Z} = \frac{R}{1/\omega C} = \omega RC = \frac{1}{\tan\varphi} = \tan\delta$$

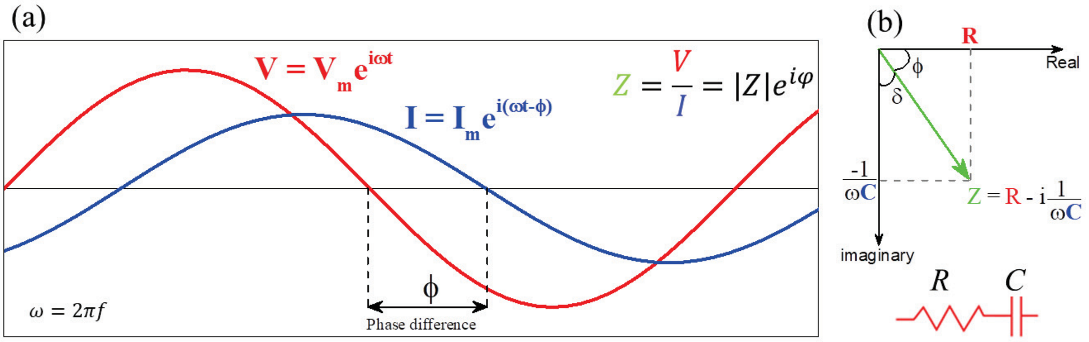

Figure 1.25. (a)Wave forms of applied alternative voltage and alternative current and (b) real and imaginary parts of an impedance of a RC circuit.

After measuring capacitance (C) with the LCR meter, the dielectric constant (ε_r) of the material sandwiched between parallel conductive plates is calculated using the following expression, which is related to the thickness (d) of material, area (A) of conductive plates and the permittivity of vacuum (ε_0 = 8.85 pF/m);

$$\varepsilon_r = \frac{C}{\varepsilon_0}\frac{d}{A}$$

The temperature dependent dielectric constants of the materials were determined with using a Keysight E4980AL LCR meter (Figure 1.26). Alternative voltage signal with the amplitude (V_m) of 1 V was applied at four different frequencies (f = 0.1, 1, 10 and 100 kHz). The measurement was controlled with a Labview program. (During his visit to our laboratory, Prof. Dr. Nandang Mufti, who is at State University of Malang, Indonesia, created the LabVIEW program that can automatically measure the temperature dependent dielectric constant at a single frequency. By modifying this program, I was able to upgrade it into a program that can take measurements for multiple frequencies.) Temperature of the material which is mounted on the sample holder was increased from 25 °C to 250 °C with the rate of 3 °C/min by the temperature controller of TF1000. Sample temperature is measured by a temperature sensor in the sample holder located very close to the sample.

Figure 1.26. The LCR meter (KEYSIGHT, E4980AL) that can measure impedance, capacitance and dielectric loss of samples between 20 Hz and 300 kHz.

1.4.6. Piezoelectric Coefficient Measurements

In this study, the piezoelectric coefficient d_{33} values of the poled ceramics were determined using a SINOCERA YE2730A model d_{33} meter (Figure 1.28). In all measurements by using this device, the force amplitude of 250 N with a vibration frequency of 110 Hz is applied to the samples. The d_{33} meter can measure piezoelectric constant up to 2000 pC/N.

Figure 1.27. Room temperature piezoelectric d_{33} coefficient measurement tool; d_{33} Meter (SINOCERA YE2730A).

1.4.7. Ferroelectric and Strain Measurements

The ferroelectric and field-induced strain properties of the produced ceramics in this study were determined by measuring polarization-electric field (P-E) loops and strain-electric field (S-E) curves simultaneously, as a function of temperature between 25 and 250 °C. The samples were mounted into the sample holder (Figure 1.28(a)) and P-E and S-E hysteresis loops were measured by using the analyzer (Aixacct TF Analyzer 1000) (Figure 1.28(f)) that is connected with the high-voltage amplifier (TREK 610E) (Figure 1.28(c)) and laser interferometer (SIOS) (Figure 1.28(b,d)) and the temperature was controlled with the temperature controller (aixACCT) (Figure 1.28(e)). The voltage applied during the measurements was in the form of a triangular wave and was usually applied with the frequencies of 1, 10 or 100 Hz. The frequency is usually increased up to 100 Hz for some lossy samples in order to eliminate the conductivity contribution.

With the laser interferometer, the thickness change of the sample (i.e. the displacement) under the electric field is determined. The laser beam emitted from the source hits the mirror at an angle of 45º and reflects at 45º. The laser is incidence on the sample holder that is sensitive to the movement of the sample and reflects back. It follows the same path, and reaches the detector. The path difference between incident and reflected laser beam that corresponds the thickness displacement in the sample is determined. The strain value of a sample is determined from the ratio of the thickness displacement (Δd) measured by laser interferometer to the thickness of the sample (d) (Figure 1.29).

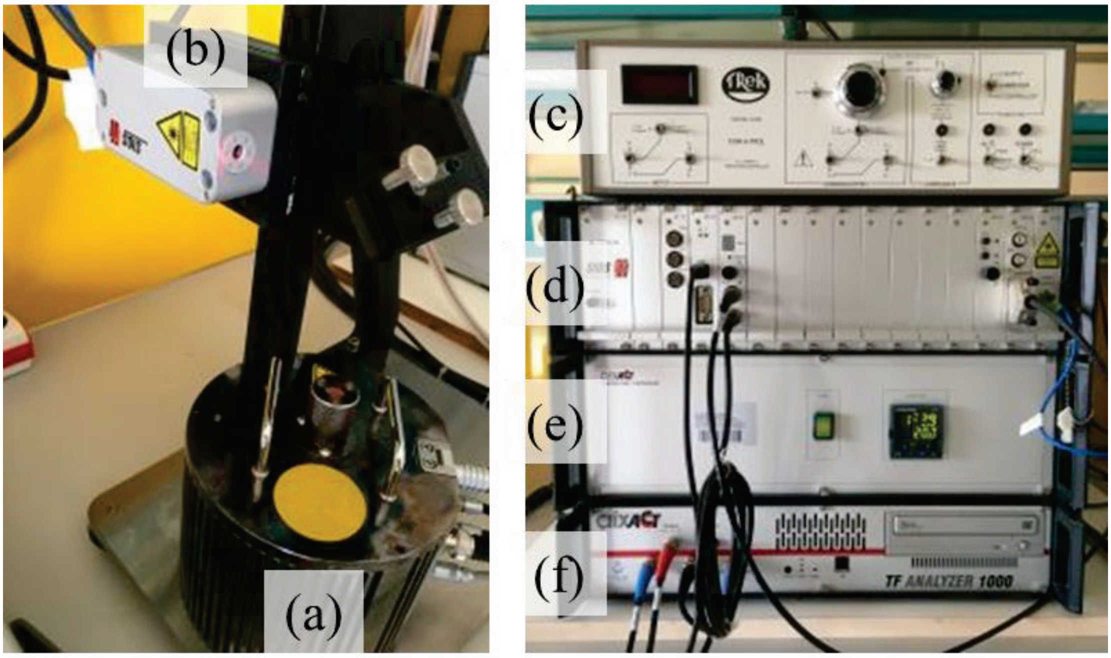

Figure 1.28. (a) Piezo sample holder (aixACCT, TFA 423-7), (b) the laser beam source of the interferometer and instruments for ferroelectric and strain measurements; (c) high voltage amplifier (TREK 610E), (d) SIOS laser interferometer main unit, (e) aixACCT temperature controller and (f) aixACCT TF analyzer 1000.

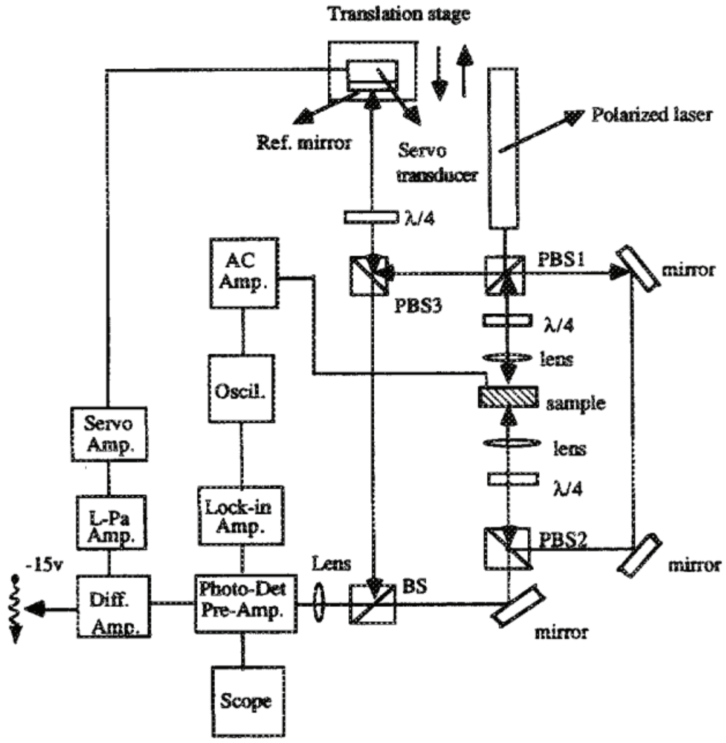

Figure 1.29. Schematic representation of the double beam laser interferometer [101].

1.4.8. Electron Paramagnetic Resonance Measurements

Electron paramagnetic resonance (EPR) is a measurement method to analyze materials that have unpaired electrons. EPR spectroscopy is frequently used for studying paramagnetic metals, metal complexes or organic radicals. The EPR spin Hamiltonian is expressed as a sum of magnetic interactions between the electron spin and magnetic moments in its environment. The EPR spin Hamiltonian is expressed as;

$$\mathrm{H} = \beta_{\mathrm{e}}\mathbf{B_0}\cdot\mathbf{g}\cdot\mathbf{S} - \beta_{\mathrm{n}}\mathrm{g}_{\mathrm{n}}\mathbf{B_0}\cdot\mathbf{I} + \mathbf{S}\cdot\mathbf{A}\cdot\mathbf{I} + \sum_{\mathrm{k}=2,4,6}^{-\mathrm{k}\leq\mathrm{q}\leq\mathrm{k}} \mathrm{B}_{\mathrm{k}}^{\mathrm{q}}\mathrm{O}_{\mathrm{k}}^{\mathrm{q}}(\mathrm{S}_{\mathrm{X}},\mathrm{S}_{\mathrm{Y}},\mathrm{S}_{\mathrm{Z}})$$

The first term represents electronic interactions and second term represents nuclear Zeeman interactions and the third term describes hyperfine interaction with nuclei (fine structure). Where β_e and β_n are electron end nuclear Bohr magnetons respectively, g and g_n are gyromagnetic constants of electron and nuclei respectively, $\mathbf{B_o}$ donates applied magnetic field, **S** represents spin magnetic moment, **I** represents nuclear magnetic moment, **A** describes dipole–dipole interaction between the electron spin **S** and the nuclear spin I. In the last term B_k^q are the fine structure Hamiltonian parameters and O_k^q are the extended Stevens spin operators [102].

In Figure 1.30, EPR spectra and energy states for three different models which have different spin-Hamiltonian interactions are shown. A single resonance signal is obtained for S = 1/2 and I = 0 state (Figure 1.30(a, d)). The interaction of S = 1/2 and I = 0 gives quartet resonance signals which have equal intensity (Figure 1.30(b, e)). Fine-structure interaction of S = 3/2 gives triplet resonance signal which have different intensity due to strongly varying orientation dependencies (Figure 1.30(c, f)). For high spin systems (S > 1/2) that have more than one unpaired electron, fine structure interaction is considered. After carefully analyzing fine structure parameters of system, information about possible lattice vacancies, the strength and the symmetry of the crystal field can be obtained.

Room temperature X-band EPR measurements of Mn doped ceramics which have mentioned in chapter 3rd were carried out by using a CMS 8400 (Adani) EPR spectrometer with a TE102 resonator cavity at a microwave frequency of 9.4 GHz.

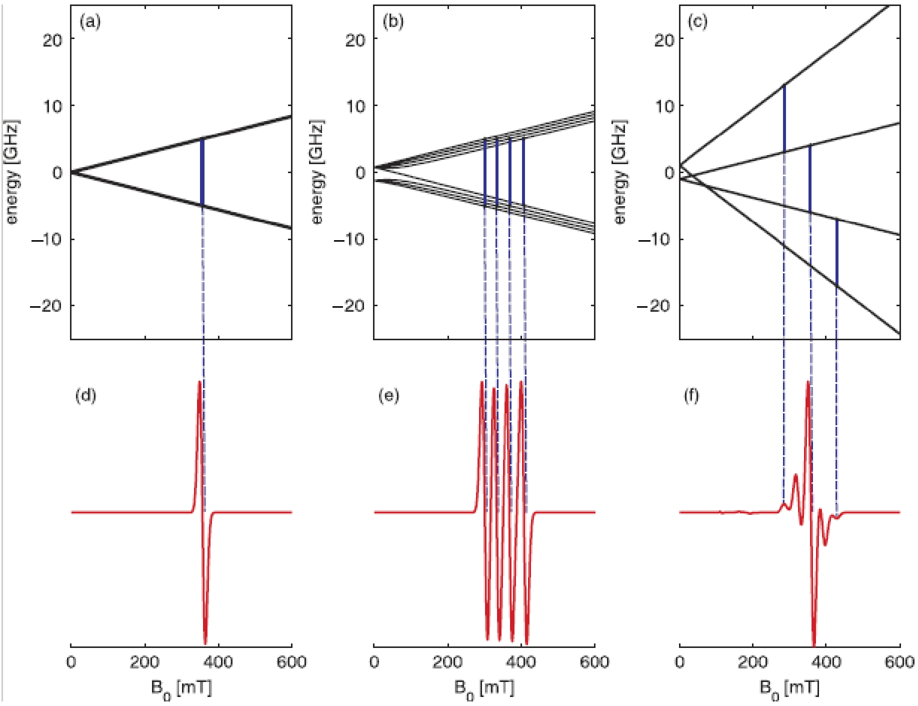

Figure 1.30. Schematic representation of energy levels and corresponding EPR spectra for (a,d) S = 1/2 and I = 0 interaction (b, e) S = 1/2 and I = 3/2 interaction (c, f) fine-structure interaction with S = 3/2 [102].

CHAPTER 2

ENERGY STORAGE IN FERROELECTRICS

2.1. Energy Storage Density in Dielectric Capacitors

Dielectric capacitors have great importance due to their high power densities (i.e. fast charge-discharge capability) for high pulse power required energy storage applications such as high frequency inverters, electromagnetic pulse bombs, hybrid electric vehicles [103]. However, they have low energy storage densities compared to batteries and super-capacitors (Figure 2.1). Improving the energy density of dielectric capacitors would help to reduce the volume, weight, and cost of consumer electronics, pulsed power systems and commercial defibrillators and might even result to make them competitive in energy storage against batteries and fuel cells [104]. In addition to improving energy storage density in ceramic capacitors another important issue is to maintain temperature stability of energy storage capacitors, because some electronic devices can be exposed to extreme temperature changes.

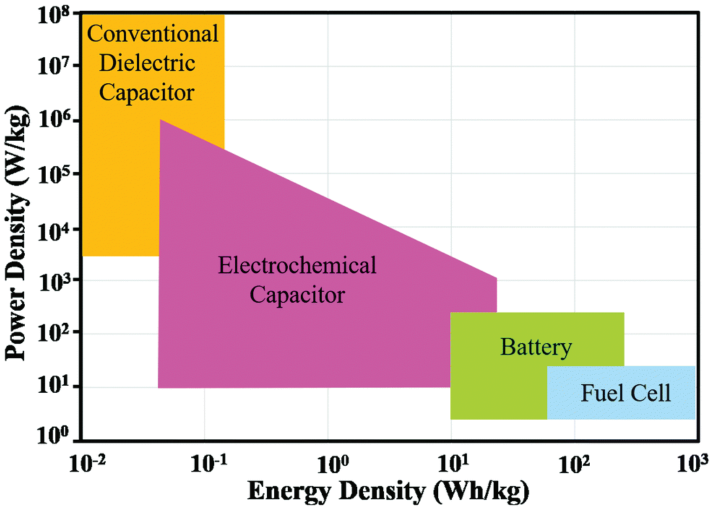

Figure 2.1. Comparison of power densities versus energy densities of various energy storage devices [105].

2.1.1. Energy Storage Density Calculations

The energy storage density of a dielectric material can be dynamically calculated from its polarization-electric field hysteresis loops (P-E). [106] The total energy density (W_{tot}) which is stored in the dielectric capacitor corresponds to the area between the charging curve and the polarization axis ($W_{tot} = W_{rec} + W_{loss}$) in the P-E loop. However, due to the hysteresis behaviour of the dielectric material, the energy transferred to the system corresponds to the area between the discharging curve and the polarization axis (W_{rec}) and the area between the charging and the discharging curve (W_{loss}) corresponds to the energy loss which cannot be transferred to the system, i.e., the remaining energy density within the dielectric material (see Figure 2.2). The recoverable energy storage density (W_{rec}) of dielectric materials is calculated as follows,

$$W_{rec} = \int_{P_r}^{P_m} E\,dP$$

Where P_m and P_r are the maximum and remnant polarization, respectively. Therefore, in order to achieve high energy storage density, the dielectric should have large maximum polarization (P_m) and dielectric breakdown field (E_b) and low remnant polarization (P_r). In addition, low hysteresis loss is required to obtain high efficiency. Energy efficiency (η) which is expressed by the formula $\eta = W_{rec}/W_{tot}$.

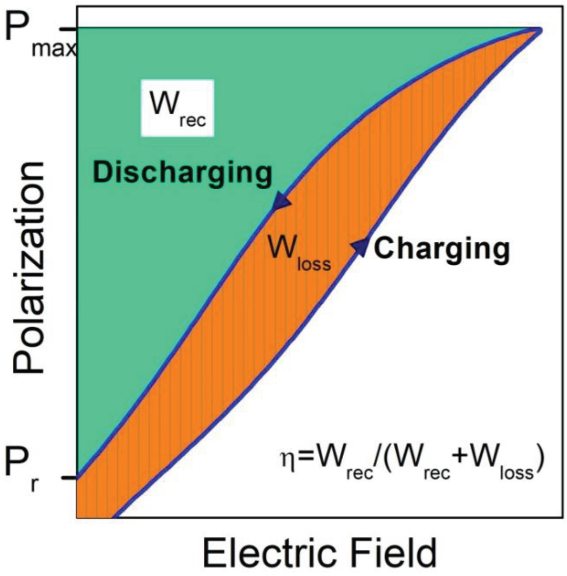

Figure 2.2. Schematic demonstration of energy storage areas within a polarization-electric field (P-E) loop.

2.1.2. Energy Storage Properties of Different Types of Dielectrics

Dielectrics can be grouped into four different classes according to their P-E behavior namely, (1) linear dielectrics (2) normal ferroelectrics, (3) relaxor ferroelectrics and (4) antiferroelectrics (Figure 2.3). For energy storage applications, linear dielectric materials [107] have some advantages due to their high efficiency (no hysteresis loss) and dielectric breakdown strength. However, linear dielectrics have lower polarization and dielectric constant compared to ferroelectric, relaxor ferroelectric or anti-ferroelectric [108] materials. Normal ferroelectrics have a relatively large polarization and a breakdown strength, but their high remnant polarization or high hysteresis loss cause a lower recoverable energy storage density and efficiency. Relaxor ferroelectrics (RFE) have lower remnant polarizations and smaller hysteresis loss which result in relatively high energy storage density and efficiency, respectively. Since antiferroelectrics have low remnant polarization and high maximum polarization, high recoverable energy storage is expected for them. However, they have relatively low efficiency due to their strong double hysteresis characteristic. Ergodic relaxor ferroelectrics also have a similar double-loop hysteresis behavior, which is associated with electric-field induced transition of weakly polar nano-domains to ferroelectric domains, but compared to antiferroelectrics, they have higher efficiency due to their slimmer loop. Therefore, ergodic relaxor materials have a remarkable importance in energy storage applications. In Figure 2.4 (in the middle), the domain structure and P-E behaviour of an ergodic relaxor is depicted.

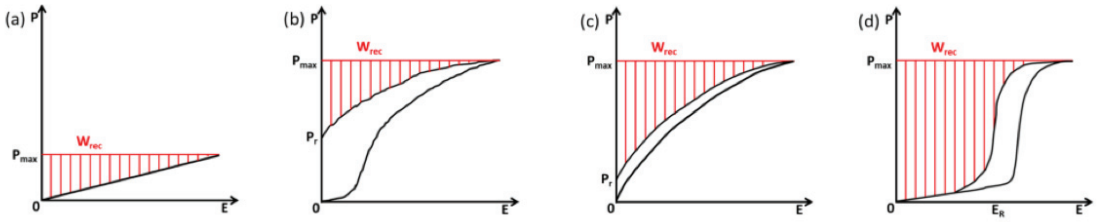

Figure 2.3. P-E characteristics of (a) linear, (b) ferroelectric, and (c) relaxor (d) antiferroelectric dielectrics. Shaded areas represent energy storage capacity of each dielectric [109].

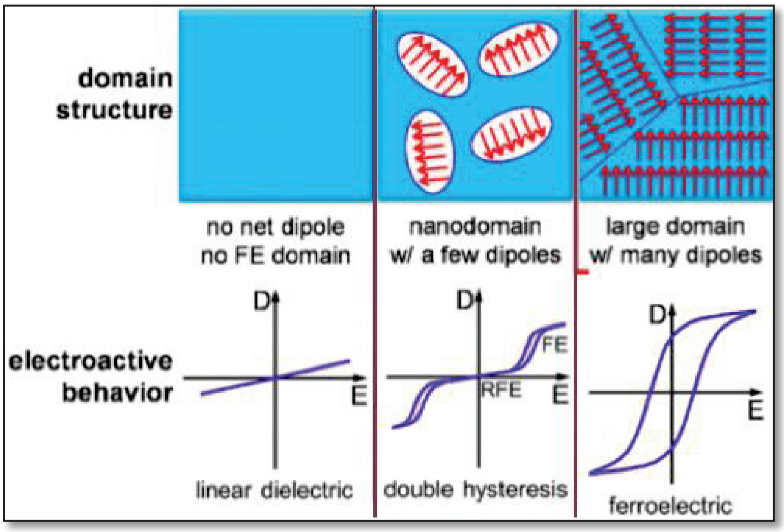

Figure 2.4. Domain structures and P-E behavior of linear dielectrics, antiferroelectric relaxors and ferroelectrics [110].

2.1.3. Lead Free Energy Storage Materials

Although they are toxic and environmentally harmful, lead-based ceramics are still studied, produced and marketed due to their high energy storage properties, such as W_{REC} = 7.63 J/cm^3 in bulk form [111] and W_{REC} = 53 J/cm^3 in film form [112]. On the other hand, the dramatic increase in lead-free energy storage ceramics, with almost twice as much study in the last decade as the previous year, is critical to replacing lead-based materials [105]. Reported details of various lead free ferroelectric ceramics according to their energy storage properties are listed in the Table 2.1 and Table 2.2.

Among lead-free ferroelectric ceramics, $AgNbO_3$ (AN) based ceramics are known to have the highest energy storage densities up to 5.2 J/cm^3 [113] but show moderate efficiency between 56-69% and these values are obtained at high electric fields between 150-290 kV/cm. On the other hand, AN-based ceramics are more costly produced and require sintering process in an oxygen atmosphere. Also $K_{0.5}Na_{0.5}NbO_3$ (KNN) based ceramics have very close energy storage properties with AN-based ones (W_{REC} = ~ 4 J/ cm^3 and η = 52-62 %) at high electric fields 300-400 kV/cm. Although $BaTiO_3$-based solid solutions lag behind others in terms of energy storage properties, it is seen that $BaTiO_3$-$BiMeO_3$ solid solutions [114] approach the energy storage properties of NBT-based ceramics by gaining the relaxor characteristic with $BiMeO_3$ (Me represents cations such as Zr, Nb, Mg etc.) components.

$Na_{0.5}Bi_{0.5}TiO_3$ (NBT)-based systems have been studied intensively in recent years not only for their piezoelectric properties but also as candidates for energy storage. NBT has large polarization compared to other $BaTiO_3$ (BT) and $K(Na,Nb)O_3$ (KNN) based Pb-free materials and large coercive field (E_c ~ 73 kV/cm). However, they have relatively weak piezoelectric properties because of their large coercive field making it difficult to polarize the material [115]. In order to overcome this problem, various solid solutions with different end members such as $BaTiO_3$ [116] , $K_{0.5}Bi_{0.5}TiO_3$ (KBT) [117], $KNaNbO_3$ [118], $SrTiO_3$ [119] are formulated with NBT based ceramics. Examples of these NBT-based solid solutions reported with high energy storage properties are listed in Table 2.2. The comparison of energy storage properties of AN, NBT, BT, KNN and NN based ferroelectrics is given in Figure 2.5 in terms of; (a) W_{REC} vs efficiency, (b) W_{REC}/E vs efficiency, (c) W_{REC} vs applied electric field and (c) W_{REC}/E vs applied electric field. These figures show plots of the data from Table 2.1 and Table 2.2. It is striking that the most optimal values of energy storage density per unit electric field and efficiency belongs to NBT-based ceramics. Therefore, NBT-based materials are among the most studied lead-free energy stored ceramics.

Table 2.1. Energy storage densities of AN, BT, KNN and NN based ceramics [105].

Base	*Composition*	W_{REC}	η	*E*	W_{REC}/E	*Ref.*
		J/cm^3	*(%)*	*kV/cm*	(C/cm^2)	
AN	$(Ag_{1-2x}Sr_x)NbO_3$	2.9	56	190	15.26	120
AN	$Ag(Nb_{1-x}Ta_x)O_3$	4.2	69	233	18.03	108
AN	$AgNbO_3$-Mn	2.5	56	150	16.67	121
AN	$Ag(Nb_{1-x}W_x)O_3$	3.3	56	188	17.55	122
AN	$AgNbO_3$	2.1	50	175	12	123
AN	$Ag_{1-3x}Bi_xNbO_3$	2.6	86	200	13	124
AN	$Ag_{0.97}La_{0.01}NbO_3$	3.2	62	190	16.84	125
AN	$Ag_{0.94}La_{0.02}NbO_3$	4.4	73	270	16.3	126
AN	$Ag_{0.88}Gd_{0.04}NbO_3$	4.5	65	290	15.52	127
AN	$0.99AgNbO_3$-$0.01Bi(Zn_{2/3}Nb_{1/3})O_3$	4.6	57.5	220	20.91	128
AN	$(Sm_{0.02}Ag_{0.94})(Nb_{0.9}Ta_{0.1})O_3$	4.87	63.5	280	17.39	129
AN	$(Sm_{0.03}Ag_{0.91}NbO_3$	5.2	68.5	290	17.93	113
BT	0.9BaTiO3-$0.1Bi(Mg_{2/3}$Nb1/3$)O_3$-Mn	1.7	90	210	8.1	130
BT	BaTiO3–xBi(Mg2/3Nb1/3)O3	1.13	92	143	7.9	131
BT	$BaTiO_3$–$0.12Bi(Mg_{1/2}Ti_{1/2})O_3$	1.18	88	224	5.27	132
BT	$BaTiO_3$–$xBiYbO_3$	0.71	82.6	93	7.63	133
BT	$0.9BaTiO_3$-$0.1(Bi_{0.9}Na_{0.1})(In_{0.8}Zr_{0.2})O_3$	1.33	88	180	7.39	134
BT	$BaTiO_3/Al_2O_3$-SiO_2-ZnO	0.83	70	150	5.53	135
BT	$BaTiO_3/SrTiO_3$	0.198	90	47	4.21	136
BT	$BaTiO_3$	1.24	85.6	90	13.78	137
BT	$BaTiO_3$+0.25wt%MgO	0.9	73.3	130	6.92	138
BT	$BaTiO_3/La_2O_3/SiO_2$	0.54	85.7	136	3.97	139
BT	$Ba_{0.7}Ca_{0.3}TiO_3$	1.41	61	150	9.4	140
BT	$0.85(BaZr_{0.2}Ti_{0.8})O_3$-$0.15(Ba_{0.7}Ca_{0.3})TiO_3$	0.68	72	170	4	103c
BT	$0.88BaTiO_3$-$0.12Bi(Mg_{1/2}Ti_{1/2})O_3$	1.6	99.6	150	10.67	141
BT	$0.8BaTiO_3$-$0.2BiNbO_4$	0.31	99.7	117	2.65	142
BT	$0.9BaTiO_3$-$0.1Bi(Mg_{2/3}Nb_{1/3})O_3$	1.7	90	210	8.1	130
BT	$0.86BaTiO_3$-$0.14Bi(Zn_{1/2}Ti_{1/2})O_3$	0.81	94	120	6.75	143
BT	$0.85BaTiO_3$-$0.15Bi(Mg_{1/2}Zr_{1/2})O_3$	2.9	86.8	280	10.36	144
BT	$0.875BaTiO_3$-$0.125Bi(Mg_{2/3}Nb_{1/3})O_3$	1.89	83	240	7.88	145
BT	$0.88BaTiO_3$-$0.12Bi(Zn_{1/2}Zr_{1/2})O_3$	0.758	98	100	7.58	146
BT	0.9BaTiO3-$0.1Bi(Ni_{1/2}Sn_{1/2})O_3$	2.526	93.9	240	10.53	114
KNN	$(K_{0.5}Na_{0.5})NbO_3$–$xBi(Mg_{2/3}Nb_{1/3})O_3$	4.08	62.7	300	13.6	147
KNN	$(K_{0.5}Na_{0.5})NbO_3$–$xSrTiO_3$	4.03	52	400	10.08	148
NN	$0.93NaNbO_3$-$0.07Bi(Mg_{1/2}Zr_{1/2})O_3$	2.31	80.2	255	9.06	149
NN	$0.9NaNbO_3$-$0.1Bi(Mg_{2/3}Nb_{1/3})O_3$	2.8	82	300	9.33	150
NN	$0.80NaNbO_3$-$0.20SrTiO_3$	3.02	80.7	323	9.35	151
NN	$0.86NaNbO_3$-$0.14(Bi_{0.5}Na_{0.5})HfO_3$	3.51	80.1	350	10.03	152
NN	$Na_{0.7}Bi_{0.1}NbO_3$	3.44	80.7	250	13.76	153

Table 2.2. Energy storage properties of NBT based ferroelectric ceramics [105].

Base	*Composition*	W_{REC} J/cm^3	η *(%)*	*E* *kV/cm*	W_{REC}/E (C/cm^2)	*Ref.*
NBT	NBT-6BT–xKNbO$_3$	0.89	71.7	100	8.9	154
NBT	(0.7 NBT-0.3Bi$_{0.2}$Sr$_{0.7}$TiO$_3$)-xNaNbO$_3$	1.03	85.8	85	12.12	155
NBT	NBT-6BT–0.05K$_{0.5}$Na$_{0.5}$NbO$_3$	0.9		100	9	156
NBT	Bi$_{0.487}$Na$_{0.427}$K$_{0.06}$Ba$_{0.026}$TiO$_3$-xCeO$_2$	0.94	54	75	12.53	157
NBT	NBT-BT-xNN	0.71	66	70	10.14	158
NBT	(0.9-x)[NBT-8BT]-xSrZrO$_3$-0.10NaNbO$_3$	0.95	66	110	8.64	159
NBT	0.97(NBT-6BT)-0.03CZ	0.7		70	10	160
NBT	Ca and Zr doped NBT-BT	0.87	82.37	93.5	9.3	161
NBT	0.85[(1-x)NBT–xBT]–0.15Na$_{0.73}$Bi$_{0.09}$NbO$_3$	1.4	66.3	142	9.86	162
NBT	NBT–ST–5AN	2.26	77.2	150	15.07	163
NBT	0.65NBT-0.35SrTiO$_3$	0.95	-	90	10.56	164
NBT	Nb doped 0.6NBT-0.4SrTiO$_3$	1.82	81	140	13	165
NBT	0.91(0.76NBT-0.24SrTiO$_3$)-0.09AgNbO$_3$	2.26	77.2	150	15.07	163
NBT	0.5 NBT -0.5SrTiO$_3$-+3wt% MgO	2.17	50	200	10.85	166
NBT	0.99(0.72 NBT -0.28SrTiO$_3$)-0.01BiAlO$_3$	1.24	71	120	10.33	167
NBT	0.6 NBT -0.4Sr$_{0.7}$Bi$_{0.2}$TiO$_3$	2.2	75	160	13.75	168
NBT	0.55 NBT -0.45Sr$_{0.8}$Bi$_{0.1}$TiO$_3$	1.1	73	80	13.75	169
NBT	(1-x)(NBT -7BT)-xNa$_{0.73}$Bi$_{0.09}$NbO$_3$	0.9	69.3	127	7.09	162
NBT	Nd doped NBT -8BT	1.53	93	73	20.96	170
NBT	(1-x)(NBT -5BT)-xBi(Zn$_{2/3}$Nb$_{1/3}$)O$_3$	2.83	67	180	15.72	171
NBT	(1-x)(NBT -8BT)-xNaTaO$_3$	1.2	74.8	100	12	172
NBT	NBT -8BT-5BLT	1.03	70	89.22	11.55	173

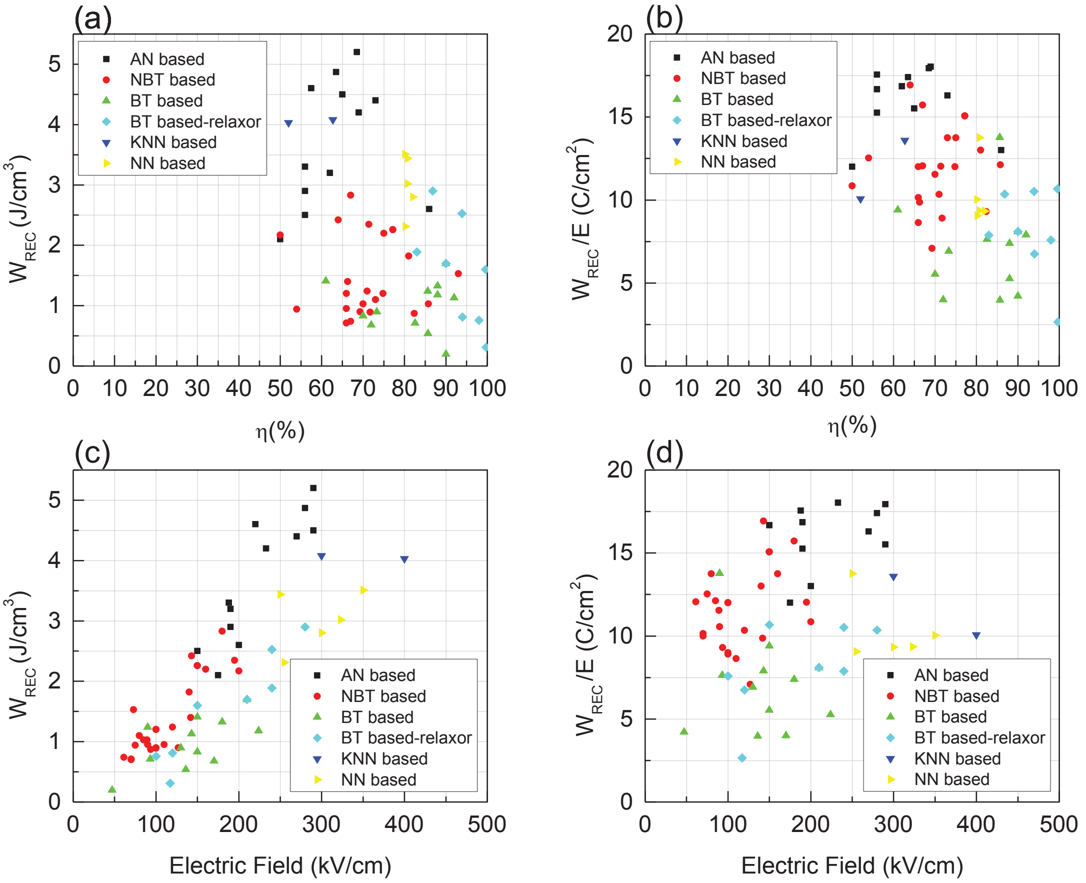

Figure 2.5. Comparison of energy storage properties of AN, NBT, BT, KNN and NN based ferroelectrics; (a) W_{REC} vs efficiency, (b) W_{REC}/E vs efficiency, (c) W_{REC} vs applied electric field and (c) W_{REC}/E vs applied electric field (see references in Table 2.1 and Table 2.2).

In particular, NBT-BT solid solution with a morphotropic phase boundary (MPB) between rhombohedral and tetragonal phases (Figure 2.6) is established as one of the most promising candidates for piezoelectric [174] applications. For the energy storage, (1–x)NBT–xBT systems which have a rhombohedral-tetragonal MPB between x = 0.06 and 0.11 [175], have been actively studied [176]. Previously, NBT-BT was thought to be in the tetragonal antiferroelectric (AFE) phase above the depolarization temperature (T_d) because the hysteresis loops were pinched [115b], however today's most accepted view holds that NBT–BT is only a relaxor with coexisting rhombohedral R3c and tetragonal P4bm polar nanoregions [177]. According to unpoled NBT-BT phase diagram [178] (Figure 2.6(b)), x = 0.06–0.11 compositions (MPB region) exhibit weakly polar P4bm tetragonal phase which corresponds to relaxor phase above T_d.

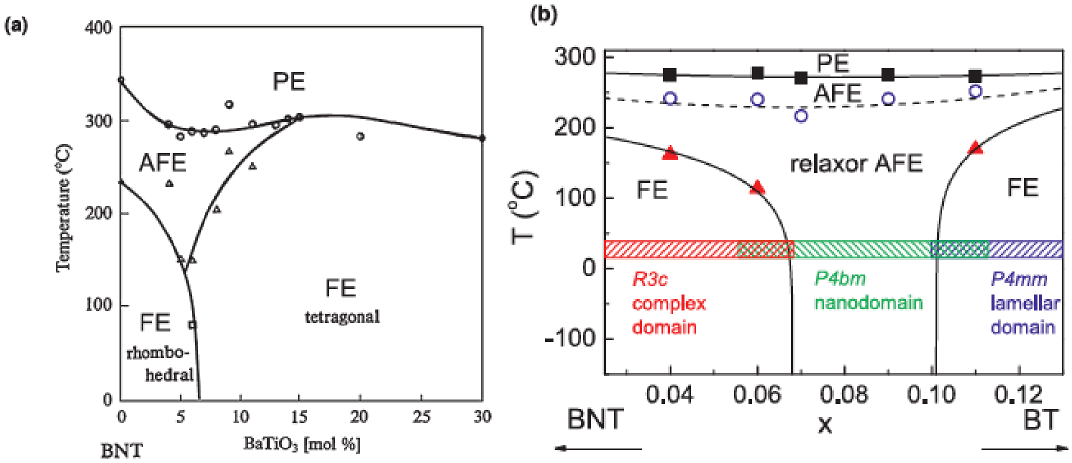

Figure 2.6. The phase diagram for (a) poled [179] and (b) unpoled [178] (1–x)($Na_{0.5}Bi_{0.5}$)TiO_3–x$BaTiO_3$ (NBT–BT) binary system.

The origin of pinched, double P–E loops observed above T_d is attributed to the electric field induced transformation from weakly polar relaxor phase to the ferroelectric phase [180]. On the other hand, it was observed that tetragonal P4bm phase dominates and rhombohedral R3c phase disappears above T_d [180], therefore, above T_d electric field induced transition occurs from weakly polar P4bm to strongly polar P4mm and shows ergodic relaxor character, as the initial P4bm state is restored after the removal of the electric field. The field dependence behavior of the material below T_d is different due to the presence of polar R3c phase: under electric field, the material transforms into a ferroelectric with long range order and large remnant polarization which is unfavorable for energy storage. This is the nonergodic relaxor behavior as the field-induced ferroelectric state is retained [158]. In order to obtain an ergodic relaxor with double-like P–E loops with low P_r and high P_m, favorable for energy storage, the weakly polar phase should be enhanced. For the (1−x)NBT–xBT system, in the x = 0.07–0.09 range, it is demonstrated that the amount of the weakly polar tetragonal phase is relatively larger compared to that of the rhombohedral phase [178].

2.1.4. The Material Selection for This Study: BLT substituted NBT-BT Ceramics

By adding a third component to the base NBT–BT composition it is possible to reduce the depolarization temperature below room temperature and thereby to obtain an ergodic relaxor behavior over a wide temperature range. Among different substitutions, Bi-based titanates have not been studied a lot. It was demonstrated that in ternary systems NBT-6BT–xBi(MeTi)O_3, in which Me is Zn, Ni, Mg, Co at the B-site, ergodic relaxor phase with a T_d below the room temperature can be induced with a little amount of Bi(Me,Ti)O_3 (around 2%–3%) and consequently, large strain values could be obtained as in [181]. In a similar study, Bi(MgTi)O_3 modified BNT-8BT composition has been shown to have improved energy storage properties [176b]. However, energy storage properties were not reported in that study. In a similar study Bi(Mg,Ti)O_3 modified NBT–8BT composition has been shown to have improved energy storage properties [176b].

Among Bi(Me,Ti)O_3, Bi($Li_{1/3}Ti_{2/3}$)O_3 (BLT) does not form a stable phase at ambient pressure however it has been used to form solid solutions with $BaTiO_3$ [182]. Increasing BLT content in the solid solution was shown to induce relaxor ferroelectricity [182]. Only study where Li containing bismuth titanate was used in a solid solution with NBT involves Li at the A-site: NBT–BT–$Bi_{0.5}Li_{0.5}TiO_3$ [183]. In contrast to Bi(Me,Ti)O_3, more than 10% $Bi_{0.5}Li_{0.5}TiO_3$ could be substituted and depolarization temperature still remains above the room temperature [183], showing that Li at the A-site is not that effective in suppressing ferroelectricity compared to that at the B-site.

In this study, we aim to improve the energy storage properties of BNT–BT ceramics by introducing a Bi-based titanate, Bi($Li_{1/3}Ti_{2/3}$)O_3. due to its larger amount of weakly polar tetragonal phase which might more easily facilitate relaxor ferroelectricity upon BLT substitution. To enhance energy storage density, Bi($Li_{1/3}Ti_{2/3}$)O_3 (BLT), which is expected to weaken the polar phase and provide ergodic relaxor behavior, is substituted to the base system in low amounts (x = 2%, 3% and 5%). The change of the (micro) structural, dielectric, ferroelectric and energy storage properties of all compositions are thoroughly investigated.

2.2. Experimental Procedure for NBT-BT-BLT Ceramics

The conventional solid state reaction method was used to prepare the ceramics with the composition (1–x)(0.92NBT–0.08BT)–xBLT (x = 0, 0.02, 0.03 and 0.05). The high purity metal oxides and carbonates Bi_2O_3 (99.9%), Na_2CO_3 (99.8%), Li_2CO_3 (99.999%), $BaCO_3$ (99%) and TiO_2 (99.9%) were used as starting raw materials. All powders were pre-dried at 200 ºC for overnight. The powder was mixed in a nalgene bottle using zirconia balls in ethanol media by planetary ball milling (Retsch PM100) for 18 h. After drying, the powder was ground in an agate mortar. The reaction of calcination process was carried out in pellet form at 850 ºC for 2 h in order to obtain the composition $[(1–x)(0.92Na_{0.5}Bi_{0.5}TiO_3–0.08BaTiO_3)–xBi_{2/3}Li_{2/3}TiO_3]$ phase;

$$(0.25(1\text{-}x)0.92)Na_2CO_3 + (0.25(1\text{-}x)0.92+x/3)Bi_2O_3 + (x/6)Li_2CO_3 + ((1\text{-}x)0.08)BaCO_3 + TiO_2 \longrightarrow Na_{0.5(1\text{-}x)0.92}Bi_{0.5(1\text{-}x)0.92+2x/3}Ba_{(1\text{-}x)0.08}Li_{x/3}TiO_3 + CO_2$$

After the calcination, the pellets were again ground into powder in an agate mortar and then powder was ball milled for 18h, in ethanol. After drying, the powders were mixed thoroughly with 4 wt% polyvinyl alcohol (PVA) binder and water solution and then ball milled for 18h. Then powders were dried, sieved and pressed into pellets (~10 mm in diameter, ~1 mm thick) under a pressure ~100 MPa. Then the PVA binder was burned out at 600 ºC for 4 h. After burnout the pellets were sintered at 1100 ºC for 2 h with a heating rate 5 ºC/min. To minimize the evaporation of volatile Na and Bi, the pellets were fully embedded in the powder of the same composition and alumina crucible was covered during sintering.

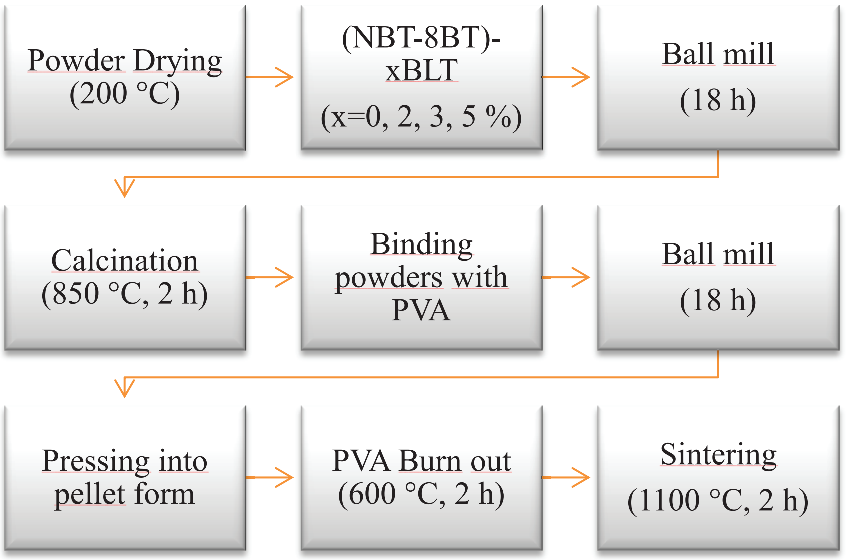

Figure 2.7. Schematic illustration of the synthesis routes of NBT-8BT-xBLT ceramics.

Table 2.3. The list of the samples with different BLT content and abbreviations $(1-x)(0.92Bi_{0.5}Na_{0.5}TiO_3-0.08BaTiO_3)-xBi(Li_{1/3}Ti_{2/3})O_3$ (NBT–8BT–xBLT).

Base ceramic	BLT composition (x)	Sample name
NBT–8BT	**0**	**NBT–8BT**
	0.02	**NBT–8BT–2BLT**
	0.03	**NBT–8BT–3BLT**
	0.05	**NBT–8BT–5BLT**

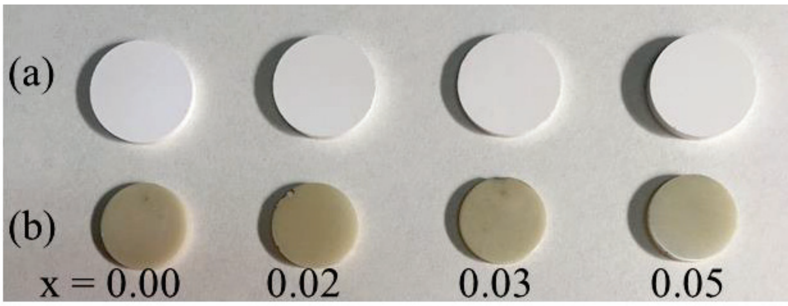

Figure 2.8. Photographs of the samples (NBT–8BT–xBLT) in pellet form (a) after calcination and (b) after sintering.

X-ray diffraction (XRD) experiments were carried out with a Philips X'Pert Pro diffractometer having Cu K_α radiation and a Bruker D2 Phaser. The microstructure of ceramics was studied on thermally etched (at 1000 ºC, for 1h) surfaces using a scanning electron microscope (SEM, FEI QUANTA 250 FEG). For dielectric and polarization-electric field measurements, both surfaces of polished pellets were coated with silver paste and was dried at 200 ºC for 20 min. The temperature dependence of dielectric constant and loss was measured at different frequencies (1, 10 and 100 kHz) by a Keysight E4980AL LCR meter between room temperature and 250 ºC (this is the maximum temperature of the setup). Polarization-electric field (P-E) loops were obtained by using an Aixacct TF 1000 combined with a high voltage amplifier (TREK 610E). Displacement was also collected simultaneously by a laser-interferometer (SIOS). For the temperature dependent dielectric and hysteresis measurements, sample holder of TF1000 was used and temperature was controlled by a temperature controller.

In order to determine the depolarization temperature (T_d), samples were poled under a dc field of 30–40 kV/cm at 50 ºC for 20 min in silicone oil bath and cooled down to the room temperature in the field.

2.3. Results and Discussions

2.3.1. Phase and Structure Properties of NBT-BT-BLT Ceramics

XRD patterns of all compositions are shown in Figure 2.9. All samples show peaks that belong to perovskite structure and no impurity peaks could be observed. Since the starting 0.92NBT–0.08BT composition is close to the MPB, a mixture of tetragonal and rhombohedral phases is expected for the samples. Rietveld refinements of the patterns were performed using GSAS II [95] to clarify the influence of BLT substitution on the evolution of the phase fractions of tetragonal P4bm and rhombohedral R3c phases and the lattice parameters. Refined patterns are included in appendix (see Figure A.1). These results are summarized in Table 2.4. All refinements have weighted profile R values (R_{wp}) below 7.5%. Refinements results, summarized in Table 2.4, show that with the BLT substitution, the weight fraction of the tetragonal P4bm phase increases from 50.4% for the x = 0 sample to 61%–64% for BLT substituted compositions. We have labeled the diffraction peaks in Figure 2.9b according to the refinements. In Figure 2.9b, in the 2θ range around 40º both tetragonal (201) and rhombohedral (202) peaks can be observed apart from a peak due to the $K\alpha_2$ radiation. The broad peak around 46º corresponds to (002) peak of the tetragonal phase. The subtle reduction in (002) peak intensity with the addition of BLT can be associated with the increase in the tetragonal P4bm phase fraction [158, 176c, 177, 180] which is confirmed by the refinement results. Tetragonality (c/a ratio) of the tetragonal phase also slightly decreases with the BLT substitution similar to the case in $Bi(Mg_{0.5}Ti_{0.5})O_3$ substituted NBT-BT samples [184].

Table 2.4. Calculated phase fractions and lattice parameters of (1-x)(0.92NBT-0.08BT)-xBLT compositions.

Composition	**Phase**	**Weight Fraction (%)**	**a (Å)**	**c (Å)**	**c/a**	**Rwp (%)**
x = 0	R3c	49.6	5.5115 (3)	13.50886 (6)	2.451031	7.489
	P4bm	50.4	5.53197 (9)	3.97974 (8)	0.719407	
x = 0.02	R3c	39.0	5.52427 (2)	13.53601 (6)	2.45028	6.266
	P4bm	61.0	5.53725 (8)	3.95912 (6)	0.714998	
x = 0.03	R3c	36.4	5.52605 (2)	13.52795 (1)	2.448033	6.851
	P4bm	63.6	5.54027 (6)	3.96102 (5)	0.714951	
x = 0.05	R3c	35.9	5.53073 (4)	13.56487 (3)	2.452636	6.083
	P4bm	64.1	5.5458 (9)	3.9625 (8)	0.714505	

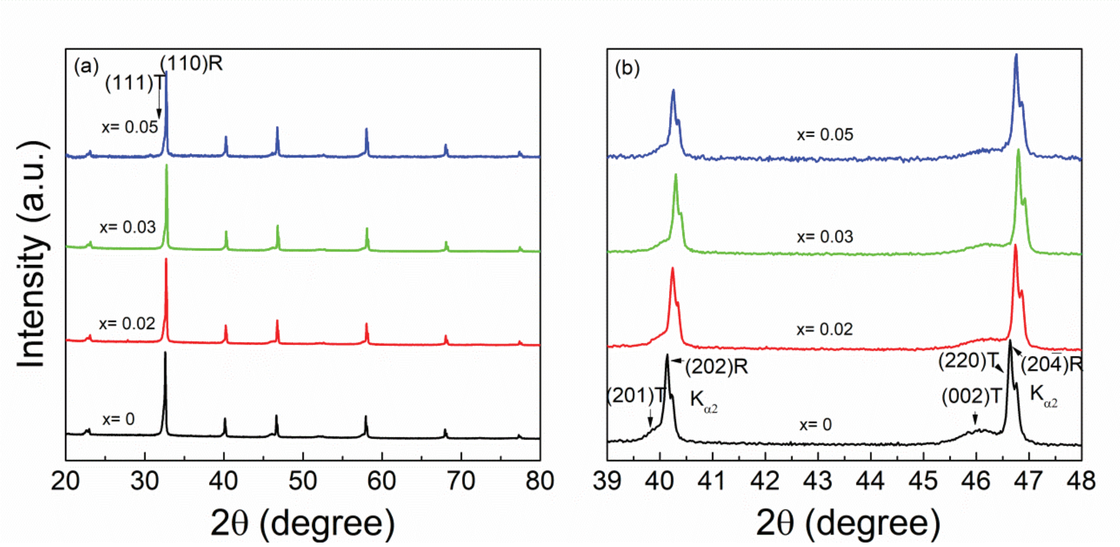

Figure 2.9. (a) XRD patterns of all (1-x)(0.92NBT-0.08BT)-xBLT compositions, (b) selected 2θ range between 39°- 48°.

2.3.2. Density and Microstructure of NBT-BT-BLT Ceramics

The bulk densities were measured as 5.48 g/cm^3, 5.41 g/cm^3, 5.63 g/cm^3 and 5.32 g/cm^3 for x = 0, 0.02, 0.03 and 0.05, respectively by using a density determination kit based on Archimedes principle, corresponding to relative densities of 93.38%, 91.64%, 95.21% and 89.53%. The SEM micrographs of all samples are presented in Figure 2.10. All compositions exhibit homogeneous and dense microstructures without secondary phases or pores. The average grain sizes, which were calculated by the linear intercept method are 1.45, 0.82, 0.65, 0.56 μm for BLT content x = 0, 0.02, 0.03 and

0.05, respectively. This means that BLT addition to NBT–BT system inhibits the grain growth, which will be discussed in further section.

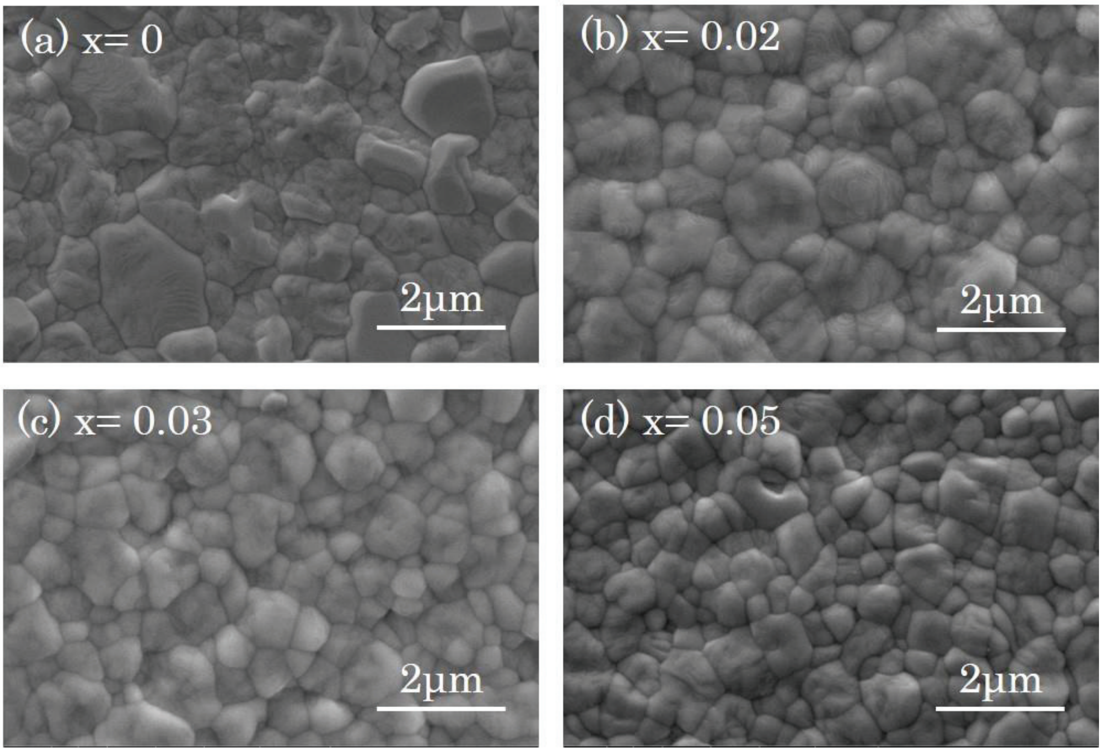

Figure 2.10. SEM surface images of (1–x)(0.92NBT–0.08BT)–xBLT ceramics with (a) x= 0, (b) x= 0.02, (c) x= 0.03, and (d) x= 0.05.

2.3.3. Dielectric Properties of NBT-BT-BLT Ceramics

In Figure 2.11(b) and (d)–(f), dielectric constant and dielectric loss as a function of temperature measured at 1, 10 and 100 kHz are presented for unpoled $(1-x)$(0.92NBT–0.08BT)–xBLT (x = 0, 0.02, 0.03 and 0.05) ceramics. Temperature dependent dielectric constant of these unpoled ceramics shows an anomaly which is generally called as shoulder temperature (T_S) in this temperature range. T_S was obtained at 1 kHz as ≈ 140 ºC, 108 ºC, 97 ºC and 84 ºC for x = 0, 0.02, 0.03, and 0.05 samples, respectively. There is frequency dispersion for unpoled ceramics up to this shoulder temperature due to the diffuse distribution of polar nano regions [180]. Its dependence on frequency and the gradual disappearance of the anomaly as the frequency increases indicate that T_S does not correspond to a phase transition [154]. According to an impedance study [185] it is concluded that the two different sets of relaxation processes causes an anomaly at T_S in the dielectric constant, however, the origin of T_S is still under discussion. It is evident from Figure 2.11(a) that T_S and the magnitude of the dielectric constant both decrease with increasing BLT composition. The decrease of the dielectric constant might be due to the additional disorder introduced by BLT, decreasing further the correlations between the polar nanoregions [163]. The decrease of T_S with increasing of BLT composition might be attributed to the increase in the fraction of tetragonal weakly polar P4bm phase and to the decrease in the grain size of the samples, upon BLT substitution.

A peak is observed in the temperature dependent dielectric loss curves of the all unpoled samples as shown in Figure 2.11 (a). This temperature of this loss peak does not coincide with T_S and is frequency dependent. It shifts to lower temperatures as the BLT content increases, similar to the trend in T_S. Thus, the change in the fraction of the tetragonal weakly polar P4bm phase depending on the composition can be estimated from these anomalies/peaks. Determination of the depolarization temperature T_d is crucial to understand the temperature dependent ferroelectric behavior and thus energy storage properties. Depolarization temperature is where the transition from the field induced ferroelectric to weakly polar relaxor phase occurs [186]. We have done poling in order to determine T_d. The temperature dependent dielectric permittivity and loss of poled NBT–8BT sample is given in Figure 2.11 (c). A new peak appeared in dielectric loss at 59.6 ºC which is marked as T_d. The dielectric constant become frequency dependent above T_d, consistent with the field induced ferroelectric to relaxor transition. Poled BLT substituted compositions did not show any additional peak upon doing suggesting that their T_d is lower than room temperature. This shows that BLT strongly suppresses field-induced ferroelectric phase similar to other $Bi(Me_{0.5}Ti_{0.5})O_3$ (Me = Zn, Mg, Ni, Co) ceramics [181].

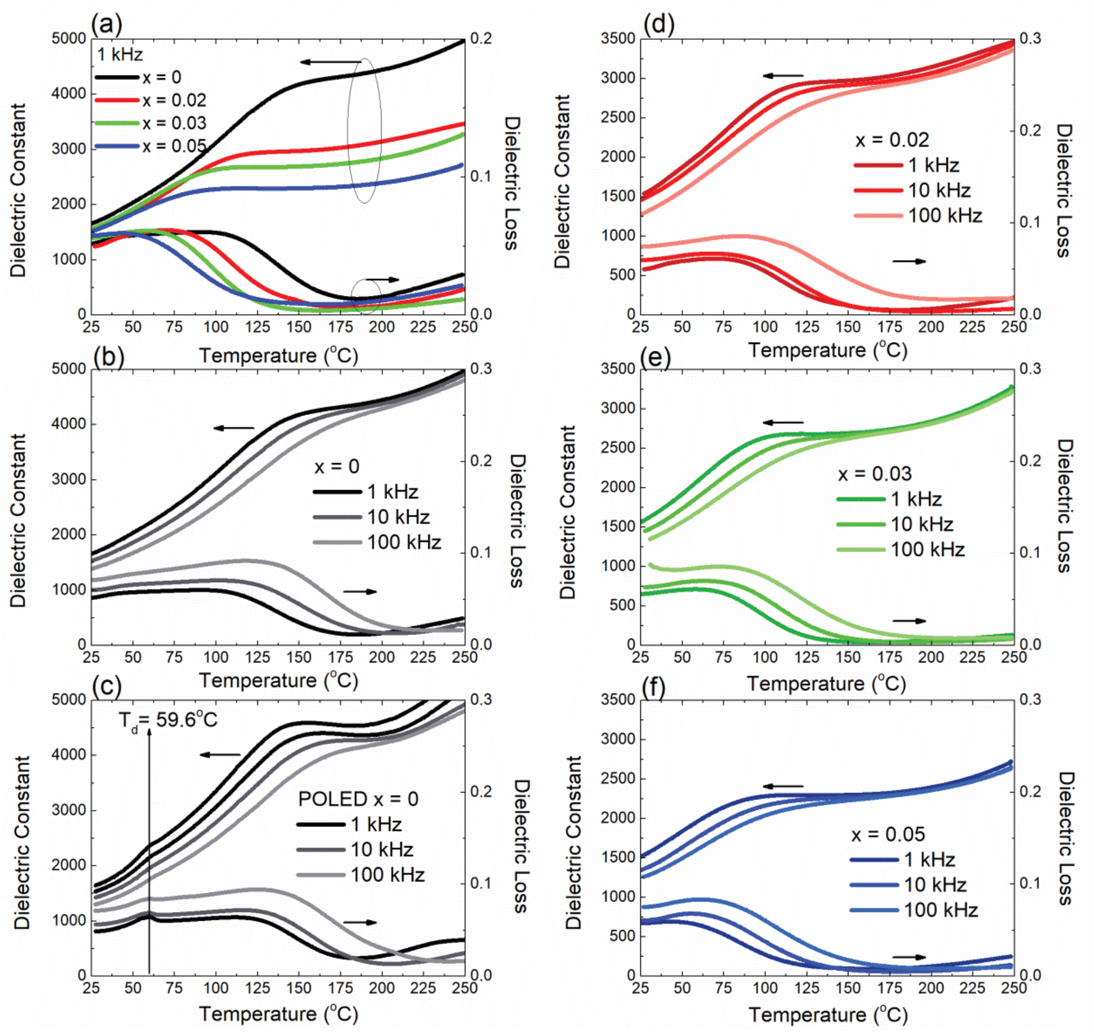

Figure 2.11. Temperature dependence of the dielectric constant and dielectric loss of (1-x)(0.92NBT-0.08BT)-xBLT ceramics (a) for x= 0, 0.02, 0.03 and 0.05 compared at 1 kHz, (b) for unpoled x= 0 and (c) poled x= 0 (d) x= 0.02, (e) x= 0.03, and (f) x= 0.05 measured at 1, 10 and 100 kHz.

2.3.4. Ferroelectric and Piezoelectric Properties of NBT-BT-BLT Ceramics

Polarization-Electric field loops of all compositions measured at 1 Hz are shown in Figure 2.12(a). NBT-8BT (x = 0) sample shows nonergodic behavior with normal ferroelectric-like hysteresis loop with a slightly pinched character and relatively low coercive field. As the depolarization temperature of the sample is just above the room temperature, the sample is close to the region where the transition from nonergodic to ergodic behavior takes place and therefore pinching already started at room temperature.

BLT containing compositions show ergodic relaxor character with pinched loops and very low P_r. Both P_r and E_c decreases abruptly with BLT substitution and further increase in the BLT content decreases them more. NBT.8BT.5BLT has a pinched and slim hysteresis loop with $P_m = 30\ \mu C/cm^2$, $P_r = 3\ \mu C/cm^2$ and $E_c = 9.5$ kV/cm. Bai et al. [181] has used the well-known tolerance factor;

$$t = \frac{r_A + r_O}{\sqrt{2}(r_B + r_O)}),$$

where r_A, r_B, and r_O are the ionic radii of the ions at the A and B-sites and oxygen, respectively in ABO_3 perovskite structure, as an indicator to estimate the amount of $Bi(Me,Ti)O_3$ substitution that causes the transition from the non-ergodic to ergodic state upon $Bi(Me,Ti)O_3$ substitution of NBT–6BT ceramics, where Me is Zn, Ni, Mg, Co at the B-site [181]. They show that as the tolerance factor of the Bi containing component gets lower, less amount of it will be sufficient to induce an ergodic state in the samples. For example, ergodic state was induced upon x = 2.75% $Bi(Zn_{0.5}Ti_{0.5})O_3$ (BZT) substitution for (0.94−x)NBT–0.06BT–xBZT, when t = 0.9810 (they assumed r_{Bi}^{3+} = 1.35 Å). In our case, tolerance factor we calculated for 2% BLT substituted NBT–8BT is 0.98289, which is slightly higher than that of 2.75% BZT substituted NBT–BT. A 2% BLT substitution is already enough to induce an ergodic state, which is a bit less than expected amount by looking at the tolerance factor. This difference must be caused by higher BT in our samples, which contain higher weakly polar tetragonal phase, facilitating ergodic relaxor behavior. Transition from the non-ergodic to ergodic relaxor character is also reflected in the strain electric field (S–E) curves plotted in Figure 2.12(b). Slightly distorted ‘butterfly’ shaped strain curve with remnant strain (0.045%) and negative strain (0.075%) has been obtained for NBT–8BT, whereas ‘sprout’ shaped strain curves that is typical for ergodic relaxors have been obtained for all BLT substituted samples. Maximum strain was obtained as 0.2% for the NBT–8BT sample, while neither negative nor remnant strain has been observed in the strain curves of BLT substituted samples, consistent with the ergodic relaxor behavior. After NBT–8BT sample, largest strain was obtained for x = 0.02 sample, followed by x = 0.03 and x = 0.05. This trend must originate from the differences in the proximity of respective Td’s to room temperature. In NBT based Pb-free piezoelectrics, field induced strain is maximized near T_d [187]. All BLT substituted samples have T_d’s below room temperature and as the BLT content increases, T_d is expected to decrease further away from the room temperature. We note that for the NBT–8BT ceramics, a slightly pinched loop at room temperature like ours is uncommon but not unique [158, 188]. Depolarization temperature of our NBT–8BT ceramic is lower than most reports in the literature. This might originate from excess bismuth at the A-site, as Na^+ is more volatile than Bi^{3+} [189]. Even though the pellets were buried in the powder of the same composition during sintering, Bi and Na evaporation cannot be completely prevented. Slight Bi excess at the A-site of NBT–6BT has been shown to cause significant decrease in T_d [189-190]. This decrease was related to the decrease of oxygen vacancies as they delay depolarization [190]. As T_d decreases towards room temperature, even though non-ergodic behavior is dominant, transition into ergodic state must have been already started, evident from slightly decreased P_r and pinching of the otherwise non-ergodic looking hysteresis loop. Additionally, possibility of excess Bi in the samples might also explain the decreasing grain size with increasing BLT substitution if we also assume a higher Bi excess with increasing BLT substitution. As Bi excess results in a decrease of the oxygen vacancies and oxygen vacancies typically cause grain growth by enabling diffusion [163], higher BLT containing samples will have smaller grains as in our case.

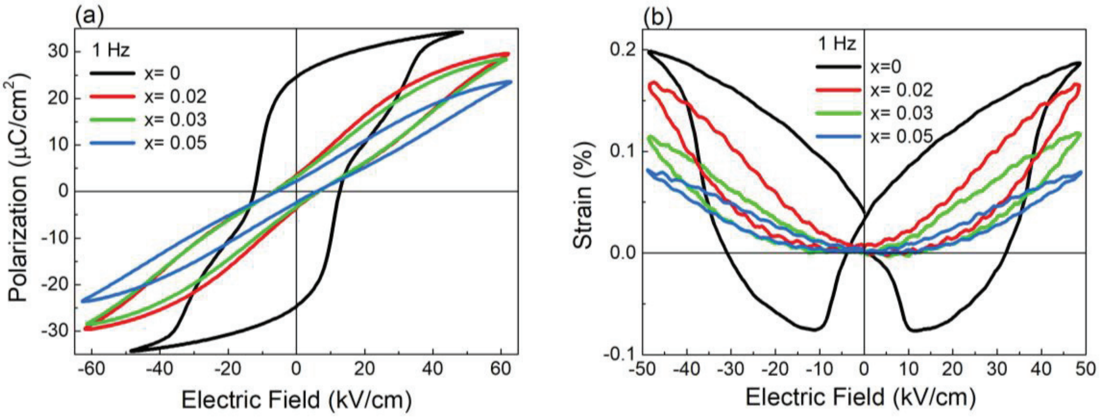

Figure 2.12. Composition dependent (a) polarization–electric field hysteresis loops and (b) strain-electric field loops of (1−x)(0.92NBT–0.08BT)–xBLT ceramics at room temperature.

Figure 2.13 (a-d) presents polarization-electric field (P-E) and current-electric field (I-E) hysteresis loops of NBT-8BT and NBT-8BT-2BLT ceramics under different temperature. The maximum electric field is 48.5 kV/cm and 65 kV/cm for NBT-8BT and NBT-8BT-2BLT respectively. For NBT-8BT, as the temperature increases, P_{max} P_r and E_c parameters gradually decreases as seen in (e). As temperature decreases from 50

°C to 75 °C, the P_r decreases dramatically from 19.04 to 4.19 μC/cm^3 where T_d = 59.6 °C coincides this temperature range. And it is also observed that P_{max}, is almost stable at room temperature and 50 °C, while it decreases more rapidly above T_d.

As seen in (b), four current peaks (±E_1, ±E_2) emerge for the room temperature I-E loop of sample NBT-8BT. As the applied electric field increases, the weakly polar tetragonal phase (P4mm) in the NBT-8BT structure transfer to the strongly polar ferroelectric phase (P4bm) and therefore the peak in the I-E loop is generated at E_2 [158]. During the opposite electric field application, the previous state with weakly polar phases is regained at -E_1 [158]. It is clearly seen from Figure 2.13 (b) that as the temperature increases the peaks at ±E_1 ,±E_2 start to disappear and new four peaks at ±E_3 ,±E_4 start to appear. Firstly, when we look at the temperature-dependent behavior of E_2, which causes electric field induced the weakly polar tetragonal phases to the ferroelectric phase transition, it is seen that the E_2 value does not change much but completely disappears at temperatures above 100 °C (Figure 2.13 (f)). It can be said that at higher temperature the weakly polar phase becomes unstable [180] and cannot be transferred to the polar phase by electric field inducing, therefore, E_2 disappears. On the other hand, the temperature dependent behavior of E_1 peak also provides information about the electric field induced phase transformation.

The peak E_1 corresponds to the E_c where domain switching occurs in a normal ferroelectric material. However, in a material which has pinched hysteresis loop, E_1 does not correspond exactly to E_c. It is seen from Figure 2.13 (b) and (f) that E_1 peak shifts to the negative electric field side above T_d and decreases linearly with increasing temperature. The linear interception with the temperature axis, where E_1 corresponds to zero electric field, it is realized that the temperature also corresponds to the depolarization temperature obtained from dielectric measurements. This means that; Because the strongly polar ferroelectric domains induced by the electric field become unstable above the depolarization temperature, the transition from polar phase to weakly polar phase occur only while unloading cycle of electric field at -E_1[180].

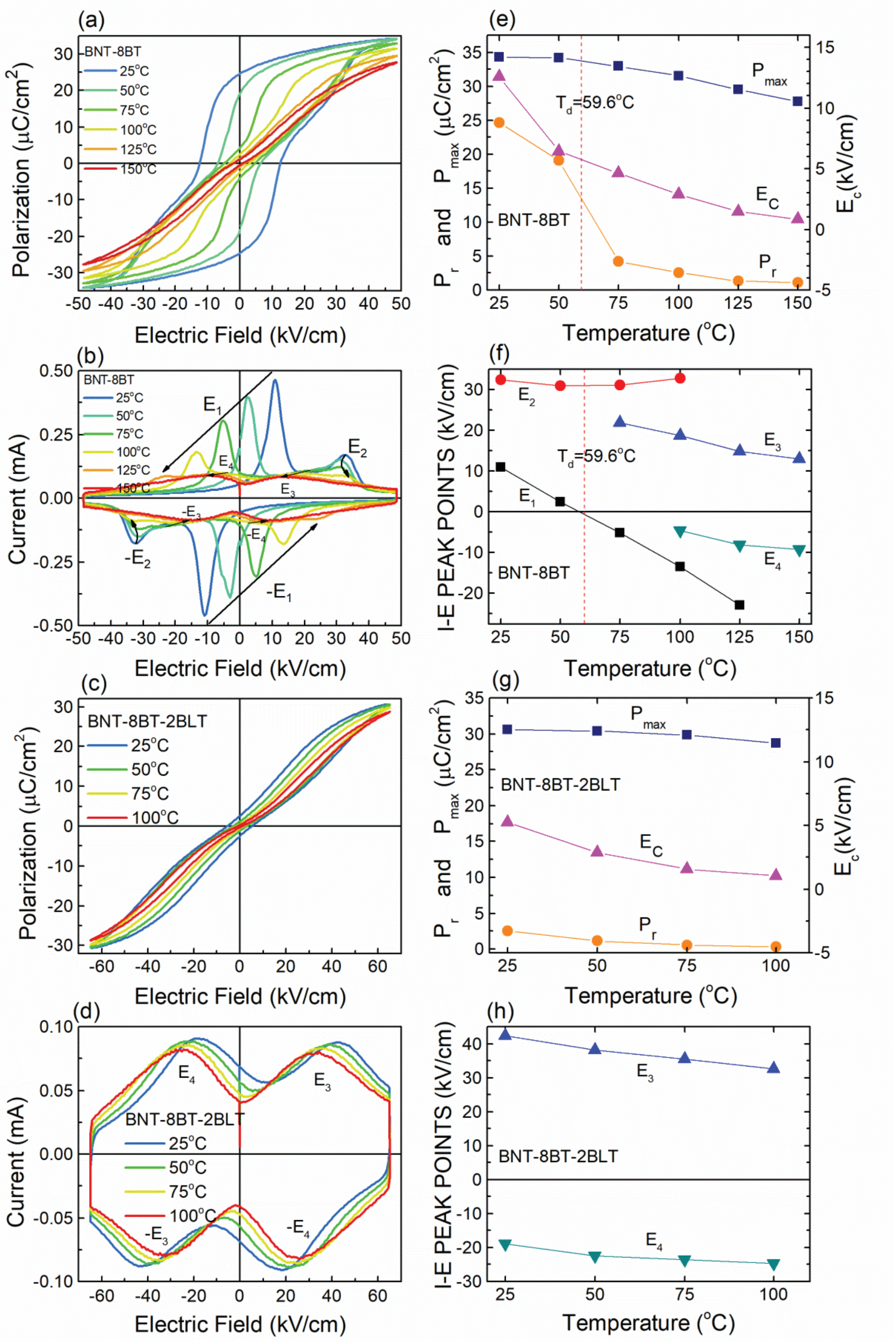

Figure 2.13. Temperature dependent (a,c) P-E loops, (b,d) C-E loops and corresponding temperature dependent (e,g) P_r, P_{max}, E_c and (f,h) I-E peak points of x = 0 and x = 0.02 ceramics respectively.

The disappearance of peak E_1 above 125 ° C, similar to E_2, can be attributed the reduced polar phase [191]. The peaks at E_3 and E_4 correspond to typical peaks of the I-E loop of the material exhibiting ergodic relaxor behavior. In NBT-8BT, these peaks begin to appear at 75 and 100 °C, and above 125 °C, only these peaks take place in the I-E loop. The peaks E_3 and E_4 occur at the temperature zone where the remnant polarization of the material decreases and the ergodic relaxor characteristic begins. On the other hand, at E_3 and E_4, the reversible transitions occur from the relaxor phase to the ferroelectric phase by exhibiting ergodic relaxor phase [191].

In the BLT doped materials, here NBT-8BT-2BLT is given as an example, the ergodic relaxor characteristic is exhibited as seen in Figure 2.13 (c, d). As the temperature increases, it is seen that P_m remains almost constant, while E_c and P_r decrease gradually (Figure 2.13 (g)). The E_3 and E_4 peaks decrease with increasing temperature (Figure 2.13 (h)) because reversible transitions from the relaxor ferroelectric phase to the ferroelectric phase require less electric field. These conditions are desirable for energy storage applications due to the temperature stability of P_m and low hysteresis loss.

2.3.5. Energy Storage Properties of NBT-BT-BLT Ceramics

Energy storage density and efficiency of the samples were calculated using the equations provided in the introduction section, based on the hysteresis loops presented in Figure 2.12(a). In order to compare the energy storage density of the BLT substituted samples, hysteresis loops collected at the same electric field of ≈ 61 kV/cm were used (see Figure 2.12(a)). As can be inferred from the hysteresis loops, largest energy storage density was obtained for x = 0.02 sample (W_{rec} = 0.656 J/cm^3), followed by x = 0.03 (W_{rec} = 0.614 J/cm^3) and x = 0.05 (W_{rec} = 0.559 J/cm^3). This result is expected from the hysteresis loops as the ergodic behaviour is already achieved for x = 0.02 with low P_r and E_c while due to the lowest BLT content, P_m of x = 0.02 sample is higher than those of x = 0.03 and x = 0.05.

Maximum electric field that could be applied to samples (dielectric breakdown strength) differs from composition to composition. Calculated maximum energy storage densities were 0.74, 0.61 and 1.03 J/cm^3 for x = 0.02, 0.03 and 0.05 at applied electric fields of 65.78, 61.41, 89.21 kV/cm respectively, as shown in Figure 2.14. The x = 0.05 yields the maximum energy storage density as it sustains the maximum electric field. While a systematic study is necessary to obtain accurate dielectric breakdown strength of all samples, the trend in the same can be correlated to the different thickness of the measured samples as well as the grain size. It is well known that a thinner material can exhibit higher dielectric breakdown field [192]. The thicknesses of the BLT substituted ceramics used in this study were 1.02 mm, 1.27 mm and 0.71 mm for x = 0.02, 0.03 and 0.05, respectively. Lowest grain size of the x = 0.05 sample might also play a role in its large breakdown strength.

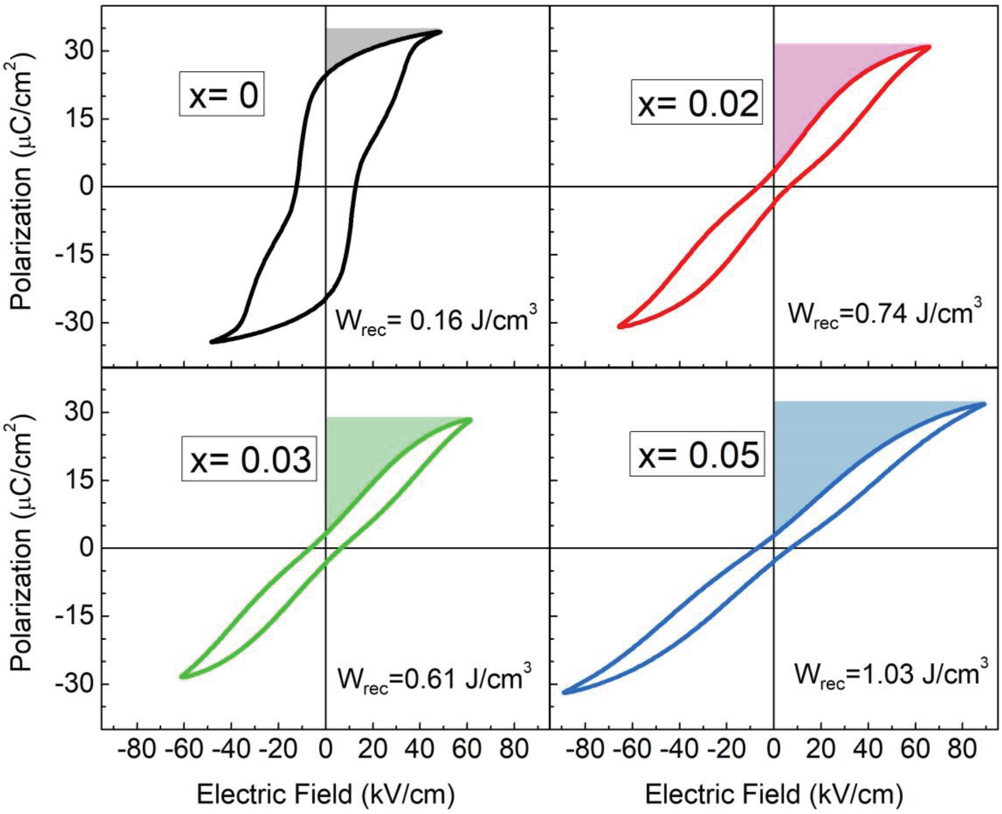

Figure 2.14. Room temperature *P–E* loops at 1 Hz and energy storage densities of $(1-x)$(0.92NBT–0.08BT)–xBLT samples.

Figure 2.15(a) shows the temperature-dependent unipolar hysteresis loops of NBT-8BT-2BLT, the sample with the high energy storage density at different temperature. The calculated energy storage densities and efficiencies are also presented in Figure 2.15(b). At the room temperature, the energy storage density and the efficiency have been calculated as $W_{rec} = 0.74$ J/cm^3 and $\eta = 67\%$ under an electric field of 65.78 kV/cm. As the temperature increases, energy storage density and efficiency both increases, reaching 0.88 J/cm^3 and 96.7% respectively, at 125 °C. This indicates that x = 0.02 composition is suitable for high temperature applications.

In Figure 2.15(c) and Figure 2.15(d) unipolar P-E loops as a function of increasing electric field and corresponding energy storage densities of NBT-8BT-5BLT composition, at room temperature are shown respectively. A large energy density of 1.03 J/cm^3 with high efficiency of approximately 70% under an electric field of 89 kV/cm can be achieved.

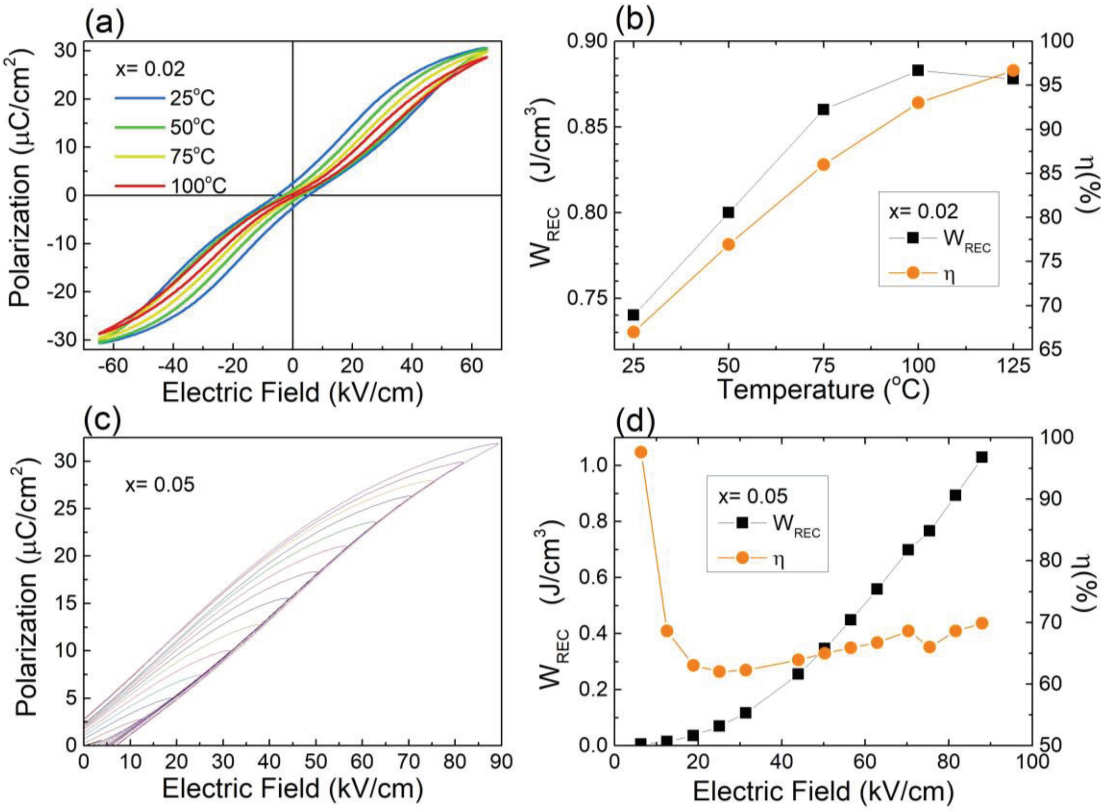

Figure 2.15. Temperature dependent (a) P–E loops at 1 Hz and (b) recoverable energy storage density, W_{REC} and efficiency, η of NBT–8BT–2BLT. Room temperature (c) Unipolar P–E loops at 1 Hz, under different applied electric fields and (d) electric field dependent energy storage densities of NBT–8BT–5BLT.

Energy storage densities of NBT based ceramics have been reported to lie between 0.7-2.42 J/cm^3, with 54-86% efficiency and under 70-195 kV/cm maximum electric field [154-163, 193]. In this work, we have not pushed the maximum electric field we apply to the samples; we limited ourselves to the effect of BLT substitution. Therefore, it is more reasonable to compare the energy storage density values obtained per unit applied electric field. Figure 2.16 shows energy storage density obtained per unit applied field and energy storage efficiency values for x = 0.02 and x = 0.05 samples, in comparison with other NBT-based samples in the literature. It can be seen that our BLT substituted NBT ceramics perform quite well among NBT based ceramics in both indicators.

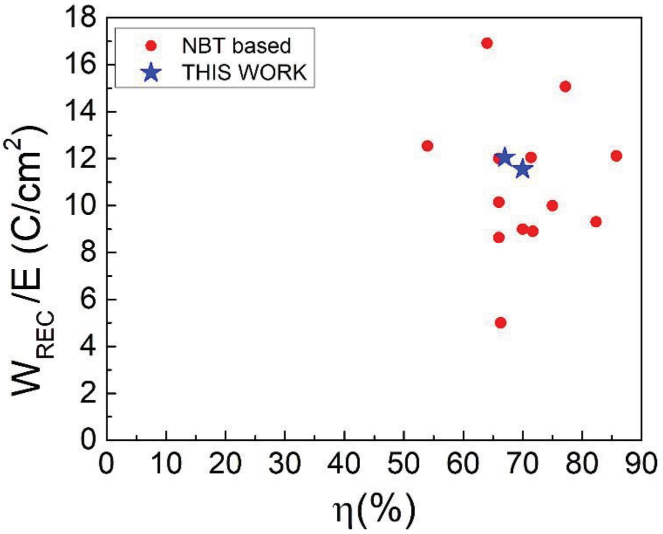

Figure 2.16. Obtained energy storage density normalized by the applied electric field and energy efficiency values of NBT-based ceramics [154-163, 193].

2.4. Conclusions

In conclusion, it has been investigated the effect of BLT substitution on the energy storage properties of (1−x)(0.92NBT–0.08BT)–xBLT samples. Non-substituted NBT–8BT showed usual non-ergodic relaxor characteristics with normal-like hysteresis loops and butterfly-like strain-electric field loops. Only 2% of BLT substitution induced room temperature ergodic relaxor behavior, with low P_r and high P_m, favorable for energy storage as well as sprout shaped strain-electric field loops. Increasing BLT content causes decrease in the grain size, with x = 0.05 having the smallest grain size and possibly highest dielectric breakdown strength of all compositions. Largest energy density (W_{rec}) at 61 kV/cm was obtained for x = 0.02 sample (0.656 J/cm^3), followed by x = 0.03 (W_{rec} = 0.614 J/cm^3) and x = 0.05 (W_{rec} = 0.559 J/cm^3). When these values are normalized with respect to the applied field, it is shown that BLT substitution is quite successful for energy storage among NBT based ceramic compositions. The x = 0.02 sample keeps its energy storage density at high temperatures (i.e. W_{rec} = 0.88 J/cm^3, η = 97%, E_m = 65 kV/cm at 125 ºC). Larger electric field (up to 89 kV/cm) could be applied to the x = 0.05 sample with the lowest grain size and energy density of 1.03 J/cm^3 was reached.

CHAPTER 3

AGING AND ELECTROCALORIC PROPERTIES OF MN DOPED CERAMICS

3.1. Ferroelectric Aging Effect

Acceptor-doping is frequently applied to ferroelectric ceramics to improve the ferroelectric properties by lowering dielectric losses and increasing mechanical quality factor [194]. However, they might also cause ferroelectric aging due to the formation of point defects and defect dipoles. Aging typically causes deterioration of the dielectric and ferroelectric properties and in particular can lead to pinched polarization hysteresis loops [195]. Ferroelectric aging, which involves diffusion of oxygen vacancies and therefore, a time dependent effect, does not always cause deterioration of the properties. On the contrary, it can lead to better electromechanical [196] and even electrocaloric properties [197]. Therefore, maximizing the benefits of acceptor doping and minimizing the disadvantages of the aging effect on properties, i.e. optimization, is important in this context.

3.1.1. Aging Mechanism

In general, the ferroelectric aging process is explained by the tendency of the gradual domain stabilization by defect diffusion [14, 198]. There are three different mechanisms (volume, domain wall and grain boundary effect) which explain the ferroelectric aging or domain stabilization according to their length scales and microstructural changes (Figure 3.1).

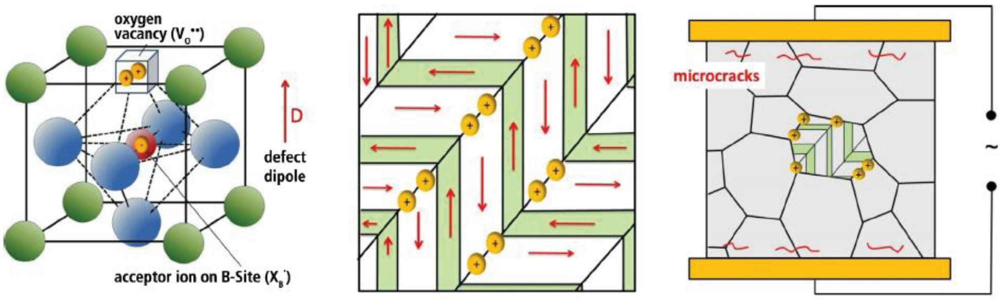

(a) Volume effect (b) Domain effect (c) Grain boundary effect

Figure 3.1. Classification of aging mechanisms [199].

The volume effect mechanism is explained by the symmetry conforming short range ordering (SC-SRO) [200] principle which constitutes the driving force for the reorientation of the defect dipoles to follow symmetry of the crystal. At equilibrium, the symmetry of the short-range ordered defect dipoles tends to follow the crystal symmetry. The symmetry property of point defects is schematically demonstrated in Figure 3.2 by considering a typical ferroelectric perovskite ABO_3 structure. If a D^{3+} acceptor ion is doped into the B^{4+} site of the crystal structure, the possibility of forming an oxygen vacancy in one of its nearest neighbors becomes inevitable in order to maintain the charge neutrality. Statistical distribution of O^{2-} vacancies around a defect ion D^{3+} depends on the crystal symmetry. For the D^{3+} defect ion in a cubic crystal, the probability of finding an oxygen vacancy is the same in all its neighboring oxygen sites (1, 2, 3, and 4). Therefore, the symmetry of the crystal with the D^{3+} point defect is in cubic symmetry (Figure 3.2(a)). In the tetragonal symmetry neighboring sites of the defect D^{3+} are not equivalent (site 1 and 2 are equivalent but 3 and 4 are not) (Figure 3.2(b)). Equivalent sites are expected to have the same probability of finding oxygen vacancies, and non-equivalent sites are expected to have different probability of finding oxygen vacancies. Thus, at equilibrium, the symmetry of the short-range ordered distribution of point defects tends to follow the crystal symmetry [196a]. This indicates the symmetry-conforming property of point defects.

The equilibrium defect symmetry has polar crystal symmetry due to non-centric distribution of charged defects. The oxygen vacancy has an effective charge of 2+ due to absence of O^{2-} and D^{3+} has 1- effective charge due to the absence of Ti^{4+} ion. Therefore, in the defect structure, a defect dipole moment P_D is also formed along the polarization direction of P_S.The demonstration of the symmetry-conforming property of point defects is shown schematically in Figure 3.2.

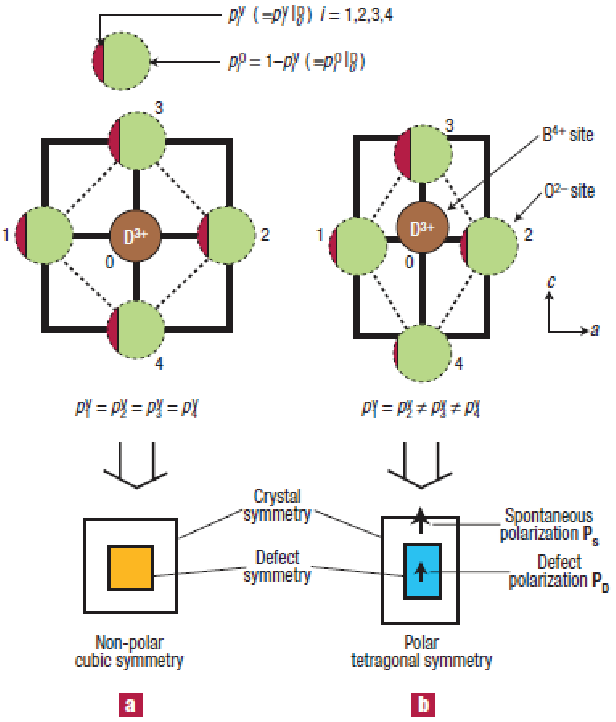

Figure 3.2. B-site acceptor doped (a) nonpolar/ centrosymmetric cubic paraelectric state, and (b) polar tetragonal ferroelectric state [196a].

3.1.2. Factors Affecting Ferroelectric Aging or Domain Stabilization

In this section, we will discuss how defect dipoles and ferroelectric domains are stabilized during aging and what factors effects in this process. Since the internal electric field E_i formed by the defect dipole will reach its maximum value when the domain is stabilized, E_i is generally considered in domain stabilization factors. Factors affecting ferroelectric aging and domain stabilization are discussed under six main following sections: grain size, acceptor doping concentration, acceptor doping elements, local structure of the perovskite, temperature and electric field.

3.1.2.1. Grain size

The grain-size effects on the aging behavior of ferroelectric ceramics have been investigated in some studies [201]. Guo et al demonstrated that the larger grained samples show clear aging effects while the fine grained ceramics show suppressed aging effects

[201a] (see Figure 3.3). The underlying mechanism of this grain size effect has been interpreted as that the small lattice tetragonal deformation in fine grained ceramics gives rise to a relatively weak thermodynamic driving force. On the other hand, the grain boundary barrier effect was demonstrated as another inevitable reason that suppresses the ferroelectric aging effect due to the kinetically limited migration of oxygen vacancies in grain boundaries. In the other study [201b] they observed that with the aging time increasing the remnant polarization of large grained ceramics drop sharper than that of small grained ones. They attributed the reason as a competition between aging-induced internal defect field E_i and grain boundary generated back field, which restricted forward domain switching (E_1) and helped backward domain switching (E_2).

It is also demonstrated that at the grain boundaries a fast transport occurs due to enhanced vacancy concentration, segregation, and possibly space-charge effects, on the other hand, local structure of a grain boundary ensures a migration path with remarkably lower barrier [202]. According to this statement, it is expected that the oxygen vacancies will be faster at the grain boundary and the aging time will be faster in the fine-grained structure.

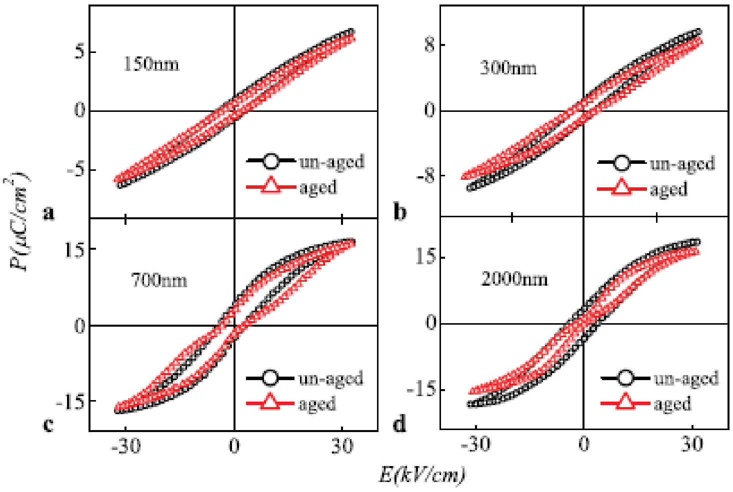

Figure 3.3. P-E hysteresis loops at room temperature under E = 32 kV/cm for different grained ceramics. (a) 150 nm, (b) 300 nm, (c) 700 nm, and (d) 2000 nm samples show their loops in the unaged (fresh) states and after aging for 48 days at 70°C [201a].

3.1.2.2. Acceptor doping concentration

Another effect on the aging behavior of ferroelectric ceramics is the acceptor doping concentration. It has been showed in many studies that ferroelectric-paraelectric phase transition temperature T_c slightly decreases in accordance with the decrease of tetragonality parameter c/a by increasing acceptor concentration [203]. Decrease in c/a implies decrease in lattice distortion. In this context the substitution of $Mn^{2+/}Mn^{3+}$ into Ti^{4+} site will create oxygen vacancies resulting in a distortion in crystal lattice.

On the other hand, the internal field E_i increases due to the increasing defect dipoles by increasing acceptor doping concentration. In Figure 3.4, hysteresis loops for the unaged and aged $Ba(Mn_xTi_{1-x})O_3$ samples with different Mn concentration have been given. The hysteresis loops of all unaged samples show the normal loops except the sample with x = 1.3% which shows double hysteresis (Figure 3.4 (d)). From this behaviour, it was deduced that the more Mn is doped, the more oxygen vacancy is generated [203a]. Thus, it takes a short time to form the internal field and pinched double hysteresis loop.

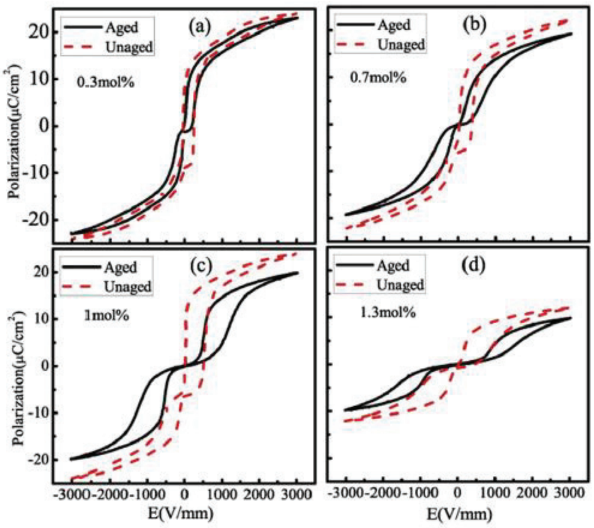

Figure 3.4. Hysteresis loops for the unaged and aged samples of $Ba(Mn_xTi_{1-x})O_3$ (a) 0.3 mol%, (b) 0.7 mol%, (c) 1.0 mol%, (d) 1.3 mol% [203a].

3.1.2.3. Acceptor Doping Elements

Some methodical studies [199] of aging effects on different acceptor doping elements have been done and given in Figure 3.5. It is clearly seen that internal electric field depends significantly on the dopant element. According to these studies, it is seen that the element that creates the most internal electric field and causes the best domain stabilization is Fe. At the same time, as the concentration increases internal electric field increases nonlinearly and saturates at higher concentrations probably due to limited solubility limits of doping elements.

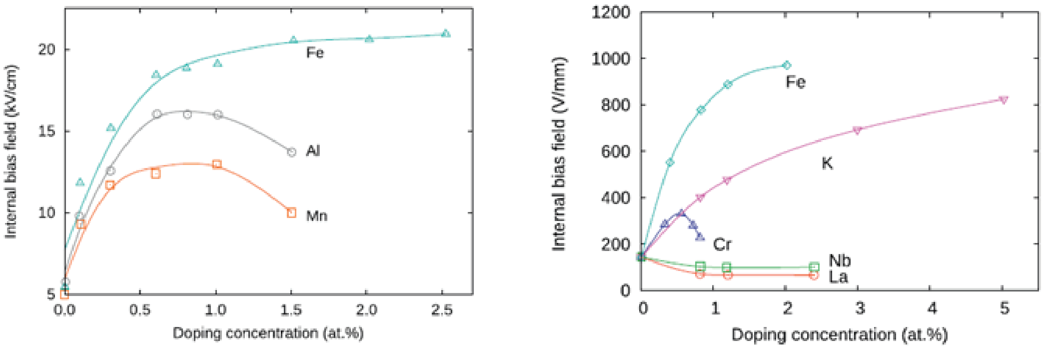

Figure 3.5. Doping effects on the internal bias field emerging in PZT from Carl et al. (left) and Takahashi et al. (right) [199].

3.1.2.4. Local structure of the perovskite

Another factor affecting domain stabilization is the local effect in the perovskite structure. In a study Ba$_{1-x}$Sr$_x$TiO$_3$-1Mn samples (x = 0, 0.05, 0.15, and 0.20) and Pb$_{1-x}$Sr$_x$TiO$_3$-1Mn (x = 0.50, 0.55, and 0.60) samples were studied to investigate this effect [204]. Figure 3.6 shows the schematic representation of Mn doped PT and BT structures. In this figure Pb or Ba ions are in the center and oxygen vacancy is represented as square. Smaller Pb ionic size (Pb ions (1.20 Å) < Ba ions (1.34 Å)) facilitates easy hopping of oxygen vacancy and a larger Pb ionic shift occur and much larger defect dipole field Ei (long solid arrow) is ensured than that of BT system. It means that PT system has much “stronger” domain stabilization strength due to its larger A site ion.

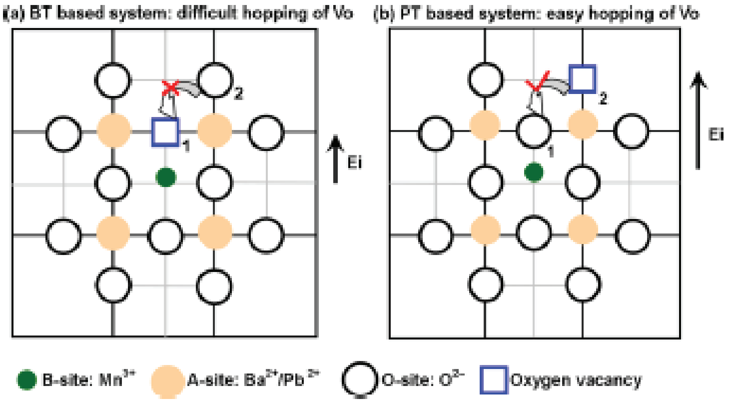

Figure 3.6. Local structure of perovskite ABO_3 structure BT (a) and PT (b) system, with dopant Mn at centered Ti site, and surrounded by near oxygen sites like O1, O2, etc. [204].

This effect was verified from the polarization loops of well-aged samples by calculating E_1 and E_2 switching peaks from dP/dE curves (Figure 3.7). Under the same aging processes, it was observed that the defect dipole field E_i, which represents domain stabilization, decreased with increasing Sr ratio and decreasing c/a ratio for both BT and PT systems. However, it was shown that the highest E_i field occurs in the PT system anyway. The reason for this is the local structure effect as explained above.

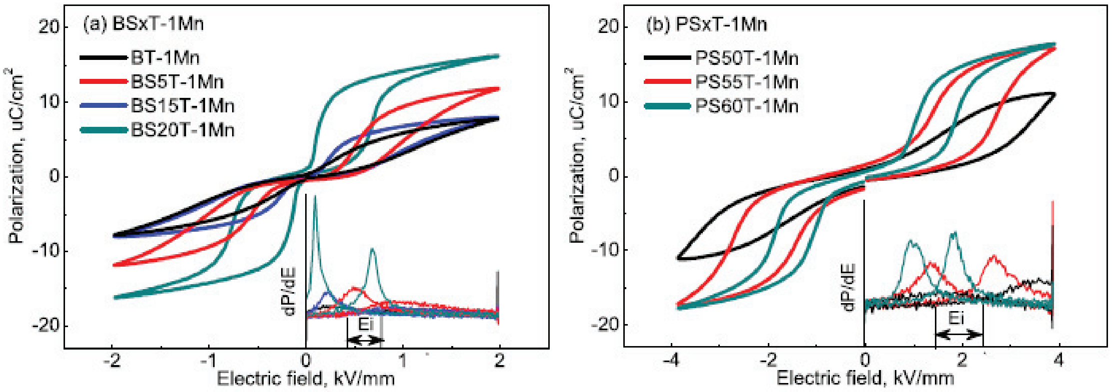

Figure 3.7. Double P-E loops of the well-aged (a) BS_xT-1Mn samples (x= 0, 0.05, 0.15, and 0.20) and (b) PS_xT-1Mn (x= 0.50, 0.55, and 0.60) samples. Each inset figure shows the dP/dE curves, and defect dipole field E_i [204].

3.1.2.5. Temperature

Providing a high temperature environment is the most common method to accelerate the ferroelectric aging time [200b]. However, the material must be in the ferroelectric state during this process. Thus the temperature should not exceed T_c. Generally, a temperature closes to T_c but lower than T_c is chosen during the aging process. An increase in the aging time is expected, as the diffusion of the oxygen vacancy, which provides the formation of defect dipoles, will accelerate if the temperature is at this optimal level.

It is known that sintering temperature likely changes the valence of the acceptor ions. Consequently, this will affect domain stabilization. It is known that MnO_2 can transform into different oxide forms at different sintering temperatures [205] as follows;

$$MnO_2 \xrightarrow{535\,°C} Mn_2O_3 \xrightarrow{1080\,°C} Mn_3O_4 \xrightarrow{1650\,°C} MnO$$

This means that valence states of Mn ions are influenced by the sintering temperature and with sintering temperatures above 1000°C different Mn valences can be found.

3.1.2.6. Electric field

In order to understand the effect of the electric field on the domain stabilization, the internal electric field change can be examined for the unaged sample to which a DC electric field is applied for a long time [206]. In Figure 3.8(b) polarization hysteresis loops of a acceptor doped and poled (or DC electric field applied) sample have been given. The calculation of E_i for both unpoled and poled state gives the E_i of 0.73 kV/mm and 0.71 kV/mm, respectively. Similar numbers of E_i means domain is stabilized in aged samples similar to poled samples [204].

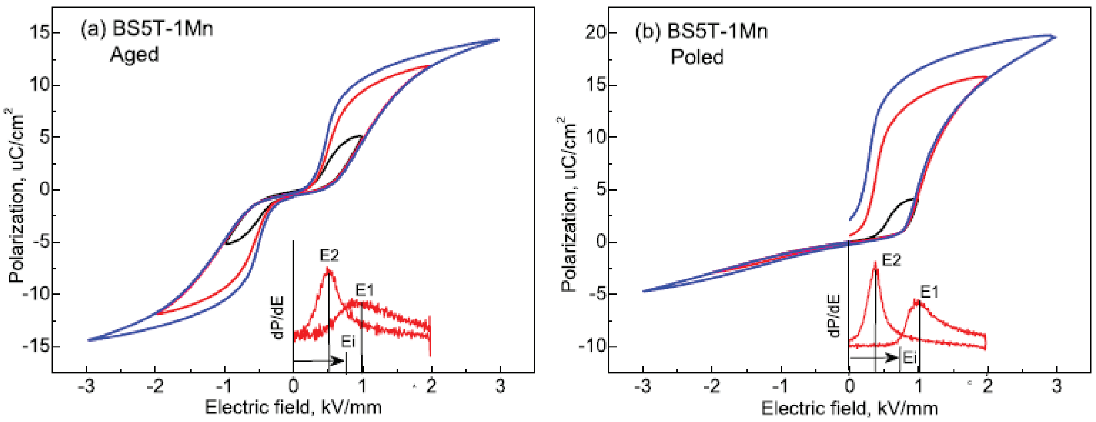

Figure 3.8. P-E loops in (a) the aged sample and (b) P-E loops in the poled (3 kV/mm) and aged sample [204].

3.1.3. Mn Doping and Defect Formation

Mn-doping has been utilized in piezoelectric ceramics for different purposes. Mn-doping at the Ti-site was reported to decrease the leakage current of $BaTiO_3$ by forming defect dipoles with oxygen vacancies, which, in turn, reduce the mobility of oxygen vacancies [207] or by trapping of electron and holes [208]. It serves as acceptor doping and can help to obtain reversible domain switching and large electrostrain [196a].

There is no consensus in the literature about the valence of Mn ions in sintered $BaTiO_3$-based ceramics. While many authors suggest that Mn takes the valence of 3+ when sintered in air [196b, 209], an electron paramagnetic resonance (EPR) spectroscopy-based study suggest that even though majority of Mn exists in 3+ state, some 4+ and also 2+ are also possible [208]. Some other studies mention only about Mn^{2+} formation by using X-Ray Photoelectron Spectroscopy (XPS) data [210].

Mn valence affects the aging behavior and resulting domain stabilization by the formation of different defect dipole pairs. If the Mn^{3+} ion is incorporated to Ti^{4+} position of the $BaTiO_3$ system, one positive charge will be lost, causing an effective negative charge (Mn_{Ti}'). An oxygen vacancy ($V_O^{\cdot\cdot}$) with +2 effective charge will form in order to maintain the charge neutrality in the system. The corresponding equation in Kröger-Vink notation is as follows:

$$2BaO + Mn_2O_3 \rightarrow 2Ba_{Ba}^{\times} + 2Mn_{Ti}' + 5O_O^{\times} + V_O^{\cdot\cdot}$$

If the Mn^{4+} ion is incorporated to Ti^{4+} position of the $BaTiO_3$ system, charge neutrality will be maintained and no oxygen vacancy will form: ($Mn_{Ti}^{\times}$). The corresponding equation is:

$$BaO + MnO_2 \rightarrow Ba_{Ba}^{\times} + Mn_{Ti}^{\times} + 3O_O^{\times}$$

Of course, the oxygen in the system can spontaneously turn into oxygen gas (reduction of an oxide), causing an increase in electrons and an oxygen vacancy formation in the system;

$$O_O^{\times} = \frac{1}{2}O_2(g) + V_O^{\cdot\cdot} + 2e'$$

In addition, Mn ions can be found in different forms in the system by reduction and oxidation reactions among themselves;

$$Mn_{Ti}^{\times} + e' \rightarrow Mn_{Ti}'$$
$$Mn_{Ti}' + e' \rightarrow Mn_{Ti}''$$

Oxygen vacancies ($V_O^{\cdot\cdot}$) (formed to maintain the charge neutrality) can interact with Mn ions, and these formations are called as defect dipoles. While a neutral defect dipole ($(Mn_{Ti}'' + V_O^{\cdot\cdot})^{\times}$) is formed in the interaction between Mn^{2+} and oxygen vacancies. In the interaction between Mn^{3+} and the oxygen vacancy, a positively charged defect dipole ($(Mn_{Ti}' + V_O^{\cdot\cdot})^{\cdot}$) is formed;

$$Mn_{Ti}'' + V_O^{\cdot\cdot} \rightarrow (Mn_{Ti}'' + V_O^{\cdot\cdot})^{\times}$$
$$Mn_{Ti}' + V_O^{\cdot\cdot} \rightarrow (Mn_{Ti}' + V_O^{\cdot\cdot})^{\cdot}$$

Since Mn valence might affect the defect dipole formation and aging behavior, it is of interest to study whether the Mn-precursor will have any effect on the resulting valence of the Mn-doped ceramics. Despite the many studies on the effect of Mn doping on the electrical properties of $BaTiO_3$-based Pb-free piezoelectrics, no systematic study can be found in the literature where the effect of Mn source on the ferroelectric aging and aging-affected electrical properties.

Therefore, in this study, we have investigated the effect of Mn precursor on the resulting Mn-valence, aging behavior and electrical properties of the BT-based ceramics. In order to decrease the Curie temperature (T_C) of the $BaTiO_3$ samples slightly by Sr doping and for easy comparison with the existing literature, we have selected $Ba_{0.95}Sr_{0.05}TiO_3$ composition. Two different sintering temperatures (1325 ºC and 1400 ºC) to examine the grain size effect, two different Mn content (0.3 and 1%) to examine the defect dipole formation rate around solubility limit (1%) of Mn and away from it (0.3%) and two different Mn precursors (MnO_2 and Mn_2O_3) to examine the possible different Mn valence formation and different defect dipole types were used. We show by combining EPR spectroscopy and the evolution of the tetragonality with Mn-doping that we obtained from the XRD data, that Mn is slightly better incorporated into the perovskite structure when MnO_2 is used as Mn precursor. (When MnO_2 is used as Mn precursor we show that Mn is slightly better incorporated into the perovskite structure according to results from the evolution of the tetragonality with Mn-doping that we obtained from the XRD data and by combining EPR spectroscopy.) Ferroelectric aging causes constriction of the hysteresis loops and decreases ΔT while Mn-doping resulted in better electrocaloric properties. It has been shown that the optimal conditions for the best ΔT is obtained in samples with large grain size sintered at 1400 ºC, in samples with Mn ratio of 1% and in samples using MnO_2, where the aging effect is less.

3.2. Experimental Procedure for Mn Doped BST Ceramics

The conventional solid state reaction method was used to synthesize the samples: $(Ba_{0.95}Sr_{0.05})TiO_3$ (BST), $(Ba_{0.95}Sr_{0.05})(Mn_{0.003}Ti_{0.997})O_3$ (BST-0.3Mn), $(Ba_{0.95}Sr_{0.05})(Mn_{0.01}Ti_{0.99})O_3$ (BST-1Mn) with two different Mn oxide precursors: MnO_2 and Mn_2O_3. $BaCO_3$ (99%), $SrCO_3$ (99%), Mn_2O_3 (99%), MnO_2 (99%) and TiO_2 (99.9%) were used as starting raw materials (Table 3.1). All powders were dried at 200 ºC overnight. Then they were weighed and mixed in a 30 ml high density polyethylene (HDPE) bottle using zirconia balls in ethanol media by planetary ball milling for 18 h. After drying, the powders were ground in agate mortar. The calcination process was carried out in pellet form at 1200 ºC for 2 h. After calcination, the pellets were again ground into powder and were mixed thoroughly with 4 wt% polyvinyl alcohol (PVA) binder in water and then ball milled for 18 h. Then powders were dried, sieved, and pressed into pellets (~10 mm in diameter, ~1 mm thick) under a pressure of ~100 MPa. Then the PVA binder was burned out at 600 ºC for 4 h. After the burnout, the pellets were sintered at 1325 ºC and 1400 ºC for 2 h with a heating rate 5 ºC/min (Figure 3.9).

Table 3.1. The list of the combination of variable parameters of the samples $(Ba_{0.95}Sr_{0.05})(Mn_xTi_{1-x})O_3$ (BST-100xMn).

Base ceramic	Mn comp. (x)	Mn precursor	Sintering Temp. (°C)	Sample name
BST	0	0	1325	**BST-1325**
			1400	**BST-1400**
	0.3	MnO_2	1325	**BST-0.3Mn (MnO_2)-1325**
			1400	**BST-0.3Mn (MnO_2)-1400**
		Mn_2O_3	1325	**BST-0.3Mn (Mn_2O_3)-1325**
			1400	**BST-0.3Mn (Mn_2O_3)-1400**
	1	MnO_2	1325	**BST-1Mn (MnO_2)-1325**
			1400	**BST-1Mn (MnO_2)-1400**
		Mn_2O_3	1325	**BST-1Mn (Mn_2O_3)-1325**
			1400	**BST-1Mn (Mn_2O_3)-1400**

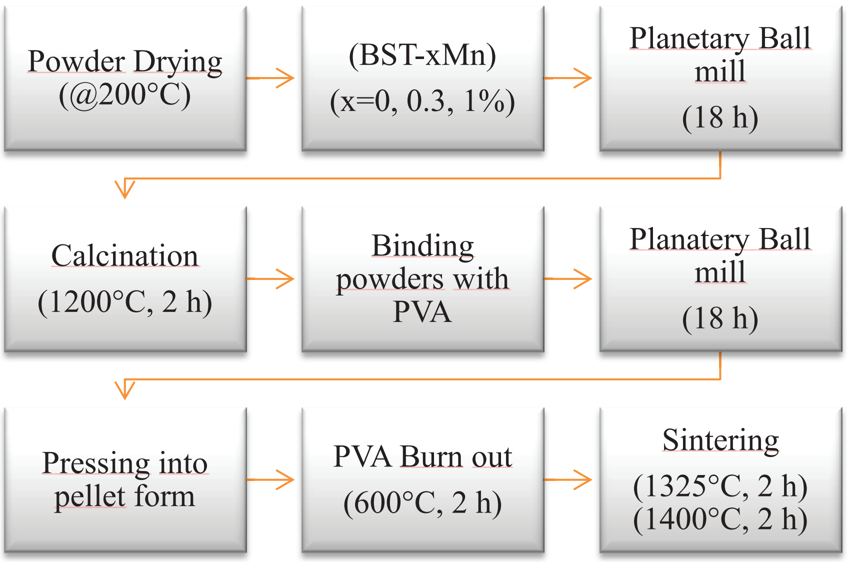

Figure 3.9. Schematic illustration of the synthesis routes of BST-xMn ceramics.

X-ray powder diffraction (XRD, Cu Ka radiation, Philips X'Pert Pro) was used to determine the phases and crystal structures of the sintered samples. The microstructure of ceramics was studied on thermally etched surfaces (at 1225 and 1300 °C, for 1 h, for the samples sintered at 1325 and 1400 °C, respectively) using a scanning electron microscope (SEM, FEI QUANTA 250 FEG). The average grain sizes were calculated by linear intercept method using ImageJ software. For dielectric and polarization-electric field hysteresis measurements, both surfaces of polished pellets were coated with silver paste and dried at 200 °C for 20 min. To obtain completely unaged state, deaging treatment was carried out at 270 °C for 30 min. for the Mn- doped samples. Then they were quenched to the room temperature. Hysteresis measurements of unaged samples were done immediately after quenching. The samples were aged at 90 °C and hysteresis loops were measured after 1, 3, 7 and 20 days of aging. Since hysteresis loops of the samples sintered at 1325 °C did not change anymore after 3 days, the aging duration of these samples was determined as 3 days. On the other hand, since no difference was observed between the 7-days and 20-days-aged P-E loops of the samples sintered at 1400 °C, the aging time for these samples was determined as 7 days. In order to test the consistency of ferroelectric aging, aging process was repeated for the aged samples after applying de-aging process to the aged samples and the same P-E loops were obtained after 7 days of aging.

The temperature dependence of dielectric constant and loss of the ceramics were measured at various frequencies (0.1, 1, 10, 100 kHz) by an LCR meter (KEYSIGHT, E4980AL). The polarization-electric field (P-E) hysteresis loops were obtained by using AIXACCT TF analyzer 1000 and a high voltage amplifier (TREK model 610E). The strain data were also collected simultaneously by a laser-interferometer (SIOS). Both for dielectric and hysteresis measurements a sample holder (AIXACCT piezo sample holder TFA 423-7) was used and temperature was controlled by AIXACCT temperature controller. X-band EPR measurements were carried out at room temperature using a CMS 8400 (Adani) spectrometer with a TE102 resonator cavity at a microwave frequency of 9.4 GHz.

The electrocaloric effect (ECE) of these samples was calculated by the indirect method. Temperature and electric field dependent polarization loops (P(E)) were used to calculate the adiabatic temperature change (ΔT) of the material. According to the Maxwell relation,$(\partial P/\partial T)_E = (\partial S/\partial E)_T$ indirect ECE is determined as,

$$\Delta T = \frac{T}{\rho C}\int_{E_1}^{E_2}\left(\frac{\partial P}{\partial T}\right)_E dE$$

where the specific heat C has been considered as constant and taken as 0.50 J/gK [211] and the densities ρ of samples that were measured by Archimedes' method have been used.

3.3. Results and Discussions

3.3.1. Phase and Structure Properties of Mn Doped BST Ceramics

In Figure 3.10, XRD patterns of $(Ba_{0.95}Sr_{0.05})(Mn_xTi_{1-x})O_3$ (BST-100xMn) ceramics sintered at 1325 and 1400 °C are shown. All patterns show tetragonal symmetry with obvious splitting between (200) and (002) peaks and no extra phases can be observed. Rietveld refinements results of all patterns are shown in Table 3.2 and fitting of XRD patterns are given in the appendix section (Figure A.2, Figure A.3, Figure A.4 and Figure A.5). All refinements have weighted profile R values (R_{wp}) below 10.4 % and have goodness of fit (GoF) values below 1.47.

Tetragonal splitting is more obvious for the samples sintered at 1400 °C (Figure 3.10(d)) than that of those sintered at 1325 °C (Figure 3.10(b)). This is also reflected in the tetragonality of the samples, which is higher for the samples sintered at 1400 °C (see Figure 3.11). This is an expected result as it is established that higher sintering temperature will lead larger grains and samples with larger grain size exhibit higher c/a value [201a]. Change of tetragonality with Mn content for all samples is also shown in Figure 3.11. It is clear from the figure that increasing Mn content decreases tetragonality. Tetragonality change can be ascribed to the incorporation of Mn ions with 2+, 3+ or 4+ valence to the Ti-site. When larger Mn^{3+} (r = 0.645 Å) or Mn^{2+} (r = 0.670 Å) ions are incorporated to the Ti^{4+} (r = 0.605 Å) positions, they cause slight increase in a-b tetragonal lattice parameters and the slight reduction in c lattice parameter [212]. Therefore c/a decreases and the peak splitting of (200) and (002) becomes less obvious for Mn doped samples [209a]. Tetragonality decrease with Mn doping implies that Mn ions have diffused into the BST lattice and caused lattice distortion [201a, 213]. However, Mn^{4+} (r = 0.530 Å) ions have smaller ionic radii compared to Ti^{4+} they might cause different effect compared to Mn^{2+} and Mn^{3+}.

On the other hand, in the samples with MnO_2 source, it is observed that the tetragonality is reduced more significantly than the samples with Mn_2O_3, even though the difference is little. This may be due to the efficient incorporation of Mn into the system in the samples with MnO_2 source (see Figure 3.11). Alternatively, we can consider that the samples derived from MnO_2 source might have resulted in more Mn^{4+} ion formation so that they have less tetragonality due to the smaller ionic radius (Mn^{4+} (0.53 Å) < Ti^{4+} (0.60 Å)).

Table 3.2. Rietveld refinement results of $(Ba_{0.95}Sr_{0.05})(Mn_xTi_{1-x})O_3$ (BST-100xMn) ceramics.

Mn comp	Mn Source	Sint. Temp. (°C)	Sample name	*a* (Å)	*c* (Å)	*c/a*	Theo. Density (g/cm^3)	R_{wp} (%)	GoF
0	-	1325	BST-1325	3.9907(2)	4.0181(3)	1.0069	5.988	9.035	1.37
		1400	BST-1400	3.9913(1)	4.0255(2)	1.0086	6.091	9.398	1.42
0.3	MnO_2	1325	BST-0.3Mn (MnO_2)-1325	3.9928(1)	4.0187(1)	1.0065	5.981	8.995	1.53
		1400	BST-0.3Mn (MnO_2)-1400	3.9915(2)	4.0246(1)	1.0083	6.015	1.0395	1.41
	Mn_2O_3	1325	BST-0.3Mn (Mn_2O_3)-1325	3.9892(3)	4.0160(2)	1.0067	5.995	9.524	1.37
		1400	BST-0.3Mn (Mn_2O_3)-1400	3.9919(1)	4.0256(1)	1.0084	6.012	8.136	1.39
1	MnO_2	1325	BST-1Mn (MnO_2)-1325	3.9929(2)	4.0181(2)	1.0063	5.983	8.870	1.35
		1400	BST-1Mn (MnO_2)-1400	3.9919(1)	4.0245(2)	1.0082	5.975	8.224	1.35
	Mn_2O_3	1325	BST-1Mn (Mn_2O_3)-1325	3.9923(1)	4.0177(2)	1.0063	5.985	9.940	1.17
		1400	BST-1Mn (Mn_2O_3)-1400	3.9917(2)	4.0247(1)	1.0083	5.977	8.642	1.47

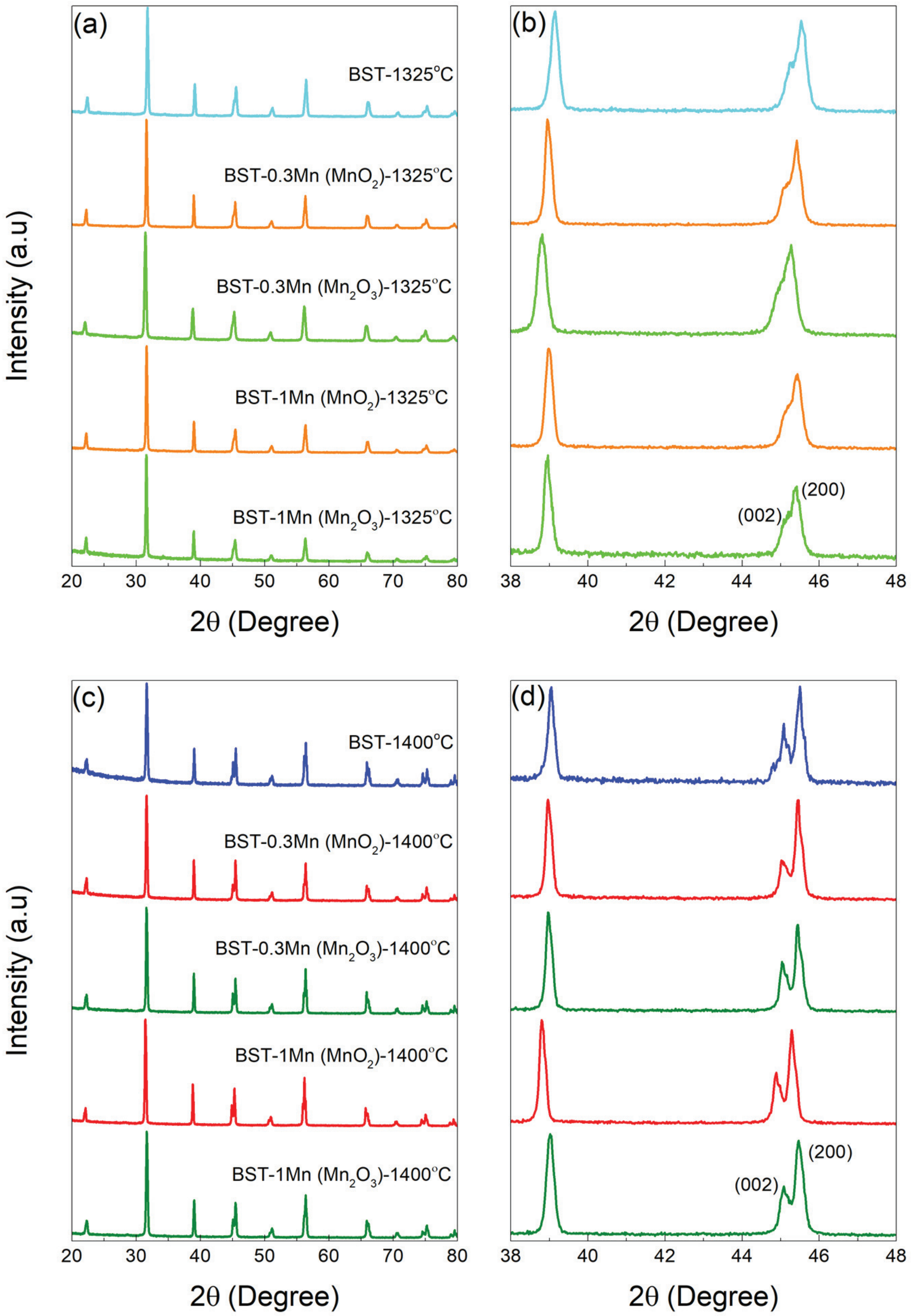

Figure 3.10 XRD patterns of $(Ba_{0.95}Sr_{0.05})(Mn_xTi_{1-x})O_3$ (BST-100xMn) ceramics (a,b) sintered at 1325 °C and (c,d) sintered at 1400 °C.

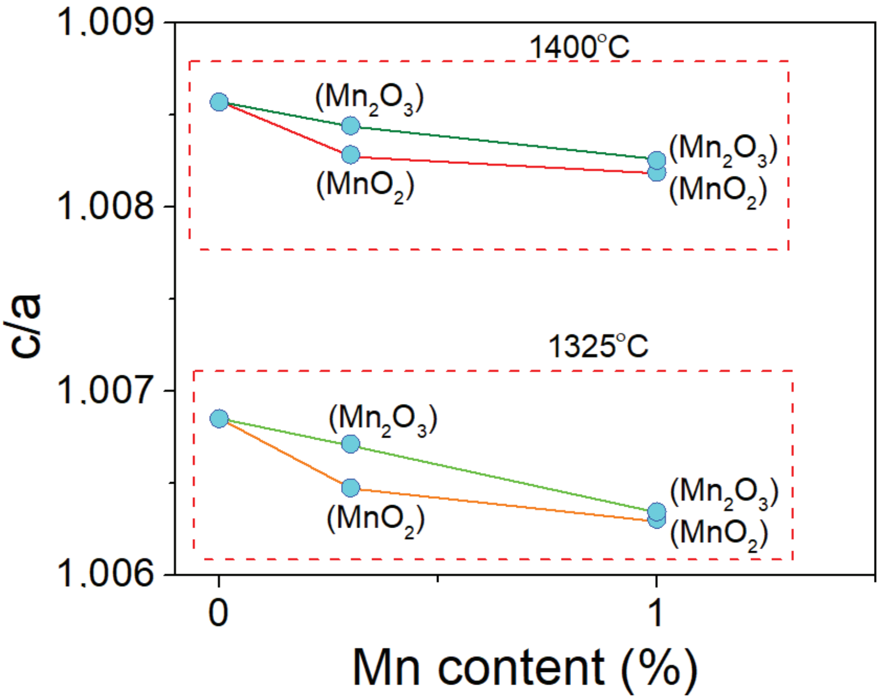

Figure 3.11. The tetragonality, c/a as a function Mn content of BST-100xMn ceramics according to the Rietveld refinement results.

3.3.2. Density and Microstructure of Mn Doped BST Ceramics

The relative density of all the samples, determined by Archimedes' method, is higher than 93 % of the theoretical density obtained by Rietveld refinements. SEM micrographs of the polished and thermally etched surfaces of the samples sintered at 1325 °C and 1400 °C are given in Figure 3.12 and Figure 3.13 respectively.

The average grain sizes of samples sintered at 1325 °C and 1400 °C were in the range of 0.68 to1.16 µm and between 24.78 and 86.16 µm, respectively (see the insets in the Figure 3.12 and Figure 3.13). Significant increase of the grain size at 1400 °C can be ascribed to increasing rates of diffusion at this temperature. Grain sizes of Mn-doped BST ceramics are clearly lower than those of pure BST. Especially in samples sintered at 1400 °C, the grain size decreases more significantly with increasing Mn content

(Figure 3.14). These results indicate that Mn-doping can inhibit the grain growth of BST ceramics as shown in other reports; such as in Mn doped PZT [214] and $BaTiO_3$-based ceramics [203b, 215]. The decrease in the grain size with Mn-doping was related to the segregation of Mn-oxides at the grain boundaries, which hinder grain growth [203b, 215].

It is observed that the average grain sizes are slightly lower in samples with Mn_2O_3 as the Mn source compared to those with MnO_2 (Figure 3.14). If the decrease in grain size is due to the increase of Mn-oxide residues which prevent the grain growth, we can deduce that amount of Mn_2O_3 residues at the grain boundaries is slightly higher than those of MnO_2. This implies that the incorporation of Mn ion into BST is more efficient in the samples with MnO_2 source. This result is consistent with the XRD results, which showed a stronger suppression of tetragonality in the samples with MnO_2 source. In addition, sintering temperature might have also affected the amount of Mn segregated at the grain boundaries. Since grain size of the samples is more significantly suppressed by Mn-segregation at the grain boundaries for the samples sintered at 1400 °C, it can be inferred that there is more Mn segregation at the grain boundaries.

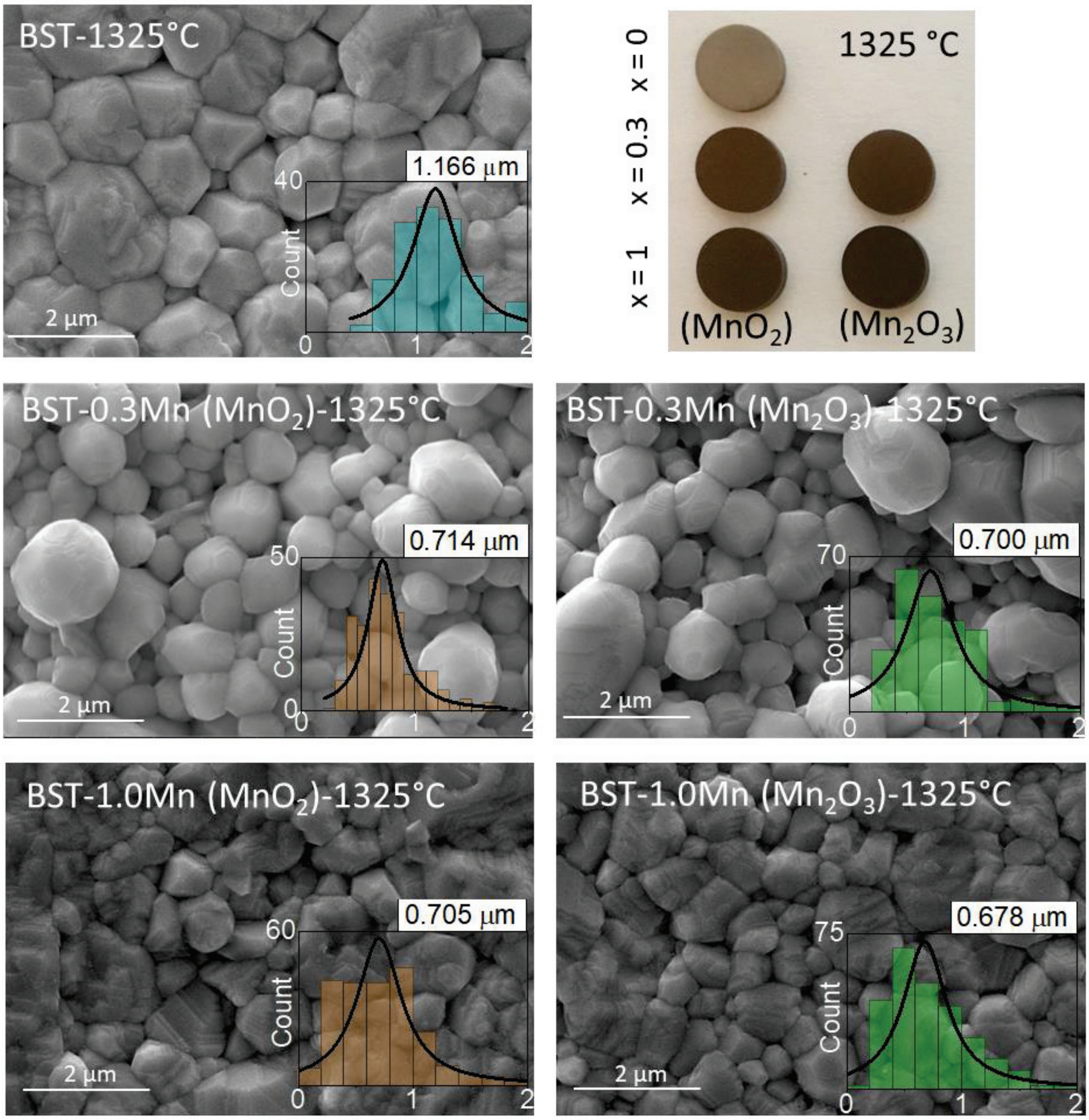

Figure 3.12. SEM images and grain size distributions of BST-100xMn ceramics sintered at 1325 °C and photographs of the samples.

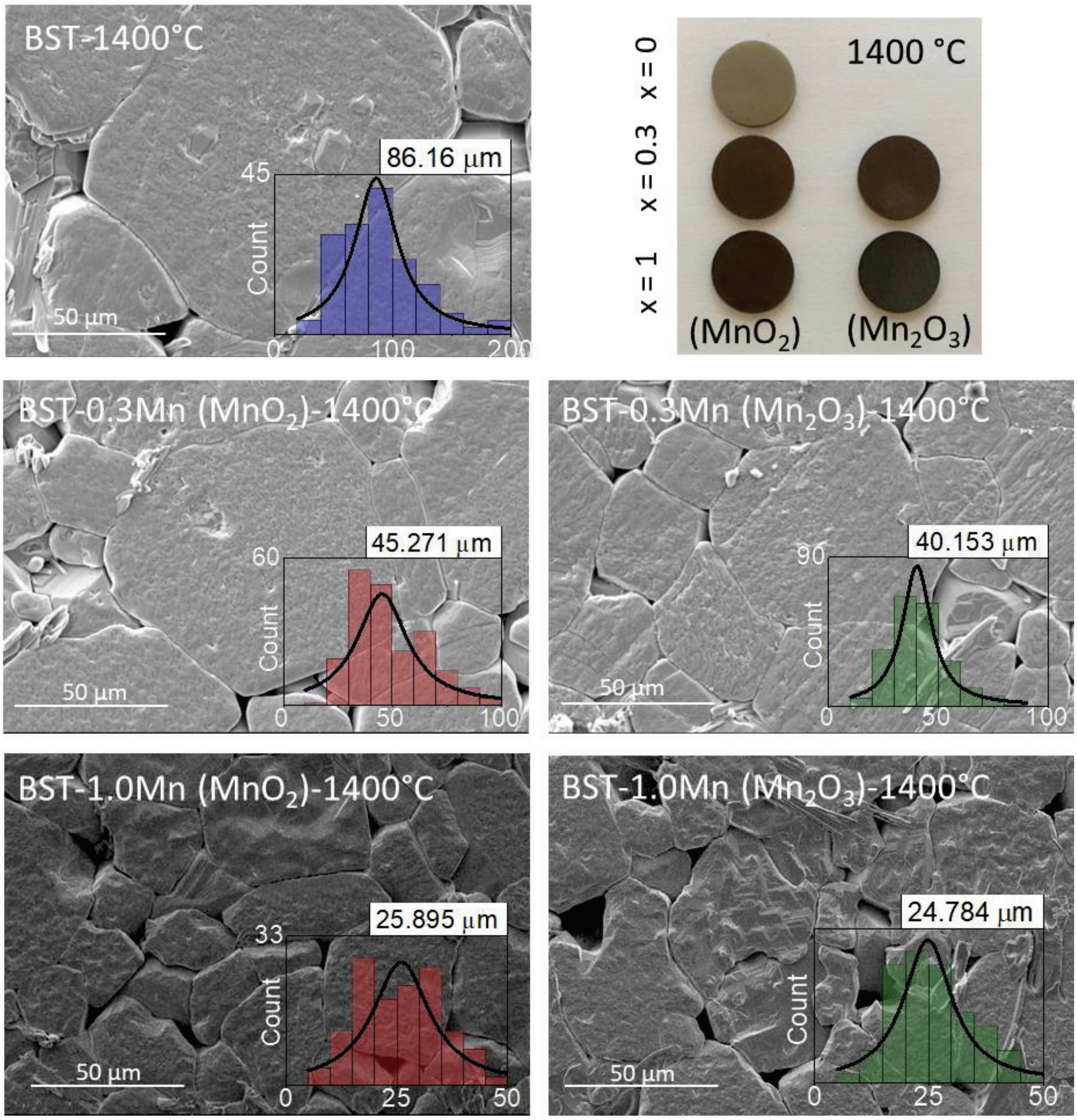

Figure 3.13. SEM images and grain size distributions of BST-100xMn ceramics sintered at 1400 °C and photographs of the samples.

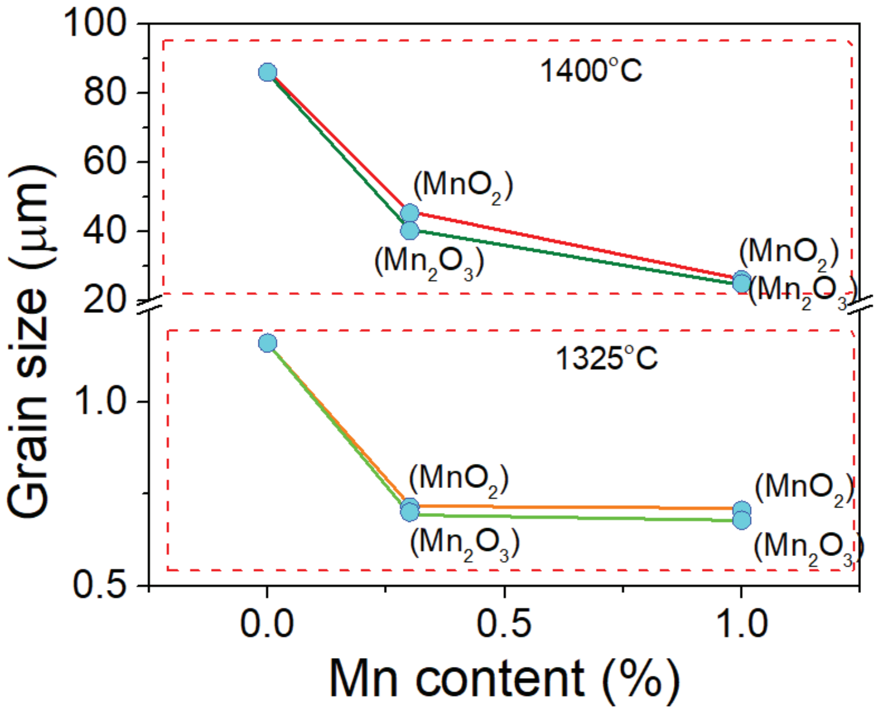

Figure 3.14. Average grain sizes of the BST-100xMn ceramics sintered at 1325 °C (lower lines; orange for MnO_2 used ones light green for Mn_2O_3 used ones) and 1400 °C (upper lines; red for MnO_2 used ones dark green for Mn_2O_3 used ones) as a function of Mn content and Mn precursor.

3.3.3. Dielectric Properties of Mn Doped BST Ceramics

Figure 3.15 shows the temperature dependence of the dielectric constant and loss of the samples with different Mn precursors and different sintering temperatures (see also Figure A. 6). Typical peak in the dielectric constant occurs at the Curie temperature (T_C) marking the transition from the ferroelectric to the paraelectric phase. T_C decreases with Mn-doping and changes in the range of 111-115 °C for BST-xMn (x = 0, 0.3 and 1 %) samples.

Dielectric constant maxima of the samples all sintered at 1400 °C are larger than those samples sintered at 1325 °C, due to the larger grain sizes of the samples sintered at 1400 °C, which reduces the clamping effect of the grain boundaries. On the other hand, at room temperature, the samples sintered at 1325 °C have slightly higher dielectric constant values compared to those sintered at 1400 °C. This result can be explained by the increasing density of 90° domain walls [216]. The samples sintered at

1325 °C have fine grains (0.68-1.66 µm) and they are expected to have smaller domain size and higher density of 90° domain walls.

Mn-doped BST ceramics show slightly lower dielectric constant than that of undoped ones for all temperatures at and below T_c. In addition, it appears that increasing the Mn content further decreases the dielectric constant. It is well known that defect dipoles that form as a result of Mn-doping will restrict the domain wall motion and thus the dielectric constant [203a]. The restriction of the domain movement in the Mn-doped samples causes a slight decrease in the dielectric constant and the loss compared to the non-doped one. Moreover, it can be observed that MnO_2 used samples exhibits slightly higher dielectric constant. The reason can be attributed to slightly larger grain size of MnO_2 containing ceramics.

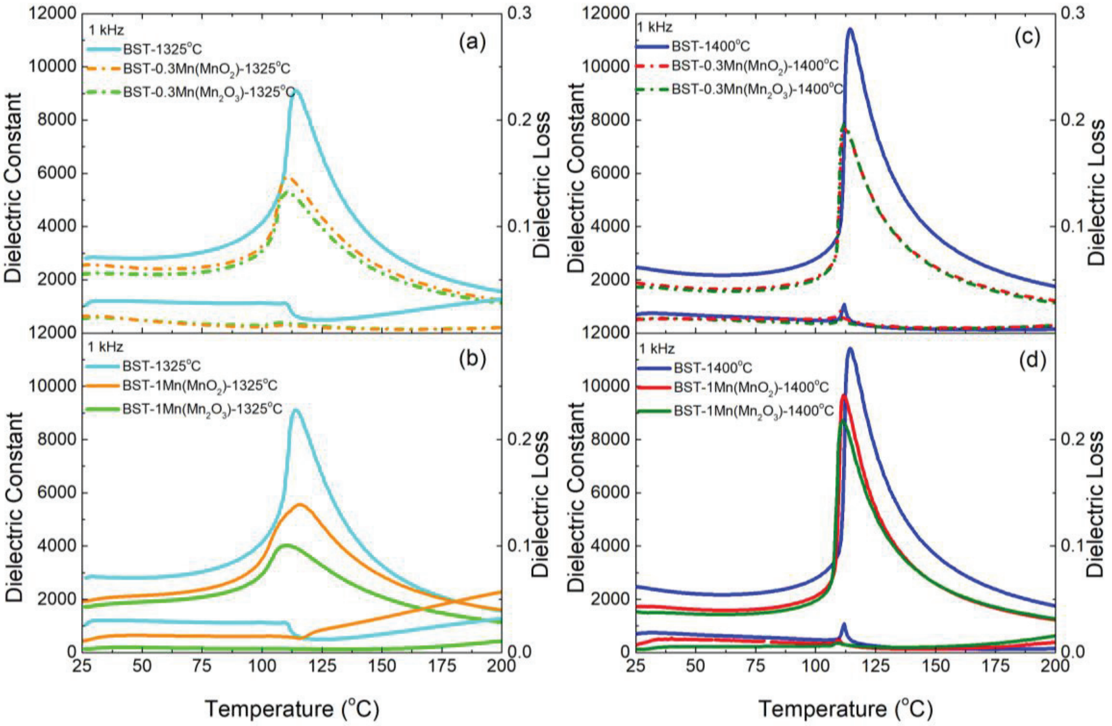

Figure 3.15. Comparison of the dielectric constant and loss of (a,b) the samples sintered at 1325 °C and (c, d) the samples sintered at 1400 °C.

3.3.4. Aging and Electrocaloric Properties of Mn Doped BST Ceramics

Room temperature polarization-electric field hysteresis loops of unaged and aged states of all ceramics are given in Figure 3.16 and Figure 3.17. For comparison, all measurements have been plotted under the same maximum electric field of 30 kV/cm. The internal electric field (E_i) values calculated from the polarization loops for each case are written inside the figures. E_i values in pink and black color represent the aged and unaged ceramics, respectively. E_i originating from the defect dipoles is expressed as,

$$E_i = \frac{(E_1 + E_2)}{2}$$

where E_1 and E_2 are the peak fields of forward and backward domain switching processes.

The most significant difference for the samples sintered at different temperatures, is the increase in remnant polarization and hysteresis behavior for the samples sintered at 1400 $^{\circ}$C. This is due to the larger grain sizes of those samples. Aging affects the samples' hysteresis loops differently. All samples have been aged under same conditions at 90 °C, below the T_C. Aging affects the hysteresis loops of the samples differently. The samples sintered at 1325 °C and 1400 °C were aged completely after 3 and 7 days, respectively. On the other hand, for ceramics sintered at 1325 °C, hysteresis loops of unaged and aged states did not differ significantly: i.e. the de-aged samples with 1% Mn sintered at 1325 °C shows constricted loops, which does not differ much after aging. This might be due to the very fast aging kinetics due to the fast oxygen diffusion at the high-density grain boundaries at this sintering temperature (Ceramics sintered at 1325 °C are fine grained and have higher density of grain boundaries). In addition, it can be observed the constriction of the hysteresis loops and E_i values of the samples sintered at 1400 °C are less than those sintered at 1325 °C samples, possibly due to the larger average grain size. The average grain size scales with the average domain size as the domain size is larger for 1400 °C samples, domain self-clamping effect (domain wall movement being restricted by the high density of domain walls) [206b] is less therefore, hysteresis loops do not show much constriction. E_i values in all cases increase with increasing Mn content from 0.3 to 1% due to increase in the defect dipole density. Finally, we observe a higher E_i in the samples with Mn_2O_3 source (Figure A. 7). This might be due to the different Mn valence of the ceramics.

Another important result is that E_i is higher in the samples with Mn_2O_3 source. This might be due to higher amount of Mn^{2+} and Mn^{3+} present in these samples, which will lead to more defect dipoles and higher E_i. Conversely, it can be deduced that there might be relatively higher concentration of Mn^{4+} ions in the samples with MnO_2. This suggestion is in agreement with our discussion of the evolution lattice parameters where we ascribed the stronger decrease of tetragonality of the samples with MnO_2 source to the stronger presence of Mn^{4+}. In addition, we attributed the higher dielectric constant of the samples with MnO_2 source to less defect dipole and oxygen vacancy formation. So, this also supports our conclusion.

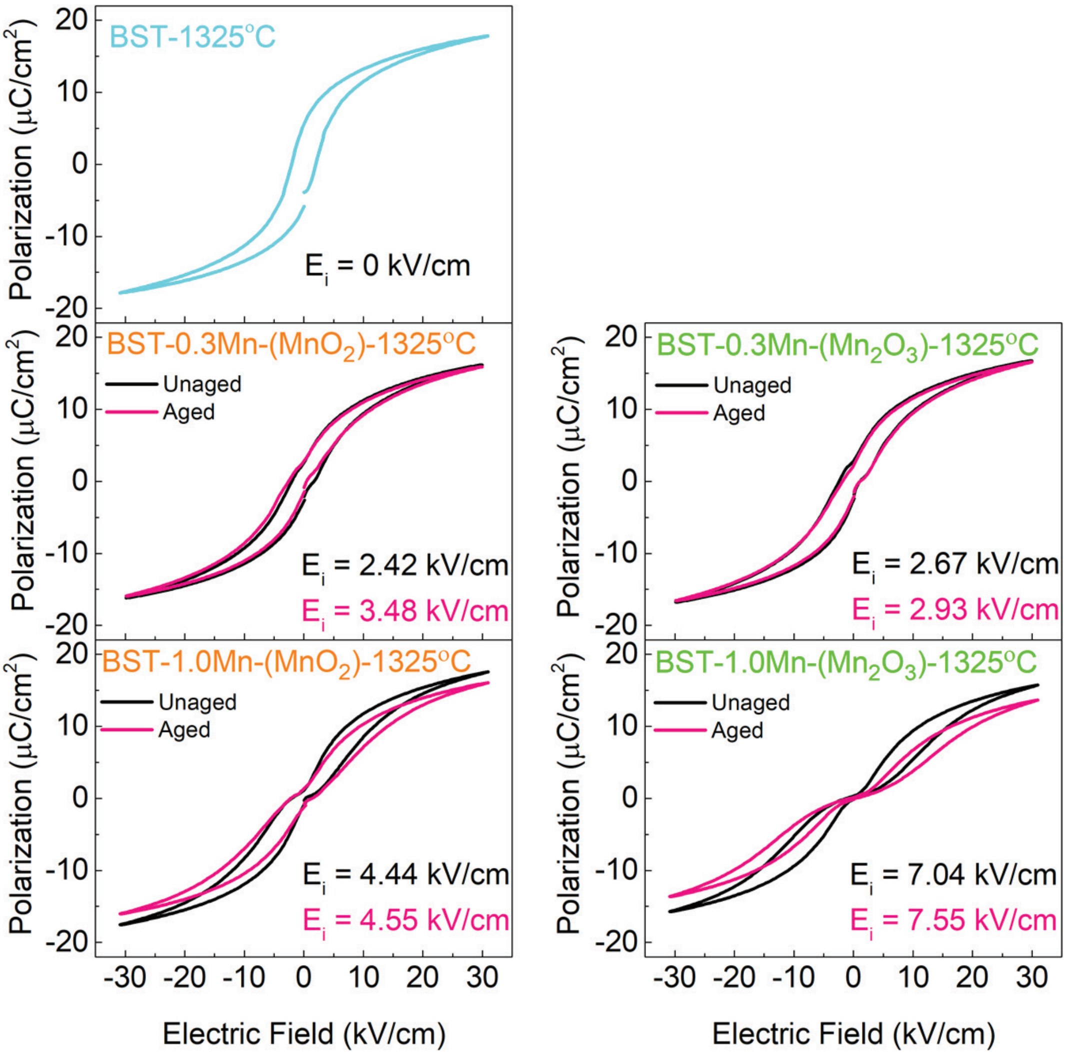

Figure 3.16. Room temperature polarization-electric field hysteresis loops of undoped BST ceramics (cyan and blue loops) and unaged (black loops) and aged (pink loops) Mn doped ceramics sintered at 1325 °C.

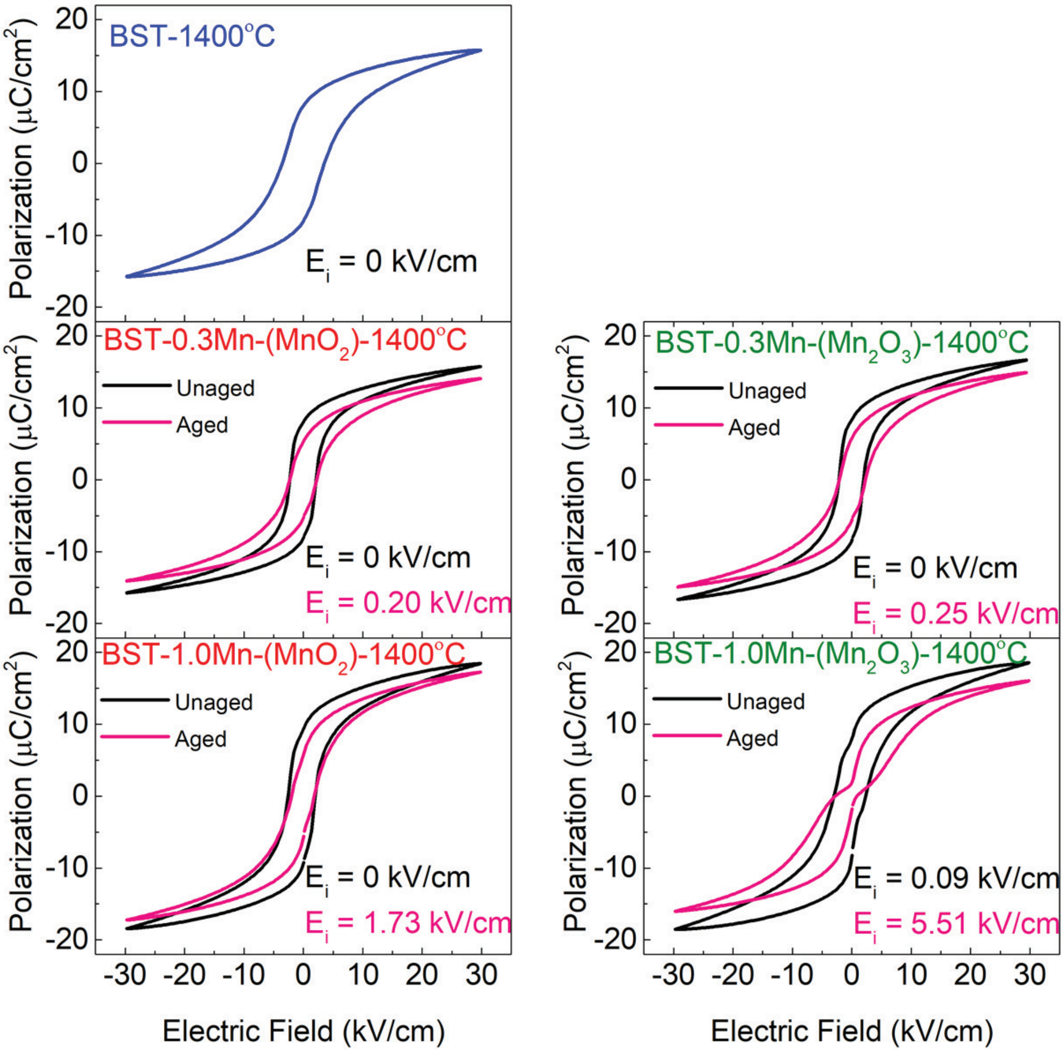

Figure 3.17. Room temperature polarization-electric field hysteresis loops of undoped BST ceramics (cyan and blue loops) and unaged (black loops) and aged (pink loops) Mn doped ceramics sintered at 1400 °C.

In Figure 3.18 and Figure 3.19, temperature dependent ΔT of unaged and aged ceramics under 30 kV/cm are shown for the samples sintered at 1325 and 1400 °C, respectively. Temperature dependence of the electrical polarization values obtained from the hysteresis loops (Figure A. 8 and Figure A. 9) at 30 kV/cm which were used to calculate ΔT are included in the insets of each figures. Maximum ΔT values obtained around T_C of each sample are written on the figures and are also tabulated in Table 3.3.

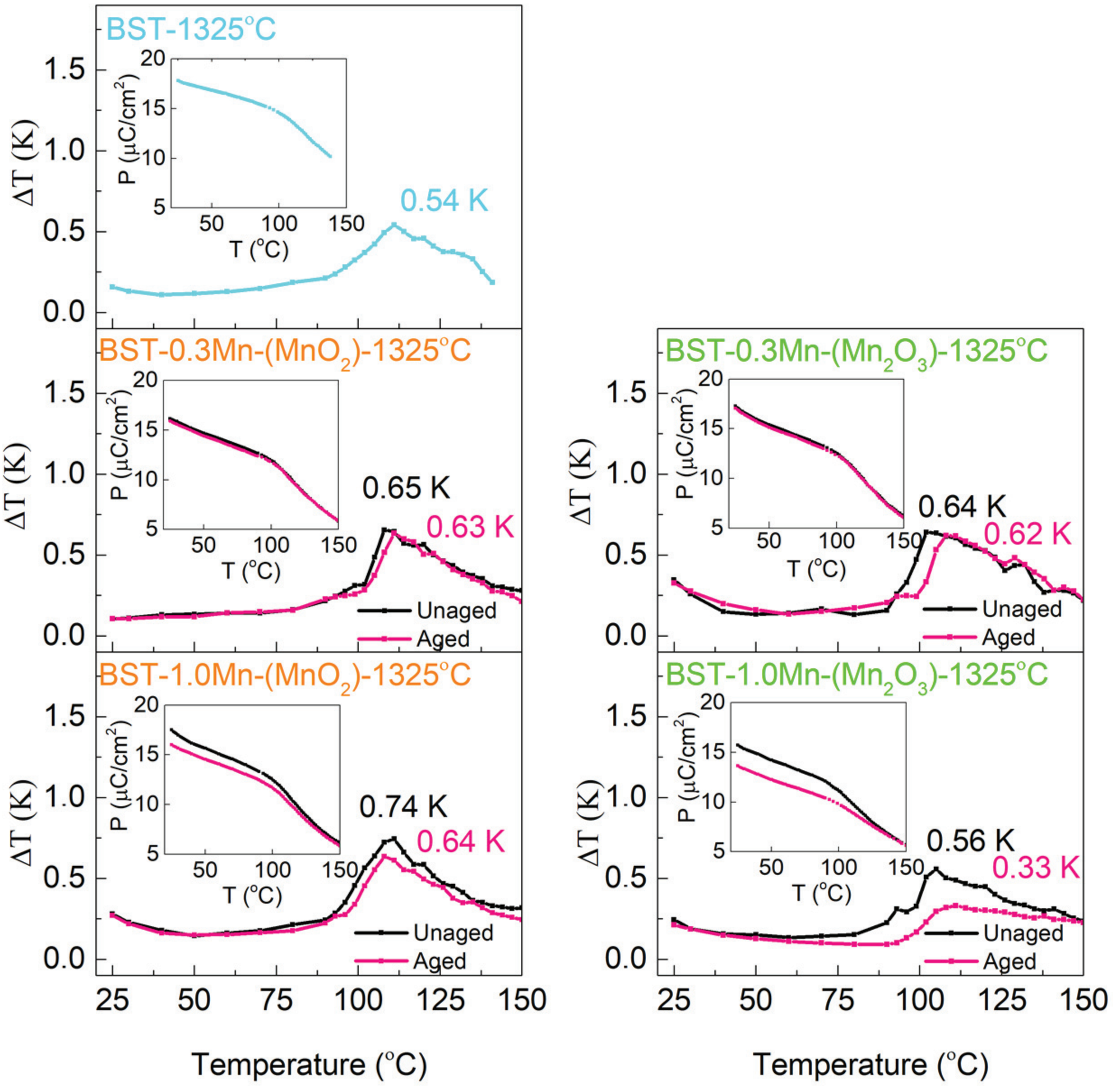

Figure 3.18. Temperature dependent ΔT values of unaged and aged ceramics sintered at 1325 °C under 30 kV/cm. Black and pink curves represent the unaged and aged states, respectively. Temperature dependence of the electrical polarization values under the same electric field are included in the insets.

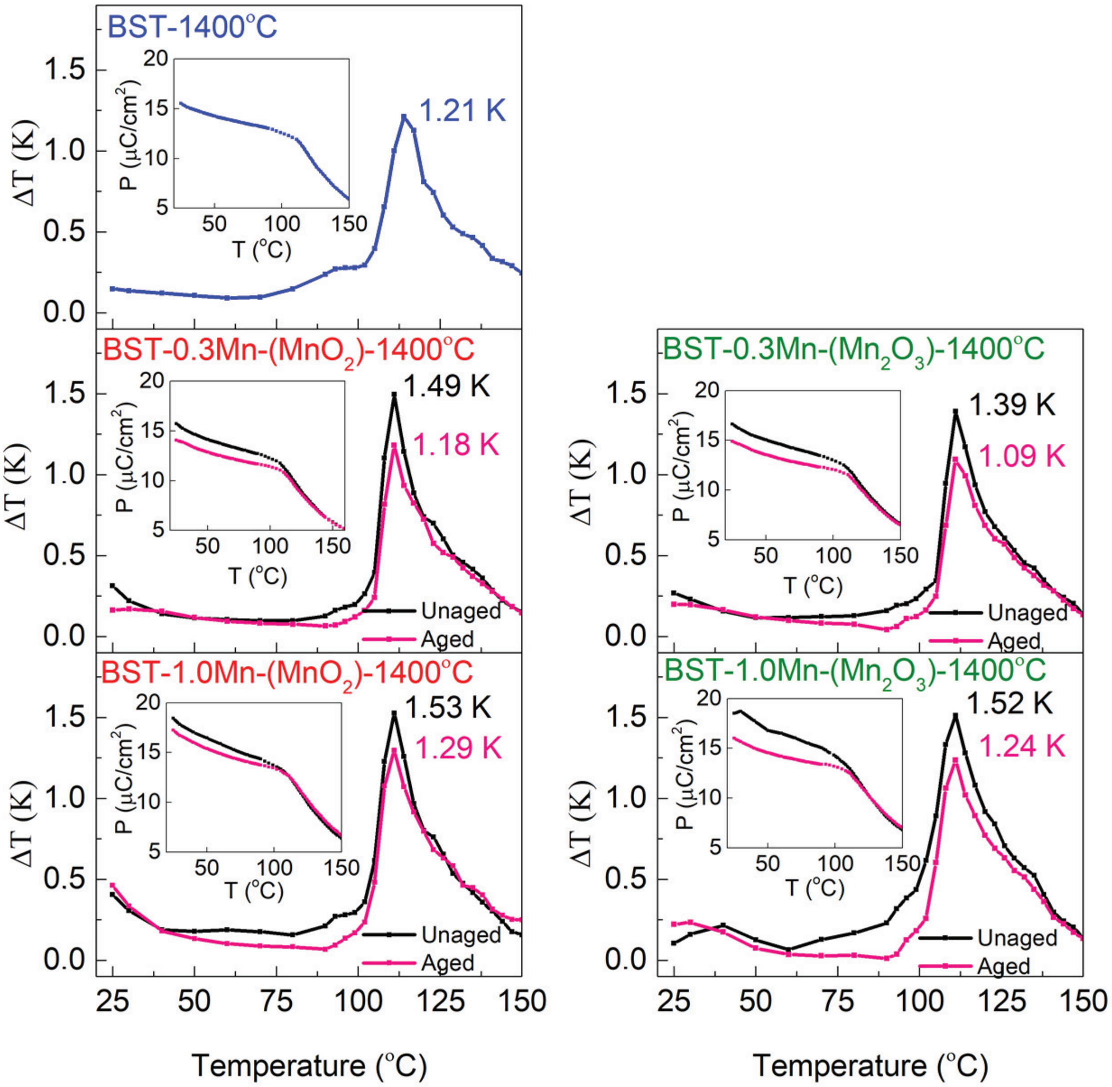

Figure 3.19. Temperature dependent ΔT values of unaged and aged ceramics sintered at 1400 °C under 30 kV/cm. P-T curves are included in the insets.

Table 3.3. Maximum ΔT values obtained for all samples under 30 kV/cm.

Sample	*ΔT (1325 °C) (unaged)*	*ΔT (1325 °C) (aged)*	*ΔT (1400 °C) (unaged)*	*ΔT (1400 °C) (aged)*
BST	0.54 K	-	1.21 K	-
BST-0.3Mn (Mn_2O_3)	0.64 K	0.62 K	1.39 K	1.09 K
BST-0.3Mn (MnO_2)	0.65 K	0.63 K	1.49 K	1.18 K
BST-1Mn (Mn_2O_3)	0.56 K	0.33 K	1.52 K	1.24 K
BST-1Mn (MnO_2)	0.74 K	0.64 K	1.53 K	1.29 K

According to these results, the following observations are made: 1) The samples sintered at 1400 °C resulted in larger ΔT compared to those sintered at 1325 °C. This can be explained by higher tetragonality, and larger grain size of the samples sintered at 1400 °C. 2) 0.3 % Mn-doped samples yielded larger ΔT compared to undoped BST samples. Increasing Mn-content from 0.3 to 1 mol % increases ΔT further for the samples sintered at 1400 °C but no systematic trend can be found for the samples sintered at 1325 °C. (Increasing Mn-content from 0.3 to 1 mol % increases ΔT further but BST-1Mn (Mn_2O_3) sample sintered at 1325 °C seems to break this trend. This may be due to its extremely pinched loop behavior even in the unaged state or its immediate aging.) It was shown with previously that Mn doping can indeed increase ΔT of $BaTiO_3$ based ceramics and this increase was correlated to the decrease of dielectric loss and increase of the saturation polarization due to the reduction of ferroelectric domains [210]. Here, if we compare the maximum polarization values of Mn-doped but not aged samples at room temperature with undoped samples, we see that the polarization increases or does not change much by Mn-doping. 3) Samples in the aged state always result in lower ΔT. This is due to the fact that aging results in a suppression of electrical polarization at temperature below T_C. This suppression is more pronounced for the samples sintered at 1400 °C. Since the slope of P(T) curves plotted as insets in Fig. 7 decreases due to this suppression, ΔT decreases. The suppression of electrical polarization is stronger when E_i larger. 4) Samples with MnO_2 precursor always result in larger ΔT. This might also be related with the slightly better incorporation of Mn ions in the Ti-site in MnO_2 sourced samples, compared to Mn_2O_3 sourced samples. Since Mn-doping increases ΔT, incorporation of more Mn ions will lead to larger ΔT.

In a previous study [209b], it was mentioned that one could obtain large electrocaloric effect (ECE) with the optimal conditions; low P_r and large P_{max}, due to causing more entropy change. In the aged samples ΔT decreased and E_i increased therefore a more pinched polarization loop with lower P_r and lower P_{max} was obtained in our study. Here, if a connection is to be established between E_i and ΔT, it is concluded that as E_i increases, ΔT also decreases.

It is noteworthy that the ΔT of the MnO_2 used samples is higher than the Mn_2O_3 used samples. The difference between the ΔT values of aged and unaged states is higher for samples with Mn_2O_3 source because E_i fields are higher in those samples.

3.3.5. Electron Paramagnetic Resonance Analysis of Mn Doped BST Ceramics

The EPR spectra of all BST-100xMn samples measured at room temperature are shown in Figure 3.20. Undoped BST ceramics are expected to be diamagnetic and they should not include any EPR active center. However, in the EPR spectra of undoped BST samples, two significant signals were observed (Figure 3.20(a) and (d)). These signals were also observed in a previous report and were associated with barium or titanium vacancies [217]. The g-factors corresponding to these signals were obtained as 1.99 and 1.97, which is in reasonable agreement with the previous reports [218].

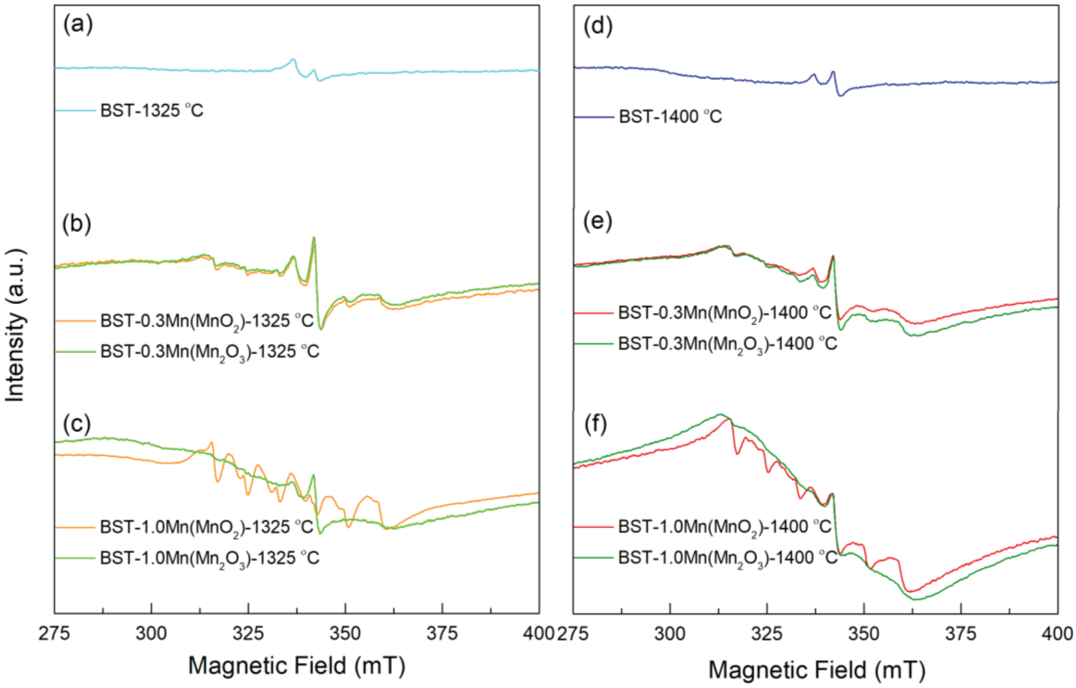

Figure 3.20. EPR spectra of all $(Ba_{0.95}Sr_{0.05})(Mn_xTi_{1-x})O_3$ (BST-100xMn) ceramics.

The EPR spectra of Mn-doped BST compounds measured at room temperature show typical Mn ion signals as shown in Figure 3.20(b, c, e, f). Especially BST-1Mn (MnO_2) sample shows a clear hyperfine sextet with a hyperfine parameter A~8.6 mT and g-factor ~2.001 that corresponds to Mn^{2+}. Mn^{2+} ion has electron and nuclear spin numbers S = 5/2 and I = 5/2, respectively. Actually, expected EPR spectra should give thirty distinct EPR signals due to the Zeeman splitting of electrons, it gives five EPR signals and each of these splits into six hyperfine lines (2I+1 = 6). However, in the EPR spectra given in Figure 3.20, we only observed six hyperfine lines. This is due to the fact that the microwave energy hence the Zeeman energy, is not high enough to overcome the large crystal field splitting energy (sometimes called zero field splitting) of the ceramic system [219]. Therefore, only the central electronic transition (ΔM_S = 1/2<->-1/2 and ΔM_I = -5/2<->-3/2; -3/2<->-1/2; -1/2<->1/2; 1/2<->3/2; 3/2<->5/2) has been resolved. Similar effect has been observed for similar Pb-free materials such as Mn doped KNN [220]. In addition to the hyperfine sextets originating from Mn^{2+}, we also observe a strong and broad (half-Gaussian) signal. Such a broad signal was reported previously to originate from Mn-oxide residues that are present at the grain boundaries, which is consistent with our understanding of grain size refinement with Mn-doping discussed earlier [219]. EPR signals that we previously have ascribed to barium or titanium vacancies [217] are also observed for undoped are also present for the Mn-doped samples in different magnitudes.

The valence of all Mn-doped samples was also determined as Mn^{2+}. Therefore, it can be said that there is no valence difference in EPR between samples with MnO_2 and Mn_2O_3 precursors. However, the inability to detect Mn^{3+} ion signals and the apparent broad signal originating from Mn oxide residues [221] as well as the signals coming from Ba or Ti vacancies may prevent this analysis result from being conclusive. We also note that we have not observed any sextets for Mn^{4+}, which were reported in a study [208].

On the other hand, we observe some subtle but important differences between Mn-doped samples. Even though there is no significant difference in Mn^{2+} sextet signals for 0.3 % Mn doped samples with Mn_2O_3 and MnO_2 precursors, an obvious difference in Mn^{2+} sextet signals of 1 % Mn doped samples have been observed for different precursors. Mn^{2+} sextet signals are almost disappeared in the samples with 1% Mn_2O_3. There may be two reasons for this: First one is Mn_2O_3 might have caused more residual Mn-oxide at the grain boundaries (less Mn is incorporated to the perovskite structure as inferred from XRD experiments) and therefore the broad half-Gaussian signal from the residual Mn-oxide stronger, sextet signals from the incorporated Mn^{2+} weaker in samples with Mn_2O_3. Second one, In the samples with Mn_2O_3 precursors, Mn^{2+} ions might have interacted more with oxygen vacancies (generate more defect dipoles), causing free Mn^{2+} signals [222] to weaken. Strong weakening of the sextet signal in samples with Mn_2O_3 source can also be explained by the lower solubility limit of Mn_2O_3 compared to MnO_2.

For the two different sintering temperatures, no clear difference in EPR signals was observed except a slight increase in the intensity of the broad signal of the samples sintered at 1400 °C samples. This might result from the higher amount of Mn-oxide residues at the grain boundaries at higher sintering temperatures.

3.4. Conclusions

We have systematically studied the effect of different Mn-precursors and Mn content as well as sintering temperature on the aging properties and resulting dielectric, ferroelectric and electrocaloric properties of Mn-doped BST ceramics. We observed subtle but important differences between the samples synthesized using different Mn precursors on the aging behavior. We deduced that Mn is incorporated better in samples with MnO_2 source compared to those with Mn_2O_3 source, from the change of tetragonality with Mn-doping. Using EPR measurements, we suggest that Mn that is not incorporated to the perovskite structure segregates at the grain boundaries as residual Mn-oxide. Average grain size of the Mn-doped samples decreases significantly due to the segregated Mn-oxide at the grain boundaries preventing the grain growth. Grain size and amount of Mn^{2+} that is incorporated to the structure determine the aging properties. Mn-doping suppresses the dielectric constant as expected. Ferroelectric aging and resulting constriction in the hysteresis loops is significantly more pronounced for the Mn-doped samples sintered at 1325 °C probably due to the faster oxygen vacancy diffusion through the grain boundaries. Aging results in suppression of ΔT however we observed an increase in ΔT of the samples with Mn-doping compared to undoped BST.

CHAPTER 4

ENHANCEMENT OF ELECTROCALORIC EFFECT BY IMPROVING TETRAGONALITY

4.1. Introduction to BT-NBT Ceramics

As lead-free piezoelectric materials, $Bi_{0.5}Na_{0.5}TiO_3$ (BNT) based materials have been widely used especially as a solid solution with $BaTiO_3$ [176]. The increased piezoelectric and dielectric properties of $(1-x)Bi_{0.5}Na_{0.5}TiO_3–xBaTiO_3$ (NBT-BT) system have been obtained at rhombohedral-tetragonal morphotropic phase boundary (MPB) which corresponds to x = 0.06–0.11 compositions [175]. However, few studies are focused on the compositions close to $BaTiO_3((1-x)BaTiO_3– xBi_{0.5}Na_{0.5}TiO_3)$(BT-NBT) [223]. The reports show that incorporation of NBT into BT up to 30% of NBT composition causes an increase of the Curie temperature (T_C) and the tetragonality (c/a) of the system. This is an unusual effect because apart from Pb, all A-site substitutions educe the ferroelectric distortion and T_C [224]. The origin of the enhancement of the tetragonality was attributed to the decrease in the oxygen-octahedral volume (Figure 4.1) rather than the off centering of the B site Ti^{+4} ion [223b]. When the NBT content is above $x = 0.15$, a gradual decrease in c and also more significant decrease in a is observed which effectively raises the tetragonality.

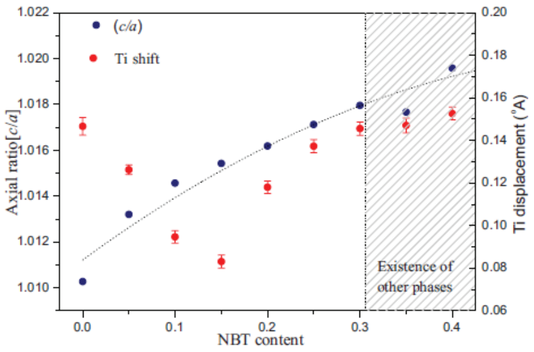

Figure 4.1. Tetragonality (c/a) and the shifts of the Ti^{4+} ion along the polar direction of the unit cell as a function of NBT content [223b].

The relation between increase in tetragonality in BT-NBT systems and their dielectric behavior was investigated in a study by collecting dielectric data under DC and AC fields [224]. According to this study, it was claimed that the enhancement of *c/a* reduces the reversible domain wall contribution to polarization due to its increased in the lattice incompatibility during the domain wall motion and irreversible domain walls which exhibit lower dielectric constants.

4.1.1. Advantages of BT-BNT Systems and Its Potential Applications

$BaTiO_3$ (BT) is preferred in capacitors due to its high-dielectric properties. However, to maintain temperature-stable dielectric constant at high temperatures is not possible due to the decrease of permittivity above the Curie temperature (125 °C). The temperature stable dielectric behavior and enhanced T_C (~180 °C) of BT-BNT ceramics are promising for positive temperature coefficient resistor (PTCR) ceramics [225], and also for multilayer ceramic capacitors (MLCCs) which can withstand high working temperature [226]. For example, the use of X7R and X8R type MLCCs as capacitors in environments with operating temperatures up to 200 °C would not be suitable as their ceiling temperatures are 125 °C and 150 °C, respectively [227]. As high Curie temperature is required for PTCR applications, the high T_C value (490 °C) of $PbTiO_3$ is more advantageous than the T_C value of $BaTiO_3$ (130 °C). For this reason, BT-NBT solid solution, which is a Pb-free material, is considered in some studies [228] as a potential material in such applications due to its high T_C and stable dielectric constant.

The influence of high tetragonality and high T_C on the electrocaloric effect and field-induced strain in these systems has not been studied yet. Therefore, in this study, the electrocaloric and piezoelectric properties of $BaTiO_3$-$xBi_{0.5}Na_{0.5}TiO_3$ (BT-NBT) ceramics with x = 0, 0.05, 0.10, 0.20, 0.30, and 0.40 compositions were investigated.

4.2. Experimental Procedure for BT-NBT Ceramics

The conventional solid state reaction method was used to prepare the ceramic samples, $(1-x)BaTiO_3$-$xBi_{0.5}Na_{0.5}TiO_3$ (BT-NBT) where x = 0, 0.05, 0.10, 0.20, 0.30, and 0.40 (see Table 4.1). The high purity metal oxides and carbonates $BaCO_3$ (99%), Bi_2O_3 (99.9%), Na_2CO_3 (99.8%), and TiO_2 (99.9%) were used as starting raw materials. All powders were dried at 200 °C overnight. Then they were weighed according to stoichiometric formula and mixed in a 30 ml HDPE bottle using zirconia balls in ethanol media by planetary ball milling for 18 h. The calcination process was carried out in pellet form at 1000 °C and 1050 °C for 2 h. After calcination the pellets were ground into powder and were mixed with 0.3% mol MnO_2 (99%) powder to enhance the insulation resistance and electrical breakdown field. The powders were mixed with 4 wt% polyvinyl alcohol (PVA) binder and water solution and then ball milled for 18h. Then powders were dried, sieved and pressed into the disc form (~10 mm in diameter, ~1mm thick) with a pressure ~100MPa. Then the PVA binder was burned out at 600 °C for 4 h. After burn out the pellets were sintered at 1200 °C for 2 h with a heating rate 5 °C/min.

X-ray diffraction (XRD, Cu Ka radiation, Philips X'Pert Pro) was used to determine the phases of the sintered samples. The microstructure of ceramics was studied on thermally etched surfaces (at 1100 °C, for 1 h) using a scanning electron microscope (SEM, FEI QUANTA 250 FEG). For dielectric and polarization-electric field hysteresis measurements, both surfaces of polished pellets were coated with silver paste and dried at 200 °C for 20 min.

The temperature dependence of dielectric properties of ceramics was measured at different frequencies (0.1, 1, 10, 100 kHz) by an LCR meter (KEYSIGHT, E4980AL). The polarization-electric field (P-E) hysteresis loops were obtained by using AIXACCT TF analyzer and a high voltage amplifier (TREK model 610E). The strain data were also collected simultaneously by a laser-interferometer (SIOS). Both for dielectric and hysteresis measurements a sample holder (AIXACCT piezo sample holder TFA 423-7) was used and temperature was controlled by AIXACCT temperature controller.

Table 4.1. Table of synthesized (1-x)$BaTiO_3$-x$Bi_{0.5}Na_{0.5}TiO_3$ (BT-NBT) ceramics.

Base ceramic	NBT comp. (x)	Sample name	Calcination	Sintering
BT	0.00	BT	1050 °C	1200 °C 2h
	0.05	BT-0.05NBT	1000 °C	1200 °C 2h
	0.10	BT-0.10NBT	1000 °C	1200 °C 2h
	0.20	BT-0.20NBT	1000 °C	1200 °C 2h
	0.30	BT-0.30NBT	1000 °C	1200 °C 2h
	0.40	BT-0.40NBT	1000 °C	1200 °C 2h

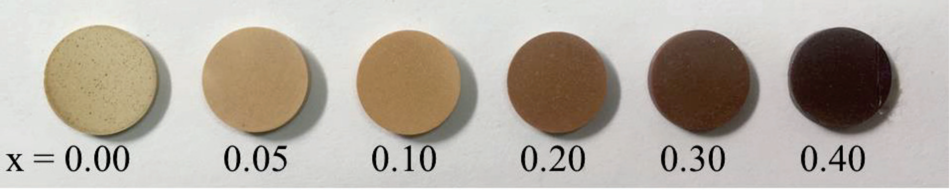

Figure 4.2. Photographs of the samples (BT–xNBT) in pellet form after sintering.

4.3. Results and Discussions

4.3.1. Phase and Structure of BT-NBT ceramics

Figure 4.3(a) shows the x-ray diffraction patterns of the NBT-BT ceramics as a function of NBT composition. There is no observed impurity peak for any compositions. A gradual increase of the tetragonal peak splitting as a function of NBT composition is seen from Figure 4.3(b) which demonstrates the X-ray diffraction patterns of the (002) and (200) peaks. It can be realized that the (200) peak position shifts to a higher angle, while a little change occurs in the (002) peak position with the increasing NBT composition. It corresponds to a slight increase in the lattice parameter *c* while a continuous decrease in the lattice parameter *a* occurs as obtained from Rietveld refinement of the XRD patterns. In Table 4.2 and Figure 4.4 the obtained lattice parameters *a, c*, and their ratio (*c/a*) have been summarized. The systematic increase in *c/a* values shows that the tetragonality is enhanced dramatically by NBT incorporation, despite the substitution of two heterovalent Na^{+1} and Bi^{+3} ions into A-site. Generally, when cations such as Zr, Sn and Sr are doped into $BaTiO_3$, they are known to weaken the ferroelectric distortion and reduce the tetragonality or T_C [229]. Here, on the other hand, tetragonality is increased by substituting $Na_{0.5}Bi_{0.5}$ into the A-site. Rao et al explained this increase [230] with the shortening of A-site-oxygen bond distances and strengthening of the covalent character, resulting in the strengthening of spontaneous tetragonal strain.

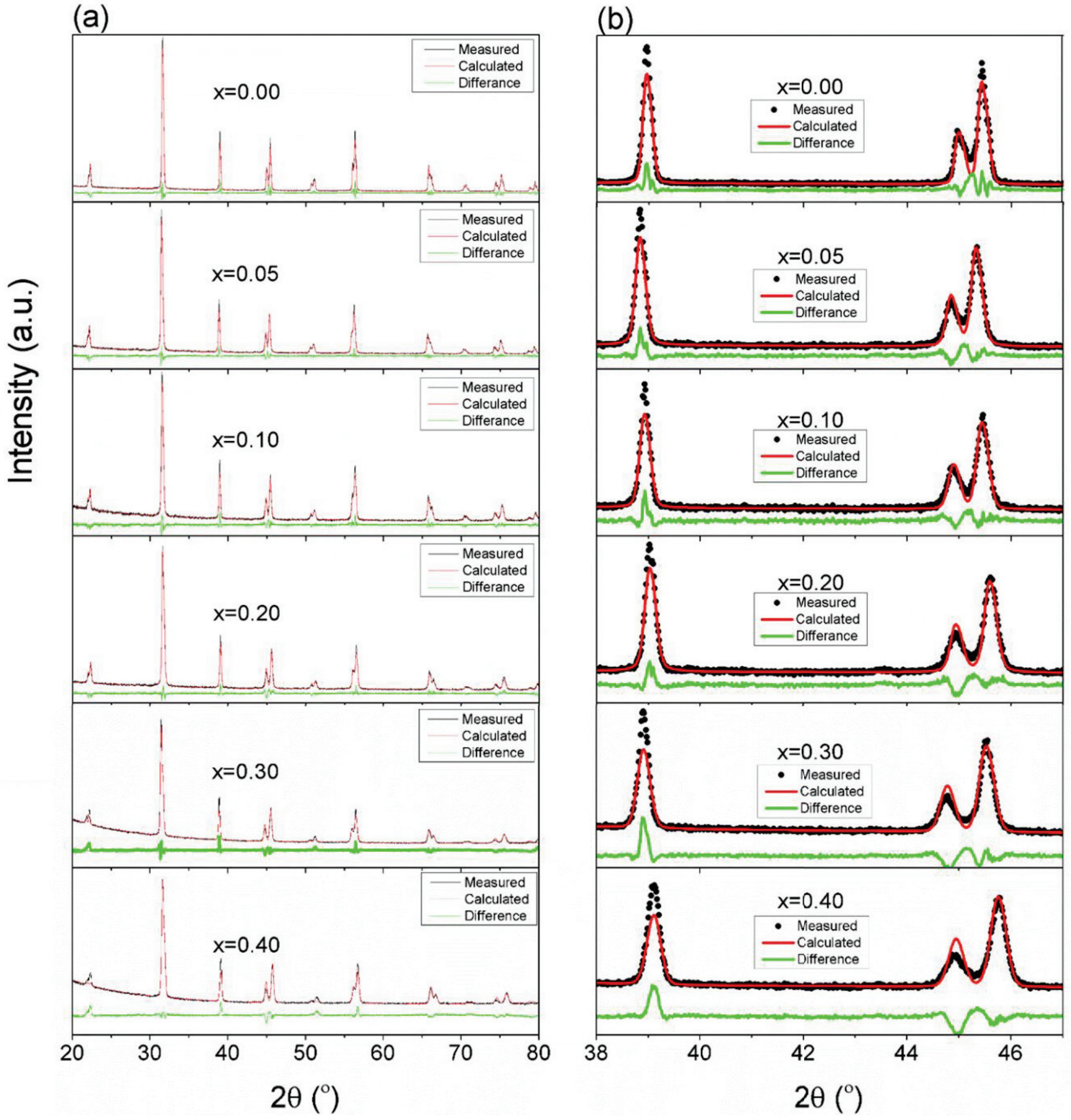

Figure 4.3. Refined XRD patterns of $(1-x)BaTiO_3-xBi_{0.5}Na_{0.5}TiO_3$ (BT-NBT) ceramics for x = 0, 0.05, 0.10, 0.20, 0.30 and 0.40 compositions in the range between (a) 20°-80° and (b) 38°-47°.

Table 4.2. Rietveld refinement results of (1-x)$BaTiO_3$-x$Bi_{0.5}Na_{0.5}TiO_3$ (BT-NBT) ceramics.

	a	*c*	*c/a*	Theoretical Density	R_{wp}
SAMPLE	(Å)	(Å)	(Å)	(g/cm^3)	(%)
BT	3.9939(1)	4.0313(1)	1.0093	6.022	11.208
BT-0.05NBT	3.9932(2)	4.0336(2)	1.0101	5.994	8.888
BT-0.10NBT	3.9886(1)	4.0346(1)	1.0115	5.979	8.986
BT-0.20NBT	3.9778(1)	4.0327(1)	1.0137	5.958	8.695
BT-0.30NBT	3.9674(2)	4.0300(2)	1.0157	5.938	6.514
BT-0.40NBT	3.9602(2)	4.0274(2)	1.0170	5.909	6.233

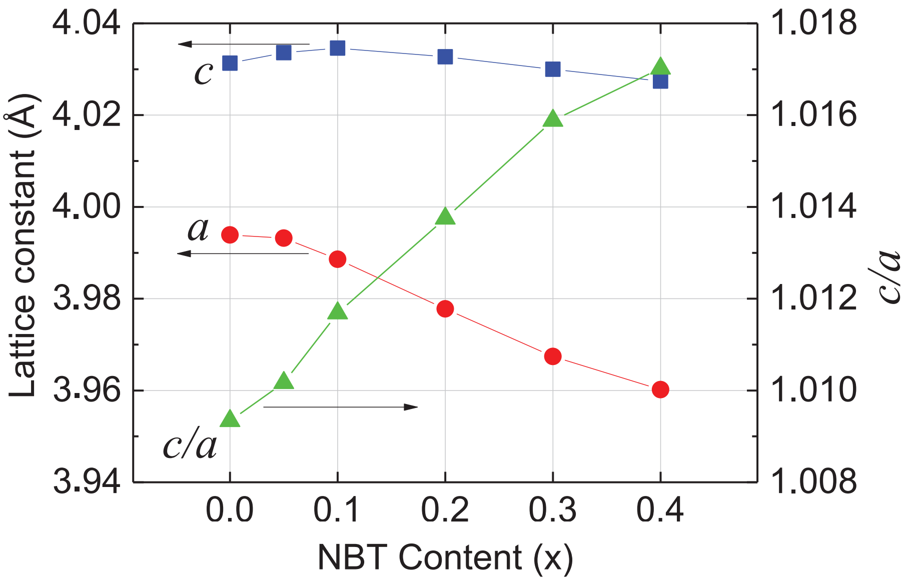

Figure 4.4. Lattice parameters and tetragonality (*c/a*) of BT-NBT ceramics as a function of NBT content according to Rietveld refinement results.

4.3.2. Microstructure of BT-NBT ceramics

The SEM images of the (1-x)$BaTiO_3$-x$Bi_{0.5}Na_{0.5}TiO_3$ ceramics which were sintered at 1200 °C have been given in Figure 4.5. The average grain sizes of the samples for x = 0, 0.05, 0.10, 0.20, 0.30, and 0.40 compositions are calculated as 0.24, 0.56, 0.65, 0.83, 1.29 and 1.85 μm, respectively by linear intercept method and their distribution plots are given in the insets of Figure 4.5. The increase in the grain size as the NBT incorporation shows that NBT enhances the grain growth and cause some microstructural differences even under the same synthesis conditions. The x = 0.00, 0.05 and 0.10 samples appear to have incomplete grain growth as evidenced by their submicron grain sizes and pores around grain boundaries. As the x = 0.20, 0.30 and 0.04 samples have similar dense microstructures, their electrical properties can be more appropriately compared.

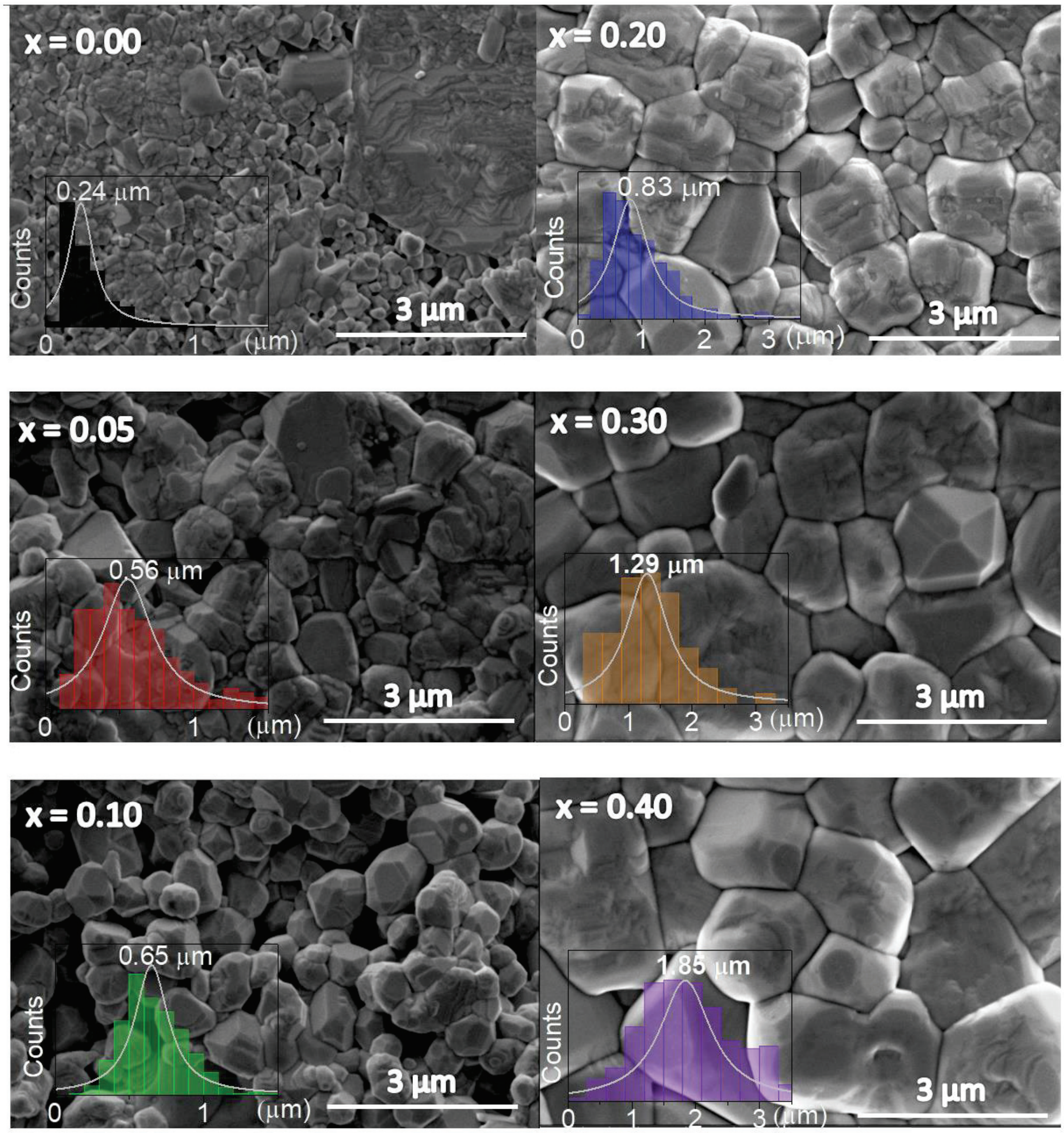

Figure 4.5. SEM images of (1-x)$BaTiO_3$-x$Bi_{0.5}Na_{0.5}TiO_3$ (BT-NBT) ceramics for x = 0, 0.05, 0.10, 0.20, 0.30, and 0.40 compositions.

4.3.3. Dielectric Properties of BT-NBT ceramics

Figure 4.6 shows the dielectric constant and dielectric loss data of the BT-NBT samples. In Figure 4.6(a) and (b) comparison of dielectric constant and dielectric loss of the samples for all compositions at 10 kHz are shown, respectively. According to these results, an obvious trend depending on the NBT composition has been realized. Consistent with the literature, the T_C value increases as the NBT composition incorporation increases. This is an expected result in accordance with the increase in the tetragonality (*c/a*) with NBT composition [223b]. The increase in T_C was attributed to shortening of the Ti–O bonds by calculating the bond-valence sum (BVS) of the Ti ion that it approaches its ideal value by NBT incorporation [223b]. On the other hand, it can be seen that the dielectric constant at T_C has been also increased as the NBT composition increased up to x= 0.20 composition and decreases again for 0.30 and 0.40 compositions (Figure 4.6a).

The increase in the NBT incorporation seems to induce the decreased dielectric constant below T_C which is originated from decrease in domain wall mobility. It is known that 90° domain wall fluctuations (or mobility) contribute most effectively to increase the dielectric constant around room temperature [231]. Therefore, the higher 90° domain wall density, the greater its contribution to the dielectric constant. Generally, the increase in 90° domain wall density and hence increase in dielectric constant around room temperature are expected with the increase of grain size [28, 216a]. However, in the BT-NBT samples, by NBT incorporation the room temperature dielectric constant decreases even increasing grain size, therefore the strong increase in *c/a* probably suppresses the 90° domain wall mobility, so tetragonality becomes the main effect that causes a decreased dielectric constant [224, 232]. Because, the increase of tetragonality can cause a decrease in the domain wall mobility due to the intergranular constraints [18] consequently cause decrease in dielectric constant. In another words, the decrease in the dielectric constant around room temperature by NBT incorporation can be attributed to high tetragonality that reduces 90 ° domain walls mobility. Additionally, the increase in dielectric constant around T_C up to x = 0.20 NBT composition can be attributed to grain size or grain boundary effects. This situation causes the dielectric function to form a sharper step around T_C, especially for the x = 0.20 composition. This sharp step can be advantageous for the electrocaloric effect due to the possible first order phase transition.

Figure 4.6(c-f) demonstrates temperature dependent dielectric constants and loss of the samples for x = 0, 0.05, 0.10, 0.20, 0.30 and 0.40 compositions respectively for 0.1-100 Hz. A trend of peak sharpening can be seen with increasing NBT concentration. This first order like phase transition especially seen in that of x = 0.20 composition. However for 0.30 and 0.40 compositions the phase transition become more diffuse that can be a result of occurrence of frozen impurities, vacancies, or nonstoichiometric regions [223b].

The peaks around room temperature, observed in the dielectric constant and dielectric loss of the x = 0, 0.05 and 0.10 compositions, do not correspond to any phase transition because they have been inhibited as the frequency increases. However this peak occurrence can be a result of the contribution from space-charge polarization effect or Schottky diode effect [223b] possibly occurs in grain boundary pores.

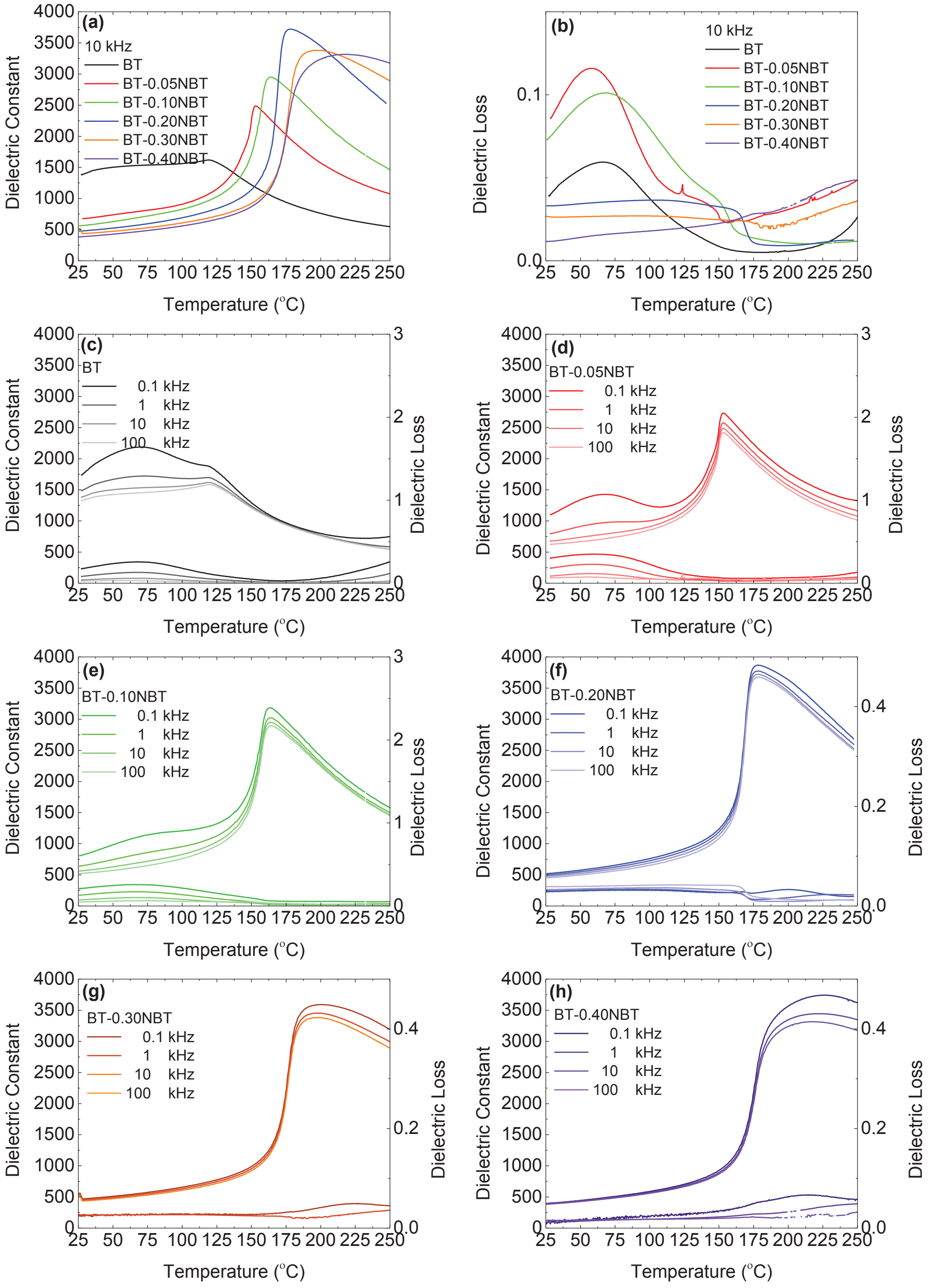

Figure 4.6. Comparisons of (a) dielectric constant and (b) loss of the samples for all compositions at 10 kHz and (c-f) dielectric constant and loss of the samples for x = 0, 0.05, 0.10, 0.20, 0.30, and 0.40 compositions, respectively.

4.3.4. Ferroelectric and Electrocaloric Properties

In Figure 4.7 temperature dependent polarization and strain-electric field hysteresis loops of all specimens (except x = 0 and 0.40) have been given. Due to the contribution of conductivity in undoped BT sample, measurement was carried out at 50 Hz but the sample experienced dielectric breakdown at 50 °C. The conductivity contribution is also present in the x = 0.05 composition, which is evident from the lossy hysteresis behavior around $T_C = 150$ °C (Figure 4.7(a)). For x = 0.10 composition the conductivity contribution is not observed at all and the P-E loops are slim above $T_C = 163$ °C as expected in the paraelectric phase (Figure 4.7(b)). The lack of conductivity contribution is also supported by the fact that the loss value of x = 0.10 composition above T_C (see Figure 4.6(e)) does not increase with increasing temperature. The positive strain values reach their maximum at T_C for the x = 0.10, 0.20 and 0.30 compositions (Figure 4.7(d, f, h)). Interestingly, it is observed that the polarization loops of the x = 0.20 and 0.30 compositions at T_C have double loop-like shapes (Figure 4.7(e, g)). This rare behavior is attributed to their strongly tetragonal ferroelectric domain structure and occurrence of the sudden phase transition at T_C indicating first order like phase transition [233]. Polarization and strain behavior is similar for x = 0.20 and 0.30 compositions. The coercive fields of these latter samples increase as the NBT content increases.

In order to support the unusual observation of the first-order phase transition, besides the electric field dependent hysteresis behavior of polarization (P-E) (Figure 4.8 (b)) at T_C, DSC measurements (Figure 4.8(a)) and temperature dependent behavior of remnant polarization (P_r - T) (Figure 4.8(c)) have been also investigated. The heat flow peak around T_C of the x = 0.20 and 0.30 compositions is sharper which implies a sharper phase transition behavior [234]. P-E hysteresis loops in T_C have double loop behavior for x = 0.20 and 0.30 compositions as shown in Figure 4.8(b). On the other hand, the sudden decrease in T_C in the P_r - T graphs of x = 0.20 and 0.30 compositions might also indicate first-order like nature of the phase transition as shown in Figure 4.8(c).

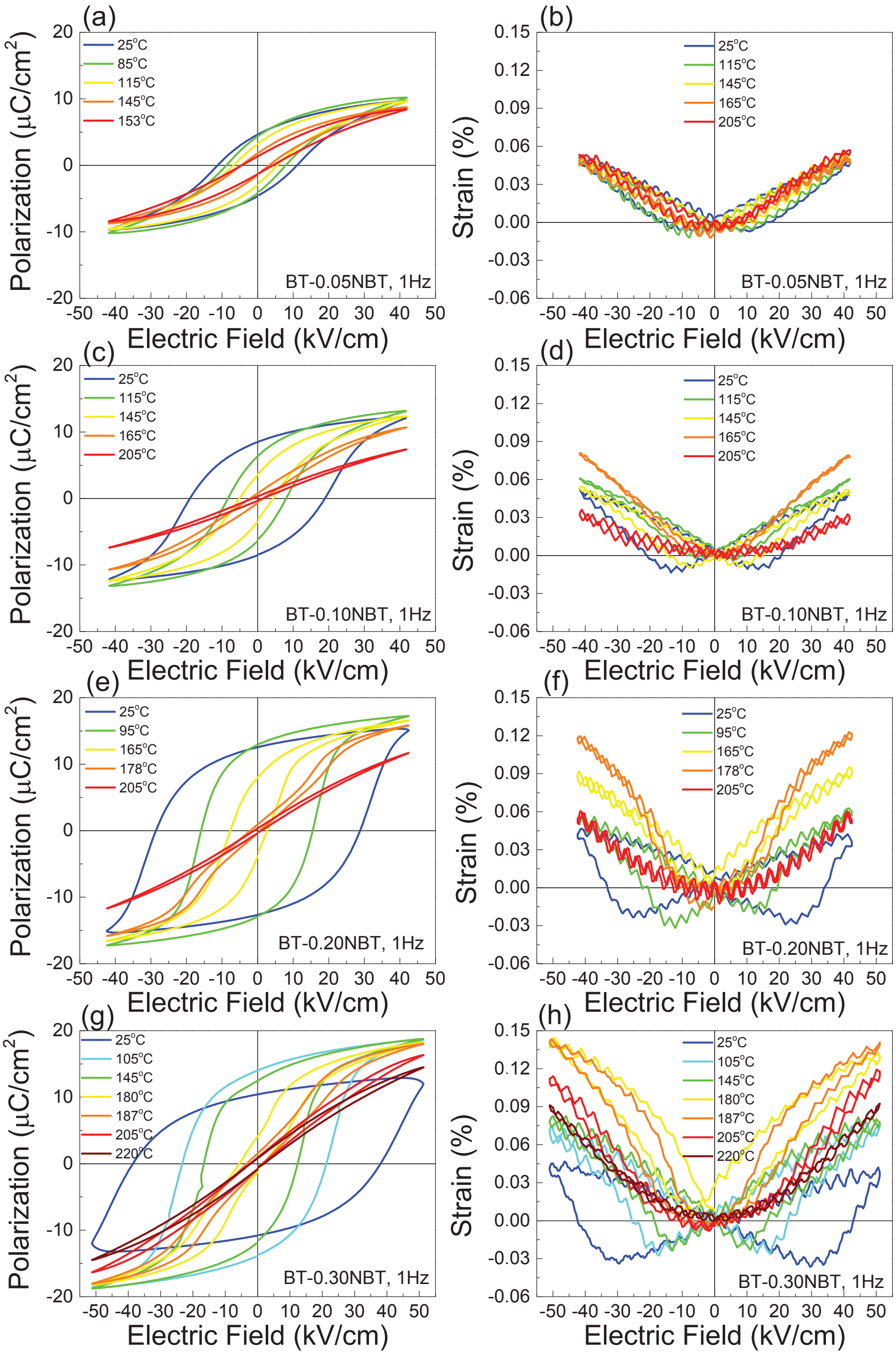

Figure 4.7. Temperature dependent (a-d) polarization and (e-h) strain-electric field hysteresis loops the ceramics.

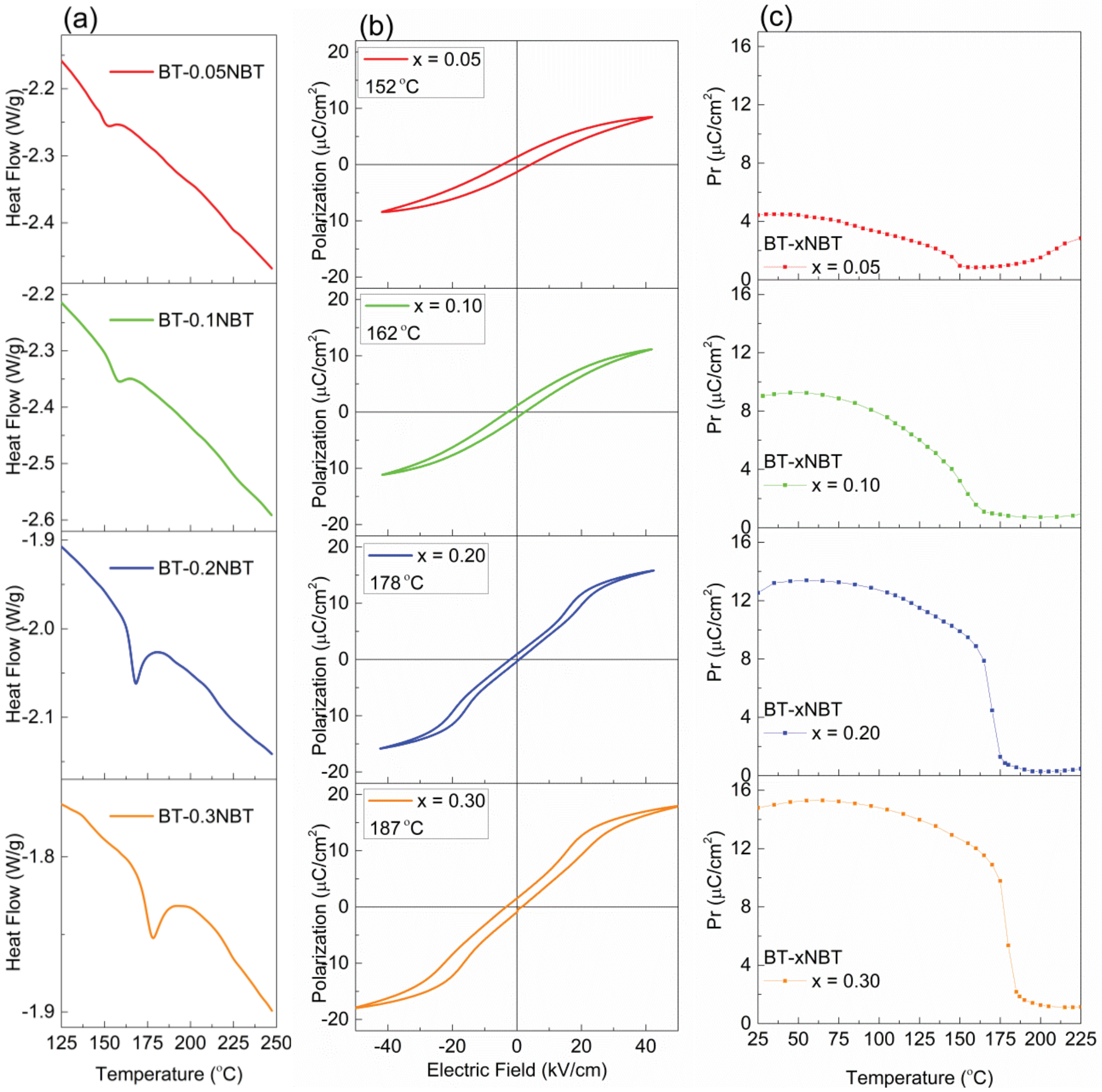

Figure 4.8. Comparison of phase transition behavior of samples at T_C via (a) DSC measurements, (b) P-E measurements and (c) temperature dependent remnant polarization

According to polarization-electric field hysteresis loop comparison (Figure 4.9(a) as NBT content increases P_S, E_C and P_r also increases considerably. The spontaneous polarization (which is proportional to saturation polarization) also increased but in proportion to the tetragonality (*c/a*). The reasons for this can be given as (1) the restriction of domain wall motion due to the increased tetragonality or the reduction of 90 º domain wall densities and (2) less change in the lattice parameter *c* competed to *a* which can cause lower P_S dipole.

Strain-electric field hysteresis loop comparison for all compositions at 40 kV/cm is shown in Figure 4.9(b). It is observed that the positive strain slightly decreases as the NBT content increases. Simultaneously, the negative strain increases and a more evident butterfly-shaped loop characteristic emerges with the increase in NBT content. In fact, the decreased negative strain in x = 0.05 and 0.10 compositions can be attributed to the incomplete grain growth and the small grain size that restricts the formation of long range ordered ferroelectric domains. On the other hand, the decreased the positive strain with the NBT incorporation indicates that the NBT restricts the domain switching behavior despite the increase in grain size.

Temperature dependence of the electrical polarization and corresponding ΔT values at 40 kV/cm are shown in Figure 4.9(c, d). The maximum ΔT values were obtained as 0.36, 1.30, 2.63, and 3.02 K for compositions x = 0.05, 0.10, 0.20 and 0.30, respectively. (Although a max ΔT value of 1.78 K was obtained for the x = 40 composition, this sample was excluded from the comparison for now due to its conductivity contribution around T_C). On the other hand, their corresponding ΔT/E ratios are 0.090, 0.325, 0.657 and 0.755 K m/MV respectively. The highest ΔT values belong to the x = 0.20 and 0.30 compositions. The reason for this can be ascribed to the first order like phase transition behavior [235] and abrupt polarization drop around T_C.

The comparison of d_{33} coefficient and so called high field d_{33} coefficients of the samples are given in Figure 4.10. It can be observed that the increase in NBT content decreased both d_{33} and d_{33}* coefficients. The positive strain has been also decreased slightly but the negative strain has been increased significantly by NBT incorporation as it given in Figure 4.9(b). These piezoelectric properties indicate that the increase in tetragonality or coercive field restricts the domain switching behavior and domain wall motion despite the decrease in grain boundary effect with the increase of NBT content.

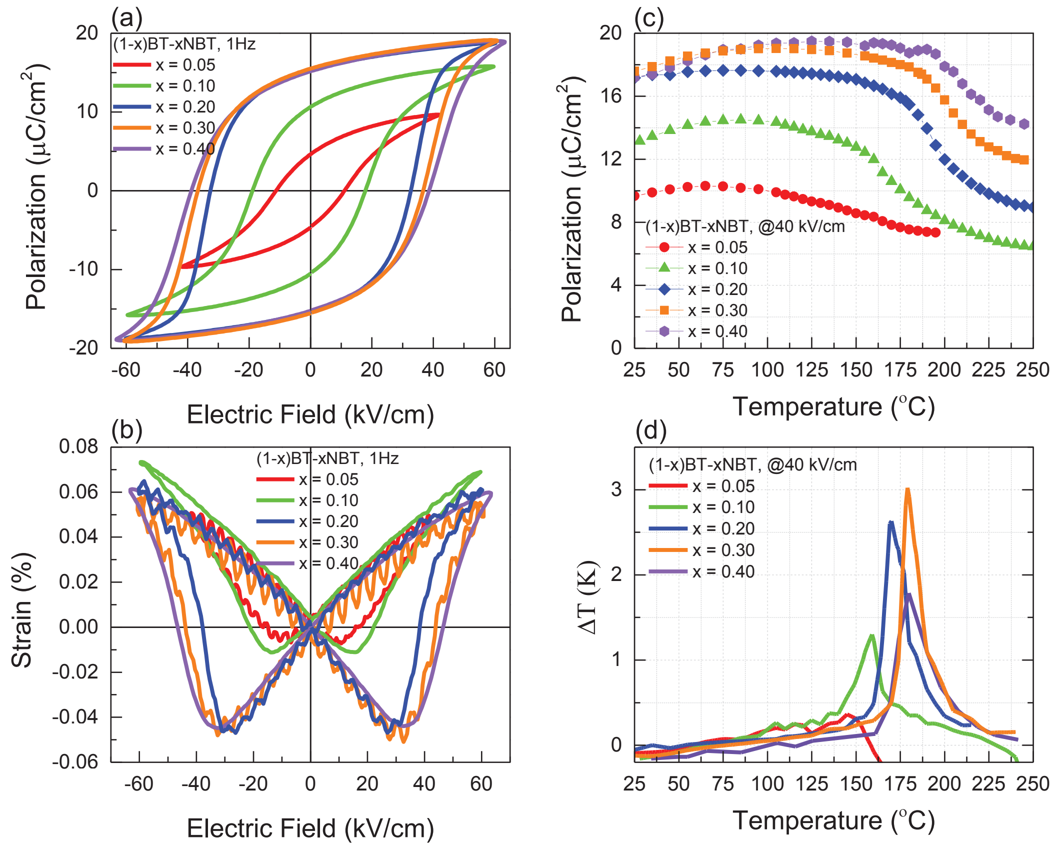

Figure 4.9. Room temperature (a) polarization and (b) strain-electric field hysteresis loop comparison for all compositions and (c) temperature dependence of the electrical polarization and corresponding (d) ΔT values at 40 kV/cm.

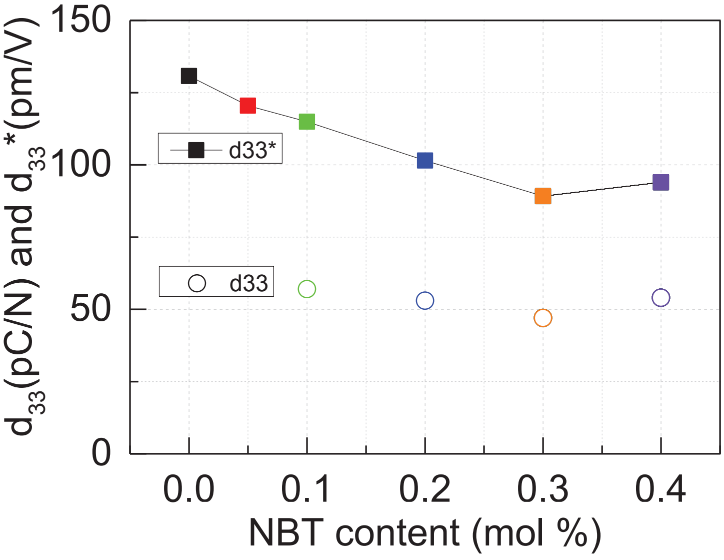

Figure 4.10. Room temperature piezoelectric coefficient (d_{33}) and high-field piezoelectric coefficient (d_{33}*) as a function of NBT content.

4.4. Conclusions

In this study, by NBT incorporation to the BT system, increase in tetragonality has been obtained. According to the dielectric, piezoelectric and ferroelectric findings, the increase in the T_C value, increase in negative strain and increase in coercive field were associated with the restriction of domain switching due to enhanced tetragonality by NBT incorporation. In addition, electrocaloric properties of BT-NBT systems were measured indirectly for the first time, and it was shown that the increase in tetragonality by NBT incorporation also increased the electrocaloric effect. The highest $\Delta T = 3.02$ K has been obtained for $x = 0.30$ compositions at 187 °C and at 40 kV/cm electric field that corresponds to $\Delta T/E = 0.755$ K m/MV. The reason for the enhancement of ΔT has been associated with the increased first order like phase transition behavior around T_C by NBT incorporation.

CHAPTER 5

ELECTROCALORIC PROPERTIES OF TEXTURED KNBT CERAMICS

5.1. Introduction

In the development of lead-free ceramics together with chemical composition development, obtaining crystallographically oriented ceramics provides important advantages in increasing the electrical properties. Dielectric and electro-mechanical properties can be developed at high levels from the ceramics produced as crystallographically oriented, close to single crystal properties [174]. One of the most promising lead-free ceramics for actuator applications is the textured KNN-based piezoelectric material $(((K_{0.5}Na_{0.5})1\text{-}xLi_x)(Nb_{1-y}Ta_y)O_3)$ which was developed by Saito et al. in 2004 [236]. While a d_{33} value of 300 pC/N was obtained in randomly oriented ceramics, d_{33} increased to 416 pC/N in ceramics textured along (00l) direction [236]. The results reveal that development can improve piezoelectric properties of ferroelectric ceramics. In the aforementioned study, grain oriented materials were produced using the templated grain growth (TGG) method. Prior to TGG studies, it is known that high piezoelectric coefficient and low hysteresis properties were obtained in certain crystallographic orientations [237]. In the TGG method, an oriented microstructure is obtained using a seed crystal (sometimes called a template), which is a single crystal oriented along a crystallographic direction, by growing the matrix grains around them (Figure 1.24). It was previously shown that pyroelectric effect is improved with texturing [93]. The pyroelectric effect is defined as the change of electrical polarization with temperature in polar materials (dP/dT). Therefore, materials with a high pyroelectric coefficient (dP/dT) are potentially expected to exhibit a large electrocaloric effect [238].

In this study, the contribution of texturing in $0.82(Na_{0.5}Bi_{0.5}TiO_3)$-$0.18(K_{0.5}Bi_{0.5})TiO_3$ (0.82NBT-0.18KBT) samples (abbreviated as 0.82NBT-0.18KBT or KNBT in this study), to the electrocaloric effect was investigated. The reason for choosing this composition is that a large electrocaloric efficiency has been reported among Pb-free ferroelectrics which is related to the presence of a MPB [239]. Previously reported electrocaloric temperature change in the behavior of this material is shown in Figure 5.1. It can be observed that the electrocaloric temperature change is maximum near the depolarization temperature.

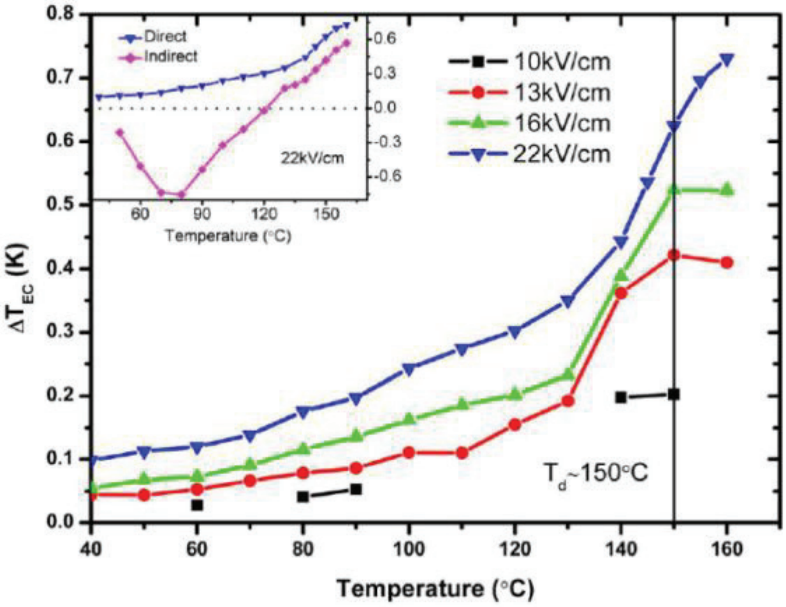

Figure 5.1. Electrocaloric temperature change of $0.80Na_{0.5}Bi_{0.5}TiO_3$-$0.20K_{0.5}Bi_{0.5}TiO_3$ ceramics [239].

5.2. Experimental Procedure for KNBT Synthesis

The samples studided in this section was synthesis by Muhammet Ali Ünal with the assistance of Dr. Gökçe Yıldırım Özarslan under the supervision of Prof. Dr. Ender Suvacı. To produce templated $0.82Na_{0.5}Bi_{0.5}TiO_3$-$0.18K_{0.5}Bi_{0.5}TiO_3$ (0.82NBT-0.18KBT) samples, $Na_{0.5}Bi_{0.5}TiO_3$ (NBT) and $K_{0.5}Bi_{0.5}TiO_3$ (KBT) powders were synthesized separately and the desired stoichiometry was mixed. For NBT and KBT powder synthesis, the stoichiometric mixtures of Na_2CO_3, K_2CO_3, Bi_2O_3 and TiO_2 raw material powders were calcined after homogenous mixtures were obtained in the attritor mill. Furnace regimes arranged to 5 °C/min rate, NBT calcination carried out at 800 °C and 2 hours at KBT calcined at 850 °C for 2 hours. After calcination of NBT and KBT powders, they were homogeneously ground and mixed in an attritor mill at the desired stoichiometric ratios (0.82NBT-0.18KBT).

The tape casting production of KNBT samples with 0%, 7% and 10% NBT template ratio was carried out by using the recipe available in the Master of Science thesis of Muhammet Ali Ünal [92]. To avoid deviation from MPB, raw powders were weighed according to the stoichiometric ratio, considering the ratios of NBT templates [240]. The dispersant abbreviated as TEGO was used to keep powders homogeneous in solvents. The combination of MEK (methyl ethyl ketone) and Ethanol with 50-50% rate was used as solvent medium. The other components, PVB (Polyvinyl Butyral) and DBP (dibutyl phthalate) were used as binder and plasticizer respectively.

Using this recipe, KNBT ceramics were tape casted. Afterwards, they were cut into 1 cm^2 pieces and stacked on top of each other so that the approximate height was 1 mm after pressing and pressed with a laminating press. Pressing was done at 30 °C with a pressure of 100 MPa. The binder burnout process was carried out at 400 °C for 1 hour, and 600°C for 6 hours. After binder burnout, the obtained samples were pressed with cold isostatic press (CIP) at 300 MPa pressure for 10 seconds. Afterwards, all samples were sintered at 1150 °C for 24 hours. The calcination and sintering conditions are shown in the Table 5.1.

Table 5.1. Calcination and sintering conditions of KNBT samples.

NBT TEMPLATE	Sample name	Calcination of NBT	Calcination of KBT	Calcination of KNBT	Sintering
0%	KNBT-0PL	800 °C, 2 h	850 °C, 2 h	700 °C, 10 min	1150 °C 24 h
7%	KNBT-7PL	800 °C, 2 h	850 °C, 2 h	700 °C 10 min	1150 °C 24 h
10%	KNBT-10PL	800 °C, 2 h	850 °C, 2 h	700 °C 10 min	1150 °C 24 h

5.3. Results and Discussions

5.3.1. Structure of KNBT ceramics

XRD patterns of sintered 0 %, 7 % and 10 wt% templates containing samples are shown in Figure 5.2. When the XRD results are examined, it is seen that a single-phase perovskite structure is obtained for all samples. On the other hand, depending on the template amount, it is observed that the intensity of the peak belonging to the (110) plane decreases while the intensity of the (200) peak, increases. As a result, it was understood that the tape casting method provides orientation along (200) plane (Lotgering factor ≈ 47%) even in the KNBT-0PL ceramic material which does not contain any templates. The weak presence of (002) peak is related with the KBT content in the solid solution and points to the contribution from the tetragonal phase [240]

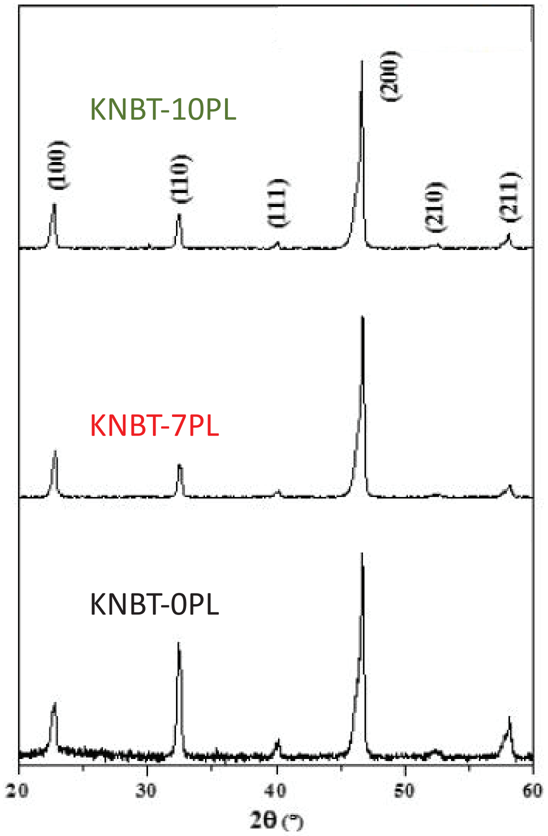

Figure 5.2. XRD patterns of samples containing 0%, 7% and 10% template sintered for 24 hours at 1150°C.

5.3.2. Microstructure of KNBT ceramics

In Figure 5.3 SEM surface images of polished and etched KNBT samples sintered for 24 hours at 1150 °C are shown. According to these SEM images, it is observed that the densification has occurred to a certain level. If the KNBT sample containing 7 wt% template is considered, it is seen that the templates do not completely swallow the matrix powders, and the grains formed by the matrix powders growing in the structure. The lower orientation level in XRD pattern of this sample also supports this situation. With the increase in the amount of template, it is seen that the templates absorb the matrix grains more during sintering in the sample containing 10 % template comparted to the sample containing 7 % template. Average grain sizes are 3.2, 5.8 and 6.2 μm for 0%, 7% and 10% template containing KNBT samples, respectively. The density of the samples, slightly decreases with increasing template content (5.71, 5.61, 5.57 g/cm^3 for 0%, 7%, 10% template containing KNBT samples, respectively).

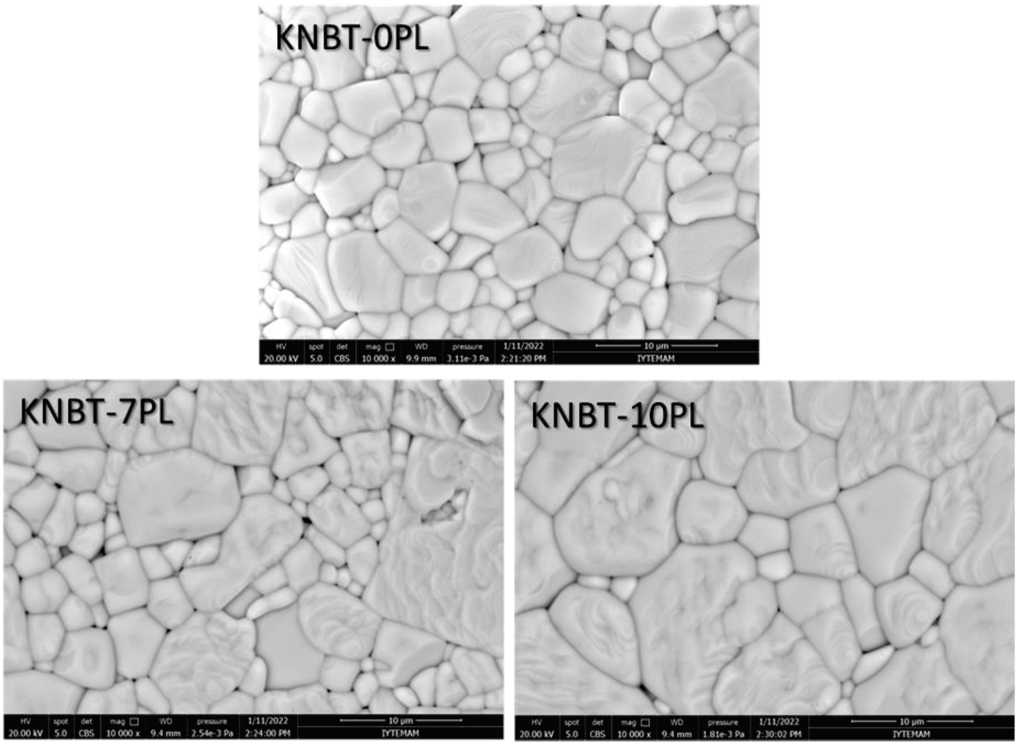

Figure 5.3. SEM surface images of samples containing 0%, 7% and 10% template, sintered for 24 hours at 1150 °C.

5.3.3. Dielectric and Ferroelectric Properties of KNBT Ceramics

In Figure 5.4(a), the comparison of the dielectric constant and dielectric loss measurement results at 1 kHz of KNBT samples containing 0, 7 and 10 % templates are given. The shoulder temperature (T_S) is around 145 °C for both samples containing KNBT-7PL and KNBT-10PL, while T_S is around 125 °C in the sample without templates (KNBT-0PL). Thus, T_S increases with the addition of the template. The temperature T_S is proportional to the depolarization temperature (T_d) but is different from it. In the KNBT-0PL sample, the temperature at which the polarization decreases drastically was determined as T_d and it was observed that it overlaps with T_S. However, as it will be seen in the next section, due to the increase in conductivity in templated samples at high temperatures, which is also evident from dielectric losses, T_d determination from P-E loops for templated samples was not done because it would not be accurate. Therefore, T_s will be used for comparison.

The effect of texturing on the hysteresis loops at room temperature is shown in Figure 5.4(b), accordingly; the highest polarization value at room temperature was measured in the sample without any template (KNBT-0PL). As the amount of template and degree of orientation increases, the maximum polarization slightly decreases. Possible reasons for the decrease of the polarization with increasing orientation can be: (1) The NBT templates added in the templated samples cause a deviation from the morphotropic phase boundary despite the necessary stoichiometric adjustments. (2) The microstructure difference: increased the grain size of our templated samples did not cause an increase in the polarization however, it is known that the increase grain size causes increased polarization [241]. (3) The orientation difference: As expected in the templated samples, the intensity of the (200) plane increased compared to (110). However, the orientation contribution did not lead to an increase in polarization unlike previous reports in the literature [242]. The absence of this increase here indicates that other factors might be effective.

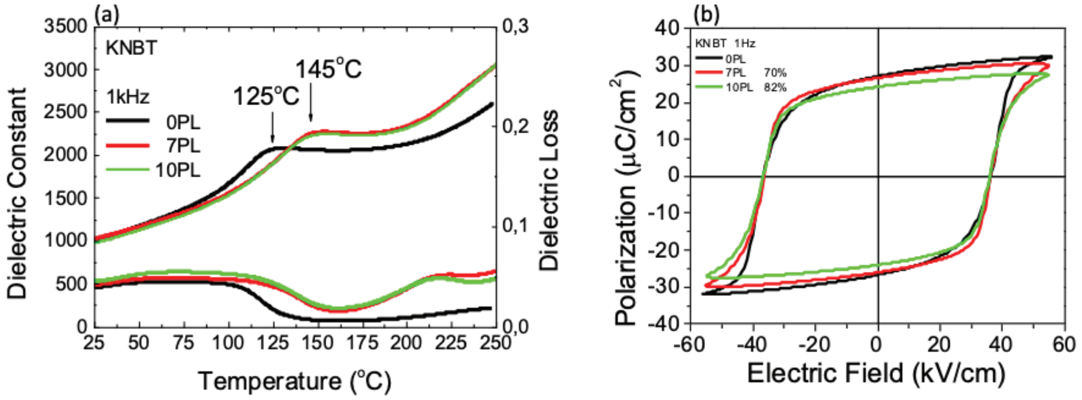

Figure 5.4. (a) Dielectric constant comparison of KNBT samples containing 0, 7 and 10% templates at 1 kHz, (b) Polarization-electric field comparison of KNBT samples containing 0, 7 and 10% templates at 1 Hz and at room temperature.

Figure 5.5 (a), Figure 5.5 (d) and Figure 5.6 (a) shows the temperature dependent polarization, strain and current hysteresis measurements of the KNBT-0PL sample respectively. An electric field up to 50 kV/cm was applied for the polarization hysteresis loop to reach saturation. With the increase in temperature, the maximum polarization increases slightly at first because, the polarization has not yet reached saturation in the highest applied electric field at room temperature and the curves can reach more saturation with the increase in temperature. The hysteresis loops get slimmer; remnant polarization and coercive field decreases as the temperature increases. With further increase in temperature, double hysteresis behavior was observed, indicating the transition from non-ergodic to ergodic state [30]. The remnant polarization (P_r) decreases drastically around the depolarization temperature, T_d = 125 °C (see Figure 5.7(a)) while the negative strain observed up to the T_d disappears above the T_d (see Figure 5.7(b)). It is also observed that the E_2 peak in the current-electric field hysteresis loops has negative values when the temperature rises above T_d. It was noticed that at T_d, the E_2 peak coincides with zero electric field. At higher temperatures (e.g. 205 °C), very slim curves with almost no hysteresis are observed. Additionally, E_1 peak vanished at high temperatures (see Figure 5.7(a)). All these observations show that there is a transition from non-ergodic relaxor to ergodic relaxor behavior.

Figure 5.5 (b,c), Figure 5.5 (e,f) and Figure 5.6 (b,c) shows the temperature dependent polarization, strain and current measurements of the KNBT-7PL and KNBT-10PL samples respectively. Templated samples have similar behavior with that of non-templated KNBT-0PL sample. However, their depolarization temperature is around T_d =

145 °C as approximated by T_S from the dielectric measurements, which was confirmed from as the sharp decrease of the remnant polarization around 145 °C and current E_1 peak that goes zero field above 145 °C. On the other hand, the templated samples shows lossy curves at 205 °C that is, the polarization increases again with temperature. This shows that above T_d the conductivity contribution increases and this masks the actual behavior of the sample at high temperatures.

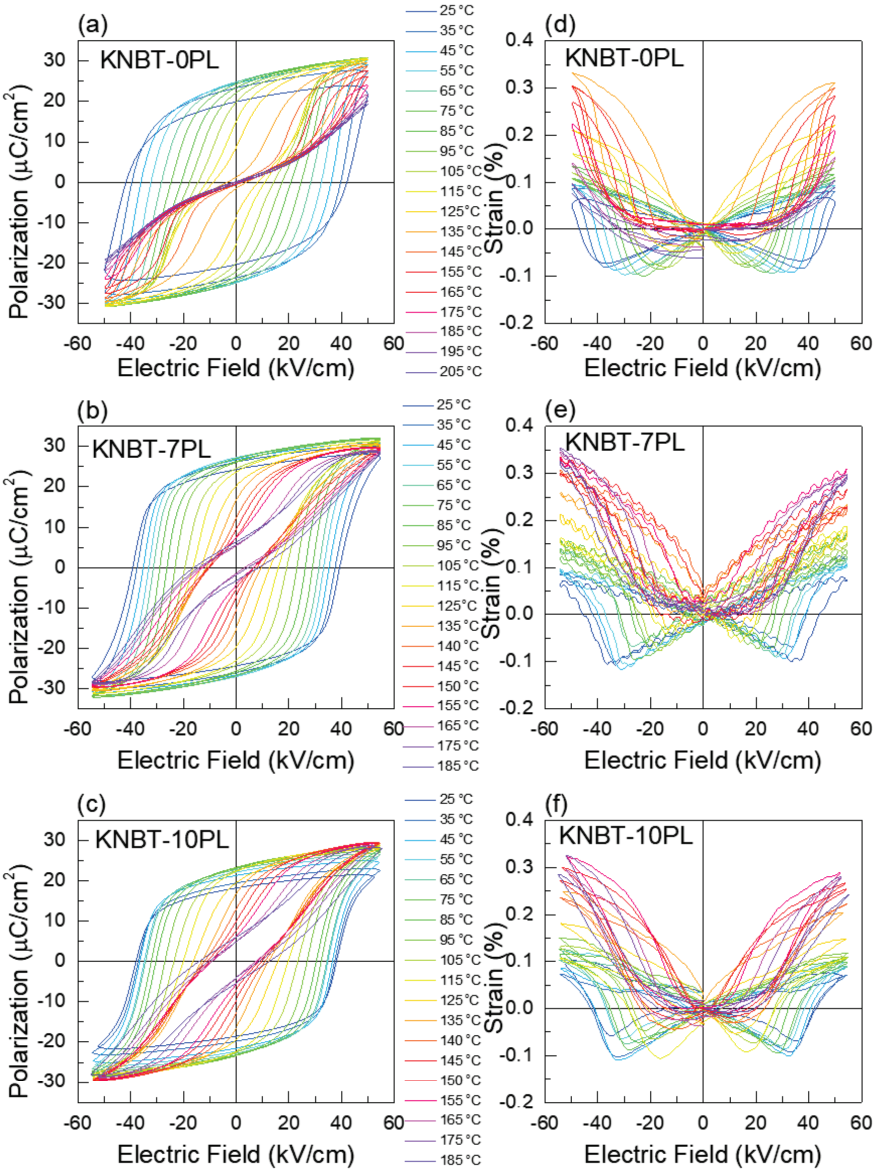

Figure 5.5. Temperature dependent (a,b,c) polarization-electric field, (d,e,f) strain-electric field and (g,h,i) current- electric field hysteresis loops of KNBT-0PL, KNBT-7PL and KNBT-10PL samples.

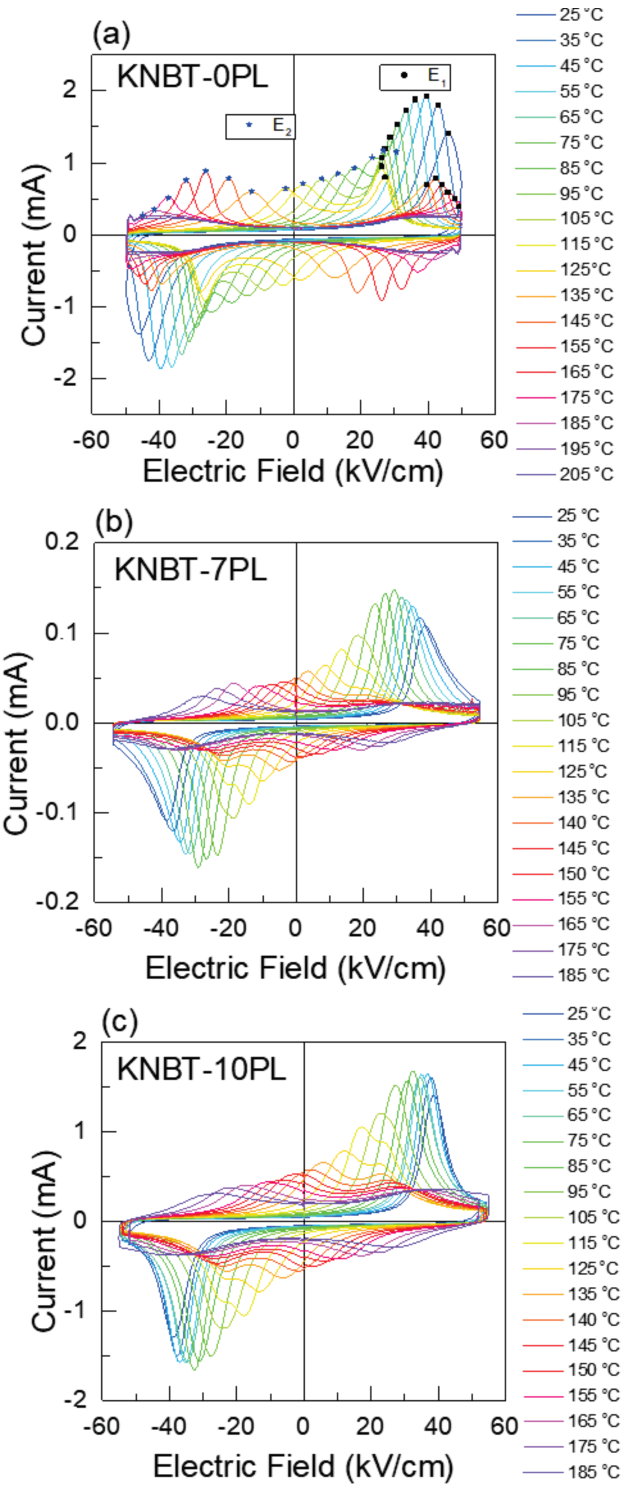

Figure 5.6. Temperature dependent current- electric field hysteresis loops of (a) KNBT-
(b) 0PL, KNBT-7PL and (c) KNBT-10PL samples.

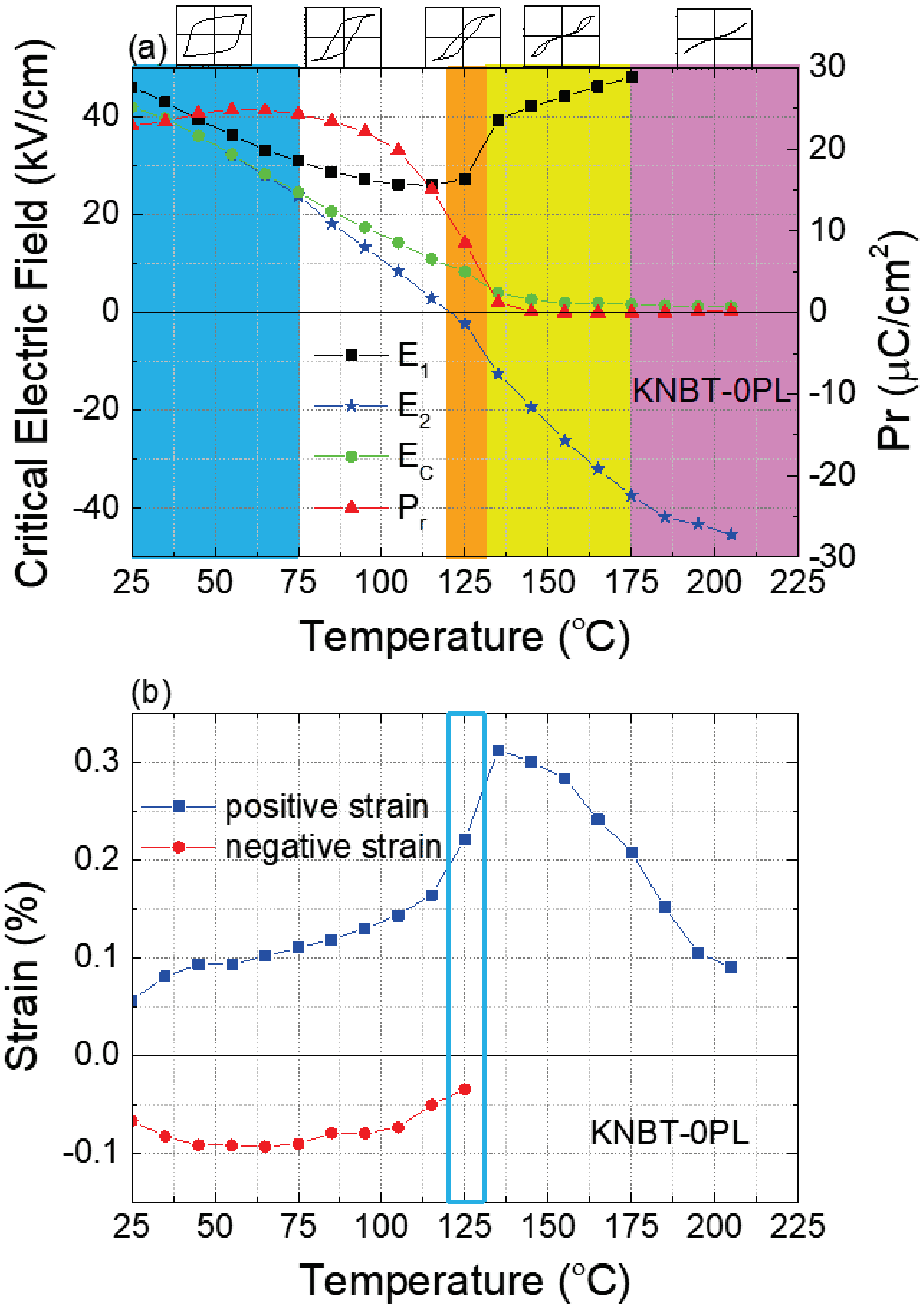

Figure 5.7. Temperature dependent (a) current- electric field critical electric fields (E_1, E_2 and E_C) and P_r and (b) positive and negative strain values of KNBT-0PL.

5.3.4. Electrocaloric properties of KNBT ceramics

The temperature-dependent variation of polarization curves (P-T) and indirectly calculated electrocaloric temperature change (ΔT) obtained under 50 kV/cm applied field for KNBT samples containing 0%, 7% and 10% templates are given in Figure 5.8. In the ΔT calculation of all KNBT samples, the specific heat was taken as 500 J/kgK from previous studies in the literature [211], and the density values measured by Archimedes' method for each sample were used as the density value. In the P(T) behavior of the KNBT-0PL sample, it is observed that the polarization gradually decreases with temperature and decreases drastically around T_d. This drastic change causes a high ΔT peak value (3.02 K). This value is considerably higher than the values obtained in the literature. The highest ΔT measured by Cao et al. with the indirect method is approximately 1 K at 30 kV/cm [243], the highest ΔT measured by Le Goupil et al. with the direct method is approximately 0.7 K at 22 kV/cm [239]. This high value is thought to be related to the average grain size and density of our KNBT samples produced by tape casting.

In the P(T) behavior of the KNBT-7PL sample, it is observed that the polarization gradually does not drastically decrease with the temperature even around T_d and some fluctuations occur due to the conductivity contribution. Although ΔT is maximum around the depolarization temperature, as expected, the conductivity contribution reduces the ΔT value. Since the conductivity contribution masks the depolarization, the expected increase is not observed in ΔT values. It is observed that the conductivity contribution in KNBT-10PL sample is more dominant in the P-T behavior than the sample containing 7% template, which leads to a sharper decrease in ΔT above the depolarization temperature.

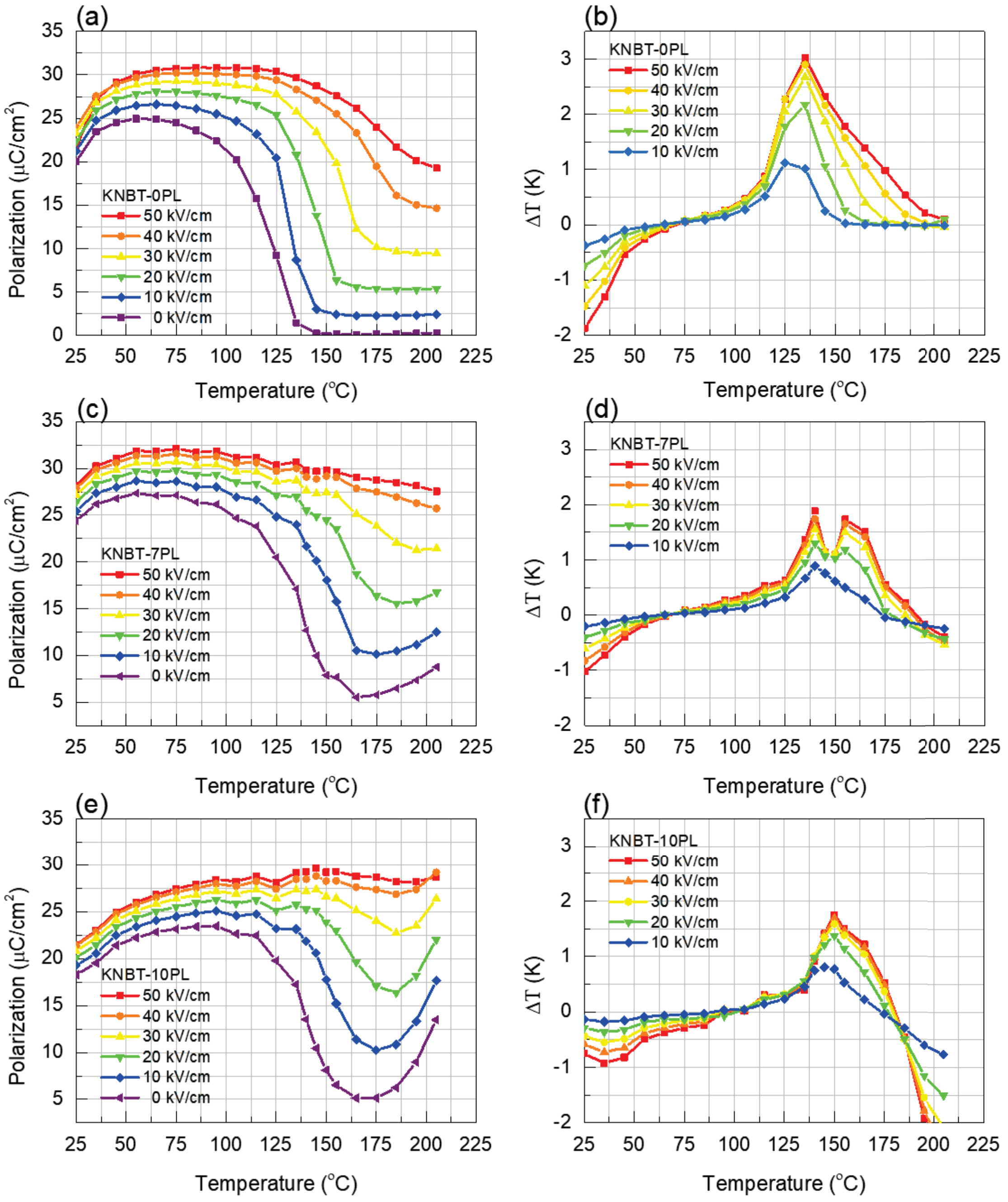

Figure 5.8. Temperature dependent polarization and indirectly calculated electrocaloric temperature change (ΔT) values up to 50 kV/cm electric field for KNBT samples containing (a,b) 0%, (c,d) 7% and (e, f) 10% templates.

Direct measurements of KNBT-0PL sample were carried out with the direct measurement setup [244] used by Dr. Lovro Fulanovic at the Technical University of Darmstadt. Direct measurement is necessary for the verification of the ΔT calculated by the indirect method in samples with relaxor ferroelectric properties. The Figure 5.9

shows the direct measurements of ΔT values obtained when an electric field up to 40 kV/cm is applied and removed. The thermistor temperature variation versus time during the measurement in which applied field is 40 kV/cm is shown in Figure 5.10. During direct measurements, since both DC voltage was applied and the samples were exposed to the voltage for a long time, the samples were electrically broken down before reaching 50 kV/cm. As a result, the highest ΔT value obtained for direct measurements was 0.9 K at around 150 °C. This result is smaller than the values obtained indirectly result since it is known that ΔT increases as the electric field increases.

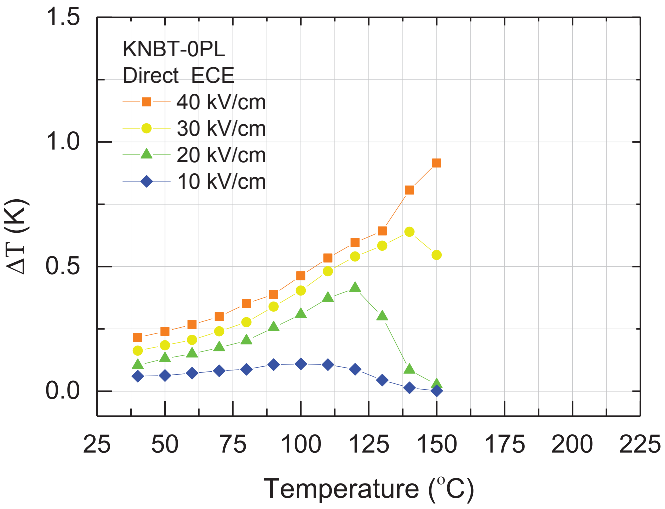

Figure 5.9. Direct electrocaloric measurement of KNBT-0PL sample measured by Dr. Lovro Fulanovic.

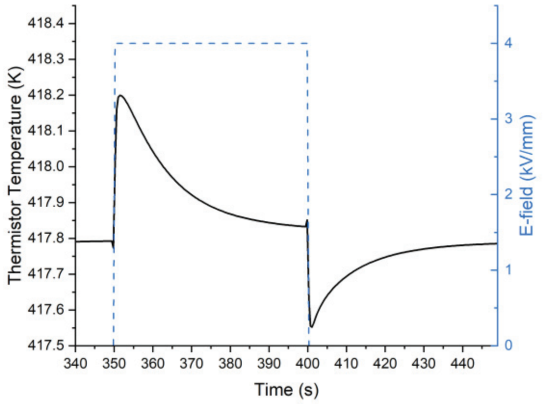

Figure 5.10. Thermistor temperature change (black solid line) as a function of time when the electric field is applied and removed (blue dashed line), during the direct measurement of the electrocaloric effect by Dr. Lovro Fulanovic.

5.4. Conclusions

We have investigated the effect of tape casting process and grain orientation on the electrocaloric properties of $0.82Na_{0.5}Bi_{0.5}TiO_3$-$0.18K_{0.5}Bi_{0.5}TiO_3$ (0.82NBT-0.18KBT) ceramics at the Morphotropic Phase Boundary (MPB), using direct and indirect measurements. We observe a larger electrocaloric temperature change for the unoriented tape cast ceramics compared to grain-oriented ones. According to the indirect electrocaloric calculations, the largest $\Delta T = 2.5$ K has been obtained for unoriented sample at 30 kV/cm. This value is considerably higher than the values obtained in the literature. This large value is probably related to the average grain size and density of the samples produced by tape casting.

REFERENCES

1. Heimann, R. B., Advanced ceramic materials: products, applications and economic outlook. *Proceedings of the International School Earth and Planetary Sciences, Siena* **2001**, 1-24.

2. Kingery, W. D.; Bowen, H. K.; Uhlmann, D. R., *Introduction to ceramics*. John wiley & sons: 1976; Vol. 17.

3. Valasek, J., Piezo-electric and allied phenomena in Rochelle salt. *Physical review* **1921,** *17* (4), 475.

4. Busch, G.; Scherrer, P., Eine neue seignette-elektrische Substanz. *Naturwissenschaften* **1935,** *23* (43), 737-737.

5. Von Hippel, A.; Breckenridge, R.; Chesley, F.; Tisza, L., High dielectric constant ceramics. *Industrial & Engineering Chemistry* **1946,** *38* (11), 1097-1109.

6. Shirane, G.; Suzuki, K., Crystal structure of Pb (Zr-Ti) O3. *Journal of the Physical Society of Japan* **1952,** *7* (3), 333-333.

7. Li, Y.; Moon, K.-s.; Wong, C., Electronics without lead. *Science* **2005,** *308* (5727), 1419-1420.

8. (a) Panda, P., Environmental friendly lead-free piezoelectric materials. *Journal of materials science* **2009,** *44* (19), 5049-5062; (b) Ringgaard, E.; Wurlitzer, T.; Wolny, W. W., Properties of lead-free piezoceramics based on alkali niobates. *Ferroelectrics* **2005,** *319* (1), 97-107; (c) Zhang, N.; Zheng, T.; Wu, J., Lead-free (K,Na)NbO_3-based materials: Preparation techniques and piezoelectricity. *Acs Omega* **2020,** *5* (7), 3099-3107.

9. Lee, M. H.; Kim, D. J.; Choi, H. I.; Kim, M. H.; Song, T. K.; Kim, W. J.; Park, J. S.; Do, D., Low sintering temperature for lead-free $BiFeO_3$-$BaTiO_3$ ceramics with high piezoelectric performance. *J. Am. Ceram. Soc.* **2019,** *102* (5), 2666-2674.

10. Venkatesan, S., *Structural domains in thin films of ferroelectrics and multiferroics*. 2010.

11. Wu, J., *Advances in lead-free piezoelectric materials*. Springer: 2018.

12. Xu, Y., *Ferroelectric materials and their applications*. Elsevier: 2013.

13. Li, Z.; Yang, M.; Park, J.-S.; Wei, S.-H.; Berry, J. J.; Zhu, K., Stabilizing perovskite structures by tuning tolerance factor: formation of formamidinium and cesium lead iodide solid-state alloys. *Chemistry of Materials* **2016,** *28* (1), 284-292.

14. Damjanovic, D., Ferroelectric, dielectric and piezoelectric properties of ferroelectric thin films and ceramics. *Reports on Progress in Physics* **1998,** *61* (9), 1267.

15. Juraschek, D. M.; Meier, Q. N.; Trassin, M.; Trolier-McKinstry, S. E.; Degen, C. L.; Spaldin, N. A., Dynamical magnetic field accompanying the motion of ferroelectric domain walls. *Phys. Rev. Lett.* **2019,** *123* (12), 127601.

16. Nguyen, M. D.; Nguyen, C. T.; Vu, H. N.; Rijnders, G., Experimental evidence of breakdown strength and its effect on energy-storage performance in normal and relaxor ferroelectric films. *Current Applied Physics* **2019,** *19* (9), 1040-1045.

17. Shu, Y.; Bhattacharya, K., Domain patterns and macroscopic behaviour of ferroelectric materials. *Philosophical Magazine B* **2001,** *81* (12), 2021-2054.

18. Tutuncu, G.; Li, B.; Bowman, K.; Jones, J. L., Domain wall motion and electromechanical strain in lead-free piezoelectrics: Insight from the model system $(1-x)Ba(Zr_{0.2}Ti_{0.8})O_3–x(Ba_{0.7}Ca_{0.3})TiO_3$ using in situ high-energy X-ray diffraction during application of electric fields. *Journal of Applied Physics* **2014,** *115* (14), 144104.

19. Potnis, P. R.; Tsou, N.-T.; Huber, J. E., A review of domain modelling and domain imaging techniques in ferroelectric crystals. *Materials* **2011,** *4* (2), 417-447.

20. Rödel, J., Effective intrinsic linear properties of laminar piezoelectric composites and simple ferroelectric domain structures. *Mechanics of materials* **2007,** *39* (4), 302-325.

21. Weng, G. J., The Prager Medal Lecture: micromechanics and some aspects of phase fields in ferroelectric crystals. *Acta Mechanica* **2014,** *225* (4), 979-998.

22. Qin, Y.; Zhang, J.; Gao, Y.; Tan, Y.; Wang, C., Study of domain structure of poled (K, Na) NbO3 ceramics. *Journal of Applied Physics* **2013,** *113* (20), 204107.

23. Hooton, J. A.; Merz, W. J., Etch Patterns and Ferroelectric Domains in BaTi O_3 Single Crystals. *Physical Review* **1955,** *98* (2), 409.

24. Du, K.; Gao, B.; Wang, Y.; Xu, X.; Kim, J.; Hu, R.; Huang, F.-T.; Cheong, S.-W., Vortex ferroelectric domains, large-loop weak ferromagnetic domains, and their decoupling in hexagonal (Lu, Sc) FeO3. *npj Quantum Materials* **2018,** *3* (1), 1-7.

25. Arlt, G., The influence of microstructure on the properties of ferroelectric ceramics. *Ferroelectrics* **1990,** *104* (1), 217-227.

26. Hoshina, T., Size effect of barium titanate: fine particles and ceramics. *Journal of the ceramic society of Japan* **2013,** *121* (1410), 156-161.

27. Liu, X.; Xue, S.; Wang, F.; Zhai, J.; Shen, B., Grain size dependent physical properties in lead-free multifunctional piezoceramics: a case study of NBT-xST system. *Acta Materialia* **2019,** *164*, 12-24.

28. Fang, C.; Chen, L.; Zhou, D., Influence of domain on grain size effects of the dielectric properties of $BaTiO_3$ nanoceramics and nanoparticles. *Physica B: Condensed Matter* **2013,** *409*, 83-86.

29. Cheng, Z.-Y.; Katiyar, R.; Yao, X.; Bhalla, A., Temperature dependence of the dielectric constant of relaxor ferroelectrics. *Physical Review B* **1998,** *57* (14), 8166.

30. Weyland, F.; Acosta, M.; Vögler, M.; Ehara, Y.; Rödel, J.; Novak, N., Electric field–temperature phase diagram of sodium bismuth titanate-based relaxor ferroelectrics. *Journal of Materials Science* **2018,** *53* (13), 9393-9400.

31. Vlahos, E., *Phase transitions and domain structures in multiferroics*. The Pennsylvania State University: 2011.

32. Lines, M. E.; Glass, A. M., *Principles and applications of ferroelectrics and related materials*. Oxford university press: 2001.

33. Sen Gupta, A., Topochemical Synthesis & Characterization of Octahedral Rotation Induced Noncentrosymmetric Layered Perovskites. **2016**.

34. Bradley, C.; Cracknell, A., *The mathematical theory of symmetry in solids: representation theory for point groups and space groups*. Oxford University Press: 2010.

35. Sundar, V.; Newnham, R., Electrostriction and polarization. *Ferroelectrics* **1992,** *135* (1), 431-446.

36. Wul, B., Dielectric constants of some titanates. *Nature* **1945,** *156* (3964), 480-480.

37. http://hyperphysics.phy-astr.gsu.edu/hbase/electric/dielec.html (accessed October 15, 2022).

38. Pan, M.-J.; Randall, C. A., A brief introduction to ceramic capacitors. *IEEE electrical insulation magazine* **2010,** *26* (3), 44-50.

39. (a) Landau, L. D., Zur Theorie der phasenumwandlungen II. *Phys. Z. Sowjetunion* **1937,** *11* (545), 26-35; (b) Landau, L. D., On the theory of phase transitions. I. *Zh. Eksp. Teor. Fiz.* **1937,** *11*, 19.

40. Uchino, K., *Ferroelectric devices*. CRC press: 2018.

41. Hooker, M. W. *Properties of PZT-based piezoelectric ceramics between-150 and 250 C*; 1998.

42. Jaffe, W., Cook, and H. Jaffe, Piezoelectric Ceramics. Academic Press, New York: 1971.

43. Ballato, A., Piezoelectricity: old effect, new thrusts. *IEEE transactions on ultrasonics, ferroelectrics, and frequency control* **1995,** *42* (5), 916-926.

44. Noheda, B.; Cox, D.; Shirane, G.; Guo, R.; Jones, B.; Cross, L., Stability of the monoclinic phase in the ferroelectric perovskite $PbZr_{1-x}Ti_xO_3$. *Physical Review B* **2000,** *63* (1), 014103.

45. Kutnjak, Z.; Rožič, B.; Pirc, R., Electrocaloric effect: theory, measurements, and applications. *Wiley encyclopedia of electrical and electronics engineering* **1999**, 1-19.

46. Valant, M., Electrocaloric materials for future solid-state refrigeration technologies. *Progress in Materials Science* **2012,** *57* (6), 980-1009.

47. Birol, F., The future of cooling: opportunities for energy-efficient air conditioning. *International Energy Agency* **2018**.

48. Velders, G. J.; Fahey, D. W.; Daniel, J. S.; McFarland, M.; Andersen, S. O., The large contribution of projected HFC emissions to future climate forcing. *Proceedings of the National Academy of Sciences* **2009,** *106* (27), 10949-10954.

49. (a) Russ, B.; Glaudell, A.; Urban, J. J.; Chabinyc, M. L.; Segalman, R. A., Organic thermoelectric materials for energy harvesting and temperature control. *Nature Reviews Materials* **2016,** *1* (10), 1-14; (b) Shimizu, S.; Shiogai, J.; Takemori, N.; Sakai, S.; Ikeda, H.; Arita, R.; Nojima, T.; Tsukazaki, A.; Iwasa, Y., Giant thermoelectric power factor in ultrathin FeSe superconductor. *Nature communications* **2019,** *10* (1), 1-7.

50. (a) Franco, V.; Blázquez, J.; Ipus, J.; Law, J.; Moreno-Ramírez, L.; Conde, A., Magnetocaloric effect: From materials research to refrigeration devices. *Progress in Materials Science* **2018,** *93*, 112-232; (b) Biswas, A.; Pathak, A. K.; Zarkevich, N. A.; Liu, X.; Mudryk, Y.; Balema, V.; Johnson, D. D.; Pecharsky, V. K., Designed materials with the giant magnetocaloric effect near room temperature. *Acta Materialia* **2019,** *180*, 341-348.

51. (a) Rose, M. C.; Cohen, R. E., Giant electrocaloric effect around Tc. *Phys. Rev. Lett.* **2012,** *109* (18), 187604; (b) Qian, X.; Han, D.; Zheng, L.; Chen, J.; Tyagi, M.; Li, Q.; Du, F.; Zheng, S.; Huang, X.; Zhang, S., High-entropy polymer produces a giant electrocaloric effect at low fields. *Nature* **2021,** *600* (7890), 664-669.

52. (a) Liu, K.; Zeng, H.; Qi, J.; Luo, X.; Zhao, X.; Zheng, X.; Yuan, Y.; Chen, C.; Ma, S.; Xie, R., Microstructure and giant baro-caloric effect induced by low pressure in Heusler $Co_{51}Fe_1V_{33}Ga_{15}$ alloy undergoing martensitic transformation. *Journal of Materials Science & Technology* **2021,** *73*, 76-82; (b) Bermúdez-García, J. M.; Sánchez-Andújar, M.; Castro-García, S.; López-Beceiro, J.; Artiaga, R.; Señarís-Rodríguez, M. A., Giant barocaloric effect in the ferroic organic-inorganic hybrid $[TPrA][Mn(dca)_3]$ perovskite under easily accessible pressures. *Nature communications* **2017,** *8* (1), 1-8.

53. (a) Askalany, A. A.; Henninger, S. K.; Ghazy, M.; Saha, B. B., Effect of improving thermal conductivity of the adsorbent on performance of adsorption cooling system. *Applied Thermal Engineering* **2017,** *110*, 695-702; (b) Tu, Y.; Wang, R.; Zhang, Y.; Wang, J., Progress and expectation of atmospheric water harvesting. *Joule* **2018,** *2* (8), 1452-1475.

54. (a) Kim, G.; Park, K.; Hwang, K.; Choi, C.; Zheng, Z.; Seydel, R.; Coza, A.; Jin, S., Black textile with bottom metallized surface having enhanced radiative cooling under solar irradiation. *Nano Energy* **2021,** *82*, 105715; (b) Zhao, B.; Hu, M.; Ao, X.; Pei, G., Performance analysis of enhanced radiative cooling of solar cells based on a commercial silicon photovoltaic module. *Solar Energy* **2018,** *176*, 248-255.

55. Pakhomov, O.; Karmanenko, S.; Semenov, A.; Starkov, A.; Es'kov, A., Thermodynamic estimation of cooling efficiency using an electrocaloric solid-state line. *Technical Physics* **2010,** *55* (8), 1155-1160.

56. Sinyavsky, Y. V.; Lugansky, G.; Pashkov, N., Electrocaloric refrigeration: Investigation of a model and prognosis of mass and efficiency indexes. *Cryogenics* **1992,** *32*, 28-31.

57. Ho, J.; Jow, T. R.; Boggs, S., Historical introduction to capacitor technology. *IEEE Electrical Insulation Magazine* **2010,** *26* (1), 20-25.

58. Suchaneck, G.; Gerlach, G., Electrocaloric cooling based on relaxor ferroelectrics. *Phase Transitions* **2015,** *88* (3), 333-341.

59. Nouchokgwe, Y.; Lheritier, P.; Hong, C.-H.; Torelló, A.; Faye, R.; Jo, W.; Bahl, C. R.; Defay, E., Giant electrocaloric materials energy efficiency in highly ordered lead scandium tantalate. *Nature communications* **2021,** *12* (1), 1-7.

60. Jian, X.-D.; Lu, B.; Li, D.-D.; Yao, Y.-B.; Tao, T.; Liang, B.; Guo, J.-H.; Zeng, Y.-J.; Chen, J.-L.; Lu, S.-G., Direct Measurement of Large Electrocaloric Effect in $Ba(Zr_xTi_{1-x})O_3$ Ceramics. *ACS applied materials & interfaces* **2018,** *10* (5), 4801-4807.

61. Niu, X.; Jian, X.; Chen, X.; Li, H.; Liang, W.; Yao, Y.; Tao, T.; Liang, B.; Lu, S.-G., Enhanced electrocaloric effect at room temperature in Mn^{2+} doped lead-free $(BaSr)TiO_3$ ceramics via a direct measurement. *Journal of Advanced Ceramics* **2021,** *10* (3), 482-492.

62. Sanlialp, M.; Luo, Z.; Shvartsman, V. V.; Wei, X.; Liu, Y.; Dkhil, B.; Lupascu, D. C., Direct measurement of electrocaloric effect in lead-free $Ba(Sn_xTi_{1-x})O_3$ ceramics. *Applied Physics Letters* **2017,** *111* (17), 173903.

63. Smolenskii, G. A. e., Physical phenomena in ferroelectrics with diffused phase transition. *J. Phys. Soc. Jpn* **1970,** *28* (1), 26-37.

64. Qian, X. S.; Ye, H. J.; Zhang, Y. T.; Gu, H.; Li, X.; Randall, C.; Zhang, Q., Giant electrocaloric response over a broad temperature range in modified $BaTiO_3$ ceramics. *Advanced Functional Materials* **2014,** *24* (9), 1300-1305.

65. Li, J.; Zhang, D.; Qin, S.; Li, T.; Wu, M.; Wang, D.; Bai, Y.; Lou, X., Large room-temperature electrocaloric effect in lead-free $BaHf_xTi_{1-x}O_3$ ceramics under low electric field. *Acta Materialia* **2016,** *115*, 58-67.

66. Sanlialp, M.; Shvartsman, V. V.; Acosta, M.; Lupascu, D. C., Electrocaloric effect in $Ba(Zr,Ti)O_3$–$(Ba,Ca)TiO_3$ ceramics measured directly. *J. Am. Ceram. Soc.* **2016,** *99* (12), 4022-4030.

67. Koruza, J.; Rožič, B.; Cordoyiannis, G.; Malič, B.; Kutnjak, Z., Large electrocaloric effect in lead-free $K_{0.5}Na_{0.5}NbO_3$-$SrTiO_3$ ceramics. *Applied Physics Letters* **2015,** *106* (20), 202905.

68. Peräntie, J.; Tailor, H.; Hagberg, J.; Jantunen, H.; Ye, Z.-G., Electrocaloric properties in relaxor ferroelectric $(1-x)Pb(Mg_{1/3}Nb_{2/3})O_3$–$xPbTiO_3$ system. *Journal of Applied Physics* **2013,** *114* (17), 174105.

69. Roberts, S., Adiabatic study of the 128 °C transition in barium titanate. *Physical Review* **1952,** *85* (5), 925.

70. Wang, S.-B.; Dai, G.-Z.; Yao, Y.-B.; Zhao, X.-B.; Tao, T.; Liang, B.; Lu, S.-G., Direct and indirect measurement of large electrocaloric effect in B_2O_3-ZnO glass modified $Ba_{0.65}Sr_{0.35}TiO_3$ bulk ceramics. *Scripta Materialia* **2021,** *193*, 59-63.

71. Mischenko, A.; Zhang, Q.; Scott, J.; Whatmore, R.; Mathur, N., Giant electrocaloric effect in thin-film $PbZr_{0.95}Ti_{0.05}O_3$. *Science* **2006,** *311* (5765), 1270-1271.

72. Lu, S.; Rožič, B.; Zhang, Q.; Kutnjak, Z.; Li, X.; Furman, E.; Gorny, L. J.; Lin, M.; Malič, B.; Kosec, M., Organic and inorganic relaxor ferroelectrics with giant electrocaloric effect. *Applied Physics Letters* **2010,** *97* (16), 162904.

73. Tong, T.; Karthik, J.; Mangalam, R.; Martin, L. W.; Cahill, D. G., Reduction of the electrocaloric entropy change of ferroelectric $PbZr_{1-x}Ti_xO_3$ epitaxial layers due to an elastocaloric effect. *Physical Review B* **2014,** *90* (9), 094116.

74. Ye, H.-J.; Qian, X.-S.; Jeong, D.-Y.; Zhang, S.; Zhou, Y.; Shao, W.-Z.; Zhen, L.; Zhang, Q., Giant electrocaloric effect in BaZr0. 2Ti0. 8O3 thick film. *Applied Physics Letters* **2014,** *105* (15), 152908.

75. Crossley, S.; Usui, T.; Nair, B.; Kar-Narayan, S.; Moya, X.; Hirose, S.; Ando, A.; Mathur, N., Direct electrocaloric measurement of $0.9Pb(Mg_{1/3}Nb_{2/3})O_3$-$0.1PbTiO_3$ films using scanning thermal microscopy. *Applied Physics Letters* **2016,** *108* (3), 032902.

76. Lawless, W.; Clark, C., Dielectric and electrothermal measurements on $(Cd_{0.83}Pb_{0.17})_2Nb_2O_7$ at liquid-nitrogen temperatures. *Physical Review B* **1987,** *36* (1), 459.

77. Shebanovs, L.; Borman, K.; Lawless, W.; Kalvane, A., Electrocaloric effect in some perovskite ferroelectric ceramics and multilayer capacitors. *Ferroelectrics* **2002,** *273* (1), 137-142.

78. Kar-Narayan, S.; Mathur, N., Direct and indirect electrocaloric measurements using multilayer capacitors. *Journal of Physics D: Applied Physics* **2010,** *43* (3), 032002.

79. Bai, Y.; Zheng, G.-P.; Shi, S.-Q., Kinetic electrocaloric effect and giant net cooling of lead-free ferroelectric refrigerants. *Journal of applied physics* **2010,** *108* (10), 104102.

80. Bai, Y.; Zheng, G.-P.; Ding, K.; Qiao, L.; Shi, S.-Q.; Guo, D., The giant electrocaloric effect and high effective cooling power near room temperature for BaTiO3 thick film. *Journal of applied physics* **2011,** *110* (9), 094103.

81. Torelló, A.; Lheritier, P.; Usui, T.; Nouchokgwe, Y.; Gérard, M.; Bouton, O.; Hirose, S.; Defay, E., Giant temperature span in electrocaloric regenerator. *Science* **2020,** *370* (6512), 125-129.

82. Li, X.; Qian, X.-s.; Lu, S.; Cheng, J.; Fang, Z.; Zhang, Q., Tunable temperature dependence of electrocaloric effect in ferroelectric relaxor poly (vinylidene fluoride-trifluoroethylene-chlorofluoroethylene terpolymer. *Applied Physics Letters* **2011,** *99* (5), 052907.

83. Sebald, G.; Seveyrat, L.; Capsal, J.-F.; Cottinet, P.-J.; Guyomar, D., Differential scanning calorimeter and infrared imaging for electrocaloric characterization of poly (vinylidene fluoride-trifluoroethylene-chlorofluoroethylene) terpolymer. *Applied Physics Letters* **2012,** *101* (2), 022907.

84. Guo, D.; Gao, J.; Yu, Y.-J.; Santhanam, S.; Fedder, G. K.; McGaughey, A. J.; Yao, S., Electrocaloric characterization of a poly (vinylidene fluoride-trifluoroethylene-chlorofluoroethylene) terpolymer by infrared imaging. *Applied Physics Letters* **2014,** *105* (3), 031906.

85. Zhang, G.; Li, Q.; Gu, H.; Jiang, S.; Han, K.; Gadinski, M. R.; Haque, M. A.; Zhang, Q.; Wang, Q., Ferroelectric polymer nanocomposites for room-temperature electrocaloric refrigeration. *Advanced materials* **2015,** *27* (8), 1450-1454.

86. Jiang, Z.; Zheng, X.; Zheng, G., The enhanced electrocaloric effect in P(VDF-TrFE) copolymer with barium strontium titanate nano-fillers synthesized via an effective hydrothermal method. *RSC advances* **2015,** *5* (76), 61946-61954.

87. Li, Q.; Zhang, G.; Zhang, X.; Jiang, S.; Zeng, Y.; Wang, Q., Relaxor ferroelectric-based electrocaloric polymer nanocomposites with a broad operating temperature range and high cooling energy. *Advanced Materials* **2015,** *27* (13), 2236-2241.

88. Yang, L.; Qian, X.; Koo, C.; Hou, Y.; Zhang, T.; Zhou, Y.; Lin, M.; Qiu, J.-H.; Zhang, Q., Graphene enabled percolative nanocomposites with large electrocaloric efficient under low electric fields over a broad temperature range. *Nano Energy* **2016,** *22*, 461-467.

89. Wang, Y.; Zhang, Z.; Usui, T.; Benedict, M.; Hirose, S.; Lee, J.; Kalb, J.; Schwartz, D., A high-performance solid-state electrocaloric cooling system. *Science* **2020,** *370* (6512), 129-133.

90. (a) McColm, I., Special ceramics for modern applications: which? why? how? In *Ceramic Processing*, Springer: 1995; pp 1-33; (b) Yeong, W.; Yap, C.; Mapar, M.; Chua, C., State-of-the-art review on selective laser melting of ceramics. *High value manufacturing: advanced research in virtual and rapid prototyping* **2013,** *1*, 65-70.

91. Suvaci, E.; Messing, G. L., Critical factors in the templated grain growth of textured reaction-bonded alumina. *J. Am. Ceram. Soc.* **2000,** *83* (8), 2041-2048.

92. Ünal, M. A. BaTiO3 VE $(K,Na)_{0.5}Bi_{0.5}TiO_3$ kurşunsuz ferroelektrik seramiklerde kristalografik yönlenmenin elektrokalorik özelliğe etkisinin incelenmesi. Eskişehir Teknik Üniversitesi, 2022.

93. Venet, M.; Santos, I.; Eiras, J.; Garcia, D., Potentiality of SBN textured ceramics for pyroelectric applications. *Solid State Ionics* **2006,** *177* (5-6), 589-593.

94. Goel, H.; Saini, K.; Razdan, K.; Khurana, R. K.; Elkordy, A. A.; Singh, K. K., In vitro physicochemical characterization of nanocarriers: a road to optimization. In *Nanoparticle Therapeutics*, Elsevier: 2022; pp 133-179.

95. Ginell, K. M.; Horn, C.; Von Dreele, R. B.; Toby, B. H., Materials for learning use of GSAS-II. *Powder Diffraction* **2019,** *34* (2), 184-188.

96. Evans, J. S.; Evans, I. R., Structure analysis from powder diffraction data: Rietveld refinement in excel. *J. Chem. Educ.* **2020,** *98* (2), 495-505.

97. https://web.stanford.edu/group/glam/xlab/MatSci162_172/LectureNotes/04_Powder%20Diffraction,%20Powder%20Method.pdf (accessed 11.11.2022).

98. Geels, K.; Fowler, D. B.; Kopp, W.-U.; ckert, M. R., *Metallographic and materialographic specimen preparation, light microscopy, image analysis, and hardness testing*. ASTM international West Conshohocken: 2007; Vol. 46.

99. Ramo, S.; Whinnery, J. R.; Van Duzer, T., *Fields and waves in communication electronics*. John Wiley & Sons: 1994.

100. Chen, L.-F.; Ong, C. K.; Neo, C.; Varadan, V. V.; Varadan, V. K., *Microwave electronics: measurement and materials characterization*. John Wiley & Sons: 2004.

101. Pan, W.; Cross, L., A sensitive double beam laser interferometer for studying high-frequency piezoelectric and electrostrictive strains. *Rev. Sci. Instrum.* **1989,** *60* (8), 2701-2705.

102. Eichel, R. A., Characterization of defect structure in acceptor-modified piezoelectric ceramics by multifrequency and multipulse electron paramagnetic resonance spectroscopy. *Journal of the American Ceramic Society* **2008,** *91* (3), 691-701.

103. (a) Barber, P.; Balasubramanian, S.; Anguchamy, Y.; Gong, S.; Wibowo, A.; Gao, H.; Ploehn, H.; Zur Loye, H.-C., Polymer composite and nanocomposite dielectric materials for pulse power energy storage. *Materials* **2009,** *2* (4), 1697-1733; (b) Domonkos, M. T.; Heidger, S.; Brown, D.; Parker, J. V.; Gregg, C. W.; Slenes, K.; Hackenberger, W.; Kwon, S.; Loree, E.; Tran, T., Submicrosecond pulsed power capacitors based on novel ceramic technologies. *IEEE Transactions on Plasma Science* **2010,** *38* (10), 2686-2693; (c) Puli, V. S.; Pradhan, D. K.; Chrisey, D. B.; Tomozawa, M.; Sharma, G.; Scott, J.; Katiyar, R. S., Structure, dielectric, ferroelectric, and energy density properties of (1−x)BZT–xBCT ceramic capacitors for energy storage applications. *Journal of Materials Science* **2013,** *48* (5), 2151-2157.

104. Yang, L.; Kong, X.; Li, F.; Hao, H.; Cheng, Z.; Liu, H.; Li, J.-F.; Zhang, S., Perovskite lead-free dielectrics for energy storage applications. *Progress in Materials Science* **2019,** *102*, 72-108.

105. Zhang, H.; Wei, T.; Zhang, Q.; Ma, W.; Fan, P.; Salamon, D.; Zhang, S.-T.; Nan, B.; Tan, H.; Ye, Z.-G., A review on the development of lead-free ferroelectric energy-storage ceramics and multilayer capacitors. *Journal of Materials Chemistry C* **2020,** *8* (47), 16648-16667.

106. Hao, X., A review on the dielectric materials for high energy-storage application. *Journal of Advanced Dielectrics* **2013,** *3* (01), 1330001.

107. Wang, Z.; Cao, M.; Yao, Z.; Song, Z.; Li, G.; Hu, W.; Hao, H.; Liu, H., Dielectric relaxation behavior and energy storage properties in $SrTiO_3$ ceramics with trace amounts of ZrO_2 additives. *Ceramics International* **2014,** *40* (9), 14127-14132.

108. Zhao, L.; Liu, Q.; Gao, J.; Zhang, S.; Li, J. F., Lead-free antiferroelectric silver niobate tantalate with high energy storage performance. *Advanced Materials* **2017,** *29* (31), 1701824.

109. (a) Yao, Z.; Song, Z.; Hao, H.; Yu, Z.; Cao, M.; Zhang, S.; Lanagan, M. T.; Liu, H., Homogeneous/inhomogeneous-structured dielectrics and their energy-storage performances. *Advanced Materials* **2017,** *29* (20), 1601727; (b) Viola, G.; Tian, Y.; Yu, C.; Tan, Y.; Koval, V.; Wei, X.; Choy, K.-L.; Yan, H., Electric field-induced transformations in bismuth sodium titanate-based materials. *Progress in Materials Science* **2021,** *122*, 100837.

110. Zhu, L., Exploring strategies for high dielectric constant and low loss polymer dielectrics. *The journal of physical chemistry letters* **2014,** *5* (21), 3677-3687.

111. Chao, W.; Yang, T.; Li, Y., Achieving high energy efficiency and energy density in $PbHfO_3$-based antiferroelectric ceramics. *Journal of Materials Chemistry C* **2020,** *8* (47), 17016-17024.

112. Ma, B.; Kwon, D.-K.; Narayanan, M.; Balachandran, U. B., Dielectric properties and energy storage capability of antiferroelectric $Pb_{0.92}La_{0.08}Zr_{0.95}Ti_{0.05}O_3$ film-on-foil capacitors. *Journal of Materials Research* **2009,** *24* (9), 2993-2996.

113. Luo, N.; Han, K.; Zhuo, F.; Xu, C.; Zhang, G.; Liu, L.; Chen, X.; Hu, C.; Zhou, H.; Wei, Y., Aliovalent A-site engineered $AgNbO_3$ lead-free antiferroelectric ceramics toward superior energy storage density. *Journal of Materials Chemistry A* **2019,** *7* (23), 14118-14128.

114. Si, F.; Tang, B.; Fang, Z.; Li, H.; Zhang, S., Enhanced energy storage and fast charge-discharge properties of $(1\text{-}x)BaTiO_3\text{-}xBi(Ni_{1/2}Sn_{1/2})O_3$ relaxor ferroelectric ceramics. *Ceramics International* **2019,** *45* (14), 17580-17590.

115. (a) Chen, M.; Xu, Q.; Kim, B. H.; Ahn, B. K.; Ko, J. H.; Kang, W. J.; Nam, O. J., Structure and electrical properties of $(Na_{0.5}Bi_{0.5})_{1-x}Ba_xTiO_3$ piezoelectric ceramics. *Journal of the European Ceramic Society* **2008,** *28* (4), 843-849; (b) Takenaka, T.; Maruyama, K.-i.; Sakata, K., $(Bi_{1/2}Na_{1/2})$ TiO_3-$BaTiO_3$ system for lead-free piezoelectric ceramics. *Jpn. J. Appl. Phys.* **1991,** *30* (9S), 2236.

116. Zhang, Q.; Zhang, Y.; Wang, F.; Wang, Y.; Lin, D.; Zhao, X.; Luo, H.; Ge, W.; Viehland, D., Enhanced piezoelectric and ferroelectric properties in Mn-doped $Na_{0.5}Bi_{0.5}TiO_3$–$BaTiO_3$ single crystals. *Applied Physics Letters* **2009,** *95* (10), 102904.

117. Zhang, Y. R.; Li, J. F.; Zhang, B. P., Enhancing Electrical Properties in NBT–KBT Lead-Free Piezoelectric Ceramics by Optimizing Sintering Temperature. *J. Am. Ceram. Soc.* **2008,** *91* (8), 2716-2719.

118. Seifert, K. T.; Jo, W.; Rödel, J., Temperature-insensitive large strain of $(Bi_{1/2}Na_{1/2})TiO_3$–$(Bi_{1/2}K_{1/2})TiO_3$–$(K_{0.5}Na_{0.5})$ NbO_3 lead-free piezoceramics. *J. Am. Ceram. Soc.* **2010,** *93* (5), 1392-1396.

119. Hiruma, Y.; Imai, Y.; Watanabe, Y.; Nagata, H.; Takenaka, T., Large electrostrain near the phase transition temperature of $(Bi_{0.5}Na_{0.5})TiO_3$–$SrTiO_3$ ferroelectric ceramics. *Applied Physics Letters* **2008,** *92* (26), 262904.

120. Han, K.; Luo, N.; Mao, S.; Zhuo, F.; Chen, X.; Liu, L.; Hu, C.; Zhou, H.; Wang, X.; Wei, Y., Realizing high low-electric-field energy storage performance in $AgNbO_3$ ceramics by introducing relaxor behaviour. *Journal of Materiomics* **2019,** *5* (4), 597-605.

121. Zhao, L.; Liu, Q.; Zhang, S.; Li, J.-F., Lead-free $AgNbO_3$ anti-ferroelectric ceramics with an enhanced energy storage performance using MnO_2 modification. *Journal of Materials Chemistry C* **2016,** *4* (36), 8380-8384.

122. Zhao, L.; Gao, J.; Liu, Q.; Zhang, S.; Li, J.-F., Silver niobate lead-free antiferroelectric ceramics: enhancing energy storage density by B-site doping. *ACS applied materials & interfaces* **2018,** *10* (1), 819-826.

123. Tian, Y.; Jin, L.; Zhang, H.; Xu, Z.; Wei, X.; Politova, E.; Stefanovich, S. Y.; Tarakina, N. V.; Abrahams, I.; Yan, H., High energy density in silver niobate ceramics. *Journal of Materials Chemistry A* **2016,** *4* (44), 17279-17287.

124. Tian, Y.; Jin, L.; Zhang, H.; Xu, Z.; Wei, X.; Viola, G.; Abrahams, I.; Yan, H., Phase transitions in bismuth-modified silver niobate ceramics for high power energy storage. *Journal of Materials Chemistry A* **2017,** *5* (33), 17525-17531.

125. Xu, C.; Fu, Z.; Liu, Z.; Wang, L.; Yan, S.; Chen, X.; Cao, F.; Dong, X.; Wang, G., La/Mn codoped AgNbO3 lead-free antiferroelectric ceramics with large energy density and power density. *ACS Sustainable Chemistry & Engineering* **2018,** *6* (12), 16151-16159.

126. Gao, J.; Zhang, Y.; Zhao, L.; Lee, K.-Y.; Liu, Q.; Studer, A.; Hinterstein, M.; Zhang, S.; Li, J.-F., Enhanced antiferroelectric phase stability in La-doped $AgNbO_3$: perspectives from the microstructure to energy storage properties. *Journal of Materials Chemistry A* **2019,** *7* (5), 2225-2232.

127. Li, S.; Nie, H.; Wang, G.; Xu, C.; Liu, N.; Zhou, M.; Cao, F.; Dong, X., Significantly enhanced energy storage performance of rare-earth-modified silver niobate lead-free antiferroelectric ceramics via local chemical pressure tailoring. *Journal of Materials Chemistry C* **2019,** *7* (6), 1551-1560.

128. Yan, Z.; Zhang, D.; Zhou, X.; Qi, H.; Luo, H.; Zhou, K.; Abrahams, I.; Yan, H., Silver niobate based lead-free ceramics with high energy storage density. *Journal of Materials Chemistry A* **2019,** *7* (17), 10702-10711.

129. Han, K.; Luo, N.; Mao, S.; Zhuo, F.; Liu, L.; Peng, B.; Chen, X.; Hu, C.; Zhou, H.; Wei, Y., Ultrahigh energy-storage density in A-/B-site co-doped $AgNbO_3$ lead-free antiferroelectric ceramics: insight into the origin of antiferroelectricity. *Journal of Materials Chemistry A* **2019,** *7* (46), 26293-26301.

130. Li, W.-B.; Zhou, D.; Pang, L.-X., Enhanced energy storage density by inducing defect dipoles in lead free relaxor ferroelectric BaTiO3-based ceramics. *Applied Physics Letters* **2017,** *110* (13), 132902.

131. Wang, T.; Jin, L.; Li, C.; Hu, Q.; Wei, X., Relaxor ferroelectric $BaTiO_3$–$Bi(Mg_{2/3}Nb_{1/3})O_3$ ceramics for energy storage application. *J. Am. Ceram. Soc.* **2015,** *98* (2), 559-566.

132. Hu, Q.; Jin, L.; Wang, T.; Li, C.; Xing, Z.; Wei, X., Dielectric and temperature stable energy storage properties of $0.88BaTiO_3$–$0.12Bi(Mg_{1/2}Ti_{1/2})O_3$ bulk ceramics. *Journal of Alloys and Compounds* **2015,** *640*, 416-420.

133. Shen, Z.; Wang, X.; Luo, B.; Li, L., $BaTiO_3$–$BiYbO_3$ perovskite materials for energy storage applications. *Journal of Materials Chemistry A* **2015,** *3* (35), 18146-18153.

134. Li, F.; Zhou, M.; Zhai, J.; Shen, B.; Zeng, H., Novel barium titanate based ferroelectric relaxor ceramics with superior charge-discharge performance. *Journal of the European Ceramic Society* **2018,** *38* (14), 4646-4652.

135. Liu, B.; Wang, X.; Zhang, R.; Li, L., Grain size effect and microstructure influence on the energy storage properties of fine-grained $BaTiO_3$-based ceramics. *J. Am. Ceram. Soc.* **2017,** *100* (8), 3599-3607.

136. Wu, L.; Wang, X.; Gong, H.; Hao, Y.; Shen, Z.; Li, L., Core-satellite $BaTiO_3$@ $SrTiO_3$ assemblies for a local compositionally graded relaxor ferroelectric capacitor with enhanced energy storage density and high energy efficiency. *Journal of Materials Chemistry C* **2015,** *3* (4), 750-758.

137. Ma, J.-P.; Chen, X.-M.; Ouyang, W.-Q.; Wang, J.; Li, H.; Fang, J.-L., Microstructure, dielectric, and energy storage properties of $BaTiO_3$ ceramics prepared via cold sintering. *Ceramics International* **2018,** *44* (4), 4436-4441.

138. Liu, G.; Zhang, L.; Wu, Q.; Wang, Z.; Li, Y.; Li, D.; Liu, H.; Yan, Y., Enhanced energy storage properties in MgO-doped $BaTiO_3$ lead-free ferroelectric ceramics. *Journal of Materials Science: Materials in Electronics* **2018,** *29* (21), 18859-18867.

139. Ma, R.; Cui, B.; Shangguan, M.; Wang, S.; Wang, Y.; Chang, Z.; Wang, Y., A novel double-coating approach to prepare fine-grained $BaTiO_3$@ La_2O_3@ SiO_2 dielectric ceramics for energy storage application. *Journal of Alloys and Compounds* **2017,** *690*, 438-445.

140. Puli, V. S.; Pradhan, D. K.; Riggs, B. C.; Chrisey, D. B.; Katiyar, R. S., Investigations on structure, ferroelectric, piezoelectric and energy storage properties of barium calcium titanate (BCT) ceramics. *Journal of alloys and compounds* **2014,** *584*, 369-373.

141. Hu, Q.; Wang, T.; Zhao, L.; Jin, L.; Xu, Z.; Wei, X., Dielectric and energy storage properties of $BaTiO_3$–$Bi(Mg1_{/2}Ti_{1/2})O_3$ ceramic: influence of glass addition and biasing electric field. *Ceramics International* **2017,** *43* (1), 35-39.

142. Huang, J.; Zhang, J.; Yu, H.; Wei, M.; Chen, H.; Yang, C., Improvement of dielectric and energy storage properties in BaTiO3 ceramics with BiNbO4 modified. *Ferroelectrics* **2017,** *510* (1), 8-15.

143. Zhao, X.; Zhou, Z.; Liang, R.; Liu, F.; Dong, X., High-energy storage performance in lead-free $(1\text{-}x)BaTiO_3\text{-}xBi(Zn_{0.5}Ti_{0.5})O_3$ relaxor ceramics for temperature stability applications. *Ceramics International* **2017,** *43* (12), 9060-9066.

144. Yuan, Q.; Li, G.; Yao, F.-Z.; Cheng, S.-D.; Wang, Y.; Ma, R.; Mi, S.-B.; Gu, M.; Wang, K.; Li, J.-F., Simultaneously achieved temperature-insensitive high energy density and efficiency in domain engineered $BaTiO_3\text{-}Bi(Mg_{0.5}Zr_{0.5})O_3$ lead-free relaxor ferroelectrics. *Nano Energy* **2018,** *52*, 203-210.

145. Liu, G.; Li, Y.; Shi, M.; Yu, L.; Chen, P.; Yu, K.; Yan, Y.; Jin, L.; Wang, D.; Gao, J., An investigation of the dielectric energy storage performance of $Bi(Mg_{2/3}Nb_{1/3})O_3$-modifed $BaTiO_3$ Pb-free bulk ceramics with improved temperature/frequency stability. *Ceramics International* **2019,** *45* (15), 19189-19196.

146. Si, F.; Tang, B.; Fang, Z.; Zhang, S., Structural and dielectric relaxor properties of $(1-x)BaTiO_3$–$xBi(Zn_{1/2}Zr_{1/2})O_3$ ceramics for energy storage applications. *Journal of Materials Science: Materials in Electronics* **2019,** *30* (3), 2772-2782.

147. Shao, T.; Du, H.; Ma, H.; Qu, S.; Wang, J.; Wang, J.; Wei, X.; Xu, Z., Potassium–sodium niobate based lead-free ceramics: novel electrical energy storage materials. *Journal of Materials Chemistry A* **2017,** *5* (2), 554-563.

148. Yang, Z.; Du, H.; Qu, S.; Hou, Y.; Ma, H.; Wang, J.; Wang, J.; Wei, X.; Xu, Z., Significantly enhanced recoverable energy storage density in potassium–sodium niobate-based lead free ceramics. *Journal of Materials Chemistry A* **2016,** *4* (36), 13778-13785.

149. Qu, N.; Du, H.; Hao, X., A new strategy to realize high comprehensive energy storage properties in lead-free bulk ceramics. *Journal of Materials Chemistry C* **2019,** *7* (26), 7993-8002.

150. Ye, J.; Wang, G.; Zhou, M.; Liu, N.; Chen, X.; Li, S.; Cao, F.; Dong, X., Excellent comprehensive energy storage properties of novel lead-free $NaNbO_3$-based ceramics for dielectric capacitor applications. *Journal of Materials Chemistry C* **2019,** *7* (19), 5639-5645.

151. Zhou, M.; Liang, R.; Zhou, Z.; Yan, S.; Dong, X., Novel sodium niobate-based lead-free ceramics as new environment-friendly energy storage materials with high energy density, high power density, and excellent stability. *ACS Sustainable Chemistry & Engineering* **2018,** *6* (10), 12755-12765.

152. Yang, Z.; Du, H.; Jin, L.; Hu, Q.; Wang, H.; Li, Y.; Wang, J.; Gao, F.; Qu, S., Realizing high comprehensive energy storage performance in lead-free bulk ceramics via designing an unmatched temperature range. *Journal of Materials Chemistry A* **2019,** *7* (48), 27256-27266.

153. Zhou, M.; Liang, R.; Zhou, Z.; Dong, X., Superior energy storage properties and excellent stability of novel $NaNbO_3$-based lead-free ceramics with A-site vacancy obtained via a Bi_2O_3 substitution strategy. *Journal of Materials Chemistry A* **2018,** *6* (37), 17896-17904.

154. Wang, B.; Luo, L.; Jiang, X.; Li, W.; Chen, H., Energy-storage properties of (1−x) $Bi_{0.47}Na_{0.47}Ba_{0.06}TiO_3$–$xKNbO_3$ lead-free ceramics. *Journal of alloys and compounds* **2014,** *585*, 14-18.

155. Li, Q.; Yao, Z.; Ning, L.; Gao, S.; Hu, B.; Dong, G.; Fan, H., Enhanced energy-storage properties of $(1-x)(0.7Bi_{0.5}Na_{0.5}TiO_3-0.3Bi_{0.2}Sr_{0.7}TiO_3)-xNaNbO_3$ lead-free ceramics. *Ceramics International* **2018,** *44* (3), 2782-2788.

156. Gao, F.; Dong, X.; Mao, C.; Liu, W.; Zhang, H.; Yang, L.; Cao, F.; Wang, G., Energy-storage properties of $0.89Bi_{0.5}Na_{0.5}TiO_3–0.06BaTiO_3–0.05K_{0.5}Na_{0.5}NbO_3$ lead-free anti-ferroelectric ceramics. *J. Am. Ceram. Soc.* **2011,** *94* (12), 4382-4386.

157. Liu, G.; Fan, H.; Dong, G.; Shi, J.; Chang, Q., Enhanced energy storage and dielectric properties of $Bi_{0.487}Na_{0.427}K_{0.06}Ba_{0.026}TiO_3$-$xCeO_2$ anti-ferroelectric ceramics. *Journal of Alloys and Compounds* **2016,** *664*, 632-638.

158. Xu, Q.; Li, T.; Hao, H.; Zhang, S.; Wang, Z.; Cao, M.; Yao, Z.; Liu, H., Enhanced energy storage properties of $NaNbO_3$ modified $Bi_{0.5}Na_{0.5}TiO_3$ based ceramics. *Journal of the European Ceramic Society* **2015,** *35* (2), 545-553.

159. Liu, Z.; Ren, P.; Long, C.; Wang, X.; Wan, Y.; Zhao, G., Enhanced energy storage properties of $NaNbO_3$ and $SrZrO_3$ modified $Bi_{0.5}Na_{0.5}TiO_3$ based ceramics. *Journal of Alloys and Compounds* **2017,** *721*, 538-544.

160. Li, Q.; Wang, J.; Ma, Y.; Ma, L.; Dong, G.; Fan, H., Enhanced energy-storage performance and dielectric characterization of $0.94Bi_{0.5}Na_{0.5}TiO_3–0.06\ BaTiO_3$ modified by $CaZrO_3$. *Journal of Alloys and Compounds* **2016,** *663*, 701-707.

161. Yao, M.; Pu, Y.; Zhang, L.; Chen, M., Enhanced energy storage properties of $(1-x)\ Bi_{0.5}Na_{0.5}TiO_3$-$xBa_{0.85}Ca_{0.15}Ti_{0.9}Zr_{0.1}O_3$ ceramics. *Materials Letters* **2016,** *174*, 110-113.

162. Xu, Q.; Lanagan, M. T.; Huang, X.; Xie, J.; Zhang, L.; Hao, H.; Liu, H., Dielectric behavior and impedance spectroscopy in lead-free BNT–BT–NBN perovskite ceramics for energy storage. *Ceramics International* **2016,** *42* (8), 9728-9736.

163. Ma, W.; Zhu, Y.; Marwat, M. A.; Fan, P.; Xie, B.; Salamon, D.; Ye, Z.-G.; Zhang, H., Enhanced energy-storage performance with excellent stability under low electric fields in BNT–ST relaxor ferroelectric ceramics. *Journal of Materials Chemistry C* **2019,** *7* (2), 281-288.

164. Xu, N.; Liu, Y.; Yu, Z.; Yao, R.; Ye, J.; Lu, Y., Enhanced energy storage properties of lead-free $(1-x)Bi_{0.5}Na_{0.5}TiO_3–xSrTiO_3$ antiferroelectric ceramics by two-step sintering method. *Journal of Materials Science: Materials in Electronics* **2016,** *27* (12), 12479-12484.

165. Tong, X.-Y.; Song, M.-W.; Zhou, J.-J.; Wang, K.; Guan, C.-L.; Liu, H.; Fang, J.-Z., Enhanced energy storage properties in Nb-modified $Bi_{0.5}Na_{0.5}TiO_3$–$SrTiO_3$ lead-free electroceramics. *Journal of Materials Science: Materials in Electronics* **2019,** *30* (6), 5780-5790.

166. Huang, N.; Liu, H.; Hao, H.; Yao, Z.; Cao, M.; Xie, J., Energy storage properties of MgO-doped $0.5Bi_{0.5}Na_{0.5}TiO_3$-$0.5SrTiO_3$ ceramics. *Ceramics International* **2019,** *45* (12), 14921-14927.

167. Shi, P.; Zhu, L.; Gao, W.; Yu, Z.; Lou, X.; Wang, X.; Yang, Z.; Yang, S., Large energy storage properties of lead-free $(1-x)(0.72Bi_{0.5}Na_{0.5}TiO_3$-$0.28SrTiO_3)$-$xBiAlO_3$ ceramics at broad temperature range. *Journal of Alloys and Compounds* **2019,** *784*, 788-793.

168. Qiao, X.; Wu, D.; Zhang, F.; Niu, M.; Chen, B.; Zhao, X.; Liang, P.; Wei, L.; Chao, X.; Yang, Z., Enhanced energy density and thermal stability in relaxor ferroelectric $Bi_{0.5}Na_{0.5}TiO_3$-$Sr_{0.7}Bi_{0.2}TiO_3$ ceramics. *Journal of the European Ceramic Society* **2019,** *39* (15), 4778-4784.

169. Li, Q.-N.; Zhou, C.-R.; Xu, J.-W.; Yang, L.; Zhang, X.; Zeng, W.-D.; Yuan, C.-L.; Chen, G.-H.; Rao, G.-H., Ergodic relaxor state with high energy storage performance induced by doping $Sr_{0.85}Bi_{0.1}TiO_3$ in $Bi_{0.5}Na_{0.5}TiO_3$ ceramics. *Journal of Electronic Materials* **2016,** *45* (10), 5146-5151.

170. Huang, B.; Lu, Z.; Zhang, Y.; Xie, Y.; Zeng, M.; Yan, Z.; Liu, J.-M., Antiferroelectric polarization switching and dynamic scaling of energy storage: A Monte Carlo simulation. *Journal of Applied Physics* **2016,** *119* (17), 174103.

171. Liu, Z.; Lu, T.; Ye, J.; Wang, G.; Dong, X.; Withers, R.; Liu, Y., Antiferroelectrics for energy storage applications: a review. *Advanced Materials Technologies* **2018,** *3* (9), 1800111.

172. Tan, X.; Ma, C.; Frederick, J.; Beckman, S.; Webber, K. G., The antiferroelectric↔ ferroelectric phase transition in lead-containing and lead-free perovskite ceramics. *J. Am. Ceram. Soc.* **2011,** *94* (12), 4091-4107.

173. Karakaya, M.; Adem, U., Enhanced room temperature energy storage density of $Bi(Li_{1/3}Ti_{2/3})O_3$ substituted $Bi_{0.5}Na_{0.5}TiO_3$–$BaTiO_3$ ceramics. *Journal of Physics D: Applied Physics* **2021,** *54* (27), 275501.

174. Rödel, J.; Jo, W.; Seifert, K. T.; Anton, E. M.; Granzow, T.; Damjanovic, D., Perspective on the development of lead-free piezoceramics. *J. Am. Ceram. Soc.* **2009,** *92* (6), 1153-1177.

175. Jo, W.; Daniels, J. E.; Jones, J. L.; Tan, X.; Thomas, P. A.; Damjanovic, D.; Rödel, J., Evolving morphotropic phase boundary in lead-free $(Bi_{1/2}Na_{1/2})TiO_3$–$BaTiO_3$ piezoceramics. *Journal of applied physics* **2011,** *109* (1), 014110.

176. (a) Borkar, H.; Singh, V.; Singh, B.; Tomar, M.; Gupta, V.; Kumar, A., Room temperature lead-free relaxor–antiferroelectric electroceramics for energy storage applications. *RSC Advances* **2014,** *4* (44), 22840-22847; (b) Chen, P.; Chu, B., Improvement of dielectric and energy storage properties in $Bi(Mg_{1/2}Ti_{1/2})O_3$-modified $(Na_{1/2}Bi_{1/2})_{0.92}Ba_{0.08}TiO_3$ ceramics. *Journal of the European Ceramic Society* **2016,** *36* (1), 81-88; (c) Xu, Q.; Liu, H.; Zhang, L.; Xie, J.; Hao, H.; Cao, M.; Yao, Z.; Lanagan, M. T., Structure and electrical properties of lead-free $Bi_{0.5}Na_{0.5}TiO_3$-based ceramics for energy-storage applications. *Rsc Advances* **2016,** *6* (64), 59280-59291.

177. Jo, W.; Schaab, S.; Sapper, E.; Schmitt, L. A.; Kleebe, H.-J.; Bell, A. J.; Rödel, J., On the phase identity and its thermal evolution of lead free $(Bi_{1/2}Na_{1/2})TiO_3$-6 mol% $BaTiO_3$. *Journal of Applied Physics* **2011,** *110* (7), 074106.

178. Ma, C.; Tan, X., Phase diagram of unpoled lead-free $(1-x)(Bi_{1/2}Na_{1/2})TiO_3$–$xBaTiO_3$ ceramics. *Solid State Communications* **2010,** *150* (33-34), 1497-1500.

179. Takenaka, T.; Maruyama, K.-i. M. K.-i.; Sakata, K. S. K., $(Bi_{1/2}Na_{1/2})TiO_3$-$BaTiO_3$ system for lead-free piezoelectric ceramics. *Japanese journal of applied physics* **1991,** *30* (9S), 2236.

180. Mahajan, A.; Zhang, H.; Wu, J.; Ramana, E. V.; Reece, M.; Yan, H., Effect of phase transitions on thermal depoling in lead-free 0.94 $(Bi_{0.5}Na_{0.5}TiO_3)$–0.06 $(BaTiO_3)$ based piezoelectrics. *The Journal of Physical Chemistry C* **2017,** *121* (10), 5709-5718.

181. Bai, W.; Shen, B.; Zhai, J.; Liu, F.; Li, P.; Liu, B.; Zhang, Y., Phase evolution and correlation between tolerance factor and electromechanical properties in BNT-based ternary perovskite compounds with calculated end-member $Bi(Me_{0.5}Ti_{0.5})O_3$ (Me = Zn, Mg, Ni, Co). *Dalton Transactions* **2016,** *45* (36), 14141-14153.

182. Ma, C.; Tan, X., Morphotropic phase boundary and electrical properties of lead-free (1−x)$BaTiO_3$−$xBi(Li_{1/3}Ti_{2/3})O_3$ ceramics. *Journal of Applied Physics* **2010,** *107* (12), 124108.

183. Lin, D.; Kwok, K.; Chan, H., Structure and electrical properties of $Bi_{0.5}Na_{0.5}TiO_3$–$BaTiO_3$–$Bi_{0.5}Li0_{.5}TiO_3$ lead-free piezoelectric ceramics. *Solid State Ionics* **2008,** *178* (37-38), 1930-1937.

184. Li, L.; Zhu, M.; Wei, Q.; Zheng, M.; Hou, Y.; Hao, J., Ferroelectric P4mm to relaxor P4bm transition and temperature-insensitive large strains in $Bi(Mg_{0.5}Ti_{0.5})O_3$-modified tetragonal $0.875Bi_{0.5}Na_{0.5}TiO_3$-$0.125BaTiO_3$ lead-free ferroelectric ceramics. *Journal of the European Ceramic Society* **2018,** *38* (4), 1381-1388.

185. Viola, G.; Ning, H.; Wei, X.; Deluca, M.; Adomkevicius, A.; Khaliq, J.; John Reece, M.; Yan, H., Dielectric relaxation, lattice dynamics and polarization mechanisms in $Bi_{0.5}Na_{0.5}TiO_3$-based lead-free ceramics. *Journal of Applied Physics* **2013,** *114* (1), 014107.

186. Anton, E.-M.; Jo, W.; Damjanovic, D.; Rödel, J., Determination of depolarization temperature of $(Bi_{1/2}Na_{1/2})TiO_3$-based lead-free piezoceramics. *Journal of Applied Physics* **2011,** *110* (9), 094108.

187. Jo, W.; Dittmer, R.; Acosta, M.; Zang, J.; Groh, C.; Sapper, E.; Wang, K.; Rödel, J., Giant electric-field-induced strains in lead-free ceramics for actuator applications–status and perspective. *Journal of Electroceramics* **2012,** *29* (1), 71-93.

188. (a) Prado, A.; Ramajo, L.; Camargo, J.; del Campo, A.; Öchsner, P.; Rubio-Marcos, F.; Castro, M., Stabilization of the morphotropic phase boundary in (1−x)$Bi_{0.5}Na_{0.5}TiO_3$–$xBaTiO_3$ ceramics through two alternative synthesis pathways. *Journal of Materials Science: Materials in Electronics* **2019,** *30* (20), 18405-18412; (b) Cho, J.-H.; Jeon, C.-J.; Lee, K.-T.; Park, J.-S.; Jeong, Y.-H.; Yun, J.-S., Electric field induced polarization and strain of $(Bi_{1/2}Na_{1/2})TiO_3$–$BaTiO_3$ ceramics. *Ceramics International* **2015,** *41* (3), 4789-4797.

189. Balakt, A. M.; Shaw, C.; Zhang, Q., Large pyroelectric properties at reduced depolarization temperature in A-site nonstoichiometry composition of lead-free $0.94Na_xBi_yTiO_3$–$0.06Ba_zTiO_3$ ceramics. *Journal of Materials Science* **2017,** *52* (12), 7382-7393.

190. Seo, I.-T.; Steiner, S.; Frömling, T., The effect of A site non-stoichiometry on $0.94(Na_yBi_x)TiO_3$-$0.06BaTiO_3$. *Journal of the European Ceramic Society* **2017,** *37* (4), 1429-1436.

191. Weyland, F.; Acosta, M.; Vögler, M.; Ehara, Y.; Rödel, J.; Novak, N., Electric field–temperature phase diagram of sodium bismuth titanate-based relaxor ferroelectrics. *Journal of materials science* **2018**, 1-8.

192. (a) Lim, J. B.; Zhang, S.; Kim, N.; Shrout, T. R., High-Temperature Dielectrics in the $BiScO_3$–$BaTiO_3$–$(K_{1/2}Bi_{1/2})TiO_3$ Ternary System. *Journal of the American Ceramic Society* **2009,** *92* (3), 679-682; (b) Ogihara, H.; Randall, C. A.; Trolier-McKinstry, S., High-energy density capacitors utilizing $0.7BaTiO_3$–$0.3BiScO_3$ ceramics. *Journal of the American Ceramic Society* **2009,** *92* (8), 1719-1724.

193. (a) Yin, J.; Zhang, Y.; Lv, X.; Wu, J., Ultrahigh energy-storage potential under low electric field in bismuth sodium titanate-based perovskite ferroelectrics. *Journal of Materials Chemistry A* **2018,** *6* (21), 9823-9832; (b) Pu, Y.; Zhang, L.; Cui, Y.; Chen, M., High Energy Storage Density and Optical Transparency of Microwave Sintered Homogeneous $(Na_{0.5}Bi_{0.5})(1{-}x)Ba_xTi(1{-}y)Sn_yO_3$ Ceramics. *ACS Sustainable Chemistry & Engineering* **2018,** *6* (5), 6102-6109; (c) Hao, J.; Xu, Z.; Chu, R.; Li, W.; Juan, D.; Peng, F., Enhanced energy-storage properties of $(1-x)[(1-y)(Bi_{0.5}Na_{0.5})TiO_3$–$y(Bi_{0.5}K_{0.5})TiO_3]$–$x(K_{0.5}Na_{0.5})NbO_3$ lead-free ceramics. *Solid State Communications* **2015,** *204*, 19-22; (d) Ding, J.; Liu, Y.; Lu, Y.; Qian, H.; Gao, H.; Chen, H.; Ma, C., Enhanced energy-storage properties of $0.89Bi_{0.5}Na_{0.5}TiO_3$–$0.06BaTiO_3$–$0.05K_{0.5}Na_{0.5}NbO_3$ lead-free anti-ferroelectric ceramics by two-step sintering method. *Materials Letters* **2014,** *114*, 107-110.

194. (a) Luo, N.; Zhang, S.; Li, Q.; Yan, Q.; Zhang, Y.; Ansell, T.; Luo, J.; Shrout, T. R., Crystallographic dependence of internal bias in domain engineered Mn-doped relaxor-$PbTiO_3$ single crystals. *Journal of Materials Chemistry C* **2016,** *4* (20), 4568-4576; (b) Zeng, J.; Zhao, K.; Shi, X.; Ruan, X.; Zheng, L.; Li, G., Large strain induced by the alignment of defect dipoles in (Bi^{3+}, Fe^{3+}) co-doped $Pb(Zr,Ti)O_3$ ceramics. *Scripta Materialia* **2018,** *142*, 20-22; (c) Dai, Y.-J.; Zhao, Y.-J.; Zhao, Z.; Zhao, Z.-H.; Zhou, Q.-W.; Zhang, X.-W., High electrostrictive strain induced by defect dipoles in acceptor-doped $(K_{0.5}Na_{0.5})NbO_3$ ceramics. *Journal of Physics D: Applied Physics* **2016,** *49* (27), 275303; (d) Xu, D.; Li, W.; Wang, L.; Wang, W.; Cao, W.; Fei, W., Large piezoelectric properties induced by doping ionic pairs in BaTiO3 ceramics. *Acta materialia* **2014,** *79*, 84-92.

195. (a) Takahashi, M., Space charge effect in lead zirconate titanate ceramics caused by the addition of impurities. *Jpn. J. Appl. Phys.* **1970,** *9* (10), 1236; (b) Warren, W.; Dimos, D.; Tuttle, B.; Nasby, R.; Pike, G., Electronic domain pinning in $Pb(Zr,Ti)O_3$ thin films and its role in fatigue. *Applied Physics Letters* **1994,** *65* (8), 1018-1020.

196. (a) Ren, X., Large electric-field-induced strain in ferroelectric crystals by point-defect-mediated reversible domain switching. *Nature materials* **2004,** *3* (2), 91-94; (b) Zhang, L.; Chen, W.; Ren, X., Large recoverable electrostrain in Mn-doped (Ba,Sr)TiO_3 ceramics. *Applied Physics Letters* **2004,** *85* (23), 5658-5660; (c) Vani, K.; Anil, A.; Kumar, V., Enhanced electrostrain in Cu^{2+}-doped $Ba_{0.8}Sr_{0.2}TiO_3$. *Ferroelectrics* **2019,** *550* (1), 136-140; (d) Zhao, Z.; Dai, Y.; Li, X.; Zhao, Z.; Zhang, X., The evolution mechanism of defect dipoles and high strain in MnO_2-doped KNN lead-free ceramics. *Applied Physics Letters* **2016,** *108* (17), 172906.

197. Wu, M.; Zhu, Q.; Li, J.; Song, D.; Wu, H.; Guo, M.; Gao, J.; Bai, Y.; Feng, Y.; Pennycook, S. J., Electrocaloric effect in ferroelectric ceramics with point defects. *Applied Physics Letters* **2019,** *114* (14), 142901.

198. Hall, D.; Ben-Omran, M., Ageing of high field dielectric properties in-based piezoceramics. *Journal of Physics: Condensed Matter* **1998,** *10* (40), 9129.

199. Genenko, Y. A.; Glaum, J.; Hoffmann, M. J.; Albe, K., Mechanisms of aging and fatigue in ferroelectrics. *Materials Science and Engineering: B* **2015,** *192*, 52-82.

200. (a) Otsuka, K.; Ren, X., Recent developments in the research of shape memory alloys. *Intermetallics* **1999,** *7* (5), 511-528; (b) Sun, D.; Ren, X.; Otsuka, K., Stabilization effect in ferroelectric materials during aging in ferroelectric state. *Applied Physics Letters* **2005,** *87* (14), 142903; (c) Ren, X.; Otsuka, K., Universal symmetry property of point defects in crystals. *Phys. Rev. Lett.* **2000,** *85* (5), 1016.

201. (a) Guo, Y.; Yan, Z.; Zhang, N.; Cheng, W.; Liu, J.-M., Ferroelectric aging behaviors of $BaTi_{0.995}Mn_{0.005}O_3$ ceramics: grain size effects. *Applied Physics A* **2012,** *107* (1), 243-248; (b) Shi, X.; Wang, J.; Zhao, Y.; Liu, S.; Zhang, L., Competition effects of grain boundary and aging on the hysteresis loop behavior of $(Ba_{0.8}Sr_{0.2})(Ti,Mn)O_3$ ceramics. *Ceramics International* **2016,** *42* (4), 4734-4738.

202. Polfus, J. M.; Yildiz, B.; Tuller, H. L., Origin of fast oxide ion diffusion along grain boundaries in Sr-doped $LaMnO_3$. *Physical Chemistry Chemical Physics* **2018,** *20* (28), 19142-19150.

203. (a) Chen, W.; Zhao, X.; Sun, J.; Zhang, L.; Zhong, L., Effect of the Mn doping concentration on the dielectric and ferroelectric properties of different-routes-fabricated $BaTiO_3$-based ceramics. *Journal of Alloys and Compounds* **2016,** *670*, 48-54; (b) Chen, L.; Fan, H.; Zhang, S., Investigation of MnO_2-doped $(Ba,Ca)TiO_3$ lead-free ceramics for high power piezoelectric applications. *Journal of the American Ceramic Society* **2017,** *100* (8), 3568-3576.

204. Zhang, L.; Liu, W.; Chen, W.; Ren, X.; Sun, J.; Gurdal, E. A.; Ural, S. O.; Uchino, K., Mn dopant on the “domain stabilization” effect of aged $BaTiO_3$ and $PbTiO_3$-based piezoelectrics. *Applied Physics Letters* **2012,** *101* (24), 242903.

205. Ng, Y. S.; Alexander, S., Structural studies of manganese stabilised lead-zirconate-titanate. *Ferroelectrics* **1983,** *51* (1), 81-86.

206. (a) Tan, Y.; Zhang, J.; Wang, C., Aging behaviours of CuO modified BaTiO3 ceramics. *Advances in Applied Ceramics* **2014,** *113* (4), 223-227; (b) Glaum, J.; Genenko, Y. A.; Kungl, H.; Ana Schmitt, L.; Granzow, T., De-aging of Fe-doped lead-zirconate-titanate ceramics by electric field cycling: 180-vs. non-180 domain wall processes. *Journal of Applied Physics* **2012,** *112* (3), 034103; (c) Zhao, X.; Chen, W.; Zhang, L.; Zhong, L., The effect of the bipolar field on the aging behavior and the associated properties of the Mn-doped BaTiO3 ceramics. *Journal of alloys and compounds* **2015,** *618*, 707-711.

207. Cha, S. H.; Han, Y. H., Effects of Mn doping on dielectric properties of Mg-doped $BaTiO_3$. *Journal of applied physics* **2006,** *100* (10), 104102.

208. Chikada, S.; Kubota, T.; Honda, A.; Higai, S. i.; Motoyoshi, Y.; Wada, N.; Shiratsuyu, K., Interactions between Mn dopant and oxygen vacancy for insulation performance of $BaTiO_3$. *Journal of Applied Physics* **2016,** *120* (14), 142122.

209. (a) Yuan, Y.-J.; Zhang, J.-Y.; Yu, Z.-T.; Feng, J.-Y.; Luo, W.-J.; Ye, J.-H.; Zou, Z.-G., Impact of ligand modification on hydrogen photogeneration and light-harvesting applications using cyclometalated iridium complexes. *Inorganic chemistry* **2012,** *51* (7), 4123-4133; (b) Li, J.; Lv, J.; Zhang, D.; Zhang, L.; Hao, X.; Wu, M.; Xu, B.-X.; Otonicar, M.; Lookman, T.; Dkhil, B., Doping-induced Polar Defects Improve the Electrocaloric Performance of $Ba_{0.9}Sr_{0.1}Hf_{0.1}Ti_{0.9}O_3$. *Physical Review Applied* **2021,** *16* (1), 014033.

210. (a) Xiang, N.; Xiaodong, J.; Chen, X.; Li, H.; Liang, W.; Yingbang, Y.; Tao, T.; Liang, B.; Sheng-Guo, L., Enhanced electrocaloric effect at room temperature in Mn^{2+} doped lead-free $(BaSr)TiO_3$ ceramics via a direct measurement. *Journal of Advanced Ceramics* **2021,** *10* (3), 482-492; (b) Li, H.-X.; Jian, X.-D.; Niu, X.; Yao, Y.-B.; Tao, T.; Liang, B.; Lu, S.-G., Direct measurement of enhanced electrocaloric effect in Mn^{2+} doped lead-free $Ba(ZrTi)O_3$ ceramics. *Scripta Materialia* **2020,** *176*, 67-72.

211. Liu, Y.; Scott, J. F.; Dkhil, B., Direct and indirect measurements on electrocaloric effect: Recent developments and perspectives. *Applied Physics Reviews* **2016,** *3* (3), 031102.

212. Guo, Y.; Liu, J.-M.; Guo, Y.; Wei, T.; Guo, Y.; Zhang, N., External field effects on aging phenomenon of acceptor-doped $BaTiO_3$ ceramics. *AIP Advances* **2015,** *5* (9), 097107.

213. Wang, J.; Zhao, Y.; Shi, X.; Zhang, L., Effect of Mn dopant on the grain size and electrical properties of $(Ba,Sr)TiO_3$ ceramics. *Journal of Materials Science: Materials in Electronics* **2018,** *29* (13), 11575-11580.

214. (a) Hou, Y.; Zhu, M.; Gao, F.; Wang, H.; Wang, B.; Yan, H.; Tian, C., Effect of MnO_2 addition on the structure and electrical properties of $Pb(Zn_{1/3}Nb_{2/3})_{0.20}(Zr_{0.50}Ti_{0.50})_{0.80}O_3$ ceramics. *Journal of the American Ceramic Society* **2004,** *87* (5), 847-850; (b) Kamiya, T.; Suzuki, T.; Tsurumi, T.; Daimon, M., Effects of manganese addition on piezoelectric properties of $Pb(Zr_{0.5}Ti_{0.5})O_3$. *Japanese journal of applied physics* **1992,** *31* (9S), 3058.

215. Jiang, M.; Lin, Q.; Lin, D.; Zheng, Q.; Fan, X.; Wu, X.; Sun, H.; Wan, Y.; Wu, L., Effects of MnO_2 and sintering temperature on microstructure, ferroelectric, and piezoelectric properties of $Ba_{0.85}Ca_{0.15}Ti_{0.90}Zr_{0.10}O_3$ lead-free ceramics. *Journal of Materials Science* **2013,** *48* (3), 1035-1041.

216. (a) Arlt, G.; Hennings, D.; De With, G., Dielectric properties of fine-grained barium titanate ceramics. *Journal of applied physics* **1985,** *58* (4), 1619-1625; (b) Ghosh, D.; Sakata, A.; Carter, J.; Thomas, P. A.; Han, H.; Nino, J. C.; Jones, J. L., Domain wall displacement is the origin of superior permittivity and piezoelectricity in $BaTiO_3$ at intermediate grain sizes. *Advanced Functional Materials* **2014,** *24* (7), 885-896.

217. Kolodiazhnyi, T.; Petric, A., Analysis of point defects in polycrystalline BaTiO3 by electron paramagnetic resonance. *Journal of Physics and Chemistry of Solids* **2003,** *64* (6), 953-960.

218. (a) Lu, D. Y.; Sun, X. Y. In *A novel electron paramagnetic resonance phenomenon in a barium stronium titanate ceramic*, Advanced Materials Research, Trans Tech Publ: 2011; pp 1050-1054; (b) John, J.; Dhananjaya, M.; Suresh, S.; Savitha Pillai, S.; Sahoo, M.; Hussain, O.; Philip, R.; Mahadevan Pillai, V., Effect of manganese doping on the structural, morphological, optical, electrical, and magnetic properties of $BaSnO_3$. *Journal of Materials Science: Materials in Electronics* **2020,** *31*, 11159-11176.

219. Berksoy-Yavuz, A.; Mensur-Alkoy, E.; Erdem, E.; Alkoy, S., Electrical properties, EPR analyses and defect chemistry of Mn-doped 0.675 PMN-0.325 PT piezoceramics. *Ceramics International* **2020,** *46* (18), 28980-28986.

220. Kaftelen, H.; Kanar, D. E.; Repp, S.; Weber, S.; Erdem, E., Investigation of Mn-doped sodium-potassium niobate ($(K,Na)NbO_3$) ceramics by EPR and impedance spectroscopic methods. *Ferroelectrics* **2016,** *494* (1), 11-18.

221. Elissalde, C.; Chung, U. C.; Artemenko, A.; Estournes, C.; Costes, R.; Pate, M.; Ganne, J. P.; Waechter, S.; Maglione, M., Stoichiometry and grain boundaries control by spark plasma sintering in $Ba_{0.6}Sr_{0.4}TiO_3$:Mn/MgO composites. *Journal of the American Ceramic Society* **2012,** *95* (10), 3239-3245.

222. Zhang, L.; Hao, H.; Zhang, S.; Lanagan, M. T.; Yao, Z.; Xu, Q.; Xie, J.; Zhou, J.; Cao, M.; Liu, H., Defect structure-electrical property relationship in Mn-doped calcium strontium titanate dielectric ceramics. *J. Am. Ceram. Soc.* **2017,** *100* (10), 4638-4648.

223. (a) Gao, L.; Huang, Y.; Hu, Y.; Du, H., Dielectric and ferroelectric properties of $(1-x)BaTiO_3–xBi_{0.5}Na_{0.5}TiO_3$ ceramics. *Ceramics International* **2007,** *33* (6), 1041-1046; (b) Datta, K.; Roleder, K.; Thomas, P., Enhanced tetragonality in lead-free piezoelectric $(1-x)BaTiO_3–xNa_{1/2}Bi_{1/2}TiO_3$ solid solutions where $x = 0.05–0.40$. *Journal of Applied Physics* **2009,** *106* (12), 123512.

224. Yoon, S.-H.; Kim, M.-Y.; Kim, D., Influence of tetragonality (c/a) on dielectric nonlinearity and direct current (dc) bias characteristics of $(1-x)BaTiO_3-xBi_{0.5}Na_{0.5}TiO_3$ ceramics. *Journal of Applied Physics* **2017,** *122* (15), 154103.

225. Takeda, H.; Aoto, W.; Shiosaki, T., $BaTiO_3–(Bi_{1/2}Na_{1/2})TiO_3$ solid-solution semiconducting ceramics with Tc>130° C. *Applied physics letters* **2005,** *87* (10), 102104.

226. Yao, G.; Wang, X.; Wu, Y.; Li, L., Nb-Doped 0.9$BaTiO_3$–0.1$(Bi_{0.5}Na_{0.5})TiO_3$ Ceramics with Stable Dielectric Properties at High Temperature. *Journal of the American Ceramic Society* **2012,** *95* (2), 614-618.

227. (a) Wang, S. F.; Dayton, G. O., Dielectric properties of fine-grained barium titanate based X7R materials. *Journal of the American Ceramic Society* **1999,** *82* (10), 2677-2682; (b) Lee, W. H.; Su, C. Y., Improvement in the Temperature Stability of a $BaTiO_3$-Based Multilayer Ceramic Capacitor by Constrained Sintering. *Journal of the American Ceramic Society* **2007,** *90* (10), 3345-3348.

228. (a) Song, T. Y.; Sung, W.; Kim, H.; Kim, B.; Kwon, D.-K., Wrapping assembly of $BaTiO_3$ nanoparticles with $(Bi_{0.5}Na_{0.5})TiO_3$ nanosheets: A noble processing for nanograined BT-BNT complex perovskite relaxors. *physica status solidi (a)*; (b) Chen, L.; Wang, H.; Zhao, P.; Shen, Z.; Zhu, C.; Cen, Z.; Li, L.; Wang, X., Effect of MnO2 on the dielectric properties of Nb-doped $BaTiO_3$-$(Bi_{0.5}Na_{0.5})TiO_3$ ceramics for X9R MLCC applications. *J. Am. Ceram. Soc.* **2019,** *102* (5), 2781-2790; (c) Shen, Z.; Wang, X.; Li, L., Dielectric properties and microstructures of Ta-doped $BaTiO_3$–$(Bi_{0.5}Na_{0.5})TiO_3$ ceramics for X9R applications. *Journal of Materials Science: Materials in Electronics* **2017,** *28* (4), 3768-3773; (d) Wu, Y.; Pu, Y.; Zhang, P.; Zhao, J.; Luo, Y., The relaxor behavior and dielectric temperature stability of 0.85$BaTiO_3$–0.15 $Na_{0.5}Bi_{0.5}TiO_3$–x$LiBa_2Nb_5O_{15}$ ceramics. *Materials Letters* **2015,** *155*, 134-137; (e) Wang, S.-F.; Hsu, Y.-F.; Hung, Y.-W.; Liu, Y.-X., Effect of Ta_2O_5 and Nb_2O_5 dopants on the stable dielectric properties of $BaTiO_3$–$(Bi_{0.5}Na_{0.5})TiO_3$-based materials. *Applied Sciences* **2015,** *5* (4), 1221-1234.

229. Jaffe, B.; Cook, W.; Jaffe, H., The piezoelectric effect in ceramics. *Piezoelectric Ceramics* **1971**, 7-21.

230. Rao, B. N.; Khatua, D. K.; Garg, R.; Senyshyn, A.; Ranjan, R., Structural crossover from nonmodulated to long-period modulated tetragonal phase and anomalous change in ferroelectric properties in the lead-free piezoelectric $Na_{1/2}Bi_{1/2}TiO_3$− $BaTiO_3$. *Physical Review B* **2015,** *91* (21), 214116.

231. Chu, P.; Chen, D.; Wang, Y.; Xie, Y.; Yan, Z.; Wan, J.; Liu, J.-M.; Li, J., Kinetics of 90 domain wall motions and high frequency mesoscopic dielectric response in strained ferroelectrics: a phase-field simulation. *Sci. Rep.* **2014,** *4* (1), 1-7.

232. Leist, T.; Granzow, T.; Jo, W.; Rödel, J., Effect of tetragonal distortion on ferroelectric domain switching: a case study on La-doped $BiFeO_3$–$PbTiO_3$ ceramics. *Journal of Applied Physics* **2010,** *108* (1), 014103.

233. (a) Merz, W. J., Double Hysteresis Loop of BaTi O 3 at the Curie Point. *Physical Review* **1953,** *91* (3), 513; (b) Srivastava, N.; Weng, G., A theory of double hysteresis for ferroelectric crystals. *Journal of applied physics* **2006,** *99* (5), 054103.

234. Ott, J. B.; Boerio-Goates, J., *Chemical Thermodynamics: Advanced Applications: Advanced Applications*. Elsevier: 2000.

235. Bai, Y.; Ding, K.; Zheng, G.-P.; Shi, S.-Q.; Cao, J.-L.; Qiao, L., The electrocaloric effect around the orthorhombic-tetragonal first-order phase transition in $BaTiO_3$. *Aip Advances* **2012,** *2* (2), 022162.

236. Saito, Y.; Takao, H.; Tani, T.; Nonoyama, T.; Takatori, K.; Homma, T.; Nagaya, T.; Nakamura, M., Lead-free piezoceramics. *Nature* **2004,** *432* (7013), 84-87.

237. Park, S.-E.; Shrout, T. R., Ultrahigh strain and piezoelectric behavior in relaxor based ferroelectric single crystals. *Journal of applied physics* **1997,** *82* (4), 1804-1811.

238. (a) Bobrek, I.; Berksoy-Yavuz, A.; Kaya, M. Y.; Alkoy, S.; Okatan, M. B.; Misirlioglu, I. B.; Mensur-Alkoy, E., Temperature Dependent Electrical and Electrocaloric Properties of Textured 0.72PMN-0.28PT Ceramics. *Integrated Ferroelectrics* **2021,** *223* (1), 214-227; (b) Mensur-Alkoy, E.; Okatan, M. B.; Aydin, E.; Kilic, Y.; Misirlioglu, I. B.; Alkoy, S., Effect of texture on the electrical and electrocaloric properties of $0.90Pb(Mg_{1/3}Nb_{2/3})O_3$–$0.10PbTiO_3$ relaxor ceramics. *Journal of Applied Physics* **2020,** *128* (8), 084102.

239. Le Goupil, F.; Bennett, J.; Axelsson, A.-K.; Valant, M.; Berenov, A.; Bell, A. J.; Comyn, T. P.; Alford, N. M., Electrocaloric enhancement near the morphotropic phase boundary in lead-free NBT-KBT ceramics. *Applied Physics Letters* **2015,** *107* (17), 172903.

240. Otoničar, M.; Škapin, S.; Spreitzer, M.; Suvorov, D., Compositional range and electrical properties of the morphotropic phase boundary in the $Na_{0.5}Bi_{0.5}TiO_3$–$K_{0.5}Bi_{0.5}TiO_3$ system. *Journal of the European Ceramic Society* **2010,** *30* (4), 971-979.

241. Sun, S.; Liu, H.; Fan, L.; Ren, Y.; Xing, X.; Chen, J., Structural origin of size effect on piezoelectric performance of $Pb(Zr,Ti)O_3$. *Ceramics International* **2021,** *47* (4), 5256-5264.

242. Zhang, H.; Xu, P.; Patterson, E.; Zang, J.; Jiang, S.; Rödel, J., Preparation and enhanced electrical properties of grain-oriented $(Bi_{1/2}Na_{1/2})TiO_3$-based lead-free incipient piezoceramics. *Journal of the European Ceramic Society* **2015,** *35* (9), 2501-2512.

243. Cao, W.; Li, W.; Xu, D.; Hou, Y.; Wang, W.; Fei, W., Enhanced electrocaloric effect in lead-free NBT-based ceramics. *Ceramics International* **2014,** *40* (7), 9273-9278.

244. Wei, Q.; Fulanovic, L.; Lalitha, K. V.; Zheng, M.; Hou, Y.; Zhu, M.; Liu, L.; Chang, Y.; Xue, R., Large electrocaloric effect with ultrawide temperature span in $Na_{1/2}Bi_{1/2}TiO_3$-based lead-free ceramics. *Journal of the American Ceramic Society* **2022,** *105* (5), 3312-3321.

APPENDIX A

Table A.1. Crystal systems and corresponding 32 crystallographic point groups

Crystal System	*Crystallographic Point Groups*						
Triclinic	1	-1					
Monoclinic	2	m	2/m				
Orthorhombic	222	mm2	mmm				
Tetragonal	4	-4	4/m	422	4mm	-42m	4/mmm
Rhombohedral	3	-3	32	3m	-3m		
Hexagonal	6	-6	6/m	622	6mm	-62m	6/mmm
Cubic	23	m-3	432	-43m	m-3m		

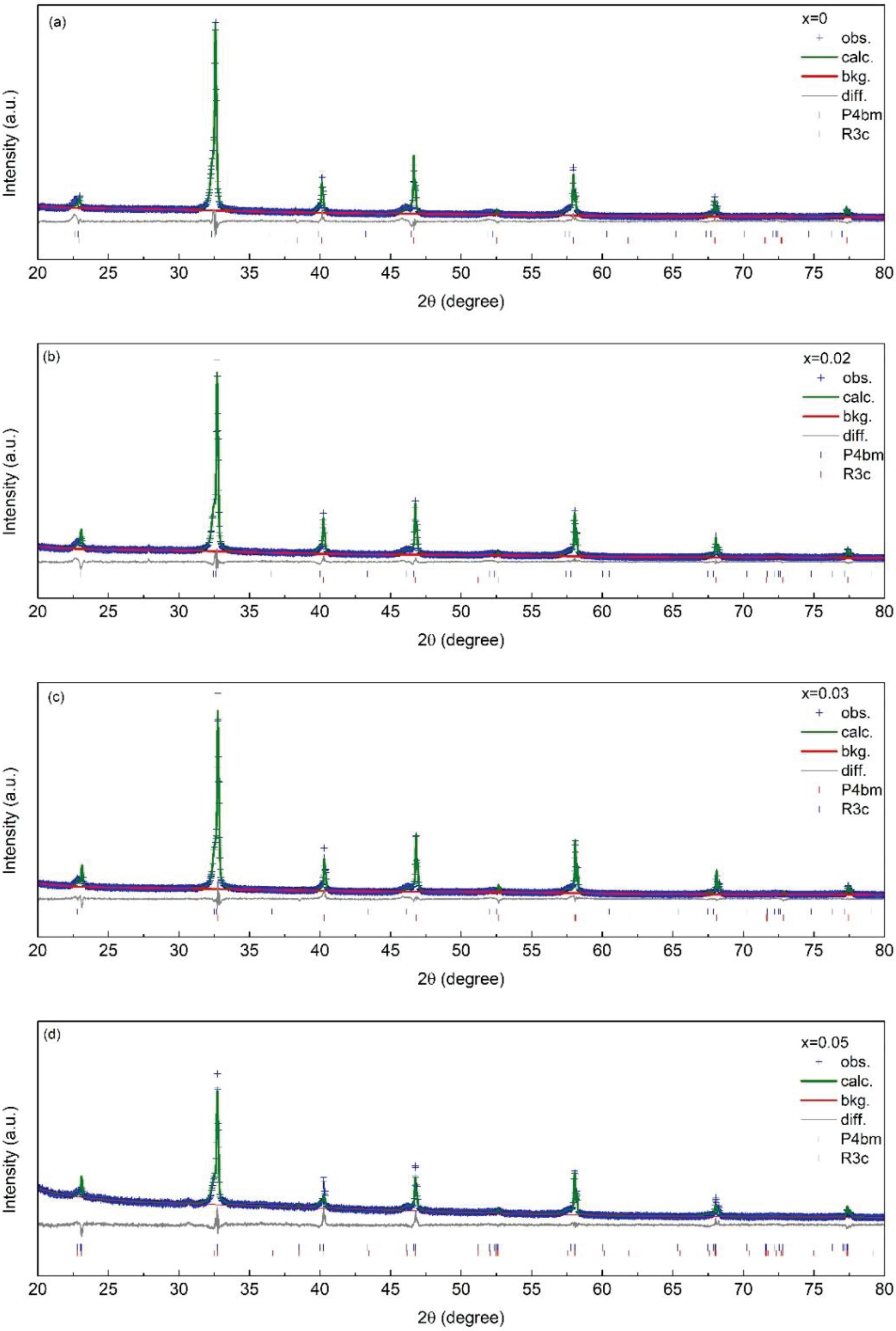

Figure A.1. XRD Rietveld refinement results of all (1-x)(0.92NBT-0.08BT)-xBLT compositions; (a) x = 0, (b) x = 0.02, (c) x = 0.03, (d) x = 0.05.

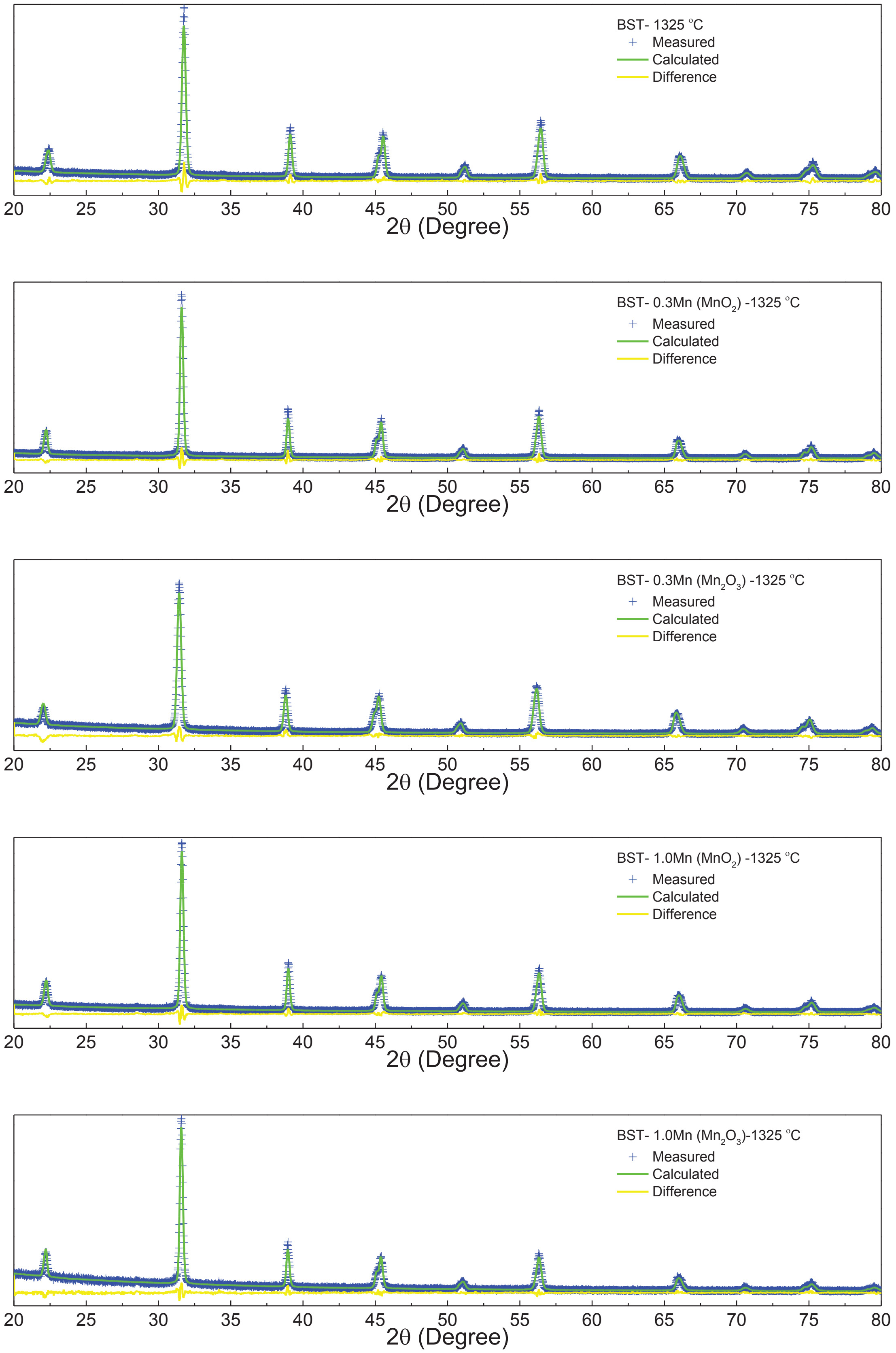

Figure A.2. XRD Rietveld refinement results of $(Ba_{0.95}Sr_{0.05})(Mn_xTi_{1-x})O_3$ (BST-100xMn) ceramics sintered at 1325 °C.

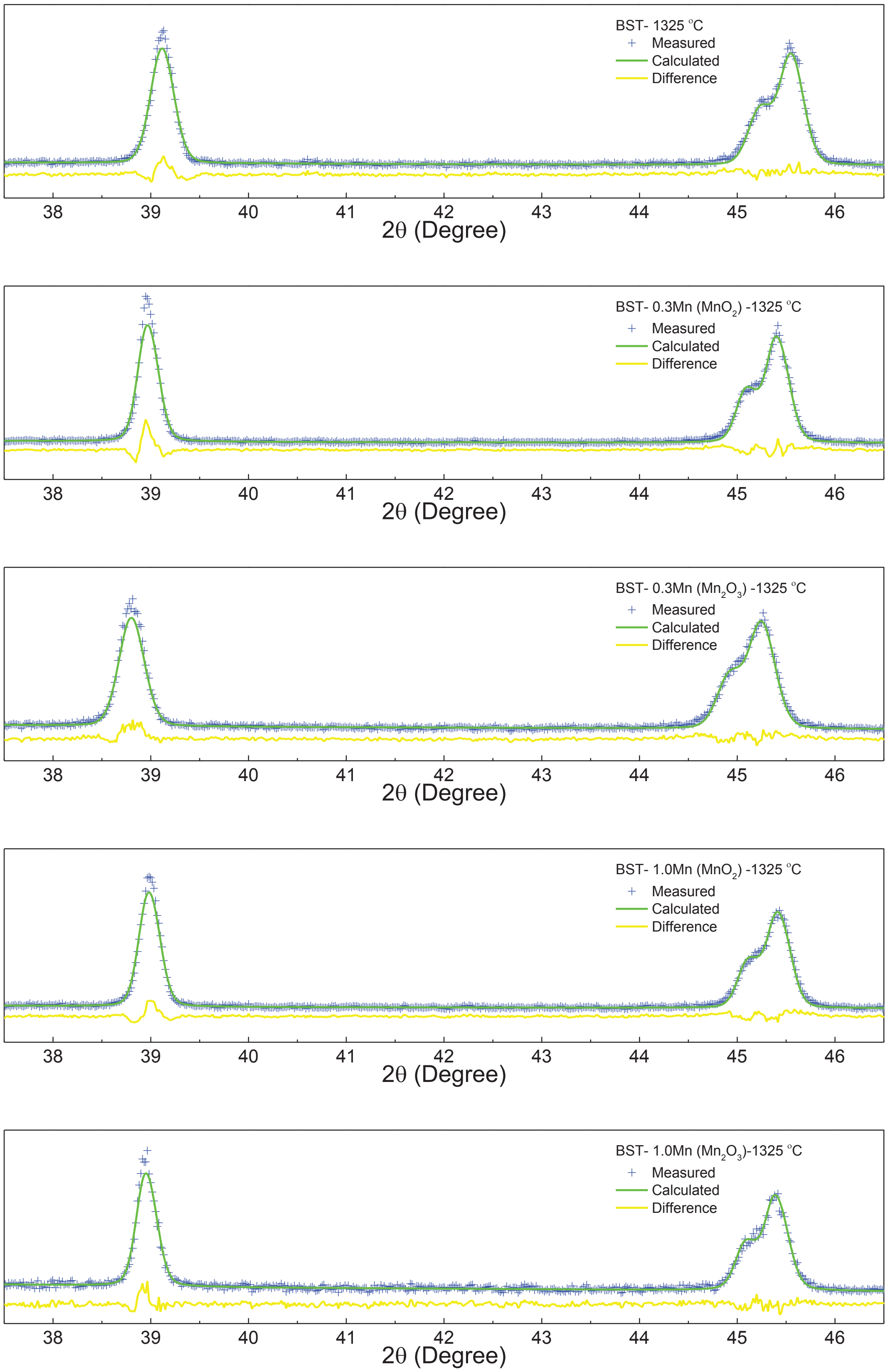

Figure A.3. XRD patterns zoomed between 37.5° - 46.5° and Rietveld refinement results of $(Ba_{0.95}Sr_{0.05})(Mn_xTi_{1-x})O_3$ (BST-100xMn) ceramics sintered at 1325 °C.

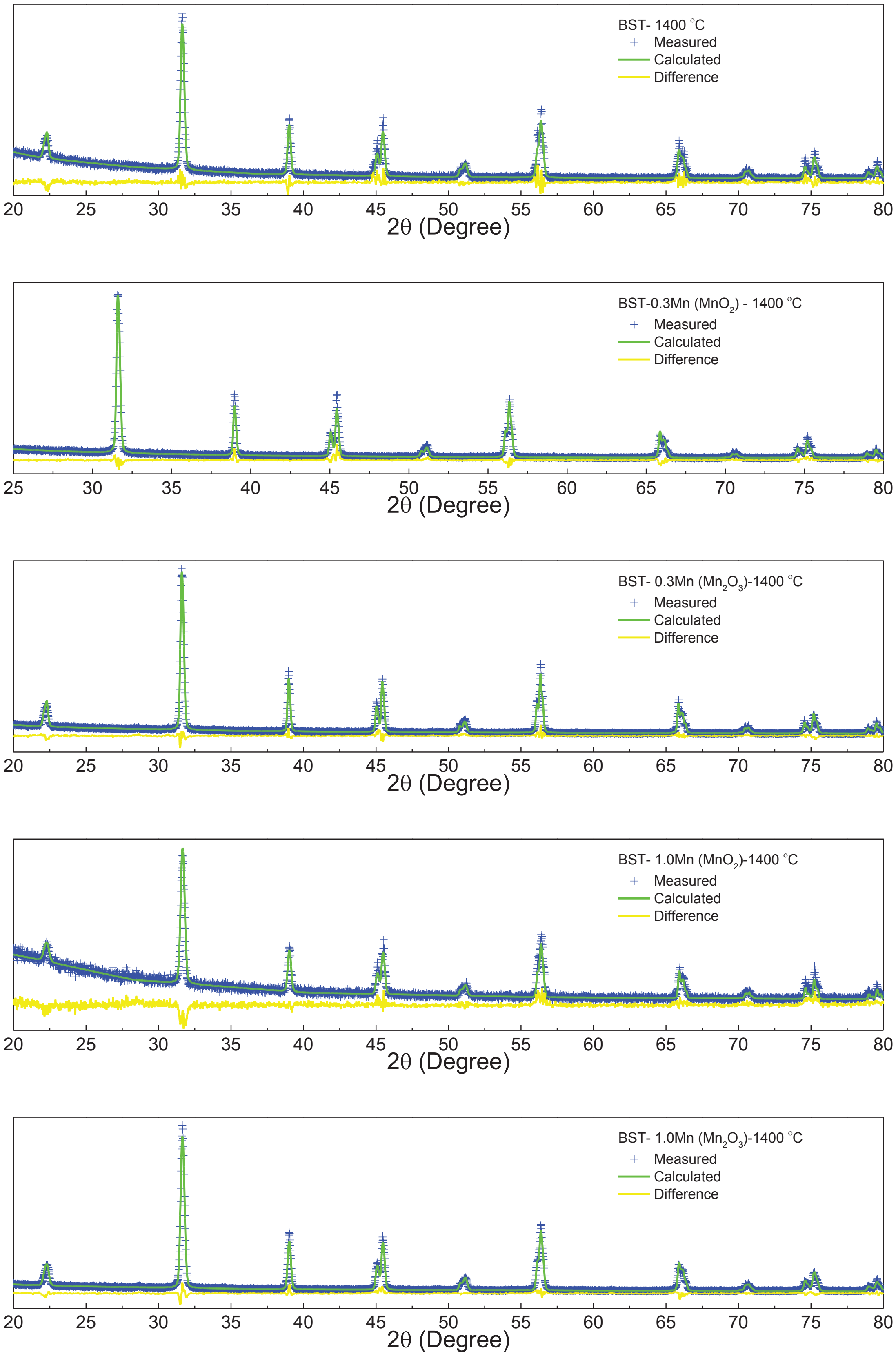

Figure A.4. XRD Rietveld refinement results of (Ba$_{0.95}$Sr$_{0.05}$)(Mn$_x$Ti$_{1-x}$)O$_3$ (BST-100xMn) ceramics sintered at 1400 °C.

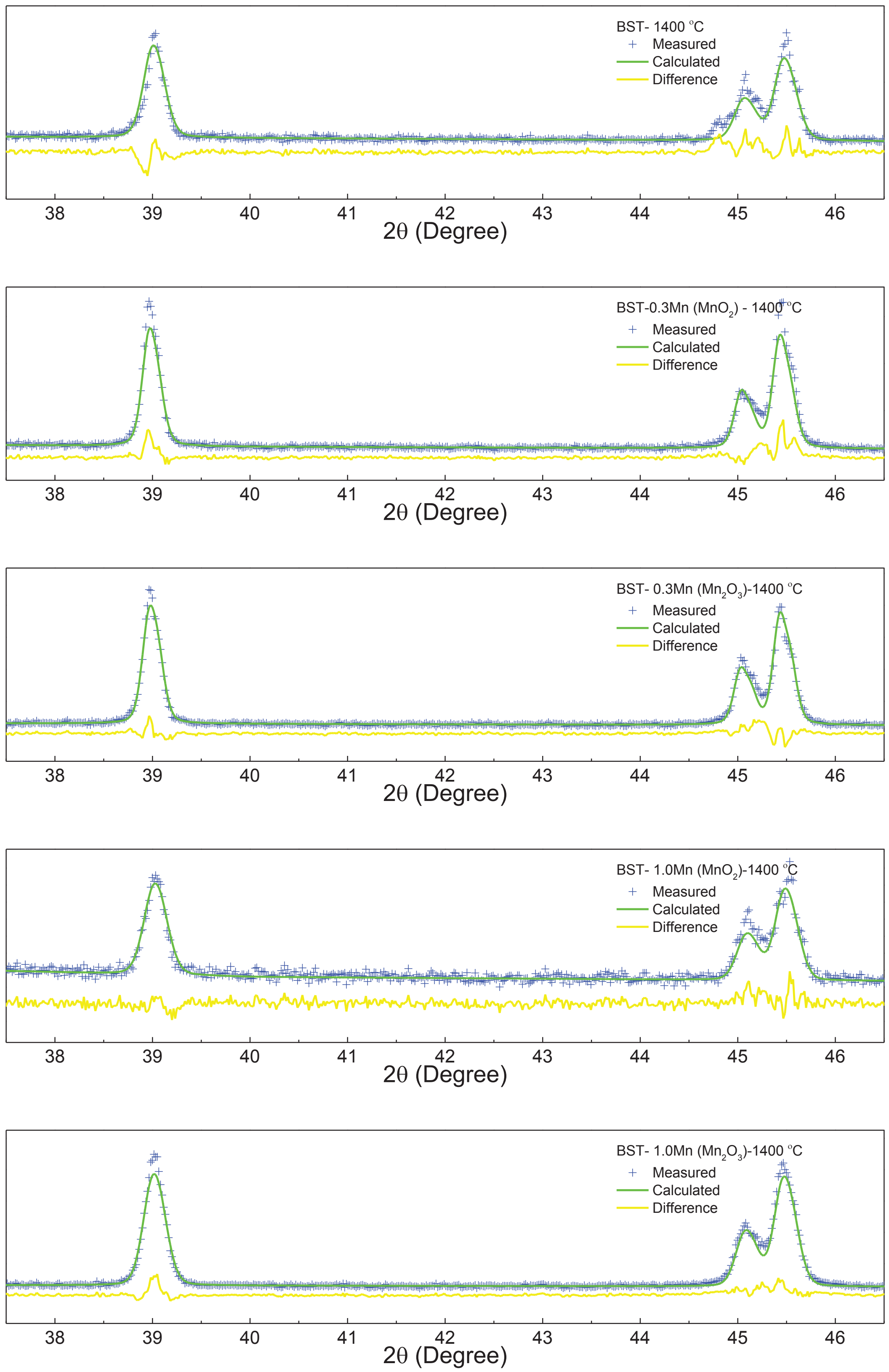

Figure A.5. XRD patterns zoomed between 37.5° - 46.5° and Rietveld refinement results of $(Ba_{0.95}Sr_{0.05})(Mn_xTi_{1-x})O_3$ (BST-100xMn) ceramics sintered at 1400 °C.

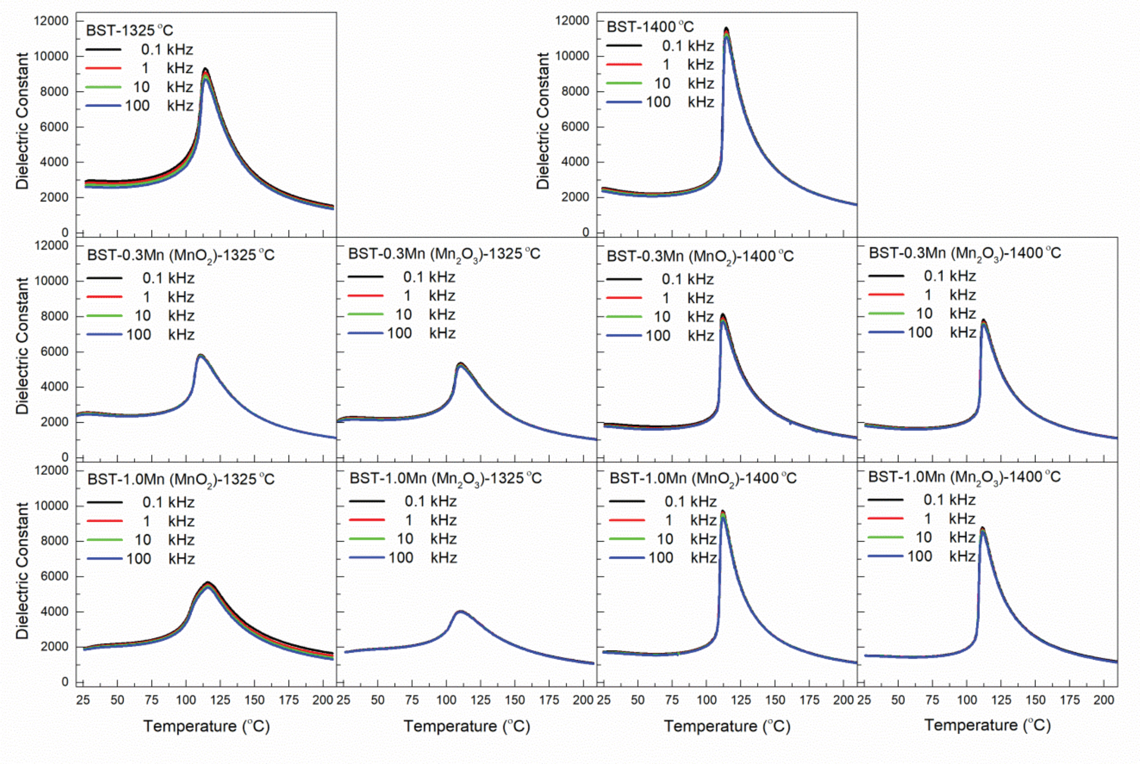

Figure A.6. Temperature dependent dielectric constants of all BST-Mn samples at different frequencies.

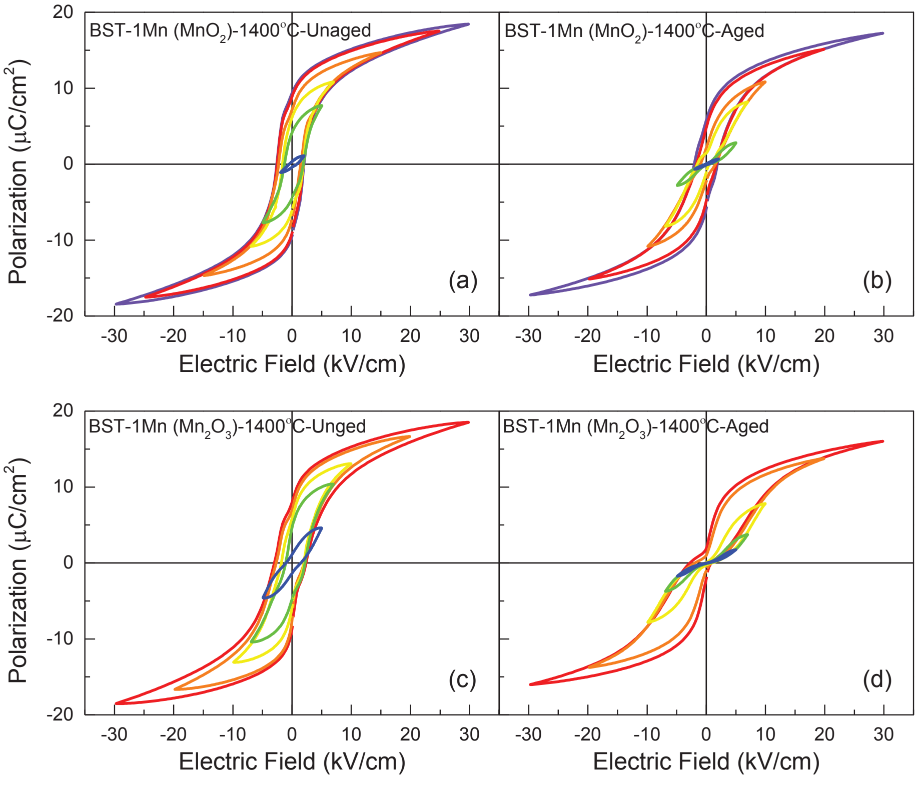

Figure A.7. Hysteresis behaviors of BST-Mn samples under different applied fields.

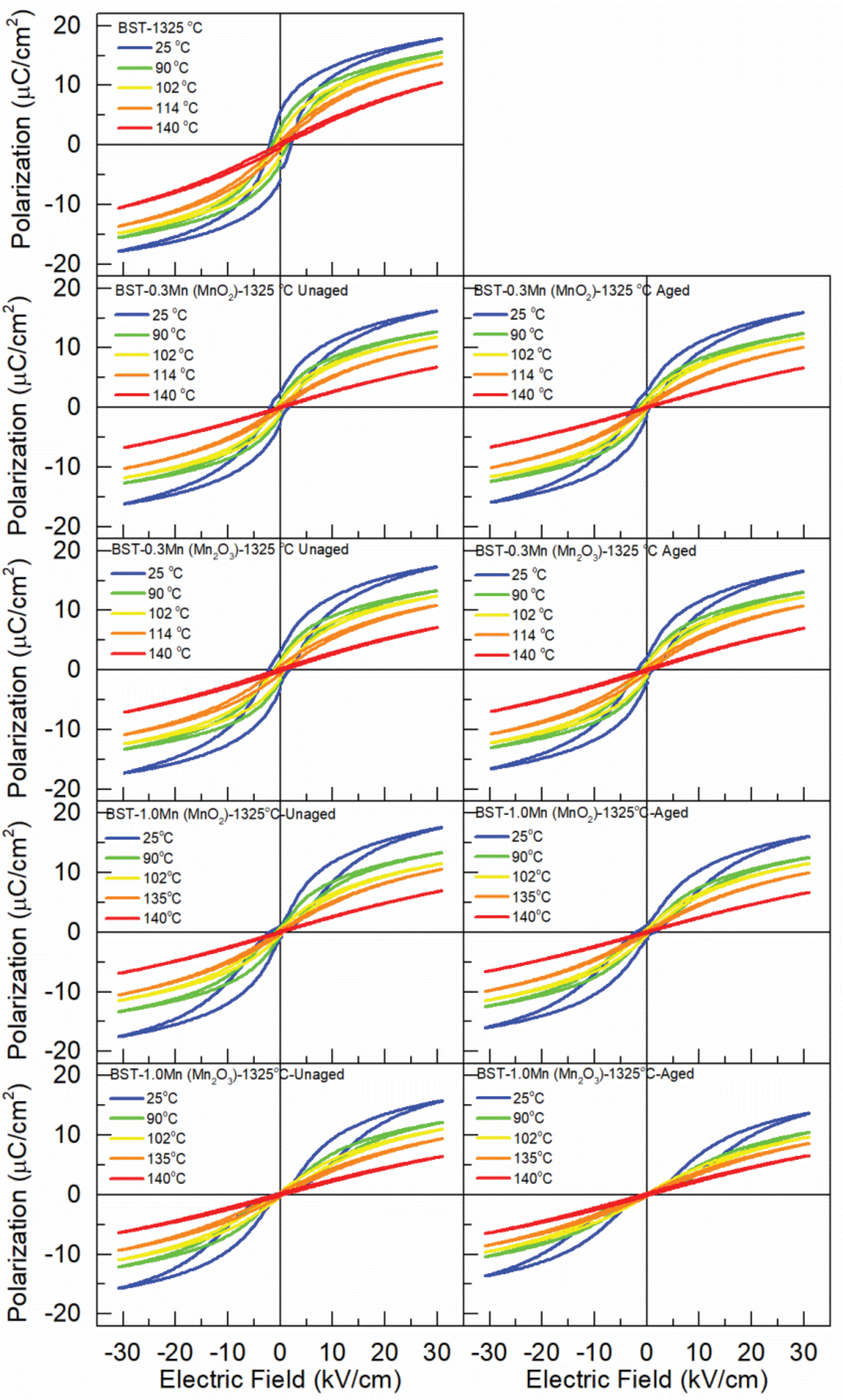

Figure A.8. Temperature dependent P-E loops of BST-Mn samples sintered at 1325 ºC.

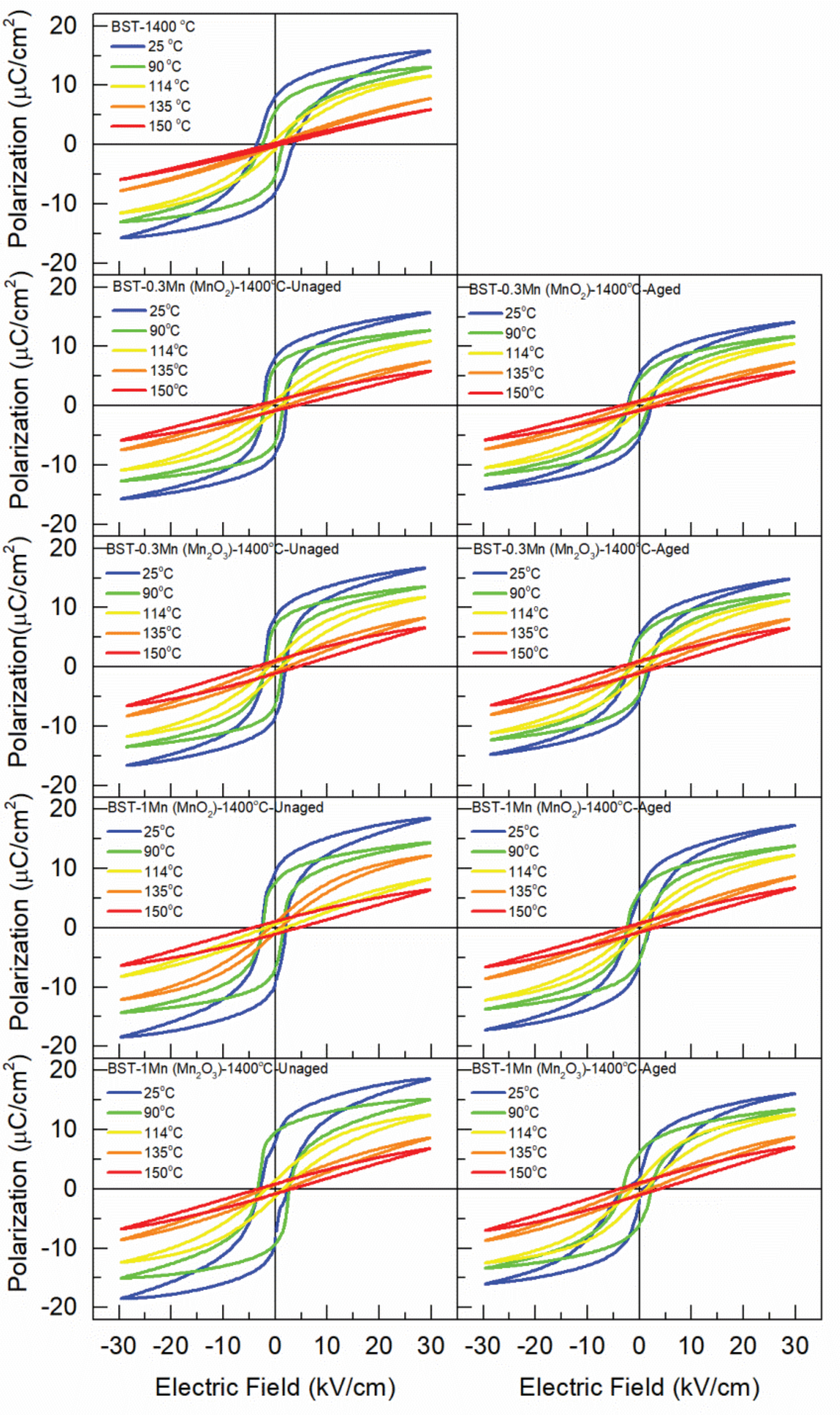

Figure A.9. Temperature dependent P-E loops of BST-Mn samples sintered at 1400 ºC.

VITA

Name, Surname: Merve Karakaya

EDUCATION

MSc in Physics, Izmir Institute of Technology, 2015

BSc in Physics, Dokuz Eylül University, 2010

WORK EXPERIENCE

Year, Place, Enrollment

2016-2023, Izmir Institute of Technology, Research Assistant

AWARDS

First graduation degree in BSc, Department of Physics, Dokuz Eylül University, 2010

PUBLICATIONS

1. In preparation: Muhammet Ali Ünal, Merve Karakaya, Tuğçe Irmak, Gökçe Yıldırım Özarslan, Murat Avcı, Lovro Fulanovic, Ender Suvacı, Umut Adem, "Electrocaloric effect of tape cast and grain oriented NBT-KBT ceramics"
2. In preparation: MerveKarakaya, İremGürbüz, UmutAdem. " Enhancement of Electrocaloric Effect of BT-NBT Ceramics by Improving Tetragonality"
3. In revision: Merve Karakaya, Emre Erdem, Yaşar Akdoğan and Umut Adem. "Effects of Different Manganese-Oxide Precursors on the Ferroelectric Aging and Electrocaloric Properties of Mn-Doped $Ba_{0.95}Sr_{0.05}TiO_3$ Ceramics" *Journal of the European Ceramic Society* (November 4, 2022)
4. Hatice Sule Coban Tetik, Ender Suvaci, A.Murat Avci, Umut Adem, Merve Karakaya "Development of Textured Lead Free NBT-Based Piezoelectric Materials in a Matrix, Synthesized by an Alternative Route, via Templated Grain Growth." *Journal of Materials Science: Materials in Electronics* (Accepted: December 6, 2022)
5. Merve Karakaya and Umut Adem. "Enhanced room temperature energy storage density of $Bi(Li_{1/3}Ti_{2/3})O_3$ substituted $Bi_{0.5}Na_{0.5}TiO_3$–$BaTiO_3$ ceramics." *Journal of Physics D: Applied Physics* 54.27 (2021): 275501.
6. Serafetin Demic, Ahmet Nuri Ozcivan, Mustafa Can, Cebrail Ozbek and Merve Karakaya "Recent progresses in perovskite solar cells." *Nanostructured solar cells* (2017): 277-304.
7. Merve Karakaya, Elif Bilgilisoy, Ozan Arı and Yusuf Selamet "Surface roughness estimation of MBE grown CdTe/GaAs(211)B by ex-situ spectroscopic ellipsometry." *AIP Advances* 6.7 (2016): 075111.
8. Ozan Arı, Mustafa Polat, Merve Karakaya and Yusuf Selamet "Growth and characterization of CdTe absorbers on GaAs by MBE for high concentration PV solar cells." *physica status solidi (c)* 12.9-11 (2015): 1211-1214.
9. Elif Bilgilisoy, Selin Özden, Emine Bakali, Merve Karakaya and Yusuf Selamet "Characterization of CdTe growth on GaAs using different etching techniques." *Journal of Electronic Materials* 44.9 (2015): 3124-3133.